



**HAL**  
open science

# Raman spectroscopy of soot produced in low pressure flames : ex situ Analyses and Online Gas Phase Studies

Thi Kim Cuong Le

► **To cite this version:**

Thi Kim Cuong Le. Raman spectroscopy of soot produced in low pressure flames : ex situ Analyses and Online Gas Phase Studies. Astrophysics [astro-ph]. Université Paris-Saclay, 2017. English. NNT : 2017SACLS068 . tel-01968017v1

**HAL Id: tel-01968017**

**<https://theses.hal.science/tel-01968017v1>**

Submitted on 2 Jan 2019 (v1), last revised 7 Jan 2019 (v2)

**HAL** is a multi-disciplinary open access archive for the deposit and dissemination of scientific research documents, whether they are published or not. The documents may come from teaching and research institutions in France or abroad, or from public or private research centers.

L'archive ouverte pluridisciplinaire **HAL**, est destinée au dépôt et à la diffusion de documents scientifiques de niveau recherche, publiés ou non, émanant des établissements d'enseignement et de recherche français ou étrangers, des laboratoires publics ou privés.

NNT : 2017SACLS068

THESE DE DOCTORAT  
DE  
L'UNIVERSITE PARIS-SACLAY  
PREPAREE A  
L'UNIVERSITE PARIS-SUD

ECOLE DOCTORALE N° 572 : EDOM  
Ondes et Matières

Spécialité de doctorat: Lasers, molécules, rayonnement atmosphérique

Par

**Mme. Thi Kim Cuong LE**

Raman Spectroscopy of Soot Produced in Low Pressure Flames: ex situ Analyses and  
Online Gas Phase Studies

**Thèse présentée et soutenue à Orsay, le 20 mars 2017 :**

**Composition du Jury :**

Mme. DESGROUX Pascale	Directrice de recherche, CNRS	Rapporteuse
M. QUIRICO Eric	Professeur, Université Joseph Fourier Grenoble 1	Rapporteur
Mme. LAUNOIS Pascale	Directrice de recherche, CNRS	Examinatrice
M. PARENT Philippe	Directeur de recherche, CNRS	Président
Mme. PRÉ Pascaline	Professeure, Institut Mines Telecom	Examinatrice
M. PINO Thomas	Directeur de recherche, CNRS	Directeur de thèse



# Acknowledgements

## *To whom accompanied me during my PhD time...*

The first person that I would like to express my sincere thanks is my supervisor: Thomas Pino, who offered me the chance to come to the beautiful country, France, to study and to gain much knowledge in science under the best conditions. Your supervision, encouragement and thoughtful care have strongly motivated me during my PhD. I am deeply thankful for your warm share and care that you have not only for me but also for my entire family. We will always remember and highly appreciate that.

I will not be able to complete my thesis without the enthusiastic supports from the scientific instrumentation and electronics groups. Christophe Lefumeux, Catherine Le Bris, Benoit Héraud helped me a lot for optics, Nicolas Tournier for vacuum systems of Nanograins, Thierry Chamailé for mechanical designs, Christophe Charrière, Julien Vincent for electronics. Particularly, I am grateful Christophe and Benoit's enthusiastic collaboration and supports through my entire experimental time. You are such excellent colleagues who created a lot of fun at work.

I would like to thank my collaborators in the project:

- Jean-Noël Rouzaud, and Damien Deldicque at Geology Laboratory in l'Ecole normale supérieure, who helped measuring Raman spectra of soot films and HRTEM images.

- Emmanuel Dartois, Lisseth Gavilan who collaborated in measuring VUV-MIR spectroscopy of soot. I have learnt a lot about astronomy and gained solid background on the subject from the discussion and knowledge exchange with you.

- Alexandre Guiliani, beamline scientist at DISCO beamline, Soleil synchrotron, helped us measuring VUV which is a part of my thesis.

- Rosario Brunetto for instructing me how to measure IR spectra and Anne Zehner at ISMO for giving me the opportunity to use her FT-IR spectrometer.

- Patrick Rairoux, Alain Miffre at Institute of Light and Matter in Lyon University who collaborated in measuring Raman signal of soot under atmospheric conditions.

I am thankful all members of the research group "Molecular System, Astrophysics and Environment", my kind and open companions: Phillipe Bréchnac, Stephane Douin, Karine Béroff, Laurent Coudert, Bérenger Gans, Anne-Lise Roche, Séverine Boyé-Péronne, Pascal Parneix, Oliver Pirali. Thank Minh Huong Ha Thi, my dear old sister, for your sharing and important helps especially during my first days in France. Thank Guy Taieb for hosting the warm new year parties. Thank my dear PhD roommate friends: Nicolas Lamarre, Maëlle Bonnin, Viet -Tiep Phung, Thejus Mahajan, Thu Trang Tran, Mali Zhao, Shuiyan Cao, Moustafe Achlan, Khalid Quertite for sharing the office and fun moments. Especially, I would like to thank Maëlle for helping me promptly when a curtain started to burn in the laboratory, an unforgettable moment and my big lesson in working with laser.

Thank Mrs. Martine Basset, secretary of EDOM, and staffs of human resource at ISMO, especially Marie-Claire Paul, Stéphanie Delhaye, Sylvie Chabot, etc. for guiding me through administrative paper works.

I am thankful my landlord neighbors for your kindness, generous and sincere helps for the last three years. Thank my old sister Khanh Hong for babysitting my daughter from time to time during weekends. Thank all my Vietnamese friends because of their encouragement and sharing.

I would like to thank all members of the jury committee for assessing my work: Pascale Desgroux, Eric Quirico, Philippe Parent, Pascaline Pré, Pascale Launois. Particularly, Pascale Desgroux and Eric Quirico spent their valuable time to read and gave wise comments in reviewing my thesis. I would like to express heartfelt thanks the jury committee for attending, and creating an open atmosphere during my defense so that I felt less stressed and had more changes for discussion. Not only the questions but other relationships/methods/additional measurements suggested by you are valuable to improve our results. Moreover, after my defense, Pascale Desgroux took her time to send me a list of her detailed comments which is very worth to improve my revision as well as my further publication. I am thankful all of you.

I acknowledge financial supports from Vietnamese government for my PhD scholarship in the project 911.

The last profound words that I would like to thank my beloved family:

Lời cảm ơn lắng đọng sau cùng tôi muốn dành cho những người thân yêu trong trái tim tôi:

Cảm ơn Ba, Má, Mẹ Chồng và các anh chị em đã động viên con/em/chị trong suốt chặng đường học tập, đặc biệt là sự tin yêu của Ba và những hy sinh lớn lao không quản ngại của Má. Con hy vọng rằng những năm tháng học tập chăm chỉ của con như lời cảm ơn nhỏ bé gửi đến tình yêu to lớn mà Ba Má luôn dành cho con.

Cảm ơn Thái, Anh thân yêu, vì những quan tâm sâu sắc và hy sinh thầm lặng mà Anh luôn dành cho em. (Em sẽ giữ và trân trọng cho riêng mình!). Cảm ơn những kiến thức Matlab lẫn kinh nghiệm nghiên cứu mà Anh chia sẻ đã giúp em tự tin hơn trên con đường khoa học. Cảm ơn Miss, con gái yêu của mẹ, làm these và sinh con thật sự không dễ với mẹ chút nào nhưng con là động lực lớn giúp mẹ hoàn thành. Mẹ yêu con.

# Abstract

*Soot is any black, blackish or brown aggregate which contains polyaromatic layers and is generated by the incomplete combustion.*

Every year, an amount of about  $10^7$  tons of soot is emitted worldwide. Soot, as part of atmospheric black carbon, has serious impacts on climate change and human health. The impacts depend on many factors including adsorbed compounds, aging and mixing processes. Therefore, in order to reduce the amount of soot, besides considering these mentioned factors, the studies of formation kinetics, structure and optical properties of soot particles are also essential. There are several methods applied in soot investigations. Raman spectroscopy plays a particular role, as it is a powerful tool for structural investigation of the carbon-based materials because it is sensitive to molecular structures. My Ph.D. project focused on the studies of soot formation processes in low pressure ethylene premixed flames using online Raman measurements, and on the determination of the optical, structural and chemical properties of a variety of sampled soot particles using multi-optical ex situ diagnostic methods in which Raman spectroscopy is the main tool.

This first chapter provides a general classification of carbonaceous particles emitted from incomplete combustion and their adverse impacts on human health and climate change. It is then followed by a brief overview of soot formation mechanism and their spectral properties before discussing some diagnostic techniques used in the combustion community, especially Raman scattering applied to the carbon research. A second chapter provides an overview of the combustion chamber, the sampling conditions and the experimental methods. The following three chapters then focus on the results.

Differential Raman cross sections of soot and some other carbonaceous particles were measured to progress toward quantitative Raman spectroscopy. The results were obtained by comparing the Raman signals of carbonaceous materials and that of the reference substance (water was chosen in our experiments) whose differential Raman cross section is well-known. These values ( $\sim 10^{-28} \text{ cm}^2\text{sr}^{-1}\text{atom}^{-1}$ ) show the feasibility of detection of black carbon/soot emission in the atmosphere using Raman spectroscopy.

Soot particles produced by premixed ethylene flames at a low pressure were investigated by ex-situ Raman measurement on deposited films. Combination of the Raman spectroscopy of soot sampled on substrates with infrared and vacuum-ultra-violet transmission spectroscopies and transmission electron microscopy allowed progressing on the interpretation of soot Raman spectra and proposing new relations between Raman parameters and structural and optical properties. From those multi-diagnostics measurements, we found structural (importance of cross-linkage, sp hybridization, polyaromatic unit mean size  $L_a$ ), optical ( $\pi - \pi^*$  transition, Tauc optical gap  $E_g$ ) and chemical (number of rings, C/H ratio) properties of soot. This was important for the interpretation of the novel study, where we measured Raman spectra of soot in the gas phase prior to deposition for the same flame conditions.

Ex situ methods on extracted samples are powerful for assessing particle size, morphology and chemical composition, but sampling and deposition may cause significant perturbations to the soot particles. Online methods developed that provide this type of information are thus to be. In the last results chapter, the online gas phase measurements provided a novel view on the soot birth and structures in low pressure flames with, for instance, the detection of a large amount of sp hybridized carbon atoms during nascent soot growth. The abundant component of sp hybridized structure in soot produced by the low pressure combustion conditions suggests that polyaromatic units as well as carbon chains are involved in soot formation, rather than mostly polycyclic aromatic hydrocarbons (PAHs). This structural information questions the nature of the precursors and the role of the reorganization within the soot nanoparticles. Nevertheless, quantitative carbon concentration into soot particles has also been determined, in which around several thousand<sup>th</sup> carbon atoms relative to that in fuel convert into those in soot particles. By using the set of spectral Raman and fluorescence parameters, evolutionary steps are identified in the evolution of soot along the flame: birth, growth and aging.

Overall, these studies pave the way to soot detection and analysis directly and quantitatively in the atmosphere. It also opens a very fresh look on soot structures and soot formation in the ethylene low pressure flame using the online Raman technique, emphasizing the role of carbon chains.

**Key words:** Soot, black carbon, Raman spectroscopy, gas phase, low pressure flame, carbon hybridization

# Résumé en français

*La suie est un agrégat noir, noirâtre ou brun qui contient des couches polyaromatiques et est générée par la combustion incomplète.*

Chaque année, une quantité de  $10^7$  tonnes de suie est produite à l'échelle mondiale. Le carbone-suie dans l'atmosphère a des effets graves sur le changement climatique et la santé humaine. Les impacts dépendent de nombreux facteurs comme les composés organiques adsorbés, le vieillissement et les processus de mélange. Par conséquent, afin de réduire la quantité de suie émise, outre l'examen de ces facteurs, les études de la cinétique de formation, de la structure et des propriétés optiques des suies sont également essentielles. Il existe plusieurs méthodes optiques dans les études sur la suie. La spectroscopie Raman occupe un rôle particulier puisqu'elle est un outil puissant pour l'étude structurale des matériaux carbonés grâce à sa sensibilité aux structures à l'échelle moléculaire. Mon doctorat a porté sur la caractérisation des suies au cours de leur formation dans des flammes prémélangées à base d'éthylène, à basse pression, en utilisant des mesures Raman en ligne. Il a aussi porté sur la détermination des propriétés optiques, structurales et chimiques d'une variété de particules de suie échantillonnées en utilisant des méthodes de multiples diagnostic optiques ex situ dans lesquelles la spectroscopie Raman est l'outil principal.

Le premier chapitre de ma thèse fournit une classification générale des particules carbonées émises par une combustion incomplète et leurs effets négatifs sur la santé humaine et le changement climatique. Il est ensuite suivi d'un bref aperçu du mécanisme de formation des suies et de leurs propriétés spectrales avant de discuter certaines techniques de diagnostic utilisées dans l'étude de la physico-chimie de la combustion, en particulier la diffusion Raman. Un deuxième chapitre donne un aperçu de la chambre de combustion utilisée, des conditions d'échantillonnage et des méthodes expérimentales. Les trois chapitres suivants se concentrent ensuite sur les résultats.

Les sections efficaces différentielles de diffusion Raman de suie et d'autres particules carbonées ont été mesurées pour progresser vers une spectroscopie Raman quantitative. Les résultats ont été obtenus en comparant les signaux Raman des matériaux carbonés avec ceux de la substance de référence (l'eau a été choisie dans nos expériences) dont la section efficace Raman est connue. Ces valeurs ( $\sim 10\text{-}28 \text{ cm}^2\text{sr}^{-1}\text{atom}^{-1}$ ) montrent la faisabilité de la détection de l'émission de carbone noir / suie dans l'atmosphère en utilisant la spectroscopie Raman.

Les particules de suie produites par des flammes d'éthylène prémélangées à basse pression ont ensuite été étudiées par mesure ex situ du spectre Raman des films de suies déposées. La combinaison de la spectroscopie Raman de suies échantillonnées sur des substrats avec les spectroscopies en transmission de l'infrarouge à l'ultraviolet du vide et de la microscopie électronique en transmission a permis de progresser sur l'interprétation des spectres Raman de suies. Grâce à ces mesures, de nouvelles relations entre les paramètres Raman et les propriétés structurales et optiques ont pu être proposées. À partir de ces mesures multi-diagnostiques, nous avons trouvé une relation forte entre la structure (importance de la réticulation, hybridation  $sp$ , taille moyenne de l'unité polyaromatique  $L_a$ ), les caractéristiques des transitions optiques

(transition  $\pi$ - $\pi^*$ , gap optique de Tauc  $E_g$ ) et la composition chimique (ratio C / H). Cela a été important pour l'interprétation des spectres Raman des suies mesurés directement dans la phase gazeuse avant le dépôt pour les mêmes conditions de flamme.

Les méthodes ex situ sur les échantillons extraits sont puissantes pour évaluer la taille des particules, la morphologie et la composition chimique, mais l'échantillonnage et le dépôt peuvent provoquer des perturbations importantes pour les particules de suie. Les méthodes en ligne qui fournissent ce type d'information sont donc nécessaires et à développer. Grâce à ces développements, dans le dernier chapitre des résultats, les mesures en la phase gazeuse et en ligne ont fourni une nouvelle vue sur la naissance et les structures de la suie dans des flammes à basse pression. Par exemple, cela a permis la détection d'une grande quantité d'atomes de carbone hybridé sp lors de la naissance et de la croissance de la suie. Cette composante abondante de structures sp dans la suie produite par les conditions de combustion à basse pression suggère que les unités polyaromatiques ainsi que les chaînes de carbone sont impliquées dans la formation de suie plutôt qu'uniquement des hydrocarbures aromatiques polycycliques (HAP). Cette information structurelle interroge donc la nature des précurseurs des suies et le rôle de la réorganisation dans les nanoparticules de suie. La concentration de carbone dans les particules de suie naissante a également été déterminée, dans lesquelles autour de plusieurs millièmes d'atomes de carbone par rapport à celui du combustible se transforment en particules de suie. En utilisant l'ensemble des paramètres spectraux de Raman et de fluorescence, des étapes sont identifiées dans l'évolution du suie le long de la flamme: naissance, croissance et vieillissement.

Dans l'ensemble, ces études ouvrent la voie à la détection et à l'analyse de la suie directement et quantitativement dans l'atmosphère. Il ouvre également un regard très nouveau sur les structures de suie et la formation de suie dans la flamme à basse pression d'éthylène en utilisant la technique Raman en ligne, en soulignant le rôle des chaînes de carbone.

**Mots clés :** Carbone-suies, spectroscopie Raman, phase gazeuse, flamme basse pression, hybridations du carbone

# Table of contents

Acknowledgments .....	<i>ii</i>
Abstract .....	<i>iv</i>
Résumé en français page vi.....	<i>vi</i>
Table of contents .....	<i>viii</i>
List of figures .....	<i>xi</i>
List of tables .....	<i>xv</i>
List of abbreviations .....	<i>xvi</i>
<b>Chapter 1: Background .....</b>	<b>1</b>
<b>1.1 Overview of carbon particles in the atmosphere.....</b>	<b>2</b>
1.1.1 Carbonaceous particle matters formation and classification.....	2
1.1.2 Environmental effects and human health impacts of carbonaceous particles in atmosphere.....	4
<b>1.2 Soot formation in flame and its spectral properties.....</b>	<b>5</b>
1.2.1 Soot formation mechanism.....	6
1.2.2 Spectral properties.....	12
<b>1.3 Detection of soot in the laboratory and in the atmosphere.....</b>	<b>14</b>
<b>1.4 Raman spectroscopy and its application to study of carbon related materials ....</b>	<b>15</b>
1.4.1 Raman spectroscopy.....	15
1.4.2 Raman spectroscopic study of carbon related materials .....	17
<b>1.5 Conclusions .....</b>	<b>20</b>
<b>References.....</b>	<b>22</b>
<b>Chapter 2: Experimental setup.....</b>	<b>28</b>
<b>2.1 Nanograins combustion chamber .....</b>	<b>29</b>
2.1.1 The principle of a premixed combustion.....	29
2.1.2 Nanograins components .....	30
<b>2.2 Flame conditions and soot production.....</b>	<b>32</b>
2.2.1 Soot deposition and measurements .....	32
2.2.2 Soot production for measurements in the gas phase .....	33
2.2.3 Samples for differential Raman cross section measurements .....	37
<b>2.3 Instruments and principles of soot characterization.....</b>	<b>37</b>

2.3.1 Infrared spectroscopy .....	39
2.3.2 Ultraviolet-Visible spectroscopy .....	40
2.3.3 Instrumentation for Raman spectroscopic measurement.....	43
2.3.4 High resolution transmission electron microscope (HRTEM).....	45
<b>2.4 Conclusions .....</b>	<b>46</b>
<b>References.....</b>	<b>47</b>
<b>Chapter 3: Result I: Differential backscatter Raman cross section of several carbonaceous materials .....</b>	<b>48</b>
<b>3.1 Introduction .....</b>	<b>49</b>
<b>3.2 Principles.....</b>	<b>50</b>
3.2.1 Differential Raman cross section .....	50
3.2.2 Method.....	50
<b>3.3 Experimental arrangement .....</b>	<b>52</b>
3.3.1 Sample preparation.....	52
3.3.2 Instrumentation.....	53
3.3.3 Experimental setup.....	54
3.3.4 Spectral correction.....	55
<b>3.4 Results and discussion.....</b>	<b>55</b>
3.4.1 Observations.....	55
3.4.2 Measurement of differential Raman cross sections.....	59
3.4.3 Discussion .....	63
<b>3.5 Conclusions .....</b>	<b>66</b>
<b>References.....</b>	<b>68</b>
<b>Chapter 4: Result II: Raman scattering: spectral analysis and structural information of deposited soot .....</b>	<b>70</b>
<b>4.1 Introduction .....</b>	<b>71</b>
<b>4.2 Experiment.....</b>	<b>74</b>
4.2.1 Soot production .....	74
4.2.2 Raman and HRTEM measurements.....	74
<b>4.3 Results and analysis.....</b>	<b>75</b>
4.3.1 Raman spectra of soot produced by various flame conditions.....	75
4.3.2 Spectral analysis by curve fitting .....	77
<b>4.4 Discussion of soot structural information .....</b>	<b>90</b>



4.4.1 Analysis of disorder.....	90
4.4.2 Indices of aromatization .....	94
4.4.3 The second order .....	99
4.4.4 The sp hybridized bond .....	102
<b>4.5 Conclusions .....</b>	<b>102</b>
<b>Reference .....</b>	<b>104</b>
<b>Chapter 5: Result III: Detection of soot in the gas phase.....</b>	<b>107</b>
<b>5.1 Introduction .....</b>	<b>108</b>
<b>5.2 Experimental arrangement .....</b>	<b>109</b>
5.2.1 Experimental setup.....	109
5.2.2 Flame conditions .....	112
<b>5.3 Results.....</b>	<b>114</b>
5.3.1 Data summary.....	114
5.3.2 The flame with 1.05 C/O ratio at 40 mbar .....	122
5.3.3 Properties of C/O 1.05 soot in the gas phase via Raman spectroscopy.....	133
<b>5.4 Conclusions and remarks .....</b>	<b>147</b>
<b>References.....</b>	<b>148</b>
<b>Chapter 6: Conclusions and perspectives .....</b>	<b>153</b>
<b>5.5 Conclusions .....</b>	<b>154</b>
<b>5.6 Perspectives.....</b>	<b>156</b>
Appendix A	
Curriculum vitae	

# List of figures

Fig. 1.1: Visualization of soot aggregates .....	6
Fig. 1.2: Soot formation process.....	7
Fig. 1.3: Schematic representation of the first aromatic ring formation in flame. ....	8
Fig. 1.4: Schematic representation of oxidation and pyrolysis routes.....	10
Fig. 1.5: Raman process explained by energy diagram.....	17
Fig. 1.6: a) top: a typical Raman spectrum of defected graphene excited by 532 nm. b) phonon scattering process responsible for main Raman peaks presented by electron dispersion and interband transitions. Top of b) shows phonon scattering process in intervalley $K, K'$ . Bottom b) phonon scattering process in intravalley $K$ responsible for $D'$ peak.....	18
Fig. 1.7: a) ternary phase diagram of amorphous carbons. b) three-stage model of visible Raman spectrum with increasing disorder.....	19
Fig. 2.1: Nanograins, an experimental setup .....	31
Fig. 2.2: Typical HRTEM image of the soot directly deposited on the Lacey carbon by inserting of the TEM grid into the molecular flow.....	33
Fig. 2.3: Vertex 70 components and beam path .....	40
Fig. 2.4: Different transitions between the bonding and antibonding electronic states in UV-Vis spectroscopy.....	41
Fig. 2.5: On the left, the layout of DISCO beamline in the experimental hall at SOLEIL. On the right, there are the photos of APEX chamber and the sample holder.....	42
Fig. 2.6: Transmission spectrum of an ultra-thin soot measured with several instruments at DISCO beamline on the SOLEIL synchrotron .....	43
Fig. 2.7: The Renishaw inVia confocal Raman microspectrometer, the zoomed in photo is the sampling platform. ....	44
Fig. 2.8: A schematic outline of a TEM .....	45
Fig. 3.1: Qualitative comparison of five samples in the form of powder (5mg/each sample) (the first row) and their mixtures in 40 ml water (the second row). The third row shows the images of thin films floated on the surfaces of the mixtures.....	52
Fig. 3.2: Scheme of differential Raman cross section measurement at ISMO.....	54
Fig. 3.3: Spectral responses of the experimental instruments as a function of wavelength. ....	55
Fig. 3.4: Raman intensities of several carbon-based materials as a function of Raman shift. ....	56
Fig. 3.5: Raman spectrum of $O_2$ and $N_2$ in the air with $2\text{ cm}^{-1}$ as resolution. ....	57
Fig. 3.6: Raman spectrum of pure water .....	57

Fig. 3.7: Raman spectra of various carbonaceous particles in water as a function of Raman shift .....	58
Fig. 3.8: Raman spectra of the coal mixtures at different concentrations. a) shows D and G band of coal in the mixtures; b) shows O – H stretching band of water in the mixtures. ....	59
Fig. 3.9: Comparison of the Raman spectra of coal in form of powder and that of coal after mixing in water.....	60
Fig. 3.10: a) Ratios of Raman intensities of D and G peaks with such intensity of water measured in coal / water mixtures at different concentration. b) Differential Raman cross section of D and G peaks of coal.....	60
Fig. 3.11: Deconvolution of the Raman spectrum of Ensaco 350 G powder .....	61
Fig. 3.12: a) Ratios of Raman intensities of D and G peaks with water measured in Ensaco 350G / water mixtures at different concentration. b) Differential Raman cross section of D and G peaks of Ensaco 350G.....	62
Fig. 3.13: Deconvolution Raman spectrum of Diesel soot SRM 2975 (NIST).....	63
Fig. 3.14: Distribution of coal, Ensaco 350G and diesel soot particles in drops of the mixtures after evaporation via transmission optical microscopy.....	64
Fig. 4. 1. Raman spectrum of flame soot.....	71
Fig. 4. 2: Variation of the ID/IG ratio with La .....	73
Fig. 4. 3: Raman spectra of soot produced by various flame conditions at HAB = 30 mm .....	76
Fig. 4. 4: First and second order spectral deconvolution of soot produced by C/O = 0.82 flame collected at varying HAB (in mm) .....	78
Fig. 4. 5: First and second order spectral deconvolution of soot produced by C/O = 1 flame collected at varying HAB (in mm). ....	80
Fig. 4. 6: First and second order spectral deconvolution of soot produced by C/O = 1.05 flame collected at varying HAB (in mm.....	84
Fig. 4. 7: First and second order spectral deconvolution of soot produced by C/O = 1.3 and collected at varying HAB (in mm). ....	86
Fig. 4. 8: FWHMs and peak positions of D1 and G peaks of our spectra and a selection of soot data from the literature.....	90
Fig. 4. 9: HRTEM images of C/O 1.05 soot at 24, 36 and 50 mm of HAB corresponding to three columns (from left to right side).....	91
Fig. 4. 10: Position relation of D1 and G peaks in Raman spectra with sp <sup>3</sup> defect and C=C stretching bands in IR spectra.....	93
Fig. 4. 11: Relation of the ID1/IG ratio with position of C=C stretching and sp <sup>3</sup> defect bands .....	93
Fig. 4. 12: Comparing the peak height ratio and the peak area ratio in our spectra.....	94
Fig. 4. 13: FWHM(D1) and FWHM(G) as a function of ID1/IG.....	95

Fig. 4. 14: Evaluating La from ID1/IG .....	95
Fig. 4. 15: Comparing La obtained via Raman and visible transmission spectroscopy .	96
Fig. 4. 16: The relation between G peaks and the Tauc gap $E_g$ .....	98
Fig. 4.17: Integrated area under 2D1 Raman peak ( $\sim 2740 \text{ cm}^{-1}$ ) as a function of the integrated area under D1 Raman peak ( $\sim 1355 \text{ cm}^{-1}$ ).....	99
Fig. 4. 18: relation of position and FWHM between 2D1 and D1 peaks .....	99
Fig. 4. 19: Classification of our soot in various carbonaceous materials .....	101
Fig. 4. 20: The evolution of sp bond vs HAB (mm).....	102
Fig. 5.1: Scheme of online measurement of soot in the gas phase .....	110
Fig. 5.2: Spectral response of the instruments as a function of wavelength using grating 3 of the spectrometer.....	114
Fig. 5.3: Vertical and horizontal polarization components in spectra of various flame conditions. The acquisition time is 200 sec .....	116
Fig. 5.4: Raman spectra of soot produced by 1.05 C/O ratio flame at 33, 40 and 48 mbar .....	117
Fig. 5.5: From the left to the right, gas phase Raman spectra of flames whose C/O ratios are respectively 0.78, 1.1 and 1.3 as a function of Raman shift. The acquisition time is 200 sec .....	118
Fig. 5.6: Effect of the excitation power on spectra measured for Flame (C/O = 1.05, P = 40 mbar) at 20 and 36 mm with 200 sec for acquisition time .....	120
Fig. 5. 7: Power excitation dependence of fluorescence (a) and Raman (b) signals of C/O = 1.05 flame at HAB = 20 mm .....	121
Fig. 5. 8: The evolution of spectra of including the gas phase Raman of soot from the blue zone to the orange zone for a series of the flame conditions .....	122
Fig. 5. 9: The evolution of gas phase Raman spectra of soot produced by 1.05 C/O ratio flame at the sampling distances from 6 to 50 mm .....	124
Fig. 5. 10: Normalized gas phase spectra of soot produced by 1.05 C/O ratio flame at the sampling distances from 11 to 50 mm .....	125
Fig. 5. 11: Fluorescence and Raman signal in spectra of soot produced at 14 mm (a), and 22 mm (b).....	126
Fig. 5. 12: Gas phase Raman spectra of soot from the as a function of Raman shift after subtracting the first and second fluorescence components.....	127
Fig. 5. 13: Deconvolution of Raman spectra of soot in the gas phase with HAB = 50 mm .....	127
Fig. 5. 14: a) Raman spectrum of soot at HAB = 50 mm before subtracted background. b) Raman spectrum of soot at HAB = 50 mm after subtracted background .....	128
Fig. 5. 15: Curve fit with band combination for the first and second order of online Raman spectra of soot produced by 1.05 C/O Ethylene flame. ....	130

Fig. 5. 16: Raman spectra (a) and Raman signal intensity (b) of ethylene versus HAB .....	133
Fig. 5. 17: Dispersion of the ratio intensity of D1 and G peaks versus their positions	134
Fig. 5. 18: a) FWHMs of D1 and G peaks versus G position. b) Intensity ratio of D1 and G peaks, in gas phase, vs HAB .....	135
Fig. 5. 19: Experimental Raman spectra of some carbon solids and nanostructures ...	136
Fig. 5. 20: Raman spectra of soot produced by 1.05 C/O flame at 18 mm excited by the continuous laser in the gas phase and deposited substrate.....	137
Fig. 5. 21: Decomposition of Raman spectra of soot in the gas phase (a) and in the deposited phase (b) .....	137
Fig. 5. 22: FWHM and position of two peaks C1 and C2 appearing along the flame .	138
Fig. 5. 23: a) The ratio between the integrated intensity of the C band and of the (D + G) band versus HAB. b) The evolution of the sp - sp <sup>2</sup> ratio versus HAB.....	139
Fig. 5. 24: a) Blue-shift of the G peak versus <i>ICrel</i> for different HAB. b) Relation of FWHM of G peak and <i>ICrel</i> .....	140
Fig. 5. 25: The relation of ID/IG versus the <i>ICrel</i> .....	141
Fig. 5. 26: The evolution of the first fluorescent component vs HAB .....	142
Fig. 5. 27: The evolution of second fluorescent component vs HAB .....	144
Fig. 5. 28: The maximum peak position of 750 nm emission band vs HAB .....	144
Fig. 5. 29: The evolution of soot along ethylene premixed flame.....	146

# List of tables

Table 2.1: Characterization of four flames and list of measurements on their products ...	34
Table 2.2: Spectral regions and associated transition nature.....	38
Table 3.1: Differential Raman cross sections for some carbon-based materials from literatures.....	65
Table 4.1. Fit parameters of spectral decomposition, with $d$ [mm], $\omega$ [ $\text{cm}^{-1}$ ], $\gamma$ [ $\text{cm}^{-1}$ ], $A$ are HAB, peak position, FWHM and Area of peaks respectively.....	87
Table 5.1: Summary of flame conditions where soot Raman spectra detected successfully.....	113
Table 5.2: Band combinations tested for curve fitting of the first and second order Raman spectra of soot in the gas phase (L = Lorentzian, G = Gaussian).....	128
Table 5.3: Raman fit parameters. Note that the uncertainty of the peak position is lower than 10% of its peak width.....	131

# List of abbreviations

- AALH: Aromatic-aliphatic-linked hydrocarbons
- BC: Black carbon
- BrC: Brown carbon
- CB: Carbon black
- CCD: Charge coupled device
- DRCS: Differential Raman cross-sections
- EC : Elemental carbon
- EPA: Environmental Protection Agency
- UV: Extreme violet
- FUV: Far ultraviolet
- FWHM: Full width at half maximum
- HAB: Height Above the Burner
- HRTEM: High-resolution transmission electron microscope
- HOMO: Highest occupied molecular orbital
- HACA: Hydrogen-abstraction-carbon-addition
- HAC: Hydrogenated amorphous carbon
- IR: Infrared
- ISMO: Institute of Molecular Sciences in Orsay
- ISA: Integrated Science Assessment
- LII: Laser-induced incandescence
- LIF: Laser-induced fluorescence
- LAC: Light absorbing carbon
- LUMO: Lowest unoccupied molecular orbital
- MIR: Mid-infrared
- NOC: Nano organic compounds
- OC: Organic carbons
- PM: Particle matter
- PCAH: Peri-condensed aromatic hydrocarbons
- PCAB: Peri-condensed aromatic with an aliphatic branch
- PAH: Polycyclic Aromatic Hydrocarbons
- RR: Resonance Raman
- RSRs: Resonantly stabilized radicals
- SMPS: Scanning mobility particle size
- TEM: Transmission electron microscope
- VUV: Vacuum ultraviolet
- VAST: Vietnam academy of science and technology
- WHO: World health organization

## Math symbol

- Adiabatic temperature ( $T_{af}$ )
- Constant fractal prefactor:  $k_f$
- Differential Raman cross section:  $\beta = \frac{\partial \sigma}{\partial \Omega}$  [ $\text{cm}^2 \cdot \text{molecule}^{-1} \cdot \text{sr}^{-1}$ ]
- Dipole moment vector ( $\vec{P}$ )

- Electric field ( $\vec{E}$ )
- Flame temperature ( $T_f$ )
- Fractal dimension:  $D_f$
- Gap energy:  $E_g$
- Intensity ratio of the  $D$  and  $G$  Raman bands:  $I_D/I_G$
- Laser photon flux:  $P_D$  [photons.  $s^{-1} \cdot cm^{-2}$ ]
- Mixture composition ( $\Phi$ )
- Normalization parameter:  $D(\lambda)$
- Number of condensed rings:  $N_R$
- Polarizability ( $\alpha$ )
- Primary particle diameter:  $d_p$
- quantum efficiency of the detector:  $Q$  [ $e^-/\text{photon}$ ]
- Size of the polyaromatic unit:  $L_a$
- Solid angle of the spectrometer  $\Omega_D$  [sr]
- Tortuosity ratio:  $R_{Tor}$
- Wavelength dependent pre-factor:  $C(\lambda_L)$



# Chapter 1

## Background

### Contents

---

<b>1.1. Overview of carbon particles in the atmosphere .....</b>	<b>2</b>
1.1.1. Carbonaceous particle matters formation and classification.....	2
1.1.2. Environmental effects and human health impacts of carbonaceous particles in the atmosphere .....	4
<b>1.2. Soot formation in flame and its spectral properties .....</b>	<b>5</b>
1.2.1. Soot formation mechanism .....	6
1.2.2. Spectral properties.....	12
<b>1.3. Detection of soot in the laboratory and in the atmosphere.....</b>	<b>13</b>
<b>1.4. Raman spectroscopy and its application to study of carbon related materials .....</b>	<b>15</b>
1.4.1. Raman spectroscopy .....	15
1.4.2. Raman spectroscopic study of carbon related materials .....	17
<b>1.5. Conclusions .....</b>	<b>20</b>
<b>References .....</b>	<b>21</b>

---

After several decades of research on carbonaceous materials, although there are still many critical gaps, major progresses were achieved toward understanding of their characteristics, formation and evolution mechanisms at work and their adverse effects on human life. This first chapter will concisely provide a general view of our objects. It is divided into four sections. First, we discuss their emission and lifecycle in the atmosphere. The second section focuses on soot formation and ageing. The third section reviews soot detection methods and the last one introduces the Raman spectroscopy of carbons.

## **1.1. Overview of carbon particles in the atmosphere**

Although accounting for only 0.2% of the total mass of our planet, carbon atom plays an essential building block role in nature allowing the miracle of life to happen [1]. Because of its self-combination ability in different bond types, carbon atoms can produce various solids and materials leading to diverse allotropies for carbonaceous matter, both natural and artificial. The former, found on Earth or through the carbon lifecycle in our universe, plays an effective bridge-building role between astrophysics and geophysics. The latter, as the results of human activities, was created since the use of fire. This section will provide a short discussion on their formation as well as on their adverse effects on human life.

### **1.1.1. Carbonaceous particle matters formation and classification**

Carbon can produce various carbon-based solid materials or fuels. Combustion of carbon-based fuels, including fossil fuels, biomass and biofuels is still the main source of energy utilized by mankind. During their oxidation or burning process, combustion emits various substances depending on combustion conditions.

Combustion conditions are classified into complete and incomplete combustion. While water and carbon dioxide are produced from the complete combustion of carbon-based fuels, additional products of incomplete combustion are often more complex, happening when there is not enough oxygen to burn the fuel completely or when the combustion is quenched by a heat sink. For almost all fuels such as liquid fuels (e.g. gasoline, ethanol, biodiesel, etc.) and solid fuels (e.g., wood, charcoal, crop residues, etc.) pyrolysis occurs before flaming combustion. The emitted smokes contain harmful particulate matters and toxic gasses.

In the incomplete combustion, particle matter (PM) emissions are generically known as soot, black carbon (BC) and potentially brown carbon (BrC) although this may result from ageing of secondary organic aerosols in atmospheric chemistry. Contemporaneous with soot formation, soot particles may be completely oxidized forming carbon monoxide and carbon dioxide if oxygen content and temperature remain sufficiently high [1]. During the flaming process, soot quantity depends largely on combustion conditions, for instance, the amount of soot reaches large quantities in open and uncontrolled burning. That is the reason why closed combustion is designed to increase the mixing of air and fuels and ensure high temperature. Besides the flaming process, smoldering processes are also at work, where no soot is formed and smokes are light-colored, and the emitted BrC are made of a variety of organic particles [2]. Consequently, carbonaceous matter emissions originate mainly from the incomplete

organic combustion by-products. The by-products are strongly-absorbing carbon nanoparticles classified into various substances:

*Elemental carbon (EC)* has three forms: graphite, diamond, and solid C<sub>60</sub>. Graphite consists of sp<sup>2</sup> bonded carbon in planar layers and diamond contains sp<sup>3</sup> bonded carbon in the crystalline form. According to atmospheric chemistry, EC labels the carbon matter with a high stability at elevated temperature, i.e. which does not volatilize below 550°C or dissolve in hydrogen peroxide [2].

*Carbon black (CB)* is a commercial product composed of more than 97% of carbon, manufactured by combustion or thermal decomposition of hydrocarbons under controlled conditions. In addition to carbon, CB contains hydrogen, oxygen, and sulfur (less than 1% each) [3].

*Coal* is geologically processed vegetable matter under high pressure and elevated temperature conditions on geological time scale. It may contain a high fraction of sp<sup>3</sup> bonds and nitrogen and oxygen bridges between carbon atoms, depending on its maturity [2].

*Graphite* is one of the pure crystalline forms of elemental carbon. It contains exclusively sp<sup>2</sup> bonds and could be considered lying at the most aromatized end of the coal continuum [2].

*Amorphous carbon* is a solid that has neither long nor short range crystalline order, composed of a mixture of sp<sup>2</sup> and sp<sup>3</sup> bonds with the exception of material with sp<sup>2</sup>-bonded clusters greater than 1 nm in extent. Amorphous carbon is often generated by vapor deposition and may contain hydrogen and nitrogen [2], [4].

*Organic carbons (OC)* are mixtures of compounds containing carbon and other elements like hydrogen or oxygen. Their radiative properties fall into a continuum from light-absorbing to light-scattering particles. OC is formed during incomplete combustion or oxidation of volatile organic compounds.

*Soot* is any black, blackish or brown aggregate which contain polyaromatic layers and are generated by the incomplete combustion [5]. The polyaromatic layers are characteristic of soot, thus these particles can be easily distinguished from other carbonaceous aerosol particles which are lacking this distinctive feature [6]. Soot exists in the atmosphere as clusters of spherules.

*Black carbon (BC)* is probably the most widely used term for the light absorbing carbonaceous aerosols which have strong absorption across a wide spectrum of *visible wavelengths* [2]. It is made of soot, organic matter and other compounds like sulfate, etc. due to its lifecycle in the atmosphere [6]. BC results from undesired, incomplete combustion byproducts.

*Brown carbon (BrC)* is light-absorbing organic matter (other than soot) in atmospheric aerosols of various origins, e.g. soil humic, humic-like substances, tarry materials from combustion, bio-aerosols, etc [5]. It can strongly absorb light at UV wavelengths while weakly, relatively to BC, in the visible range [7], [8].

*Light absorbing carbon (LAC)* contains CB, BC, BrC, and soot.

A *particle matter (PM)* is a complex mixture of small airborne particles and droplets, typically containing agglomerates of primary particles (spherules of ~ 20 – 30 nm diameter) and smaller nucleation mode particles. PM sizes range from nanometer up to micrometer particles, referring to their aerodynamics diameters. PMs are classified by their maximum diameter, like 10 or 2.5  $\mu\text{m}$  ( $\text{PM}_{10}$  or  $\text{PM}_{2.5}$ ). The carbonaceous particles usually dominate the fine particles below one  $\mu\text{m}$  diameter, and nearly systematically below few hundreds of nanometers.

In conclusion, solar energy-absorbing ability, co-emitted pollutants, short atmospheric lifetime, tiny sizes are general characteristics of these particle emissions from combustion. They adversely affect the environment and human health, which we discuss in more details in the next section.

### **1.1.2. Environmental effects and human health impacts of carbonaceous particles in the atmosphere**

Naturally, when sunlight penetrates down to the Earth's surface, it is reflected by the bright surface, especially snow and ice and it is scattered or reflected by clean clouds. These processes help to reduce the amount of solar energy absorbed by the surface. However, if LACs are suspended in the atmosphere, they absorb some coming sunlight, heating the atmosphere. Moreover, the LACs existing in drops of clouds can increase the solar absorbing ability of clouds, reducing the atmospheric lifetimes and precipitation compared to clean clouds. If the LACs are deposited on snow/ ice, the solar energy will be absorbed, increasing the rate of melting [9]. A part of absorbed energy on the surface is converted into infrared radiation emitted into space through the atmosphere. Some of them are absorbed by carbon dioxide, methane, ozone or others then are re-emitted and return to the Earth's surface causing the greenhouse effect. All these effects can be classified into the direct (direct absorption of solar or terrestrial radiation) and indirect effects (changes in cloud lifetime, albedo and composition).

The net impact of LACs on climate depends on many factors including the compounds, the presence of co-emitted pollutants, atmospheric lifetimes, altitude, ageing and mixing processes in the atmosphere in which the ageing of particles plays a key role in the estimation of both the direct and indirect climate effect [10]. The ageing processes affect the hygroscopic qualities, and then the growth behavior, the optical properties, the lifetime of particles [11]. Hence, the ageing process contributes to govern their burden and effect in the atmosphere.

In addition to climate effects, there are numerous epidemiological studies that established associations between exposure to particulate pollution and increased morbidity and mortality for respiratory and cardiovascular diseases [12]–[15]. The ability of the fine and ultrafine fractions of the aerosols to reach the distal lung together with harmful compositions, including transition metals and organic compounds, is found to cause respiratory diseases [12]. Moreover, they can also trigger intracellular production of reactive

oxygen species. The resulting oxidation activates signaling pathways leading to releasing pro-inflammatory mediators [12]. Chronic particle exposure is suspected to be the cause of the exacerbation of inflammatory diseases, for example, asthma and obstructive pulmonary disease. Integrated Science Assessment for Particulate Matter (ISA) of Environmental Protection Agency (EPA) in 2009 presented the relation between PM size fraction and exposure duration for health effects, for which long-term exposure can cause cancer, mutagenicity and genotoxicity. With the broad range of these dangerous effects containing respiratory, cardiovascular neurasthenia as well as premature death, these particles, containing BC as a part of PM<sub>2.5</sub>, are among the top ten major risk factors. Besides these health issues, soot deposition on buildings and vegetation contributes to their long-term degradation.

Every year, there is an amount of  $10^7$  tons of soot produced on the world scale [16]. Approximately 10 – 20 % of the fuels are transformed into soot in diesel engines with direct fuel injection. Ultrafine, fine and coarse PM present in the atmosphere with high concentration, especially in mega-cities, such as Bamako (Mali) is  $205.8 \mu\text{g}\cdot\text{m}^{-3}$  and Dakar (Senegal) is  $80.7 \mu\text{g}\cdot\text{m}^{-3}$  [12]. Soot occurred in 62% of total particles in the polluted air in Mexico and 35% in the troposphere above the Southern Ocean [6]. For comparison, WHO (world health organization) recommends an upper limit at  $10 \mu\text{g}\cdot\text{m}^{-3}$  averaged over one year,  $25 \mu\text{g}\cdot\text{m}^{-3}$  for peak values over 24h. North Vietnam is located at the highest hotspot of BC emission from anthropogenic origin, with similarly high concentrations in the 2000s [17], for instances BC concentrations itself can reach  $20 \mu\text{g}\cdot\text{m}^{-3}$  in Hanoi, (unpublished measurements performed in November 2016). Because the harbor city of Haiphong is the largest industrial zone and trading harbor in Vietnam, it gathers all known sources of BC. Locally, the large diesel ship fleet and harboring equipment operating in Halong bay, and in the surrounding sea, release a huge amount of BC. Coal mining activities in the Northeast of the bay also emit large amounts of coarse elemental carbon particles. Regionally, North Vietnam is under the direct influence of BC coming from China, one of the major emitters worldwide, and under recurrent biomass burning events from neighboring countries. The very high concentrations of BC in this area lead to massive deposition, as observed at the sea surface in Halong Bay, North Vietnam. The relentless rise of this emission in the atmosphere and their adverse effects are one of the main reason we pursuit the project on soot and black carbon. This is a part of the Rawdar project, which comprises a collaboration between Institute of Molecular Sciences in Orsay (ISMO, France) and Institute of Physis, Vietnam academy of science and technology (VAST). In this project, soot is our main object of interest and we will consider it in the rest of this thesis.

## **1.2. Soot formation in flame and its spectral properties**

Twenty years ago our knowledge on soot formation was limited to empirical and phenomenological observations, while since recently quantitative modeling for at least small fuel compounds can be performed [15], [18]. Nowadays, fundamental sooting processes, including the chemical soot precursors, particle nucleation, and mass/size growth have been tackled gradually. However, the mechanism of soot formation and the properties of nascent

soot still remain elusive and there are several critical gaps in the understanding of the evolution of the chemical structure and composition of the flame soot. In this section, we will delineate flame soot formation and their spectral properties.

### 1.2.1. Soot formation mechanism

We start with a description of a structure of a typical mature soot particle. In Fig 1.1a, b, under a transmission electron microscope (TEM), soot appears as clusters or chains which contain numerous spherules. Each spherule is called primary soot particle whose size in diameter mostly lies between 15 to 30 nm and soot aggregates are defined as secondary particles composed of tens to hundreds of primary particles [19]. The high-resolution transmission electron microscope (HRTEM) (Fig 1.1c) shows up every primary particle as an inner core surrounded by an outer shell containing concentric crystallites (Fig 1.1d), parallel to the particle surface. There are about  $10^3$  crystallites per spherical soot particle [20]. The thickness of a crystallite is about 1.2 nm [20] arranged in a layered structure with typically 2 to 5 platelets per crystallite. The mean layer spacing is 0.355 nm, only slightly larger than that of graphite [20]. The crystallites are the so-called basic structural units, the BSUs [21] that are used to describe polyaromatic matter. Platelets are polyaromatic units, but defects are also present. Only the outer shell is composed of polyaromatic units while the inner core contains fine particles surrounded by carbon networks [22]. These are supposed to be the reminiscence of the soot nuclei that clustered during the soot growth [23].

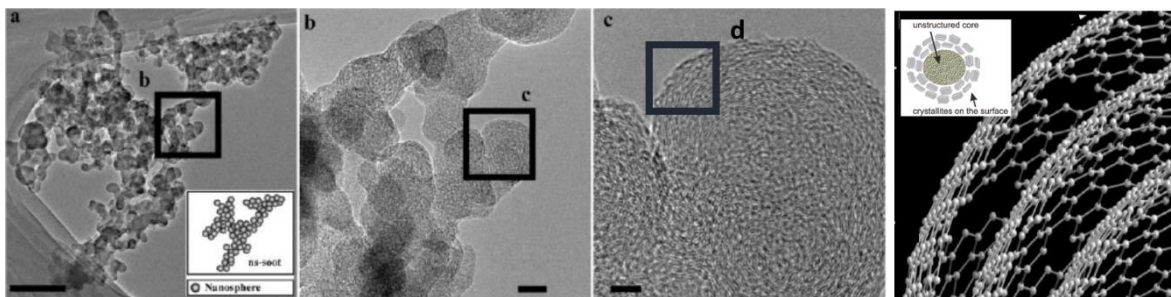


Fig 1.1. Visualization of soot aggregates. (a) A soot particle, scale bar = 200 nm; The inset shows a schematic image of carbonaceous nanoparticles aggregated to form soot. (b) Enlarged image of (a), scale bar = 20 nm. (c) High resolution image of soot particle from (b). Scale bar = 5nm. (d) Enlarged schematic image layers of (c). [6], [22], [24].

Soot formation is a complicated process, including two main stages: soot precursors formation and soot particles evolution, all of which occur typically within a few milliseconds [15]. We illustrate the whole process with the following scheme (Fig. 1.2).

Reactions and combinations in each stage vary on initial fuels and flame conditions. Based on the experimental and modeling investigation of different flames from literature, we briefly describe the main processes with some key reactions.

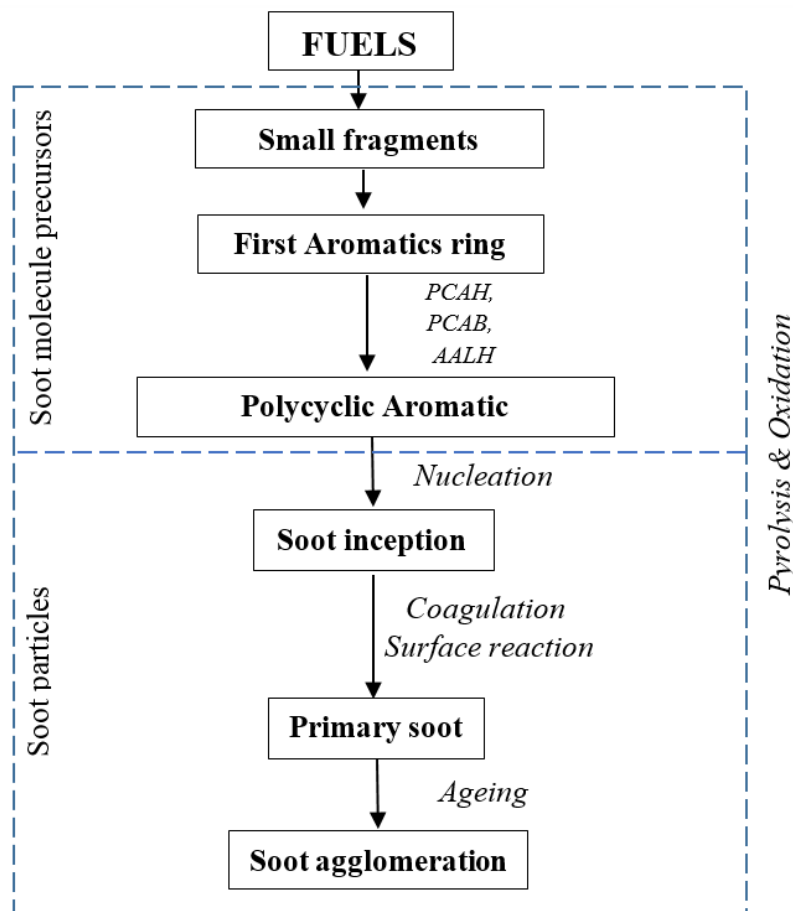

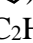



Fig. 1.2. Soot formation process. PCAH: peri-condensed aromatic hydrocarbons; PCAB: peri-condensed aromatic with an aliphatic branch; AALH: aromatic aliphatic linked hydrocarbons.

### 1.2.1.1. Soot molecular precursors

#### a. Formation of the First Aromatic Ring

In the initial stage, through pyrolysis and oxidation, aliphatic fuels are broken into small fragments, which react to form oxidation and pyrolysis products depending on oxygen availability. The formation of acetylene and aromatic radicals are considered as the building blocks of the formation of the *first aromatic ring*, usually benzene or phenyl. As Frenklach [16] and Mansurov [24] showed in their paper, benzene  $C_6H_6$  () and phenyl  $C_6H_5$  radicals () can be formed in the process of interaction of acetylene ( $C_2H_2$ ) with  $n-C_4H_5$  or  $n-C_4H_3$  radicals. However, Miller and Melius [25] stated that these reactions are less probable because these radicals are unstabilized and rapidly transformed to their corresponding resonantly stabilized isomers,  $iso-C_4H_5$ , and  $iso-C_4H_3$  [26]. Instead, they emphasized the role of resonantly stabilized radicals (RSRs), such as propargyl ( $C_3H_3$ ) or allyl radicals ( $aC_3H_5$ ), in forming the first aromatics in flame. Other efficient odd-carbon-atom cyclization reactions have been suggested, such as cyclopentadienyl  $c-C_5H_5$  () or  $i-C_5H_3$  [26], [27]. These processes are described in the scheme below.

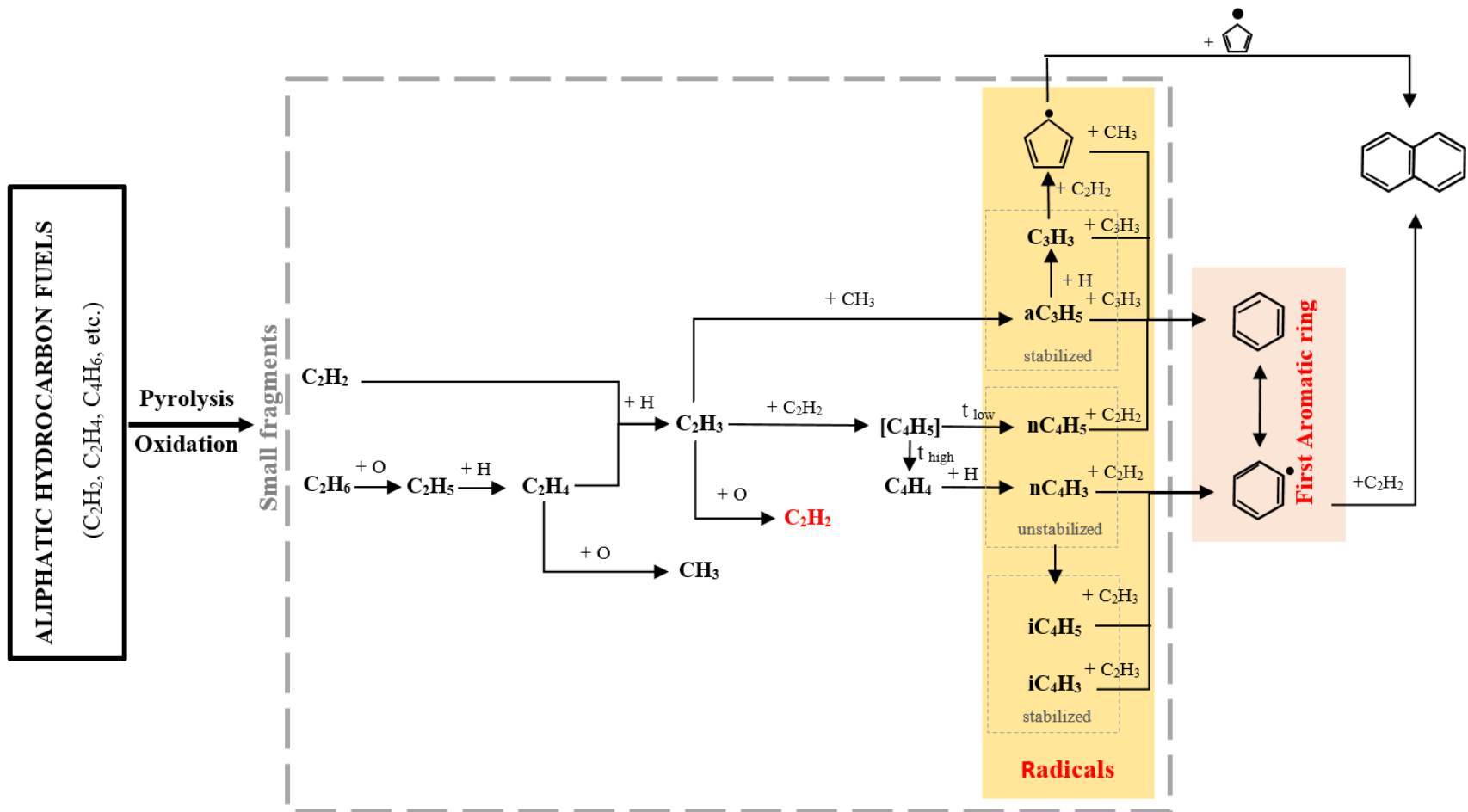


Fig. 1.3. Schematic representation of the first aromatic ring formation in flame.



*b. Growth of Polycyclic Aromatic Hydrocarbons*

Numerous experimental studies indicated that PAHs weighing from hundreds to thousands of amu and the growth of the formed aromatic rings can proceed via different routes, such as peri-condensed aromatic hydrocarbons (PCAH), peri-condensed aromatic with an aliphatic branch (PCAB) and aromatic-aliphatic-linked hydrocarbons (AALH), etc... [28]. Here, we will briefly detail two dominant pathways that are PCAH and AALH routes [15], [22].

Firstly, as shown in Fig. 1.3, the formation of naphthalene, the first compounds of the PAH series, is accomplished through two routes: the sequential addition of  $C_2H_2$  to a phenyl radical and the combination of resonantly stabilized radicals [15], [16], [22], [25], [26], [29]. The former route, hydrogen-abstraction-carbon-addition (HACA) mechanism developed by Frenklach and coworkers [30] consists of two principal steps: hydrogen abstraction to activate aromatics followed by a subsequent acetylene addition. By-products of the HACA process are alkyl-substituted PAH and five-membered aromatics such as acenaphthylene [22]. The latter one is the combination of two cyclopentadienyl radicals or the combination of benzyl ( $C_6H_5CH_2$ ) and propargyl radicals [31].

Acetylene addition is the extension of HACA mechanism to larger compounds. Because of the high number of sites where acetylene can be attached and each acetylene addition sequence may form a closed aromatic ring, it leads to formation of PCAH.

Aromatic addition to the aromatic radicals will create aromatic-linked, biphenyl-like and compounds, which might contain aliphatic and oxygen [22]. These aromatic-aliphatic-linked hydrocarbons (AALH) grow quickly.

The two types of precursors produce different precursor particles: collisions of PCAHs result in turbostratic stacks of graphene sheets, the BSUs, and collisions of AALHs produce kerogen-like material. Besides, small ring size AALH molecules will dimerize faster than equivalent ring size PCAH molecules and the former molecules have shorter lifetime than the latter ones [22], [32]. These two processes are illustrated in Fig. 1.4, the next step of Fig. 1.3, which was proposed by D'Anna, A. (2008) [32], Wang, H. (2011) [15] and Peter R. Buseck et al. (2014) [6].

**1.2.1.2. Soot particles formation**

*a. Nucleation (Soot particle inception)*

The nucleation is a transition process from a molecule to a nanoparticle. This is the less understood step of soot particle formation at present because of the difficulty in collecting experimental data, although recent results have revealed the existence of nucleation flames in which only soot nuclei are formed [33], [34]. There are several hypotheses proposed to model the formation of soot inception, in which Flenklach and Wang's PAH dimerization assumption has been widely used although it has not been proven.

There are three conceptual pathways that may be postulated for soot nucleation. In Fig. 1.4, path A is the growth of "two-dimensional" PAHs and evolution into curved, fullerene-like structure. Paths B relies on the formation of stacked clusters of PCAHs and

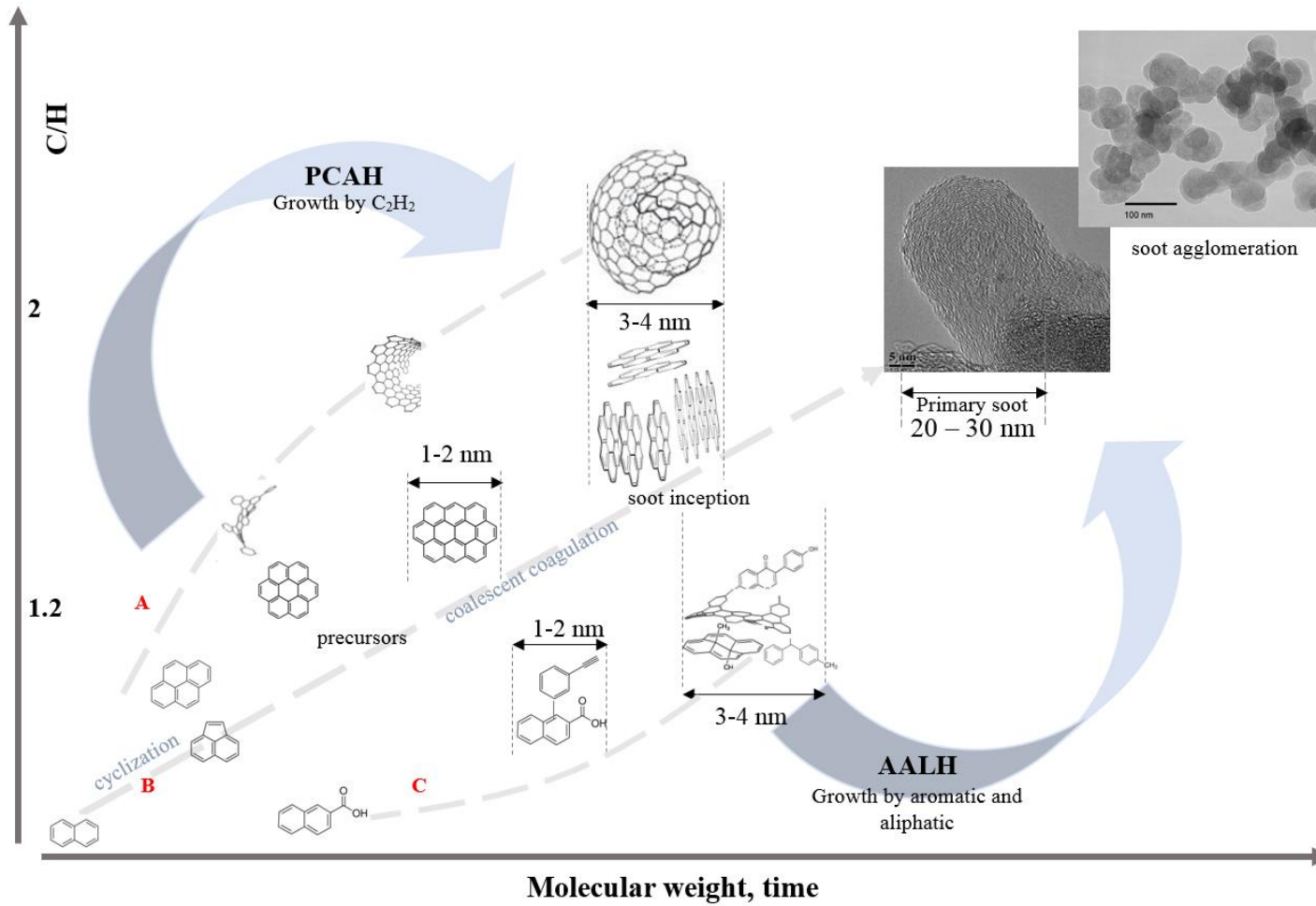


Fig. 1.4. Schematic representation of oxidation and pyrolysis routes [6], [15], [22].

path C supposes the reaction or chemical coalescence of moderate-size PAHs into crosslinked three-dimensional structure AALHs [15].

PCAHs and AALH grow up to form agglomerates of the molecules whose diameters are a few nanometers. These molecules held together by the weak van der Waals interactions. As the molecular mass of molecular compounds increase, the van der Waals interactions become stronger. Once PAH monomers have reached a certain size, they start to stick together during collision and form PAH dimers. These PAH dimers are the very first particles occurring in the gas-phase and are the basis of Miller and Frenklach hypothesis.

While individual PAHs continue to increase their size via chemical reactions, PAH dimers start colliding with PAH molecules to form trimers or colliding with other similar species to form tetramers and built up. Finally, PAH dimers become PAH clusters and then evolve into solid particles. Similar clustering process is supposed to occur for the AALHs, but chemical condensation may further stabilize the cluster rather than the van der Waals interaction only.

The first soot nuclei or nascent soot possess C/H ratios around 2 [15], [20]. Their molecular masses are probably between 500 a.m.u. and 2000 a.m.u according to L.D. Pfefferle et al [35] and D'Anna, A. et al [36]. However their detailed chemical structures, i.e. their aliphatic to aromatic ratio, the cross-linkage, the oxygen content, and their related spectral properties are under debate.

### *b. Primary particle formation and surface growth*

Nascent soot particles produced during the nucleation step will stick together to form agglomerates. The rate of coagulation is evaluated as a function of the size of the colliding particles [37]. These agglomerates are quickly covered by material from the gas phase [38], [39] and develop into *primary soot particles* forming young soot particles. Aging within the flame lead to mature soot particles. Under high resolution TEM, the mature primary soot particles show an inner core surrounded by an outer shell [40]–[42]. The outer shell is composed of graphitic structures, BSUs, whereas the inner core consists of fine particles covered by concentric BSUs [22]. The structuration retains memory of the growth process. However, the observed structuration and nanostructuration is found to be more complicated for young soot where the concentric nanostructuration may not be observed. The primary particles are usually found to be more disordered with less BSUs [41]. It should be recall that such structural analyses are performed on sampled soot, thus impaction, cooling and exposure to air, for instances, may alter the carbon network.

The outer shell originates from the by-products of early combustion stage, for young as well as mature soot, such as aromatic radicals or acetylenic species and the PAHs. There surface growth is assumed to be similar to the PAHs evolution, whereas this is a heterogeneous process where adsorption and desorption at the surface occur instead of gas-phase reactions of small molecules during PAHs evolution [19]. The overwhelming part of soot (> 95% ) is formed by surface growth rather than soot inception [43]. Contemporaneous with the addition of mass on the surface of particle proceeded by addition of acetylene and aromatics, hydroxyl radical and oxygen remove mass from the particles through the

formation of CO and HCO [22]. The equilibrium between the mass growth and destruction depends on the flame condition and particularly the richness. The chemical species absorbed onto the soot surface can be detected by laser desorption / laser ionization / time of flight mass spectrometer (TOF-MS) [38], [39], [44].

*c. Soot agglomeration*

Soot agglomeration is the late phase of soot formation when surface accretion reaction is no longer possible. Consequently, open structured aggregates are formed, consisting of tens to hundreds of primary particles [43]. The relationship between the number  $N$  of primary particles and the maximum length  $L$  of the aggregates is expressed by the following formula [43]:

$$N = k_f \cdot \left( \frac{L}{3d_p} \right)^{D_f} \quad (1.1)$$

where  $k_f$  is constant fractal prefactor,  $d_p$ : the primary particle diameter and  $D_f$ : a fractal dimension around 1.8 [43]. At this stage, aging of the primary particles is at work and the clusters are evolving.

### 1.2.2. Spectral properties

Spectral information on soot are important in many fields of research. In environmental research, a detailed knowledge of the spectral behavior of soot particles is necessary to estimate the global warming of the atmosphere produced by exhaust fumes, forest fires, and volcanic eruptions. In astrophysics, their absorption contributes to the interstellar extinction curve for example. Indeed, UV-Visible, infrared (IR), Raman spectral shapes and absorption coefficients of soot contain information on soot morphology in terms of size, shape, etc. and chemical structure as well as signatures of structural changes occurring during the soot formation process [45].

The main characteristic allowing in-situ distinction of soot particles is the light absorption property [22]. According to the pioneer work of a combustion group in Napoli, Italy, soot particles absorb strongly in a large spectral range in UV steeply decreasing towards the visible [45]. The case of the nascent soot particles is more complicated. Precursor nanoparticles were found to be almost transparent to visible light [46], unlike soot particles. The fact is that the authors have identified nanoparticles, called nano-organic compounds (NOC), that they did not consider as particles similar to very small soot particles. In addition, in the same research group, these precursors nanoparticles were observed to be fluorescent in the UV [47] showing up a typical broadband fluorescence peaking in the UV in premixed flames. A shift of the maximum of the fluorescence down to the visible was observed in non-premixed flames [47]. These properties await for more experimental evidences before generalization to all soot nuclei.

Equally important, the UV/Vis spectra of carbon species like soot can be interpreted by electronic band structure of carbonaceous materials. Electronic transitions from the bonding  $\pi$  and  $\sigma$  to the antibonding  $\pi^*$  and  $\sigma^*$  occur in the region between 180 and 260 nm ( $\pi$

-  $\pi^*$  transitions) and between 50 to 100 nm ( $\sigma$  -  $\sigma^*$  transition) [45], [48], [49], respectively. A downward trend was also seen toward the visible exhibiting the typical fine structure due to PAHs contained inside the soot [45]. The position of UV absorption peaks is strongly influenced by the electronic structure of soot, for example, the characteristics of the polyaromatic units. The visible absorption is usually associated with the size of the polyaromatic unit  $L_a$  [45] or equivalently the number of condensed rings,  $N_R$ , which can be derived from gap energy  $E_g$  via the the following relation: [4], [48], [50]–[52]:

$$L_a(nm) = \left[ \frac{0.77}{E_g(eV)} \right] \quad (1.2)$$

$$N_R = \left[ \frac{5.8}{E_g(eV)} \right]^2 \quad (1.3)$$

The narrowing of the spectral bandwidth is due to the decrease of the size distribution of the polyaromatic units [4], [45]. However this energy gap modeling was developed for amorphous carbon and may not be suitable for soot-like material. Soot is found to cover a wide range of optical gap, from nearly 0 eV to about 2.5 eV, depending on flame conditions and maturity. Only few measurements are actually performed directly in the gas phase [53].

Polyaromatic units in which carbon atoms occupy lattice sites in a two-dimensional honeycomb network have intense Raman modes, but very weak IR vibrational absorption [5]. The main features in the Raman spectra of carbons are the so-called D and G peaks, which lie at around 1360 and 1600  $\text{cm}^{-1}$ , respectively, for visible excitation. The G peak corresponds to the  $\text{sp}^2$  C=C bond stretch in disordered or amorphous material. The D peak is due to the breathing modes of 6-atom rings and requires a defect for its activation in bulk matter [54], [55]. Raman spectroscopy is considered as one of the sole method to identify polyaromatic structures at a molecular level in the atmospheric aerosol [5].

Overall, the spectral methods mentioned above are considered to be efficient tools in soot investigation. The positions, shapes and intensities of peaks are functions of polyaromatic size, morphology, and nanostructuration. Furthermore, they may contribute to soot ageing and their chemical (oxidation) properties estimation.

### 1.3. Detection of soot in the laboratory and in the atmosphere

Because of the harmful consequences of soot on human health, infrastructural degradation, global climate, their detection and measurement have become important today in science and industry. In science, many different laser-based techniques and methods have been developed to approach these purposes, including Rayleigh scattering, Raman scattering, nonlinear Raman spectroscopy, light extinction, laser-induced fluorescence (LIF), laser-induced incandescence (LII), photoionization and mass spectroscopy, etc. Among these methods, LII has been used widely [34], [44], [56]–[63]. In industry, especially in car manufacture, soot particle detection and measurement on board using sensors can be achieved by several methods, such as soot collection on filters, photo-acoustic devices,

potentiometric sensors, thermophoretic particle deposition, scanning mobility particle size (SMPS) system, etc. [64], [65]. In this section, we only give general descriptions of some methods.

Light scattering is directly related to structure factors under the assumption of no internal multiple scattering [66]. Actually, with our materials, Rayleigh scattering and extinction can yield the aggregate or particle volume equivalent sphere radius and volume fraction of soot and cluster number density of the aerosol. Combination of the optical structure factor measurement with scattering/extinction measurements allows for a remarkably complete characterization of aerosols or colloids of particles with a complex index of refraction such as soot [66]–[68].

As mentioned in the previous section, Raman spectroscopy is a strong and efficient tool used to investigate carbonaceous materials in general and soot in particular. Soot existence is easy to identify via their Raman spectra because of the appearance of *D* and *G* bands [69]–[71]. In our research, Raman spectroscopy is the main tool used to detect and investigate soot particles. Therefore, we will briefly introduce Raman spectroscopy, including history, its general principles and its application in the study of carbon related materials in the next section.

Laser-induced incandescence (LII) has been developed within recent decades and rapidly became a powerful tool for in-situ measurements of carbonaceous particles. It is used to determine soot volume fraction in complex combustion because of its ability to provide quantitative spatially and temporally resolved measurements [33], [69], [58], [72], [73]. In addition to Raman spectroscopy and LII, LIF, laser desorption / photoionisation / time-of-flight mass spectrometry has been applied to probe PAHs in soot [38], [74].

In industry, since the regulations concerning particle mass emission limits have been lowered by the European emission standard, chemical composition and particle size of soot emission have been considered by many factories. A potentiometric sensor is used to detect soot by burning soot particulates at the working electrode and measuring the electromagnetic force in the sensor materials. The SMPS system is a compact machine widely used as the standard methods to measure airborne particle size distributions. These particle sizes are also used to make accurate nanoparticle size measurements of particles suspended in liquids.

Most of the methods presented above have been done in laboratories. In the atmosphere, the photo-acoustic method is used to detect soot particles generated by fire in ambient air [75]. This technique, that has been used for decades since 1970s, is capable of picking out gas of interest among the other species. Recently, it has been developed and used to detect atmospheric aerosols. In 2006, atmospheric number size distributions of soot particles and their emission factors were estimated by D. Rose and coworkers based on volatility technique to obtain mean number fractions of externally mixed soot particles of atmospheric aerosols in differently polluted areas in different seasons [76]. In volatility techniques, by heating aerosols to 300°C, the volatility materials (sulfates, nitrates or organic acids) are evaporated, the residual non-volatility materials are measured to estimate their fraction [76].

## 1.4. Raman spectroscopy and its application to study of carbon related materials

### 1.4.1. Raman spectroscopy

Raman spectroscopy is known as non-destructive spectroscopic characterization tool. It provides identification of molecules, molecular symmetry, crystal orientation and particle sizes ... The technique is named after an Sir C. V. Raman, who discovered it in 1928 and later won a Nobel prize for this discovery. In his experiment, he used mono-chromatized sunlight to excite some sixty liquids and gasses and detect scattered light with a "crossed filter" to block this monochromatic light. It was found that a small amount of light passed through the filter. In the following years, mercury arc lamp became a popular light source for Raman excitation. Typically, the sample was stored in a tube and illuminated by a monochromatic wavelength generated by the lamp. The scattered photons were collected through optics at the end of the tube. The sample has to be highly concentrated (>1 M) and relatively large volumes (>5 mL) to get maximum Raman signal. Nowadays, the advent of laser and high technology devices have made Raman spectroscopy a very sensitive characterization tool. Typically, a sample is illuminated with a laser beam, scattered light from the illuminated spot is collected with a lens and sent through a monochromator or spectrograph. The laser line is filtered out by either an interferential filter while the rest of the collected light is dispersed by gratings onto a detector.

Raman spectroscopy relies on inelastic scattering, or Raman scattering, of monochromatic light, usually from a laser in the visible, near infrared, or near ultraviolet range. Light can be scattered in two ways elastically Rayleigh scattering in which no transfer of energy between the molecules and photons or inelastically known as Raman scatterings. Raman involves the transfer of energy between molecule and photon. Modern Raman experiment is designed to filter out the Rayleigh light because only one in million photons will be Raman scattered in a non-resonant process. Inelastic scattering loses or gains energy. When light scattered loses energy it is referred to as Stoke shift, when it gains energy it is referred to as anti-Stoke shift (Fig. 1.5). For a molecule to be Raman active, it must have a change in polarizability meaning it must has change of size, shape, or orientation of the electron cloud that surrounds the molecules. For instance this change occurs in symmetric stretching but not an asymmetric stretching.

As Raman's explanation, the Raman bands appear due to the oscillating induced dipole moment vector ( $\vec{P}$ ) caused by the electric field ( $\vec{E}$ ) of light waves interacting with the polarizability ( $\alpha$ ) of the vibrating molecules. The strength of induced dipole moment is given by:

$$P = \alpha E \quad (1.4)$$

in which  $E = E_0 \cos(2\pi\nu_0 t)$  where  $E_0$  is the maximum value of electric field,  $\nu_0$  is the frequency of incident electromagnetic wave. For small displacements, the polarization may

#### 1.4. Raman spectroscopy and its application to study of carbon related materials

be approximated by Taylor series expansion  $\alpha = \alpha_0 + \frac{\partial\alpha}{\partial Q}dQ$  where  $\alpha_0$  is the polarizability of the molecular mode at equilibrium position,  $dQ$  is the physical displacement of the atoms,  $dQ = Q_0\cos(2\pi\nu_{vib}t)$  where  $Q_0$  is the maximum displacement about the equilibrium position and  $\nu_{vib}$  is the frequency of the vibrational mode. The formula (1.4) can be rewritten:

$$P = \left( \alpha_0 + \frac{\partial\alpha}{\partial Q}Q_0 \cos(2\pi\nu_{vib}t) \right) [E_0 \cos(2\pi\nu_0t)] \quad (1.5)$$

$$P = \alpha_0 E_0 \cos(2\pi\nu_0t) + \frac{\partial\alpha}{\partial Q}Q_0 E_0 \cos(2\pi\nu_{vib}t) \cos(2\pi\nu_0t) \quad (1.6)$$

$$P = \alpha_0 E_0 \cos(2\pi\nu_0t) + \left( \frac{\partial\alpha}{\partial Q} \frac{Q_0 E_0}{2} \right) \{ \cos[2\pi(\nu_0 - \nu_{vib})t] + \cos[2\pi(\nu_0 + \nu_{vib})t] \} \quad (1.7)$$

From equation (1.7), the induced dipole moment is created at three frequencies:  $\nu_0$ ,  $\nu_0 - \nu_{vib}$  and  $\nu_0 + \nu_{vib}$ . The first one corresponds to elastic scattering, e.g. Mie or Rayleigh scattering depending on the size regime, while the latter two frequencies are Stokes scattering and anti-Stokes scattering.

When photons are scattered, most of them are elastically scattered and a very small fraction of the photons (approximately one in one million for a non-resonant process) are inelastically scattered. In thermodynamic equilibrium at room temperature, the lower states are more populated than the upper ones, thus the Stokes scattering peaks are higher than the anti-Stokes scattering peaks. This is the normal Raman effect when the excitation wavelength is lower than electronic transitions of materials. However, if the excitation wavelength is overlap or very close to an electronic transition of material, the resonance Raman (RR) could happen and the Raman scattering intensities are enhanced by a factors of  $10^2 - 10^6$  times comparing to normal Raman scattering. A noticeable point in RR effect is that the fluorescence can cause a significant background problem because both RR and fluorescence use excitation light that is tuned to a particular electronic transition.

The main differences between Raman scattering and fluorescence are the emission process, the angular distribution and the polarisation relatively to the excitation beam. Fluorescing excited states have lifetimes that depends only on the spontaneous radiative decay, and can be long-lived. Raman scattering time-profile is only dictated by the incoming pulse. In fluorescence, absorption of light transfers part of the population of the target to a higher electronic excited state. The resulting ground state population, after emission, is sensitive to the Franck-Condon factors between the electronic states involved while for Raman scattering, only the activity of the modes in the ground state are at work. Spontaneous emission is isotropic. RR may be anisotropic, and the scattered light may be strongly polarised.

Raman spectroscopy is commonly used in chemistry, to identify constituent molecules of the sample under investigated. This is because Raman is specific to the chemical



bonds, molecular vibration and symmetry of molecules. It provides a fingerprint of the molecule, for example, Raman shift of nitrogen is  $2331\text{ cm}^{-1}$  and oxygen is  $1556\text{ cm}^{-1}$ . Because Raman spectroscopy give information about vibrational mode that characterizes molecule, it can be used to study changes in structure of molecule caused by impurities or external fields [79].

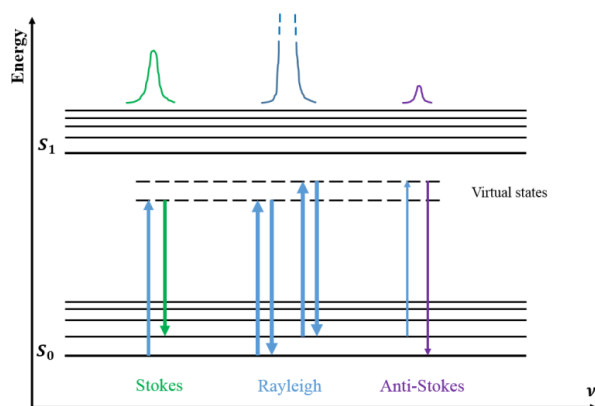


Fig. 1.5. Normal Raman process explained by energy diagram.

In solid-state physics, Raman can be used to find crystallographic orientation and characteristic phonon of crystal. Polarization of Raman signal with respect to crystal and incident laser provides information of crystal orientation if crystal point group is known. It can be used to observe low frequency excitations of the solid, such as plasmons, magnons, and superconducting gap excitations. The spontaneous Raman signal tells the population of a given phonon mode by the ratio between the Stokes (downshifted) intensity and anti-Stokes (upshifted) intensity.

### 1.4.2. Raman spectroscopic study of carbon related materials

In carbon-related materials, Raman spectroscopy has been used since decades due to its non-destructive properties and its high sensitivity in characterizing the materials via the appearance of Raman peaks, its positions, width and the dependence of excitation wavelength. Among carbon materials, graphene is one of the most studied due to its outstanding properties and potential applications in nanoelectronics [80]. Its high conductivity can be used for transparent electrodes in solar energy application [81]. Its high thermal conductivity and extremely high hardness deserves much attention.

Graphene belongs to a large family of  $sp^2$  carbon structure in which carbon are made of trivalent join via  $sp^2$  bonding. Graphene is a single layer with hexagonal honey comb structure (bottom of Fig. 1.6a). It is the basic building block of graphite which is formed by stacking multiple graphene layers. It is the basic structure for low dimension nanocarbon materials, wrapping graphene creates carbon nanotubes (1D). Thus Raman spectroscopic study of graphene was a key step forward understanding carbon-related materials. Raman spectra of graphene and graphite consist of a peak so-called *G* peak (stand for Graphite as it always present in this material) and *D* peak if there is a defect in the crystal lattice (top part

of Fig. 1.6a). The  $G$  peak, appearing at  $1575\text{ cm}^{-1}$ , results from an in-plane vibration of symmetric  $E_{2g}$  mode [82], [83]. In defect-free samples a phonon mode is only Raman active if its symmetry is correct and its wave vector is zero. This is the Raman selection rule. In graphene,  $E_{2g}$  mode satisfies this requirement. However,  $D$  peak, appearing at  $1355\text{ cm}^{-1}$ , was a debate for some decades.

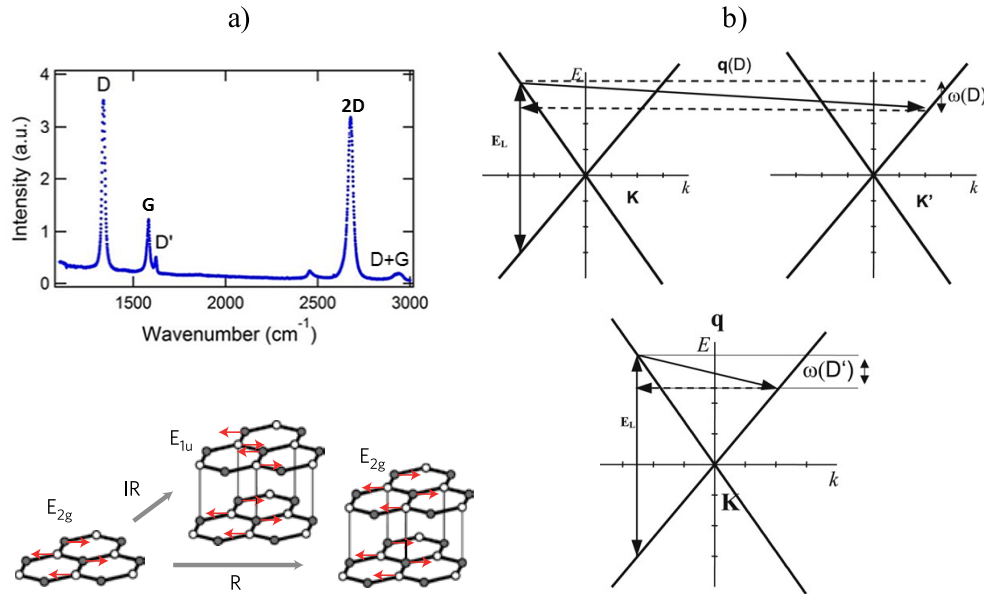


Fig. 1.6. a) Top: a typical Raman spectrum of defected graphene excited by  $532\text{ nm}$ ,  $G$  ( $1580\text{ cm}^{-1}$ ),  $D$  ( $2690\text{ cm}^{-1}$ ) [91], bottom: vibrational  $E_{2g}$  mode in single layer graphene and the transformation of  $E_{2g}$  mode from 2D graphene to 3D graphite [83]. b) phonon scattering process responsible for main Raman peaks presented by electron dispersion and interband transitions. Top of b) shows phonon scattering process in intervalley  $\mathbf{K}$ ,  $\mathbf{K}'$  (in Brillouin zone) that results in  $2D$  peak, solid arrows: photon absorption and emission, dashed arrows: phonon emission. Bottom b) phonon scattering process in intravalley  $\mathbf{K}$  responsible for  $D'$  peak.

In a Raman study of polycrystalline graphite, Tuinstra et al. assigned the peak to  $A_{1g}$  mode which become Raman active due to boundary of the crystallite [82]. However, this attribution cannot explain the dispersive properties of i)  $D$  peak position, ii) the overtone  $2D$  and iii) the intensity ratio of  $D$  and  $G$  peak [84], [85]. The most accepted theory for the  $D$  peak is based on double resonance process which is shown in top part of Fig. 1.6b. A laser excites and creates an electron-hole pair, the electron is then inelastically scattered by a phonon, a second elastic scattering by a defect occurs resulting in electron-hole recombination [86]. A similar process can take place in intra-valley (bottom Fig. 1.6b), which activates phonon with small  $\mathbf{q}$ , resulting in the  $D'$  peak at  $\sim 1620\text{ cm}^{-1}$  (Fig. 1.6a) in defected graphite [87]. The dispersive characteristic of the  $D$  peak is due to Kohn anomaly at  $\mathbf{K}$  in the Brillouin zone [88]. There is also a  $2D$  peak located at  $\sim 2690\text{ cm}^{-1}$  (Fig. 1.6a). This peak is the second order overtone of  $D$  peak. It is always present even without the  $D$  peak because

the second scattering (either on the same electron/hole or its complementary electron/hole) is also an inelastic scattering from a second phonon [89], [90].

The above overview of Raman spectroscopy of graphene and graphite provides background in understanding Raman spectroscopy of disordered or amorphous carbon that are investigated in this dissertation. Most of amorphous carbon contain a mixture of  $sp^1$ ,  $sp^2$  and  $sp^3$  bonding carbon with possible hydrogen. The compositions can be shown in a ternary phase diagram in Fig. 1.7a (neglecting the  $sp$  content), which is a triangle with three corners

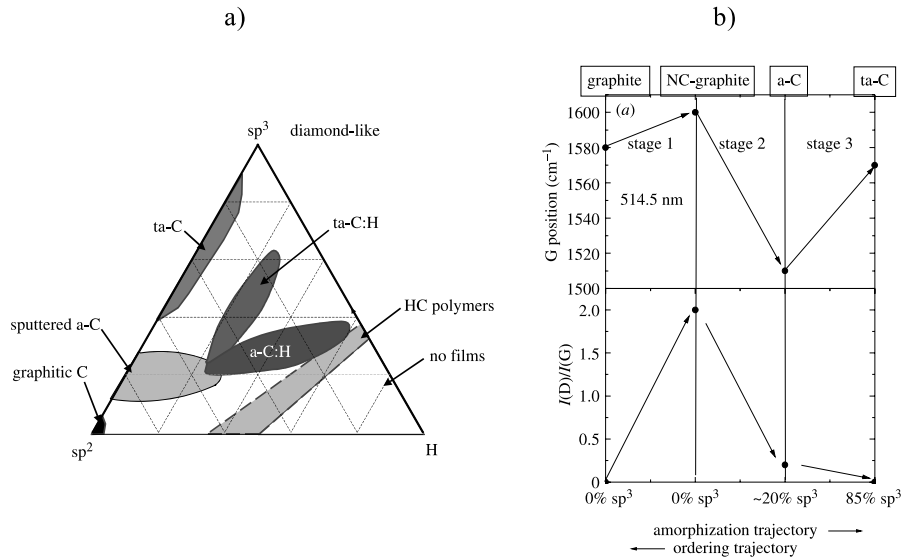


Fig. 1.7. a) Ternary phase diagram of amorphous carbons. b) three-stage model of visible Raman spectrum with increasing disorder: stage 1: graphite to crystalline graphite (NC-graphite), stage 2: NC-graphite to  $sp^2$  a-C, stage 3: a-C to ta-C.

being  $sp^3$  representing diamond-like carbon,  $sp^2$  belonging to graphitic family and H. The high  $sp^3$  content is termed tetrahedral amorphous carbon (ta-C) as it has diamond-like structure, its hydrogenated form ta-C:H. The hydrogenated a-C:H comprises less  $sp^3$  content. It should be noted that amorphous carbons may have different properties even though they have the same  $sp^3$  and H content. This is because their properties are influenced by the degree of clustering of the  $sp^2$  phase. The key parameters in these materials are: i) the  $sp^3$  content, ii) the degree of clustering of the  $sp^2$  phase forming the polyaromatic units, iii) the orientation of  $sp^2$  phase, iv) the cross sectional nanostructure, i.e. the relative orientation of the stacked polyaromatic units, and v) the H content. Raman can be used to probe  $sp^2/sp^3$  fraction in diamond-like carbon. The visible Raman spectrum is significantly dependent on the ordering of  $sp^2$  sites and only indirectly on  $sp^3$  sites [71]. Ferrari et al. introduced a three-stages model of increasing disorder to predict trends of Raman spectra in amorphous carbon. The model shows how the G peak position and the intensity ratio of D and G peak change as a function of  $sp^3$  contents when moving from ordered graphite to nanocrystalline, to amorphous carbon and finally to  $sp^3$  bonded ta-C (Fig. 1.7b).

In stage 1,  $G$  peak position shifts from  $1581\text{ cm}^{-1}$  to  $\sim 1600\text{ cm}^{-1}$  as graphite turns into nanocrystalline graphite and when measured at  $514\text{ nm}$ . The  $D$  peak appears and increases intensity as the cluster size,  $L_a$ , get smaller. This follows the Tuinstra and Koenig relation  $I_D/I_G \propto 1/L_a$ .

In stage 2, a different regime occurs as topological disorder is introduced into the graphite layer. The  $sp^2$  bonding is still dominant but the bond is weaker and soften the vibrational mode leading to a shift of the  $G$  peak position down to  $\sim 1510\text{ cm}^{-1}$  at a  $sp^3$  content of  $\sim 20\%$ . The Tuinstra-Koenig relation is no longer valid but  $I_D/I_G \propto L_a^2$  [71]. This manifests as the decrease of  $I_D/I_G$  values as the increase of  $sp^3$  content. This means  $I_D/I_G$  is proportional to the number of aromatic ring in cluster and it is inversely proportional to squared optical gap,  $1/(E_g)^2$  [71].

In stage 3,  $sp^3$  sites become dominant, as a consequence, the aromatic ring configuration converts to chain configuration. This makes  $G$  peak shift to higher wavenumber  $\sim 1570\text{ cm}^{-1}$  due to the confinement of  $\pi$  electrons in shorter chains. The ratio  $I_D/I_G = 0$  is finally due to the absence of aromatic rings. However, the  $I_D/I_G = 0$  does not mean that the value  $1/(E_g)^2 = 0$ , for example, in the case of  $ta\text{-C}$ , the  $1/(E_g)^2 = 0.2\text{ eV}^{-2}$  for  $I_D/I_G \approx 0$  this is because the gap is controlled by  $sp^2$  configuration in the chain when there is no ring.

Full width at half maximum (FWHM) of  $G$  peak is a monotonic function of disorder, thus one can measure degree of disorder by investigating this FWHM. On the other hand, we can derive content of  $sp^3$  if we know relationship between  $sp^2$  and  $sp^3$ , for example the optical gap and  $sp^3$  fraction. This three-stages model is useful in providing us hints of Raman spectra and giving guidance in the interpretation of the spectra of soot particles in this dissertation.

## 1.5. Conclusions

In this chapter, we have reviewed almost all carbonaceous particles in the atmosphere, consisting of their sources, components, optical properties as well as their adverse effects on global climate, human health, infrastructure, and their detection methods. The existence of carbonaceous particles receives more and more attention from organizations in various fields. They aim to integrate their formation mechanism, detect their presence, and limit their emission in the atmosphere. As mentioned above, there are still several critical gaps in understanding of the mechanism of soot formation. For example, the formation of nascent soot is less understood at present because some hypotheses were proposed but lacking experimental proofs. Carbon-based materials are abundant, but the database of their optical properties is not adequate, such as differential Raman cross section or optical constants. The information of their full spectral characterization in UV-Vis-MIR range also needs to be completed. Our research aims at shedding light on these hidden corners.

In addition, soot as produced in combustion will immediately undergo ageing in the atmosphere (water adsorption, surface reaction, coagulation, etc.) that will modify its properties (physical, chemical and optical). Then, monitoring of BC in the atmosphere requires adapting the knowledge on soot to real BC. Raman spectroscopy, which is mostly sensitive to the carbon skeleton of the spherule, may be particularly appropriate.

## References

- [1] P. Delhaes, *Carbon-based Solids and Materials*. John Wiley & Sons, Ltd, 2011.
- [2] T. C. Bond and R. W. Bergstrom, “Light Absorption by Carbonaceous Particles: An Investigative Review,” *Aerosol Sci. Technol.*, vol. 40, no. 1, pp. 27–67, 2006.
- [3] A. Y. Watson and P. a Valberg, “Carbon Black and Soot: Two Different Substances,” *AIHAJ - Am. Ind. Hyg. Assoc.*, vol. 62, no. 2, pp. 218–228, 2001.
- [4] J. Robertson and E. O’Reilly, “Electronic and atomic structure of amorphous carbon,” *Phys. Rev. B*, vol. 35, no. 6, pp. 2946–2957, 1987.
- [5] M. O. Andreae and A. Gelencsér, “Black carbon or brown carbon? The nature of light-absorbing carbonaceous aerosols,” *Atmos. Chem. Phys.*, vol. 6, pp. 3131–3148, 2006.
- [6] P. R. Buseck, K. Adachi, A. Gelencsér, É. Tompa, and M. Pósfai, “Ns-Soot: A Material-Based Term for Strongly Light-Absorbing Carbonaceous Particles,” *Aerosol Sci. Technol.*, vol. 48, no. 7, pp. 777–788, 2014.
- [7] H. Forrister, J. Liu, E. Scheuer, J. Dibb, L. Ziemba, K. L. Thornhill, B. Aderson, G. Diskin, A. E. Perring, J. P. Schwarz, P. Campuzano-Jost, D. A. Day, B. B. Palm, J. L. Jimenez, A. Nenes, and R. J. Weber, “Evolution of brown carbon in wildfire plumes,” *Geophysical Res. Lett.*, vol. 42, pp. 4623–4630, 2015.
- [8] A. Laskin, J. Laskin, and S. A. Nizkorodov, “Chemistry of Atmospheric Brown Carbon,” *Chem. Rev.*, vol. 115, no. 10, pp. 4335–4382, 2015.
- [9] Y. Qian, T. J. Yasunari, S. J. Doherty, M. G. Flanner, W. K. M. Lau, J. Ming, H. Wang, M. Wang, S. G. Warren, and R. Zhang, “Light-absorbing particles in snow and ice: Measurement and modeling of climatic and hydrological impact,” *Adv. Atmos. Sci.*, vol. 32, no. 1, pp. 64–91, 2015.
- [10] N. Riemer, H. Vogel, and B. Vogel, “Soot aging time scales in polluted regions during day and night,” *Atmos. Chem. Phys.*, vol. 4, pp. 1885–1893, 2004.
- [11] S. Cakmak, R. E. Dales, M. Angelica Rubio, and C. Blanco Vidal, “The risk of dying on days of higher air pollution among the socially disadvantaged elderly,” *Environ. Res.*, vol. 111, no. 3, pp. 388–393, 2011.
- [12] S. Val, C. Liousse, E. H. T. Doumbia, C. Galy-Lacaux, H. Cachier, N. Marchand, A. Badel, E. Gardrat, A. Sylvestre, and A. Baeza-Squiban, “Physico-chemical characterization of African urban aerosols (Bamako in Mali and Dakar in Senegal) and their toxic effects in human bronchial epithelial cells: description of a worrying situation,” *Part. Fibre Toxicol.*, vol. 10, p. 10, 2013.
- [13] K. Ito, R. Mathes, Z. Ross, A. Nádas, G. Thurston, and T. Matte, “Fine particulate matter constituents associated with cardiovascular hospitalizations and mortality in New York City,” *Environ. Health Perspect.*, vol. 119, no. 4, pp. 467–473, 2011.
- [14] J. Zhou, K. Ito, R. Lall, M. Lippmann, and G. Thurston, “Time-series analysis of mortality effects of fine particulate matter components in Detroit and seattle,” *Environ. Health Perspect.*, vol. 119, no. 4, pp. 461–466, 2011.

- [15] H. Wang, "Formation of nascent soot and other condensed-phase materials in flames," *Proc. Combust. Inst.*, vol. 33, no. 1, pp. 41–67, 2011.
- [16] Z. A. Mansurov, "Formation of soot from polycyclic aromatic hydrocarbons as well as fullerenes and carbon nanotubes in the combustion of hydrocarbon," *J. Eng. Phys. Thermophys.*, vol. 84, no. 1, pp. 125–159, 2011.
- [17] D. D. Cohen, J. Crawford, E. Stelcer, and V. T. Bac, "Characterisation and source apportionment of fine particulate sources at Hanoi from 2001 to 2008," *Atmos. Environ.*, vol. 44, no. 3, pp. 320–328, 2010.
- [18] J. Appel, H. Bockhorn, and M. Frenklach, "Kinetic Modeling of Soot Formation with Detailed Chemistry and Physics: Laminar Premixed Flames of C2 Hydrocarbons," *Combust. Flame*, vol. 121, pp. 122–136, 2000.
- [19] I. I. Naydenova, "Soot Formation Modeling during Hydrocarbon Pyrolysis and Oxidation behind Shock Waves," Rupertus Carola University of Heidelberg, 2007.
- [20] O. I. Smith, "Fundamentals of soot formation in flames with application to diesel engine particulate emissions," *Prog. Energy Combust. Sci.*, vol. 7, no. 4, pp. 275–291, 1981.
- [21] J. N. Rouzaud and A. Oberlin, "Structure, microtexture, and optical properties of anthracene and saccharose-based carbons," *Carbon N. Y.*, vol. 27, no. 4, pp. 517–529, 1989.
- [22] H. Bockhorn, A. D'Anna, A. F. Sarofim, and H. Wang, *Combustion Generated Fine Carbonaceous Particles*. Karlsruhe: KIT scientific publishing, 2009.
- [23] B. Apicella, X. Wang, M. Armenante, A. Bruno, and N. Spinelli, "Picosecond and nanosecond laser ionization for the on-line analysis of combustion-formed pollutant," in *Proceedings of the 32nd Meeting on Combustion*, 2009, p. I-12.
- [24] I. Naydenova, M. Nullmeier, J. Warnatz, and P. A. Vlasov, "Detailed kinetic modeling of soot formation during shock-tube pyrolysis of C<sub>6</sub>H<sub>6</sub>: direct comparison with the results of time-resolved laser-induced incandescence (LII) and CW-laser extinction measurements," *Combust. Sci. Technol.*, vol. 176, no. 10, pp. 1667–1703, 2004.
- [25] J. A. Miller and C. F. Melius, "Kinetic and thermodynamic issues in the formation of aromatic compounds in flames of aliphatic fuels," *Combust. Flame*, vol. 91, no. 1, pp. 21–39, 1992.
- [26] C. J. Pope and J. a. Miller, "Exploring old and new benzene formation pathways in lowpressure premixed flames of aliphatic fuels," *Proc. Combust. Inst.*, vol. 28, no. 2, pp. 1519–1527, 2000.
- [27] M. J. Castaldi, N. M. Marinov, C. F. Melius, J. Huang, S. M. Senkan, W. J. Pit, and C. K. Westbrook, "Experimental and modeling investigation of aromatic and polycyclic aromatic hydrocarbon formation in a premixed ethylene flame," *Symp. Combust.*, vol. 26, no. 1, pp. 693–702, 1996.
- [28] S. H. Chung and A. Violi, "Peri-condensed aromatics with aliphatic chains as key intermediates for the nucleation of aromatic hydrocarbons," *Proc. Combust. Inst.*, vol. 33, no. 1, pp. 693–700, 2011.

- [29] N. M. Marinov, W. J. Pitz, C. K. Westbrook, M. J. Castaldi, and S. M. Senkan, *Modeling of Aromatic and Polycyclic Aromatic Hydrocarbon Formation in Premixed Methane and Ethane Flames*, vol. 116–117, no. 1–6. 1996.
- [30] M. Frenklach, “Reaction mechanism of soot formation in flames,” *Phys. Chem. Chem. Phys.*, vol. 4, no. 11, pp. 2028–2037, 2002.
- [31] M. B. Colket and D. J. Seery, “No Title,” *Proc. Combust. Inst.*, vol. 25, p. 883, 1994.
- [32] A. D’Anna, “Particles inception and growth: experimental evidences and a modelling attempt,” in *Combustion Generated Fine Carbonaceous Particles*, 2007, p. 289.
- [33] H. Bladh, N.-E. Olofsson, T. Mouton, J. Simonsson, X. Mercier, A. Faccinnetto, P.-E. Bengtsson, and P. Desgroux, “Probing the smallest soot particles in low-sooting premixed flames using laser-induced incandescence,” *Proc. Combust. Inst.*, vol. 35, pp. 1843–1850, 2015.
- [34] T. Mouton, X. Mercier, M. Wartel, N. Lamoureux, and P. Desgroux, “Laser-induced incandescence technique to identify soot nucleation and very small particles in low-pressure methane flames,” *Appl. Phys. B Lasers Opt.*, vol. 112, no. 3, pp. 369–379, 2013.
- [35] L. D. Pfefferle, G. Bermudez, and J. Byle, “Benzene and Higher Hydrocarbon Formation During Allene Pyrolysis,” in *Soot Formation in Combustion Mechanisms and Models*, H. Bockhorn, Ed. Springer-Verlag, 1994, p. 25.
- [36] A. D’Anna, A. D’Alessio, and P. Minutolo, “Spectroscopic and Chemical Characterization of Soot Inception Processes in Premixed Laminar Flames at Atmospheric Pressure,” in *Soot Formation in Combustion Mechanisms and Models*, H. Bockhorn, Ed. Springer-Verlag, 1994, p. 83.
- [37] S. K. Friedlander, “A review of the dynamics of sulfate containing aerosols,” *Atmos. Environ.*, vol. 12, pp. 187–195, 1977.
- [38] A. Faccinnetto, “High sensitivity detection of Polycyclic Aromatic Hydrocarbons desorbed from soot particles using Laser Desorption/Laser Ionisation/Time-Of-Flight Mass Spectrometry : an approach for studying the soot growth process in flames,” Lille 1, 2009.
- [39] A. Faccinnetto, C. Focsa, P. Desgroux, and M. Ziskind, “Progress toward the Quantitative Analysis of PAHs Adsorbed on Soot by Laser Desorption/Laser Ionization/Time-of-Flight Mass Spectrometry,” *Environ. Sci. Technol.*, vol. 49, no. 17, pp. 10510–10520, 2015.
- [40] T. Ishiguro, Y. Takatori, and K. Akihama, “Microstructure of diesel soot particles probed by electron microscopy: First observation of inner core and outer shell,” *Combust. Flame*, vol. 108, no. 1–2, pp. 231–234, 1997.
- [41] M. Alfè, B. Apicella, R. Barbella, J. N. Rouzaud, A. Tregrossi, and A. Ciajolo, “Structure-property relationship in nanostructures of young and mature soot in premixed flames,” *Proc. Combust. Inst.*, vol. 32 I, pp. 697–704, 2009.
- [42] B. Apicella, P. Pré, M. Alfè, A. Ciajolo, V. Gargiulo, C. Russo, A. Tregrossi, D. Deldique, and J. N. Rouzaud, “Soot nanostructure evolution in premixed flames by

- High Resolution Electron Transmission Microscopy (HRTEM),” *Proc. Combust. Inst.*, vol. 35, no. 2, pp. 1895–1902, 2015.
- [43] J. Warnatz, U. Maas, and R. W. Dibble, *Combustion Physical and Chemical Fundamentals, Modeling and Simulation, Experiments, Pollutant Formation*, 4th ed. Springer- Verlag Berlin, 2006.
- [44] R. Lemaire, A. Faccinetto, E. Therssen, M. Ziskind, C. Focsa, and P. Desgroux, “Experimental comparison of soot formation in turbulent flames of Diesel and surrogate Diesel fuels,” *Proc. Combust. Inst.*, vol. 32 I, no. 1, pp. 737–744, 2009.
- [45] A. Tregrossi, R. Barbella, A. Ciajolo, and M. Alfè, “Spectral Properties of Soot in the Uv-Visible Range,” *Combust. Sci. Technol.*, vol. 179, no. 1–2, pp. 371–385, 2007.
- [46] A. D’Alessio, A. D’Anna, A. D’Orsi, P. Minutolo, R. Barbella, and A. Ciajolo, “No Title,” *Proc. Combust. Inst.*, vol. 24, p. 973, 1992.
- [47] P. Minutolo, G. Gambi, A. D’Alessio, and A. D’Anna, “Optical and spectroscopic characterization of rich premixed flames across the soot formation threshold,” *Combust. Sci. Technol.*, vol. 101, no. 1–6, p. 309, 1994.
- [48] C. Jäger, T. Henning, R. Schlögl, and O. Spillecke, “Spectral properties of carbon black,” *J. Non. Cryst. Solids*, vol. 258, no. 1, pp. 161–179, 1999.
- [49] L. Gavilan, I. Alata, K. C. Le, T. Pino, A. Giuliani, and E. Dartois, “VUV spectroscopy of carbon dust analogs: contribution to interstellar extinction,” *Astron. Astrophys.*, vol. 586, p. A106, 2016.
- [50] P. Minutolo, G. Gambi, and A. D’Alessio, “The optical band gap model in the interpretation of the UV-visible absorption spectra of rich premixed flames,” *Symp. Combust.*, vol. 26, no. 1, pp. 951–957, 1996.
- [51] E. M. Adkins and J. H. Miller, “Extinction measurements for optical band gap determination of soot in a series of nitrogen-diluted ethylene/air non-premixed flames,” *Phys. Chem. Chem. Phys.*, vol. 17, no. 4, pp. 2686–95, 2015.
- [52] J. Robertson, “Hard amorphous (diamond-like) carbons,” *Prog. Solid State Chem.*, vol. 21, no. 4, pp. 199–333, 1991.
- [53] A. Bescond, J. Yon, F. X. Ouf, C. Rozé, A. Coppalle, P. Parent, D. Ferry, and C. Laffon, “Soot optical properties determined by analyzing extinction spectra in the visible near-UV: Toward an optical speciation according to constituents and structure,” *J. Aerosol Sci.*, vol. 101, pp. 118–132, 2016.
- [54] L. G. Cançado, a. Jorio, E. H. M. Ferreira, F. Stavale, C. a. Achete, R. B. Capaz, M. V. O. Moutinho, a. Lombardo, T. S. Kulmala, and a. C. Ferrari, “Quantifying defects in graphene via Raman spectroscopy at different excitation energies,” *Nano Lett.*, vol. 11, no. 8, pp. 3190–3196, 2011.
- [55] P. Klar, E. Lidorikis, A. Eckmann, I. A. Verzhbitskiy, A. C. Ferrari, and C. Casiraghi, “Raman scattering efficiency of graphene,” *Phys. Rev. B - Condens. Matter Mater. Phys.*, vol. 87, no. 20, pp. 1–12, 2013.
- [56] A. Faccinetto, P. Desgroux, M. Ziskind, E. Therssen, and C. Focsa, “High-sensitivity detection of polycyclic aromatic hydrocarbons adsorbed onto soot particles using laser



- desorption/laser ionization/time-of-flight mass spectrometry: An approach to studying the soot inception process in low-pressure flames,” *Combust. Flame*, vol. 158, no. 2, pp. 227–239, 2011.
- [57] H. Bladh, N.-E. Olofsson, T. Mouton, J. Simonsson, X. Mercier, A. Faccinotto, P.-E. Bengtsson, and P. Desgroux, “Probing the smallest soot particles in low-sooting premixed flames using laser-induced incandescence,” *Proc. Combust. Inst.*, vol. 35, no. 2, pp. 1843–1850, 2015.
- [58] P. Desgroux, X. Mercier, B. Lefort, R. Lemaire, E. Therssen, and J. F. Pauwels, “Soot volume fraction measurement in low-pressure methane flames by combining laser-induced incandescence and cavity ring-down spectroscopy: Effect of pressure on soot formation,” *Combust. Flame*, vol. 155, no. 1–2, pp. 289–301, 2008.
- [59] H. A. Michelsen, “Understanding and predicting the temporal response of laser-induced incandescence from carbonaceous particles,” *J. Chem. Phys.*, vol. 118, no. 15, pp. 7012–7045, 2003.
- [60] C. Schulz, B. F. Kock, M. Hofmann, H. Michelsen, S. Will, B. Bougie, R. Suntz, and G. Smallwood, “Laser-induced incandescence: Recent trends and current questions,” *Appl. Phys. B Lasers Opt.*, vol. 83, no. 3, pp. 333–354, 2006.
- [61] F. Goulay, P. E. Schrader, X. Lopez-Yglesias, and H. A. Michelsen, “A data set for validation of models of laser-induced incandescence from soot: Temporal profiles of LII signal and particle temperature,” *Appl. Phys. B Lasers Opt.*, vol. 112, no. 3, pp. 287–306, 2013.
- [62] J. Zerbs, K. P. Geigle, O. Lammel, J. Hader, R. Stirn, R. Hedef, and W. Meier, “The influence of wavelength in extinction measurements and beam steering in laser-induced incandescence measurements in sooting flames,” *Appl. Phys. B Lasers Opt.*, vol. 96, no. 4, pp. 683–694, 2009.
- [63] N. E. Olofsson, J. Simonsson, S. Török, H. Bladh, and P. E. Bengtsson, “Evolution of properties for aging soot in premixed flat flames studied by laser-induced incandescence and elastic light scattering,” *Appl. Phys. B Lasers Opt.*, vol. 119, no. 4, pp. 669–683, 2015.
- [64] D. Lutic, J. Pagels, R. Bjorklund, P. Josza, J. H. Visser, A. W. Grant, M. L. Johansson, J. Paaso, P. E. Fägerman, M. Sanati, and A. L. Spetz, “Detection of soot using a resistivity sensor device employing thermophoretic particle deposition,” *J. Sensors*, vol. 2010, pp. 1–6, 2010.
- [65] D. Lutic and C. I., “detection of soot particles using a resistive transducer based on thermophoresis,” *Environ. Eng. Manag. J.*, vol. 13, no. 9, pp. 2253–2259, 2014.
- [66] C. M. Sorensen, “Light Scattering by Fractal Aggregates: A Review,” *Aerosol Sci. Technol.*, vol. 35, no. 2, pp. 648–687, 2001.
- [67] C. M. Sorensen, J. Cai, and N. Lu, “Light-scattering measurements of monomer size, monomers per aggregate, and fractal dimension for soot aggregates in flames,” *Appl. Opt.*, vol. 31, no. 30, pp. 6547–57, 1992.
- [68] U. “ O. K”oyl”u, G. M. Faeth, T. L. Farias, and M. G. Cavalho, “Fractal and projected

- structure properties of soot aggregates,” *Combust. Flame.*, vol. 100, p. 62, 1995.
- [69] J. D. Herdman, B. C. Connelly, M. D. Smooke, M. B. Long, and J. H. Miller, “A comparison of Raman signatures and laser-induced incandescence with direct numerical simulation of soot growth in non-premixed ethylene/air flames,” *Carbon N. Y.*, vol. 49, no. 15, pp. 5298–5311, 2011.
- [70] C. Casiraghi, A. C. Ferrari, and J. Robertson, “Raman spectroscopy of hydrogenated amorphous carbons,” *Phys. Rev. B*, vol. 72, no. 8, p. 85401, 2005.
- [71] A. Ferrari and J. Robertson, “Interpretation of Raman spectra of disordered and amorphous carbon,” *Phys. Rev. B*, vol. 61, no. 20, pp. 14095–14107, 2000.
- [72] P. Desgroux, X. Mercier, and K. A. Thomson, “Study of the formation of soot and its precursors in flames using optical diagnostics,” *Proc. Combust. Inst.*, vol. 34, no. 1, pp. 1713–1738, 2013.
- [73] H. A. Michelsen, C. Schulz, G. J. Smallwood, and S. Will, “Laser-induced incandescence: Particulate diagnostics for combustion, atmospheric, and industrial applications,” *Prog. Energy Combust. Sci.*, vol. 51, pp. 2–48, 2015.
- [74] S. Bejaoui, X. Mercier, P. Desgroux, and E. Therssen, “Laser induced fluorescence spectroscopy of aromatic species produced in atmospheric sooting flames using UV and visible excitation wavelengths,” *Combust. Flame*, vol. 161, no. 10, pp. 2479–2491, 2014.
- [75] T. Chen, H. Yuan, and Z. Sun, “Photoacoustic method to detect CO and soot particles generated by fire,” *2009 Int. Conf. Meas. Technol. Mechatronics Autom. ICMTMA 2009*, vol. 1, pp. 304–307, 2009.
- [76] D. Rose, B. Wehner, M. Ketzler, C. Engler, J. Voigtländer, T. Tuch, and A. Wiedensohler, “Atmospheric number size distributions of soot particles and estimation of emission factors,” *Atmos. Chem. Phys.*, vol. 6, pp. 1021–1031, 2006.
- [77] R. J. Clarke and A. Oprysa, “Fluorescence and Light Scattering,” *J. Chem. Educ.*, vol. 81, no. 5, pp. 705–707, 2006.
- [78] D. A. Long, *The Raman Effect: A Unified Treatment of the Theory of Raman Scattering by Molecules*. Wiley, 2002.
- [79] V. L. Brewster, L. Ashton, and R. Goodacre, “Monitoring guanidinium-induced structural changes in ribonuclease proteins using Raman spectroscopy and 2D correlation analysis,” *Anal. Chem.*, vol. 85, no. 7, pp. 3570–3575, 2013.
- [80] H. Raza, *Graphene Nanoelectronics: Metrology, Synthesis, Properties and Applications*. Berlin: Springer, 2012.
- [81] S. Bae, H. Kim, Y. Lee, X. Xu, J.-S. Park, Y. Zheng, J. Balakrishnan, T. Lei, H. Ri Kim, Y. Il Song, Y.-J. Kim, K. S. Kim, B. Özyilmaz, J.-H. Ahn, B. H. Hong, and S. Iijima, “Roll-to-roll production of 30-inch graphene films for transparent electrodes,” *Nat. Nanotechnol.*, vol. 5, no. 8, pp. 574–578, 2010.
- [82] F. Tuinstra and J. L. Koenig, “Raman Spectrum of Graphite,” *J. Chem. Phys.*, vol. 53, p. 1126, 1970.

- [83] A. C. Ferrari and D. M. Basko, “Raman spectroscopy as a versatile tool for studying the properties of graphene,” *Nat Nanotechnol*, vol. 8, no. 4, pp. 235–246, 2013.
- [84] R. P. Vidano, D. B. Fischbach, L. J. Willis, and T. M. Loehr, “Observation of Raman band shifting with excitation wavelength for carbons and graphites,” *Solid State Commun.*, vol. 39, no. 2, pp. 341–344, 1981.
- [85] I. Pócsik, M. Hundhausen, M. Koos, L. Ley, I. Pócsik, M. Hundhausen, M. Koós, and L. Ley, “Origin of the D peak in the Raman spectrum of microcrystalline graphite,” *J. Non. Cryst. Solids*, vol. 227–230, pp. 1083–1086, 1998.
- [86] C. Thomsen and S. Reich, “Double Resonant Raman Scattering in Graphite,” *Phys. Rev. Lett.*, vol. 85, no. 24, pp. 5214–5217, 2000.
- [87] R. J. Nemanich and S. A. Solin, “First- and second-order Raman scattering from finite-size crystals of graphite,” *Phys. Rev. B*, vol. 20, no. 2, pp. 392–401, 1979.
- [88] S. Piscanec, M. Lazzeri, F. Mauri, A. C. Ferrari, and J. Robertson, “Kohn anomalies and electron-phonon interactions in graphite,” *Phys. Rev. Lett.*, vol. 93, no. 18, pp. 1–4, 2004.
- [89] R. Narula and S. Reich, “Double resonant Raman spectra in graphene and graphite: A two-dimensional explanation of the Raman amplitude,” *Phys. Rev. B - Condens. Matter Mater. Phys.*, vol. 78, no. 16, pp. 1–6, 2008.
- [90] P. Venezuela, M. Lazzeri, and F. Mauri, “Theory of double-resonant Raman spectra in graphene: Intensity and line shape of defect-induced and two-phonon bands,” *Phys. Rev. B - Condens. Matter Mater. Phys.*, vol. 84, no. 3, pp. 1–25, 2011.
- [91] I. Childres, L. A. Jauregui, W. Park, H. Cao, and Y. P. Chen, “Raman Spectroscopy of Graphene and Related Materials,” in *New Developments in Photon and Materials Research*, J. I. Jang, Ed. Hauppauge NY: Nova Science, 2013.

# Chapter 2

## Experimental setup

### Contents

---

<b>2.1. Nanograins combustion chamber .....</b>	<b>29</b>
2.1.1. The principle of a premixed combustion .....	29
2.1.2. Nanograins components.....	30
<b>2.2. Flame conditions and soot production.....</b>	<b>32</b>
2.2.1. Soot deposition and measurements .....	32
2.2.2. Soot production for measurements in the gas phase .....	33
2.2.3. Samples for differential Raman cross section measurements .....	37
<b>2.3. Instruments and principles of soot characterization.....</b>	<b>37</b>
2.3.1. Infrared spectroscopy .....	39
2.3.2. Ultraviolet-Visible spectroscopy .....	40
2.3.3. Instrumentation for Raman spectroscopic measurement .....	43
2.3.4. High resolution transmission electron microscope (HRTEM) .....	45
<b>2.1. Conclusions .....</b>	<b>46</b>
<b>References .....</b>	<b>47</b>

---

This chapter serves as “infrastructure” of my dissertation containing all equipments, experimental setups, and methods used in our research. Firstly, we introduce the Nanograins combustion chamber which was used to produce soot and measure gas phase Raman spectra. The second section presents all different burning conditions used to produce soot. The final section is dedicated to the experimental setup and methods.

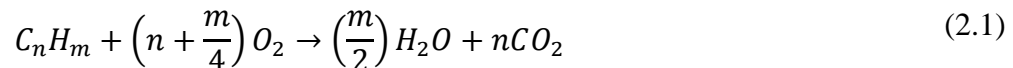
## 2.1. Nanograins combustion chamber

In combustion processes, fuel and oxidizer are mixed and burnt. It is useful to identify various categories of combustion conditions upon whether the fuel and oxidizer are mixed first and burnt later (premixed) or whether combustion and mixing occur simultaneously (diffusion). Each of these categories is further subdivided based on whether the fluid/gas flow is laminar or turbulent. Nanograins contains a laminar premixed and flat flame built and developed in the research group “Molecular Systems, Astrophysics and Environment” at the Institut des Sciences Moléculaires d’Orsay (ISMO). This reactor produces carbon-based molecules and soot, at the focus in the group [1]–[4]. This section will give information on the premixed flame and Nanograins components.

### 2.1.1. The principle of a premixed combustion

In laminar premixed flames, fuel and oxidizer are premixed before the combustion and the flow is laminar and flat if the burner is flat. The premixed flame is said to be *stoichiometric* if the amount of oxidizer and fuel are just enough to consume each other completely, forming only carbon dioxide and water. If there is an excess of fuel, the reaction is called *fuel-rich*, and if there is an excess of oxygen, it is called *fuel-lean*.

The stoichiometric reaction of hydrocarbon with O<sub>2</sub> is given by:



The combustion condition is characterized by *the fuel equivalence ratio*  $\Phi$  which is the actual mole ratio of fuel and oxidizer normalized by their stoichiometric mole ratio:

$$\Phi = \frac{(Fuel/Oxidant)_{actual}}{(Fuel/Oxidant)_{stoichiometric}} \quad (2.2)$$

Accordingly, there are three groups of the premixed combustion:

Rich combustion:	$\Phi > 1$
Stoichiometric combustion:	$\Phi = 1$
Lean combustion:	$\Phi < 1$

The flame speed is defined as the local velocity of the reactant mixture moving into the reaction zone. It depends only on the mixture composition ( $\Phi$ ), the pressure and the initial temperature [5]. If the laminar burning velocity of a flat flame is less than the velocity of the unburnt gases, the flame blows off.

These are few basic parameters of the premixed combustion influencing on burning condition and by-products. In particular, by changing the ratio of incoming gases, we obtained different kinds of soot.

### 2.1.2. Nanograins components

The experimental setup Nanograins combines a reactor chamber (working at several tens of mbar) and a sampling chamber (operated at a pressure of few  $10^{-2}$  mbar) where a molecular flow seeded with the reactor products is formed (Fig. 2.1).

The combustion chamber contains a stainless steel McKenna burner with 60 mm diameter (Holthuis & Associates), cooled by circulating water. This burner is surrounded by a shroud to produce a column of inert gas ( $N_2$ ) that shields the burning gas flow. The fuel (hydrocarbon) was premixed with  $O_2$  before flowing through the burner at a controlled rate by mass flow controllers (Brooks). The flame is ignited it by a discharge to the burner via a copper electrode charged to a high voltage (3 kV). This flame is oriented in the same direction as the gas flow, which is maintained at a constant pressure within the chamber via a butterfly valve (Fig. 2.1b). The burner can move along the horizontal axis with a 300 microns precision. The pressure, in the combustion chamber, was varied from 20 to 100 mbar. The input gas velocity was set in the 3 to 6  $l \cdot min^{-1}$  range. The flame can be probed at different burning position from 0-50 mm by varying sampling distance from the probing hole (quartz cone) to the burner surface. This distance is hereafter referred as the Height Above the Burner (HAB) as this distance is related to the chemical time in this type of flame. The flame products were mostly sampled in the sooting zone which glows more or less orange due to the growth and evolution of soot at the temperature of  $\sim 2000 \pm 500$  K.

Flame products were extracted by a water-cooled quartz cone (several were available with diameters 750 microns, 1 and 2 mm) allowing extraction of the species produced at a given HAB. The cone influences the flame by cooling and perturbing the flow, thus conditions differed slightly from one cone to the other. Most measurements were done with the 1 mm diameter one for reproducibility, the sampled volume being close to a sphere of equivalent radius. After extraction, the products passed through a 4 mm diameter Laval nozzle placed in the deposition chamber and were then expanded into the vacuum. The shape and temperature of the molecular flow are (partially) controlled by an argon gas flow inserted into the volume between the quartz cone and the Laval nozzle at a controlled total pressure of about 10 mbar. The Laval nozzle was designed to provide a supersonic molecular flow at 50K in precise conditions in our setup, but the “high” flux of sampled species does not allow matching these conditions. However, in addition to an efficient focusing effect of the soot on the flow axis, partial cooling is obtained by collisions with the argon carrier gas.

## 2.1. Nanograins combustion chamber

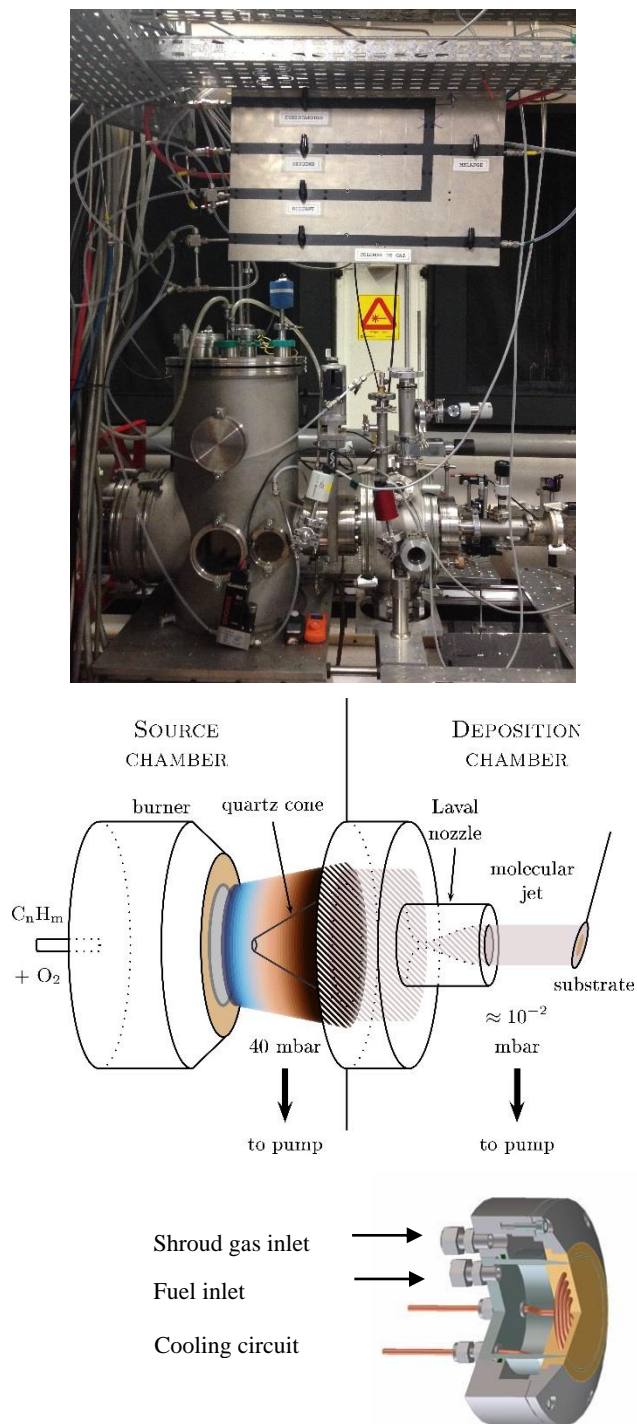


Fig. 2.1. Nanograins, an experimental setup. The first photo is the Nanograins combustion chamber at ISMO. The scheme shows the burning region, the extraction cone in quartz and the flow shaped by a Laval nozzle where soot is collected. Finally, the McKenna burner.

Windows were then placed into the flow and soot particles were deposited on these by impaction. Depending on flame conditions, HAB and purposes, the sampling time could be varied from one second to several tens of minutes. The obtained thicknesses were thus varying from few tens of nm (1 or 2 layers of soot nanoparticles) to several  $\mu\text{m}$ .

## 2.2. Flame conditions and soot production

Soot samples were produced at ISMO using the Nanograins setup. The fuel was ethylene ( $\text{C}_2\text{H}_4$ ) premixed with  $\text{O}_2$ , and the gas mixture was flowed through the burner at  $4 \text{ l}\cdot\text{min}^{-1}$  flow rate. The  $\text{N}_2$  gas shield around the burning region was applied at two controlled flow rates of 0.2 and  $3 \text{ l}\cdot\text{min}^{-1}$ . We used different C/O ratios of 0.82, 1, 1.05 and 1.3, with different pressures in the reactor chamber. Note that after any changes in sampling conditions, we had to wait at least 5 minutes until flame (temperature) is stabilized.

### 2.2.1. Soot deposition and measurements

As introduced in the first chapter, soot particles absorb strongly in a large spectral range from the UV to infrared. Their absorption/transmission spectra reflect chemical structures and morphology of soot. Our goal is to study the spectral properties of soot from far ultraviolet (FUV) to the mid-infrared (MIR) domain in order to get information on the vibrational and electronic structures.

In the atmosphere, atmospheric air and especially molecular oxygen strongly absorb UV from 180 nm and thus cut off this part of the spectrum [6], [7]. To reach shorter wavelengths, we measured the transmission spectra in vacuum chamber to cover the vacuum ultraviolet (VUV) range of wavelength. Nevertheless, below  $\sim 120 \text{ nm}$ , VUV optics are not transparent anymore. We used TEM grids covered with pure and ultrafine carbon membranes to cover the range down to 50 nm. The carbon membranes had about 10 or 25 nanometers thickness, resulting in a mean transmittance of  $\sim 10\text{-}20\%$  in the VUV.

Soot particles were deposited on magnesium fluoride ( $\text{MgF}_2$ ), sodium chloride ( $\text{NaCl}$ ) windows, potassium bromide ( $\text{KBr}$ ) and the TEM grids.  $\text{MgF}_2$ ,  $\text{NaCl}$  and  $\text{KBr}$  ( $\emptyset 20\text{mm} \times 2 \text{ mm}$ ) are provided by Korth Kristalle or Crystran.  $\text{MgF}_2$  windows offer excellent broadband transmission from 118 nm to  $8.5 \mu\text{m}$ . It is a rugged material resistant to chemical etching, laser damage and thermal shock. Transmission ranges of  $\text{NaCl}$  and  $\text{KBr}$  are available from 210 nm to  $16 \mu\text{m}$  and 250 nm to  $33 \mu\text{m}$ , respectively. We prepared thin soot films with thickness optimized for the targeted spectral range. The deposited samples on  $\text{MgF}_2$  and carbon membranes were very thin (less than 100 nm), allowing VUV-UV transmission spectroscopy. Soot samples on  $\text{NaCl}$ ,  $\text{KBr}$  windows were much thicker for use in IR spectroscopy (up to few microns). Raman spectroscopy could be performed on all substrates.

For HRTEM images, soot samples were collected by insertion of a Lacey carbon film supported by a 200 mesh copper TEM grid (Electron Microscopy Sciences) directly into the molecular flow for few seconds. A typical image of a few tens of seconds insertion is given in Fig. 2.2 where the growth of the soot depot on the carbon lacey can be observed, with an



arrangement resembling a dendritic growth. All soot samples produced for these measurements listed in Table 2.1.

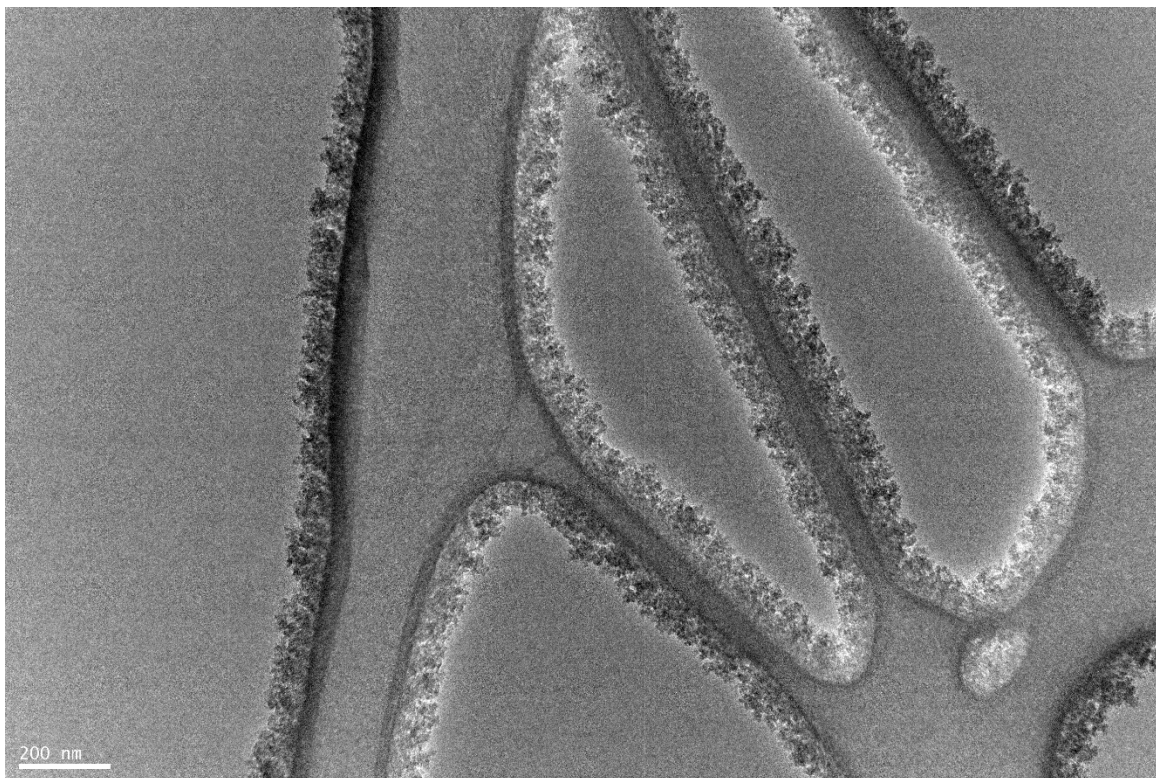



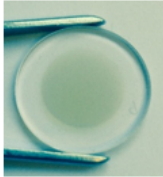
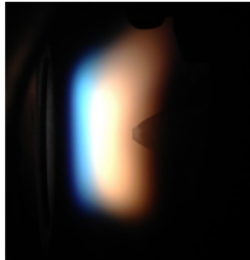
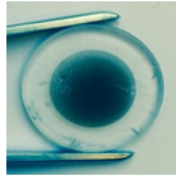
Fig. 2.2. Typical HRTEM image of the soot directly deposited on the Lacey carbon by inserting of the TEM grid into the molecular flow.

### 2.2.2. Soot production for measurements in the gas phase

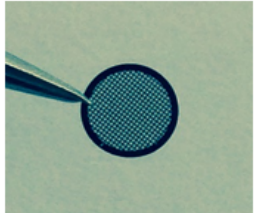
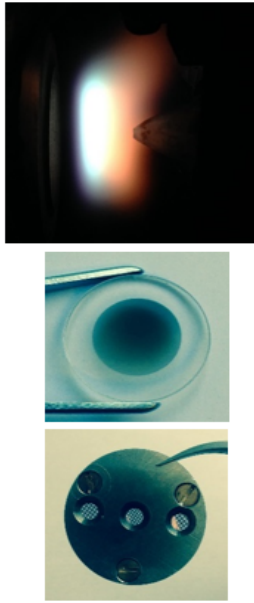
For *in situ* detection, soot particles were detected directly in the beam without deposition. We worked on different flame conditions and quartz cones. First, with a 2 mm diameter cone, Raman spectra of flames of C/O ratios = 0.74 (40 mbar), 0.78 (40 mbar), 0.82 (60 mbar), 1.05 (40 mbar) and 1.1 (40 mbar) were obtained at distances ranging from 6 to 50 mm. Then, we changed the cone into smaller diameter one (1 mm) and focused on only the flame of 1.05 C/O ratio. During our experiments, N<sub>2</sub> flow rate was maintained at 4 l.min<sup>-1</sup>. The flow of argon injected before the Laval nozzle was adjusted between 0.1 and 1 l.min<sup>-1</sup> to reach maximum overlap between the soot and incident laser beam in front of the optical collection.

Table 2.1: Characterization of four flames and list of measurements on their products.

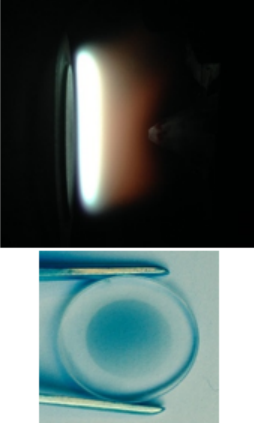
Note: Thickness\_ grid C1: 20 nm, grid C2: 10 nm

C/O Ratio	P[mbar]	dN2[l/min]	dpre[l/min]	d[mm]	Time	Substrate	Name	IR	VUV	Specord	HRTEM	Raman	Photos of flame and soot at 30 mm from the burner
1,3 ( $\phi = 3.9$ )	40	3	4	25	10min	MgF2	D1_02042015		x	x			 
					10min	Grid C1	D2_02042015		x	x			
					20min	NaCl	D3_02042015	x		x		x (532nm,514nm)	
				27	4min	MgF2	D4_02042015		x	x			
					10min	NaCl	D5_02042015	x				x (532nm,514nm)	
				30	30sec	MgF2	D6_02042015		x	x			
					30sec	Grid C1	D7_02042015						
					2min	NaCl	D8_02042015	x				x (532nm,514nm)	
				33	7sec	MgF2	D9_02042015						
					1min	NaCl	D10_02042015	x				x (532nm,514nm)	
				36	3sec	MgF2	D11_02042015						
					30sec	NaCl	D12_02042015	x				x (532nm,514nm)	
				39	1sec	MgF2	D13_02042015		x	x			
					1sec	GridC1	D14_02042015		x				
	NaCl	D15_02042015	x					x (532nm,514nm)					
1,05 ( $\phi = 3.15$ )	40	3	4	14	8min	MgF2	D7_08042015	x	x	x		x (532nm,514nm)	 
					8min	GridC2	D8_08042015		x				
				18	30sec	MgF2	D9_08042015	x	x	x		x (532nm,514nm)	
					30sec	GridC2	D10_08042015		x				
				22	7sec	MgF2	D11_08042015	x	x	x		x (532nm,514nm)	
					7sec	GridC2	D12_08042015		x				
				2min	KBr	D1_20140715					x (514nm,785nm)		
				24	10min	KBr	D4_20140715				x (514nm)		
				26	10min	KBr	D7_20140715				x (514nm)		
				28	5min	KBr	D10_20140715				x (514nm)		
				30	5min	KBr	D13_20140715				x (514nm)		
				36		KBr	D1_20150717				x (514nm)		
				38		KBr	D3_20140717				x (514nm)		
				50		KBr	D7_20140717				x (514nm,785nm)		

2.2. Flame conditions and soot production

C/O Ratio	P[mbar]	dN2[l/min]	dpre[l/min]	d[mm]	Time	Substrate	Name	IR	VUV	Specord	HRTEM	Raman	Photos of flame and soot at 30 mm from the burner						
1,05 ( $\phi = 3,15$ )	46	3	4		32	5min	KBr	D19_20140715					x (514nm)						
					34	5min	NaCl	D22_20140715							x (514nm)				
					36	5min	NaCl	D25_20140715							x (514nm)				
	55				24	3min		D9_20052015											
					30	2min		D8-20152015											
					36	2min		D5_20052015											
					42	2min		D4_20052015											
					50	1min		D2_20052015											
					24	30sec	LC200-CU	D1_10062015							HRTEM				
					20	4min		D2_15072015											
					50	1min		D1_26052015											
					40	36	1min		D3_26052015										
	24					20sec		D1_10062015											
	20					5min		D1_15072015											
	1 ( $\phi = 3$ )				28	0,2	4		21	2min	MgF2	D16_02042015	x		x				
		14min	NaCl	D17_02042015					x	x				x (532nm,514nm)					
		2min	Grid C1	D18_02042015															
		20min	LC200-CU	D3_15072015										HRTEM					
30		20sec	MgF2	D19_02042015					x	x									
		20sec	Grid C1	D20_02042015					x										
		6min	NaCl	D21_02042015					x						x (532nm,514nm)				
25		35sec	MgF2	D22_02042015										x					
		12min	NaCl	D23_02042015					x							x (532nm,514nm)			
		39	7sec	MgF2					D24_02042015	x	x								
		7sec	GridC1	D25_02042015					x										
		5min	NaCl	D26_02042015					x							x (532nm,514nm)			
21		2min	MgF2	D1_08042015					x	x	x						x (532nm,514nm)		
		2min	GridC2	D2_08042015					x										
30		30sec	MgF2	D3_08042015					x	x	x							x (532nm,514nm)	
		30sec	GridC2	D4_08042015					x										
18		8min	MgF2	D5_08042015					x	x	x							x (532nm,514nm)	
		8min	GridC2	D6_08042015					x										

## 2.2. Flame conditions and soot production

C/O Ratio	P[mbar]	dN <sub>2</sub> [l/min]	d <sub>pre</sub> [l/min]	d[mm]	Time	Substrate	Name	IR	VUV	Specord	HRTEM	Raman	Photos of flame and soot	
0,82 ( $\phi = 2,46$ )	60	0,2	4	21	4min	MgF2	D13_08042015	x	x	x				
					4min	GridC2	D14_08042015		x					
					15min	NaCl	D15_08042015	x		x		x (532nm,514nm)		
				22	4min	MgF2	D16_08042015	x	x	x				
					4min	GridC2	D17_08042015		x					
					15min	NaCl	D18_08042015	x		x		x (532nm,514nm)		
				30	150sec	MgF2	D19_08042015	x	x	x				
					150sec	GridC2	D20_08042015		x					
					10min	NaCl	D21_08042015	x		x		x (532nm,514nm)		
				20	8min	MgF2	D22_08042015	x	x	x				
					8min	GridC2	D23_08042015		x					
					20min	NaCl	D24_08042015	x		x		x (532nm,514nm)		

d<sub>N<sub>2</sub></sub>: Nitrogen flow rate

d<sub>pre</sub>: The rate of premixed fuel and oxygen

Grid C1 denotes TEM grids covered with 20 nm thickness pure carbon membranes, Grid C2 is correspond to 10 nm thickness of carbon membranes.

Red crosses (x) are the broken grids.

### **2.2.3. Samples for differential Raman cross section measurements**

Differential Raman cross section experiments were performed on three samples: coal (anthracite coal from Nui Beo open-mine in Quang Ninh province, Vietnam), industrial carbon black Ensaco 350G and diesel soot SRM 2975 (NIST). Attempts on other carbon black or soot were not successful, either due to a strong fluorescence background hiding the Raman signal, a very low albedo or due to instability of the sample under the laser beam. Each sample was mixed in deionized water at several different concentrations. The cuvettes containing the samples were put in the water tank of an ultrasonic cleaning unit (Elmasonic P 30H), operated at 37 kHz frequency and 100% power. After a half an hour, majority of their masses were dissolved or suspended in the solvent, the rest which assembled and floated on the surface was removed and weighted. The real mass of samples are thus equal to their initial masses subtracted the mass of the samples floating on the surface.

The mixtures were then probed to measure their Raman response, from the top of the solution to avoid the fluorescence signal from the cuvette itself. Note that their concentrations were ensured transparent enough for partial transmission of the laser beam. During the acquisition time, the samples were put in the ultrasonic cleaning unit, operating, to prevent from sedimentation on the bottom of the cuvette and maintain a homogeneous concentration. All detailed information can be found in chapter 3.

## **2.3. Instruments and principles of soot characterization**

In this section, we will present briefly the principle of IR, VUV-Vis, Raman spectroscopies and HRTEM and detail the experimental setups and equipment's used to study soot properties.

Spectroscopy is considered as a method of “seeing the un-seeable”, which uses electromagnetic radiation to obtain information. It is an instrumentally aided study of the interactions between matter and light. The nature of the transition depends on the spectral range, as can be seen in Table 2.2.

Table 2.2: Spectral regions and associated transition nature.

<b>Region</b>	<b>Absorption phenomenon</b>	<b>Energy range, eV</b>	<b>Wavenumber range, cm<sup>-1</sup></b>	<b>Wavelength range</b>
<b>X-ray</b>	Inner core electron transitions	$124 \times 10^3 - 124$	$10^6 - 10^8$	10 – 0.1 nm
<b>Ultraviolet</b>	Valence electron transitions	124 – 3.2	$2.5 \times 10^4 - 10^6$	400 – 10 nm
<b>Visible</b>	Valence electron transitions	3.2 – 1.7	$1.25 \times 10^4 - 2.5 \times 10^4$	800 – 400 nm
<b>Infrared</b>	Vibrational transitions	$1.7 - 12.4 \times 10^{-3}$	$10 - 1.25 \times 10^4$	1 mm – 800 nm
<b>Microwave</b>	Rotational transitions- electron spin resonance	$1.24 \times 10^{-3} - 1.27 \times 10^{-6}$	$10^{-3} - 10$	1m – 1 mm
<b>Radiofrequency</b>	Pure nuclear quadrupole resonance-nuclear magnetic resonance	$1.24 \times 10^{-6} - 12.4 \times 10^{-15}$	$10^{-11} - 10^{-3}$	$10^5$ km – 1m

### 2.3.1. Infrared spectroscopy

#### 2.3.1.1. Definition and characteristics

IR spectroscopy is mainly concerned with the study of absorption inducing vibrational excitation of covalently bonded atoms and groups. IR spectra are mainly used in structure interpretation to determine the functional groups. The IR region can be subdivided into near IR (800 nm – 2  $\mu\text{m}$ ), mid-IR (2 – 15  $\mu\text{m}$ ) and far IR (15  $\mu\text{m}$  – 1 mm), in which the middle IR region is the most commonly used because the absorption of organic molecules and their functional groups is strongest in this region.

There are two types of vibrations: stretching vibration and bending vibrations. Stretching motion is a vibration along bond causing changes of bond length. Stretching mode vibrations occur at high energy (4000 – 1250  $\text{cm}^{-1}$ ) for C, O, N and H based molecules, bending vibrations are involving bond angles variations. This vibration occurs at lower energy (1500 – 660  $\text{cm}^{-1}$ ) than bond stretches. They are classified into in-plane bending and out-plane bending when an aromatic plane can be found. The in-plane bending consists of scissoring and rocking: scissoring relates to the motion where two atoms approach each other (bond angles are decreased), and when their movements take place in the same direction the motion is called rocking. The out-plane bending motions contain wagging and twisting. Wagging is the case where two atoms move to one side of the plane (up or down) and twisting corresponds to the case where one atom moves up the plane and another atom moves down the plane. It should be recalled that vibrations in complex molecules and amorphous or disordered solids, where molecular sub-units (in size) can be found, such as those found in soot, are often a combination of all these internal motions. However, vibrations occurring in the mid-IR appear mostly dominated by one type. In addition, vibrations can still be separated into two classes: symmetrical and anti-symmetrical stretching motion because the vibrational modes remain local enough to retain the symmetry of the functional group in complex materials. The description of the vibrations can thus be transferred from simple carbonaceous molecules to more complex nanoparticles, as long as no crystalline motif (or long-range order) can be found.

According to this transferability and because vibrations are mainly local motion in the mid-IR, functional groups can be identified because they absorb at different frequencies of the IR radiation, hence give characteristic peak values in the IR spectrum. Therefore, IR spectrum of a chemical substance is “a finger print” of a molecule or a functional group in soot for instances. The mid-IR (4000 – 400  $\text{cm}^{-1}$ ) can be approximately divided into four regions, and the nature of a group frequency may generally be determined by the region in which it is located. The regions are generalized as follows: the X–H stretching region (4000 – 2500  $\text{cm}^{-1}$ ), the triple-bond region (2500 – 2000  $\text{cm}^{-1}$ ), the double region (2000 – 1500  $\text{cm}^{-1}$ ), and the fingerprint region (1500 – 600  $\text{cm}^{-1}$ ) [8].

In recent decades, there are numerous methods of obtaining an infrared spectrum. Fourier-transform infrared spectrometers are now predominantly used and have improved



the acquisition of infrared spectra dramatically [8]. In this work, IR spectroscopy is one of the tool used to characterize soot particles.

### 2.3.1.2. Fourier-Transform Infrared Spectrometer

We used a Vertex 70 FTIR spectrometer at ISMO to characterize IR spectroscopy of soot samples (Fig. 2.3). In order to improve the signal to noise ratio, each spectrum was the sum of 600 scans at  $1\text{ cm}^{-1}$  resolution (acquisition time  $\sim 40$  minutes).

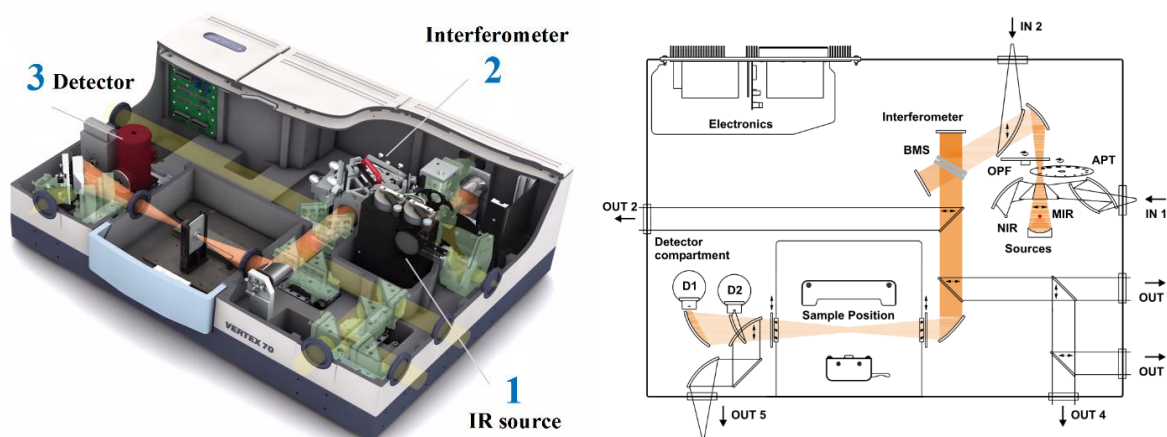


Fig. 2.3. Vertex 70 components and beam path (source: Bruker company's website)

## 2.3.2. Ultraviolet-Visible spectroscopy

### 2.3.2.1. Definition and principle

UV-Vis spectroscopy probes the electronic transitions within the valence electrons. It provides information of  $\pi$ -electron systems, aromatic compounds electronic structure, etc. When a carbonaceous compound absorbs UV-Vis light, an electron is promoted from an occupied molecular orbital (generally a non-bonding  $n$  or bonding  $\sigma$ ,  $\pi$  orbital) to an unoccupied molecular orbital (an antibonding  $\pi^*$  or  $\sigma^*$  orbital).

The lowest probable transition would appear to involve the promotion of one electron from the highest occupied molecular orbital (HOMO) to the lowest unoccupied molecular orbital (LUMO), but as shown in Fig. 2.4, there are several possible electronic transitions within the molecule.  $\sigma - \sigma^*$  is the only available transition in saturated aliphatic hydrocarbons. In general, sigma bonds are very strong so this is a high energy process and these transitions are observed at very short wavelength ( $< 150\text{ nm}$ ).  $\sigma - \pi^*$  and  $\pi - \sigma^*$  transitions have usually low transition probabilities, meaning the bands have very low or zero intensities. Most of the absorptions observed involve only  $\pi - \pi^*$ ,  $n - \sigma^*$ ,  $n - \pi^*$  transitions [9].  $\pi - \pi^*$  transition absorbs radiations down to about  $170\text{ nm}$ , the lower energy limit depending on the extent of the delocalization of the polyaromatic layer and/or the existence of defects. This transition is found in compounds with unsaturated center, e.g. simple alkenes, aromatics, carbonyl



compounds, etc.  $n - \sigma^*$  transition involves saturated compounds with one hetero atom with unshared pair of electrons. This transition is sensitive to hydrogen bonding.  $n - \pi^*$  transition need an unsaturated group in the molecule to provide the  $\pi$  electron.

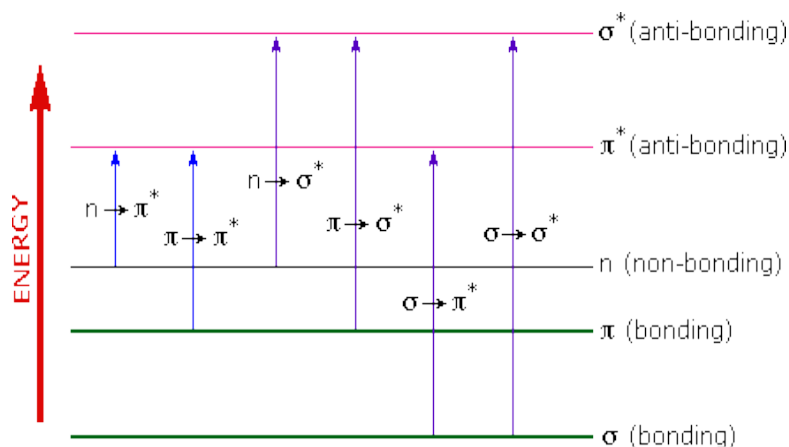


Fig. 2.4. Different transitions between the bonding and antibonding electronic states in UV-Vis spectroscopy.

The details of the transition, ranging from narrow to broad band, provide rich information on the electronic structure of the material under study. Environmental effect may alter the information (spectral shift, width) as well as the temperature. The link to the structure still needs to be explored because for soot, a strongly disordered material, the variety of structures and the complexity cannot be predicted yet. In particular, the absolute absorption cross sections for single particles still escape most of the work. There, the progresses on well-controlled nano-object as well as on knowledge on molecular sub-units like PAHs are of importance.

### 2.3.2.2. Instrumentation

Our soot VUV-Vis transmission spectra were measured at DISCO beamline, SOLEIL synchrotron. This beamline possesses three end-stations with different equipments, in which the APEX windowless branch line delivers photons in the 300 – 50 nm range (4.1 – 24.8 eV) [10].

Fig. 2.5 shows the layout of DISCO beamline. The microscopy line uses photon from 1000 nm up to 180 nm and the line is therefore maintained under static vacuum for clearness only. The situation is different for the APEX branch line, for which the differential pumping unit may be operated to maintain 1 atm helium pressure in the final chamber, the chamber can also be evacuated down to about  $10^{-6}$  mbar. Helium is ionized at 24.59 eV (50.4 nm) and starts absorbing at 21.218 eV [10]. In our experiments on the APEX chamber (a total of 4 sessions, in 2014 and 2015), we worked under vacuum.

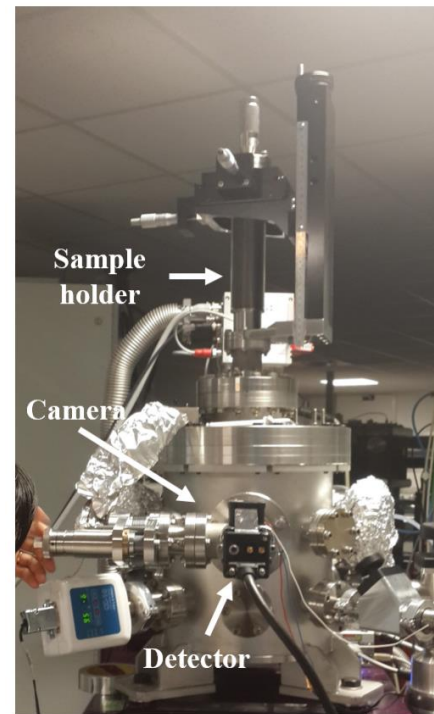
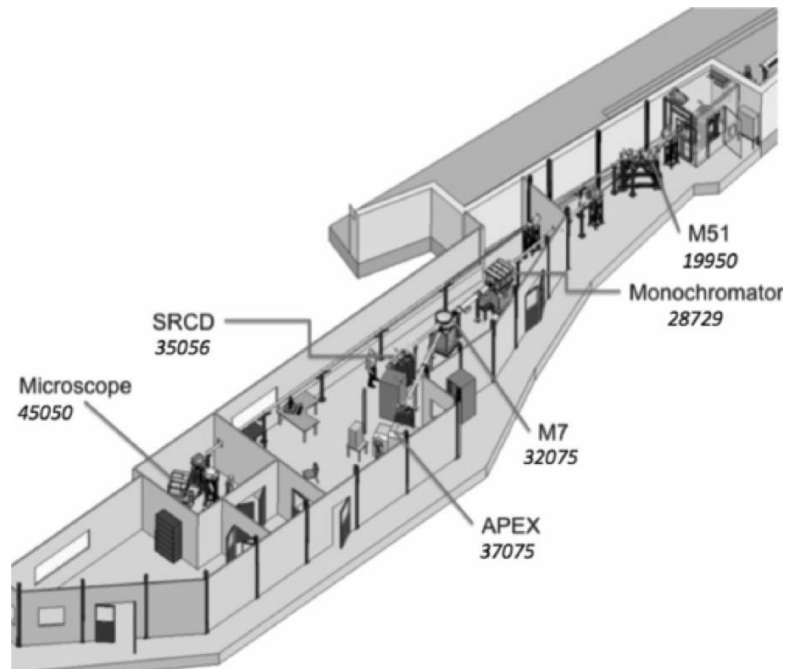


Fig. 2.5: On the left, the layout of DISCO beamline in the experimental hall at SOLEIL [10]. On the right, there are the photos of APEX chamber and the sample holder.

Our samples were placed on the sample holder bar (8 slots) inserted into the APEX chamber. The holder bar was mounted on a three-axis stage. A photodiode located after the sample to measure the transmitted photon flux. Before each measurement, the beam and its passage through the samples were controlled by a camera placed on a horizontal movable axis in front of the detector. On the beamline, a grating and slits allowed to scan the UV wavelength from 50 up to 300 nm with 0.5 or 1 nm step with a 0.5 nm spectral resolution.

The films on TEM grids were measured in the APEX chamber (50 – 200 nm). The films on MgF<sub>2</sub> were measured in the APEX chamber (115 – 300 nm) and with the ex-situ spectrometer (180 – 1000 nm, Specord, Analytik Jena) as well as those on NaCl substrates. We merged these measurements to obtain a single spectrum for each sample from 50 to 1000 nm, as shown in Fig. 2.6. The results are reported in the 2 articles found in the appendices.

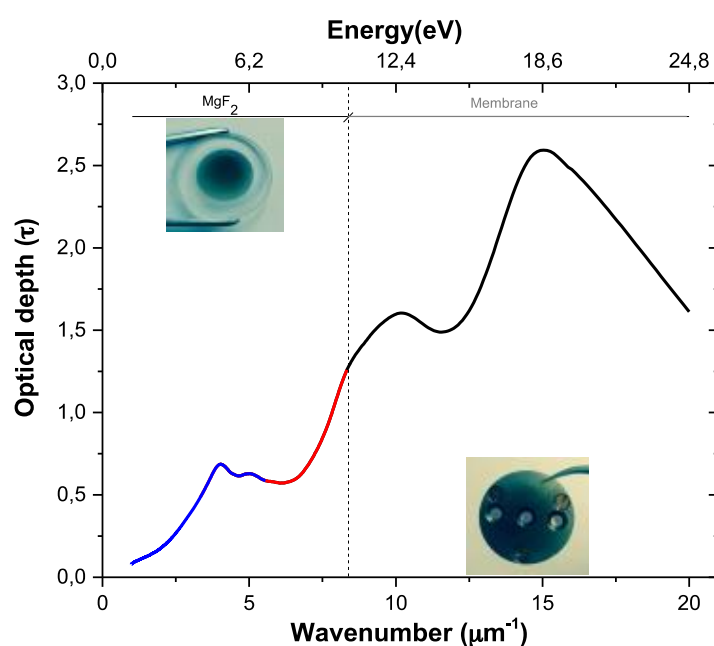


Fig. 2.6: Transmission spectrum of an ultra-thin soot measured with several instruments at DISCO beamline on the SOLEIL synchrotron. The blue part was measured with the Specord on the MgF<sub>2</sub> substrate, the red part with Disco beamline on the MgF<sub>2</sub> substrate and the black one on the Apex beamline on the thin carbon film.

### 2.3.3. Instrumentation for Raman spectroscopic measurement

Differential Raman cross section and detection of the soot Raman spectra in the gas phase were obtained at ISMO. Because Raman scattering signal is very weak, special care should be taken to distinguish it from the predominant Rayleigh scattering. A Raman system typically contains four major components: excitation source; sample and light collection optics; wavelength selector and detector. In our setup, the excitation source was a continuous laser model Verdi 5W (Coherent). This is 532 nm green laser which can deliver output power up to 5 W with a 2 mm diameter beam-size and vertical polarization. Scattered photons were

### 2.3. Instruments and principles of soot characterization

collected by a lenses system adapted to each configuration, and then passing through a razor-edge (high-pass) filter with a cut-off wavelength at 537 nm before entering a round-to-linear fiber bundle. The fiber bundle contains 19 fibers arranged in a line configuration at one end and a circular configuration at the other end. Each fiber has a 200  $\mu\text{m}$  core diameter. The linear end coupled with the slit of the spectrometer. The Acton 2300 spectrometer was assembled with a CCD camera model PIXIS 400 (Princeton). The monochromator includes a triple grating turret holding gratings 1, 2 or 3 with 1200, 1200 and 300 grooves/mm, respectively. Additionally, a notch filter (stop-line filter at 532 nm) was inserted in front of the slit of the spectrometer to assure that laser line is completely removed from the scattered light. The Razor-Edge Dichroic beam splitter and the StopLine notch filter (products of Semrock) have an optical density (OD)  $> 6$  at wavelengths around 532 nm.

The backscattering configuration in differential Raman cross section is depicted in chapter 3 and 90 degree configuration in detection of soot in the gas phase via online Raman measurement is presented in chapter 5. Let us continue to Raman spectrometer used to acquire the first and second order Raman spectra of soot sample. We used a commercial Raman microspectrometer, a Renishaw inVia confocal Raman microspectrometer, located at the Laboratoire de Géologie de l'École Normale Supérieure (Paris, France). This instrument includes: a 514 nm Ar ion laser (150mW) and a 785 nm diode laser (300 mW); 1024  $\times$  256 pixels CCD detector achieving a spectral resolution of 0.5  $\text{cm}^{-1}$  using an 1800 line/mm spectrographic grating; the sampling platform is a Leica microscope with 50x objectives lens. This spectrometer is shown in Fig. 2.7.



Fig. 2.7: The Renishaw inVia confocal Raman microspectrometer, the zoomed in photo is the sampling platform.

The conditions of measurement were: the excitation laser power was set to 0.28 mW at 514 nm wavelength, circular polarization was chosen and the laser beam was focused to a  $\sim 1 \mu\text{m}$  spot; the Raman shift was measured from 400 to 4000  $\text{cm}^{-1}$ .

## 2.3.4. High resolution transmission electron microscope (HRTEM)

### 2.3.4.1. Principle

Transmission Electron Microscope (TEM) is a powerful tool for material investigation. A high energy electron beam is shot through very thin films and the interactions between the electrons and the atoms can be used to observe the structure of materials. TEM can provide morphological, compositional and crystallographic information. High-resolution Transmission Electron Microscope (HRTEM) uses both the transmitted and the scattered beams to create an interference image. HRTEM can be used to analyze the quantity, shape, size and defects on an atomic resolution scale.

HRTEM measuring system has four main components: electron source, electromagnetic lens system, sample holder and image system as seen in this figure below. The electrons emitted from the filament are accelerated by the multiple electromagnetic lenses and then focused on the sample by the lenses. The beam passes through the sample which modifies it and imprints its sample image. An objective lens system collects all the electrons after interaction with the sample and forms the image of the sample. Finally, a set of intermediate lenses that magnify this image and project it on a phosphorous screen or charge coupled device (CCD). The speed of electrons is directly related to the electron wavelength and determines the image resolution (here 200 keV).

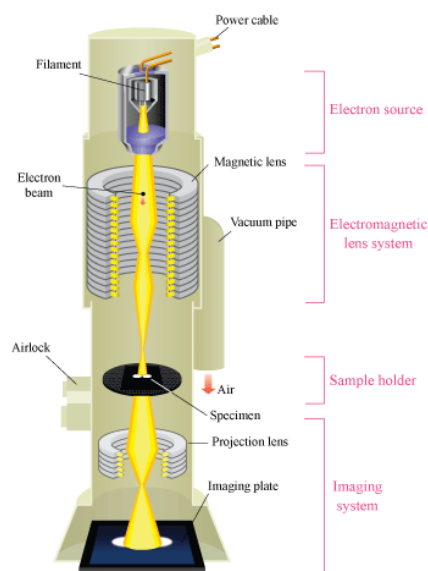


Fig. 2.8: A schematic outline of a TEM (source from website)

### 2.3.4.2. Instrumentation

The HRTEM images were measured on the JEOL-2011 High-resolution TEM operating at 200 kV using a LaB<sub>6</sub> filament (0.144 nm resolution in the lattice fringe mode). This electron microscope is equipped with a bottom-mounted Gatan Slow-Scan CCD camera, which has 4008 × 2672 pixels images with 256 grey levels. In the images recorded at

500 000x magnification (steps), the fringes represent the profile of the polyaromatic layers with point resolution equal to 0.23 nm.

## **2.1. Conclusions**

Starting from the general principle and moving to the more specific description of each configuration, sections in this chapter detailed all tools used to characterize soot particles. Based on these experimental setup, we obtained successfully the full VUV-Vis-MIR absorption spectra, the first and second order Raman spectra, and images of polyaromatic layers of different types of soot. We also detected soot particles suspended in the gas phase using Raman technique and determined differential Raman cross section of several carbonaceous materials. VUV-vis transmission spectra, IR and Raman spectra on samples, HRTEM were performed via collaborations that took place within few sessions (a total of about 1 month) excluding sample preparation time. These results contain much information on soot molecular structure and morphology as well as optical properties. These investigations will be presented in the next result chapters, dedicated to the Raman spectra. IR and VUV-vis results are provided via the articles in the appendices.

## References

- [1] T. Pino, E. Dartois, A.-T. Cao, Y. Carpentier, T. Chamaillé, R. Vasquez, A. P. Jones, L. d'Hendecourt, and P. Bréchnignac, "The 6.2  $\mu\text{m}$  band position in laboratory and astrophysical spectra: a tracer of the aliphatic to aromatic evolution of interstellar carbonaceous dust," *Astron. Astrophys.*, vol. 490, no. 2, pp. 665–672, 2008.
- [2] R. Brunetto, T. Pino, E. Dartois, A. T. Cao, L. D'Hendecourt, G. Strazzulla, and P. Bréchnignac, "Comparison of the Raman spectra of ion irradiated soot and collected extraterrestrial carbon," *Icarus*, vol. 200, no. 1, pp. 323–337, 2009.
- [3] Y. Carpentier, G. Féraud, E. Dartois, R. Brunetto, E. Charon, A.-T. Cao, L. d'Hendecourt, P. Bréchnignac, J.-N. Rouzaud, and T. Pino, "Nanostructuration of carbonaceous dust as seen through the positions of the 6.2 and 7.7  $\mu\text{m}$  AIBs," *Astron. Astrophys.*, vol. 548, p. A40, 2012.
- [4] L. Gavilan, I. Alata, K. C. Le, T. Pino, A. Giuliani, and E. Dartois, "VUV spectroscopy of carbon dust analogs: contribution to interstellar extinction," *Astron. Astrophys.*, vol. 586, p. A106, 2016.
- [5] J. Warnatz, U. Maas, and R. W. Dibble, *Combustion Physical and Chemical Fundamentals, Modeling and Simulation, Experiments, Pollutant Formation*, 4th ed. Springer- Verlag Berlin, 2006.
- [6] R. Ladenburg and C. C. van Voorhis, "The continuous absorption of oxygen between 1750 and 1300 and its bearing upon the dispersion," *Phys. Rev.*, vol. 43, pp. 315–321, 1933.
- [7] K. Watanabe, E. C. Y. Inn, and M. Zelikoff, "Absorption Coefficients of Oxygen in the Vacuum Ultraviolet," *J. Chem. Phys.*, vol. 21, no. 6, pp. 1026–1030, 1953.
- [8] B. H. Stuart, *Infrared Spectroscopy: Fundamentals and Applications*. Wiley, 2004.
- [9] B. Faust, *Modern chemical techniques: an essential reference for students and teachers*, 3rd ed. Royal Society of Chemistry, 1997.
- [10] A. Giuliani, F. Jamme, V. Rouam, F. Wien, J. L. Giorgetta, B. Lagarde, O. Chubar, S. Bac, I. Yao, S. Rey, C. Herbeaux, J. L. Marlats, D. Zerbib, F. Polack, and M. Réfrégiers, "DISCO: A low-energy multipurpose beamline at synchrotron SOLEIL," *J. Synchrotron Radiat.*, vol. 16, no. 6, pp. 835–841, 2009.

# Chapter 3

## *Result I:*

# Differential backscatter Raman cross section of several carbonaceous materials

## Contents

---

<b>3.1. Introduction .....</b>	<b>49</b>
<b>3.2. Principles .....</b>	<b>50</b>
3.2.1. Differential Raman cross section.....	50
3.2.2. Method.....	50
<b>3.3. Experimental arrangement.....</b>	<b>52</b>
3.3.1. Sample preparation .....	52
3.3.2. Instrumentation .....	53
3.3.3. Experimental setup .....	54
3.3.4. Spectral correction.....	55
<b>3.4. Results and discussion .....</b>	<b>55</b>
3.4.1. Observations .....	55
3.4.2. Measurement of differential Raman cross sections.....	59
3.4.4. Discussion.....	63
<b>3.5. Conclusions .....</b>	<b>66</b>
<b>References .....</b>	<b>68</b>

---



This chapter presents a detailed, predominantly experimental examination of differential Raman cross-sections (DRCS) of the *D* band at  $\sim 1350\text{ cm}^{-1}$  and the *G* band at  $\sim 1600\text{ cm}^{-1}$  of some carbonaceous materials. They were measured using a 532 nm continuous laser for the excitation of the Raman scattering. Raman spectrum of water was used as a standard reference to deduce the DRCS of our samples. Several types of carbonaceous particles, such as natural carbon (anthracite coal from Vietnam), industrial carbon black (Ensaco 350G, Ensaco 250P, Ensaco 250G, printex-25), graphite, soot (forklift diesel engine emission, SRM 2975, NIST), Rice soot (biomass burning emission reference from rice straw, ETH Zurich) and soot from Nanograins reactor were studied as references for black carbon. However, we succeeded only for coal powder, Ensaco 350G carbon black, and Diesel soot.

### 3.1. Introduction

Raman spectroscopy is a powerful tool for structural investigation of the carbon-based materials because it is sensitive not only to crystal structures but also to molecular structures [1]. The main features in Raman spectra of carbonaceous materials are the so-called *D* and *G* peaks for visible excitation. The pioneers in research on the origin of these two peaks are Tuinstra and Koenig in 1970. Then they were inherited and further developed by many others, such as Knight and White, Mernagh and his coworkers, Ferrari and Robertson or Cançado's group, etc. [2]–[6]. They assigned the *G* (standing for graphite) peak to the bond stretching of all pairs of  $\text{sp}^2$  sites in both olefinic chains and aromatic rings. The *D* (standing for disorder) peak is due to the breathing modes of  $\text{sp}^2$  sites in rings and its activation requires defects [7]. These defects correspond to missing atoms (vacancies), atoms moving out of their expected positions (structural defects within the polyaromatic units) or to the finite size of the polyaromatic layer. They are also due to the insertion of heteroatoms in the polyaromatic units [8]. Raman spectroscopy has been considered a powerful tool in structural researches of carbon-based materials and is now widely used in carbon research. In earlier studies, investigated substances were graphite, diamond, glassy carbon, amorphous and graphitic carbon films, coal, pitch and coal fiber, activated carbon and fullerenes, which is followed up by a variety of soot [1].

Despite the large amount of experimental data available in the literature concerning the Raman spectra of carbonaceous materials, most of the studies focused in the relative intensities of the distinctive Raman peaks of the molecule [1], [4], [9], [10]. To the best of our knowledge, there are only few published data on Raman cross section, focused on the elemental carbon (graphite, diamond, and  $\text{C}_{60}$ ) [6], [11], [12] and carbon nanotubes [13]. The present work is aimed at filling what we perceive as a gap in the literature, that is, an experimental estimation of DRCS of several natural and artificial carbon-based particles to allow Raman spectroscopy to become more a quantitative technique in particular in environmental studies. We thus developed a practical method that can be applied to quantify DRCS of other nanoparticles. By comparing observed Raman signals of samples with that of a co-mixed standard substance, pure water, we achieved measurements of DRCS of some carbonaceous particles. The rest of this chapter is organized as the following. Section 3.2 introduces theory background, followed by experimental setup and sample preparation in

section 3.3. Results and discussion are presented in section 3.4. Finally, section 3.5 gives some remarks and concludes of this chapter.

## 3.2. Principles

### 3.2.1. Differential Raman cross section

The differential Raman cross section,  $\frac{\partial\sigma}{\partial\Omega}$  (in  $\text{cm}^2\cdot\text{molecule}^{-1}\cdot\text{sr}^{-1}$ ), for a molecular vibrational mode is defined as the number of inelastically scattered photons per unit time and unit solid angle divided by the incident light flux (in the number of photons per unit time per unit area). It relates to the observed signal  $S$  (in photoelectron) as shown in the formula below [14], [15]:

$$S = \left( P_D \cdot \frac{\partial\sigma}{\partial\Omega} \cdot D \cdot K \right) \cdot (A_D \cdot \Omega_D \cdot T \cdot Q) \cdot t \quad (3.1)$$

The components appearing in formula (3.1) are the laser photon flux  $P_D$  (in photons.  $\text{s}^{-1}\cdot\text{cm}^{-2}$ ), the density of scatterers  $D$  (in molecules.  $\text{cm}^{-3}$ ), the constant of geometry  $K$  (cm), the sample area monitored by the spectrometer  $A_D$  (in  $\text{cm}^2$ ), the collection solid angle of the spectrometer  $\Omega_D$  (in sr), the transmission  $T$  of the spectrometer and collection optics (unit less), the quantum efficiency of the detector  $Q$  (in e<sup>-</sup>/photon), and  $t$  is the observation time (in seconds). The first composition is a characteristic specific intensity defined as the total Raman scattering divided by the scattering volume. The second composition is a general instrumental component containing the collection optics and spectrograph.  $S$ ,  $\frac{\partial\sigma}{\partial\Omega}$ ,  $T$  and  $Q$  are wavelength dependent and a wavelength calibration has to be performed.

### 3.2.2. Method

The DRCS in equation (3.1) is difficult to achieve directly because it depends on a large number of instrumental variables. In addition, because carbonaceous particles are also strongly absorbing, propagations of the incident and scattered light within the samples would have to be taken into account, together with the texture (clusters of nanoparticles) making the scattering properties absolute determination even more difficult to handle and model dependent. Effectively, most of the known Raman scattering cross-sections have been measured for quasi-transparent material at the excitation wavelength. This problem is solved if the samples are mixed in the reference and then the mixtures are excited by the laser. Thus we used a method that self-calibrates the instrumental and optical characteristics by using a co-mixed standard reference. This approach differs from the substitutional method which consists in measuring separately the reference material. The standard material that has been mostly used is  $\text{CaF}_2$  because scattering properties are well-known and excitations are usually far from any resonant processes.

Our method for particles consists in normalizing the observed signal of the sample to that of the standard reference (indicated by \* in the following equations). If the sample and the standard substance, whose Raman cross section is known, are measured simultaneously,

they have the same laser intensity, the same sample area monitored by the spectrometer, the same collection solid angle of the spectrometer and the same acquisition time. In this case, the ratio  $S/S^*$  is calculated from equation (3.1) as:

$$\frac{S}{S^*} = \frac{\frac{\partial\sigma}{\partial\Omega}DTQ}{\frac{\partial\sigma^*}{\partial\Omega}D^*T^*Q^*} \quad (3.2)$$

The observed signals in photoelectron are proportional to the number of digital units “counts”  $I$  of the CCD camera. So, the Eq. (3.2) is re-written:

$$\frac{I}{I^*} = \frac{\frac{\partial\sigma}{\partial\Omega}DTQ}{\frac{\partial\sigma^*}{\partial\Omega}D^*T^*Q^*} \quad (3.3)$$

The wavelength dependence of the transmission  $T$  and the efficiency  $Q$  depends on the type of detector, grating and optics used. Those parameters are contained in the sensitivity curve of the experimental setup, which can be measured with a calibration source. In our case, we use a blackbody calibration source BB4-A (Omega Engineering Inc.), whose temperature is adjustable over a range of 100<sup>0</sup> to 982<sup>0</sup>C with the accuracy of 1<sup>0</sup>C. The black body was installed at the sample position.

The area ratio between Raman peaks of the samples and the standard reference after being corrected with the spectral response is then described as follows:

$$\frac{I_{corrected}}{I_{corrected}^*} = \frac{\frac{\partial\sigma}{\partial\Omega}D}{\frac{\partial\sigma^*}{\partial\Omega}D^*} \quad (3.3)$$

From the equation (3.3), the DRCS of the sample,  $\frac{\partial\sigma}{\partial\Omega}$ , is determined by the formula:

$$\frac{\partial\sigma}{\partial\Omega} = \frac{I_{corrected}D^*}{I_{corrected}^*D} \frac{\partial\sigma^*}{\partial\Omega} \quad (3.4)$$

This is the final equation used to obtain the DRCS of the samples. In our experiment, the dimension of  $D^*$  is molecule.cm<sup>-3</sup> while that of  $D$  is carbon atom.cm<sup>-3</sup>. Therefore, the measurement relies on the knowledges of the cross section of the reference, the spectral response of the detection and the relative concentrations. The solvent used was pure water for its spectral properties and its ease to be used.

Normalizing by the number of carbon atoms implies that the inferred cross section is an effective cross section that does not take into account the scattering process itself. The value is thus particle size and shape dependent and thus should not be transferred from one carbon nanoparticle size or cluster of nanoparticles to another. However only the cluster shapes and sizes may influence the cross section of the particle, as long as the nanoparticles are smaller than the excitation wavelength (Rayleigh regime). In addition, the measurement is done in water. However, we do not expect that this would have an effect as most of the

carbon atoms do not interact with water molecules. Only the cluster shapes may differ. This effect was not probed yet and would require experiments in the aerosol phase with known concentrations.

### 3.3. Experimental arrangement

In this section, we describe the experimental apparatus and procedures.

#### 3.3.1. Sample preparation

We studied nine different samples in form of powder: coal (anthracite coal from Nui Beo open-mine in Quang Ninh province, Vietnam) which was milled by manual handling in an agate mortar method before being used; industrial carbon black Ensaco 350G, Ensaco 250G, Ensaco 250P and printex-25; graphite; various types of soot origin from transportation to biomass products such as soot collected from by-products sticking on the inner wall of the Nanograins combustion chamber; Diesel soot SRM 2975 (NIST) and Rice soot (ETH Zurich). Rice soot is not popular in developed countries but in developing and undeveloped countries biomass burning emissions of rice straw residues may be carried out near urban agglomerations and may present a potential health risk for the population.

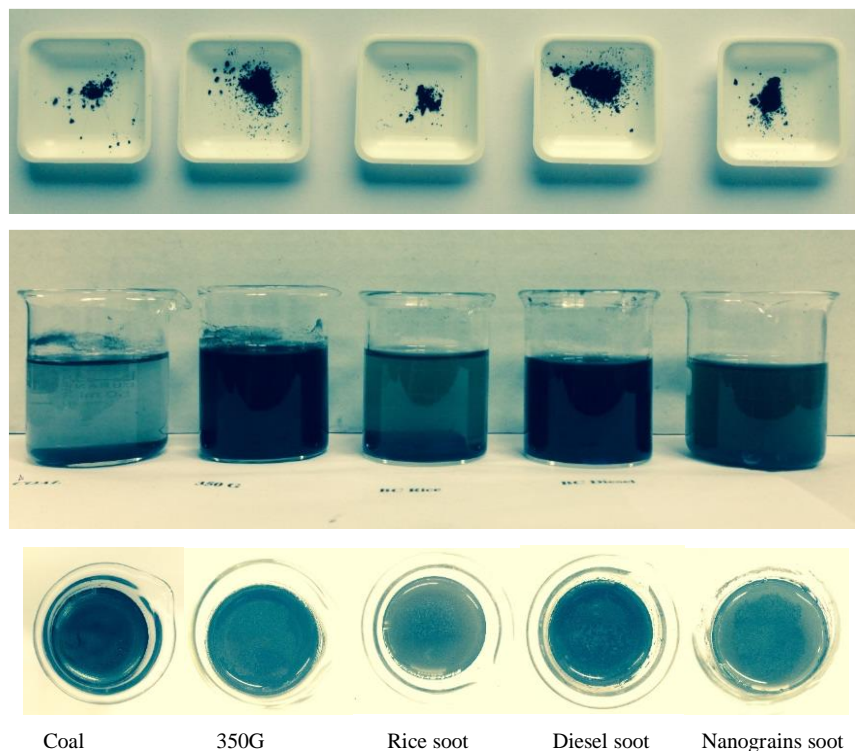


Fig. 3.1. Qualitative comparison of five samples in the form of powder (5mg/each sample) (the first row) and their mixtures in 40 ml water (the second row). The third row shows the images of thin films floated on the surfaces of the mixtures.

The reference substance was Millipore water whose dominant Raman feature is the fundamental O – H stretch mode at  $\sim 3400 \text{ cm}^{-1}$ . Each sample was mixed with water at different concentrations. The concentration of samples varied from 0.5 to 10 mg samples / 40 ml water. Samples were weight using a digital analytical balance with 1 mg readability.

Fig. 3.1 gives a qualitative observation of some samples through the sampling step. In comparison, coal colors jet black, rice soot and Nanograins soot color smoky or brown-black, diesel soot and 350 G color inky black. The colors of the mixtures of other samples in water are inky black like Ensaco 350 G so we did not show all in Fig. 3.1. With the same weight, their sample volumes increase gradually from coal, rice soot, Nanograins soot, 350G to diesel soot and when mixed with water, the colors of mixtures change from grey, brown to dark black (Fig. 3.1). Each sample was mixed in water at several different concentrations. The cuvettes were put in the water tank of an ultrasonic cleaning unit (Elmasonic P 30H) operated at 37 kHz frequency and 100% power. After a half an hour, a majority of their masses were dissolved or suspended in the solvent. The rest was assembled and found floating on the water surface and was removed. The real mass of samples mixed in water are thus equal to their initial masses subtracted the mass (weighted) of material removed from the surfaces. The mixtures were then excited from the top by the laser to measure the Raman spectra. During acquisition time, the samples were still put in the water tank of the ultrasonic cleaning unit (operated) to prevent from sedimentation on the bottom of the cuvettes.

#### 3.3.2. Instrumentation

Raman scattering signal is very weak compared to Rayleigh scattering signal, thus special care should be taken to distinguish it from the predominant Rayleigh scattering. A Raman system typically contains four major components: excitation source; sample; light collection optics; wavelength selector and detector. In our experimental setup, the excitation source was a continuous laser model Verdi 5W (Coherent Inc.). This is 532 nm green laser which can continuously deliver output power up to 5 W with a 2 mm diameter beam-size with vertical polarization. Scattered photons are collected by a lens system, and then pass through a Razor-Edge (high-pass) filter with a cut-of wavelength at 539 nm, before entering a round-to-linear fiber bundle. This filter blocks the radiations from 430 to 538.9 nm with  $\text{OD} > 6$  and permits to transmit up to 90 % for the band from 539 to 1200 nm. The fiber bundle contains 19 fibers arranged in a line configuration at one end and a circular configuration at the other end. Each fiber has a core diameter of 200  $\mu\text{m}$ . The fibers are not maintaining the polarization ensuring the same detection efficiency for all polarization states. The linear end coupled with the slit of a spectrometer which was connected with CCD camera PIXIS 400. The spectrometer used was a 0.300 m focal length imaging monochromator / spectrograph (model Acton SP2300 spectrometer from Princeton Instruments). It includes a triple grating turret for gratings 1, 2 or 3 with 1200, 1200 and 300 grooves/mm, respectively. Their blaze wavelengths are 300, 500 and 500 nm, respectively. Maximum resolutions of the first and the second grating are  $1.5 \text{ cm}^{-1}$  and that of the third grating is  $5.1 \text{ cm}^{-1}$ . A notch filter was inserted in front of the slit of the spectrometer. In fact, it could be also located in front

of the entrance of optical fiber. This StopLine notch filter (Semrock) has an OD > 6 at 532 nm and 90 % transmission band from 550.8 to 1600 nm.

### 3.3.3. Experimental setup

The backscattering configuration is sketched in Fig. 3.2. The laser beam goes into the sample, which is put into the ultrasonic tank, after reflection on two mirrors  $M_1$  and  $M_2$ .  $M_1$  is a  $45^\circ$  incidence angle laser mirror at 532 nm.  $M_2$  is a  $45^\circ$  incidence angle dielectric mirror whose reflectance is very high in the broadband range from 400 nm to 800 nm. Collected scattered photons from the sample are first reflected by the  $M_2$  mirror. A collection system containing two spherical lenses  $L_1$ ,  $L_2$  whose focal lengths are 200 and 25.4 mm and whose diameters are 50.8 and 25.4 mm, respectively, is placed at a small angle ( $<10^\circ$ ) with the incident laser beam. The distance from the sample to the entrance of optical fiber is about one meter, in which the distances between the sample and  $L_1$ ,  $L_1$  and  $L_2$ ,  $L_2$  and the entrance of optical fiber are 680, 140 and 15 mm. This configuration was set to ensure that the image of excited sample volume is smaller than the entrance size of the optical fiber (1 mm diameter) whatever the probe volume in the water mixture. In other words, during acquisition time, we could collect all scattered photons in a solid angle subtended by a region at the excited sample volume onto the  $L_1$  lens. The solid angle  $\Omega = 2\pi(1 - \cos\theta) \approx 0.0044 \text{ sr}$ , in which  $\theta$  is a half of apex angle denoted in Fig. 3.2. Furthermore, during acquisition time, the temperature of water in the tank of the ultrasonic cleaning unit increased. Fresh water was continuously (manually) added to prevent a high rise of temperature. At too high temperatures, the concentration of the mixtures would be changed because of water evaporation and a control of its level during measurements had to be performed.

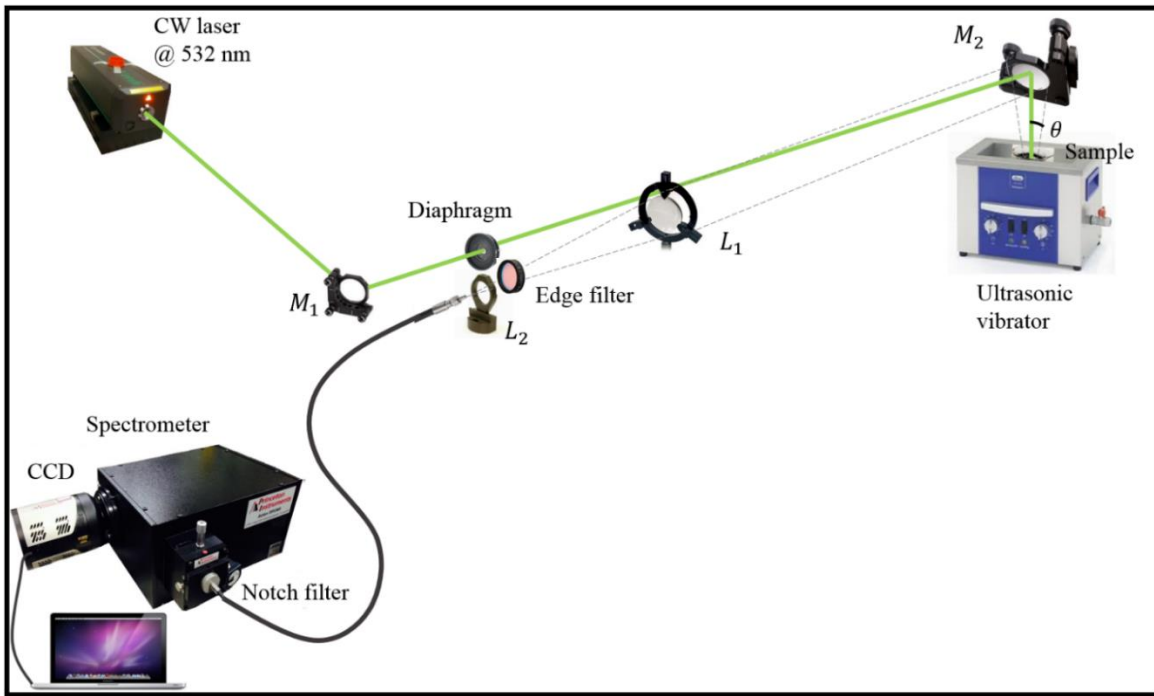


Fig. 3.2. Scheme of differential Raman cross section measurement at ISMO.

### 3.3.4. Spectral correction

At first, we calibrated the spectrometer using a Neon Mercury lamp. Then dark noise background was also measured by blocking the laser beam. Every configuration has its own sensitivity curve, depending on detector, gratings (and their positions) and optics used.

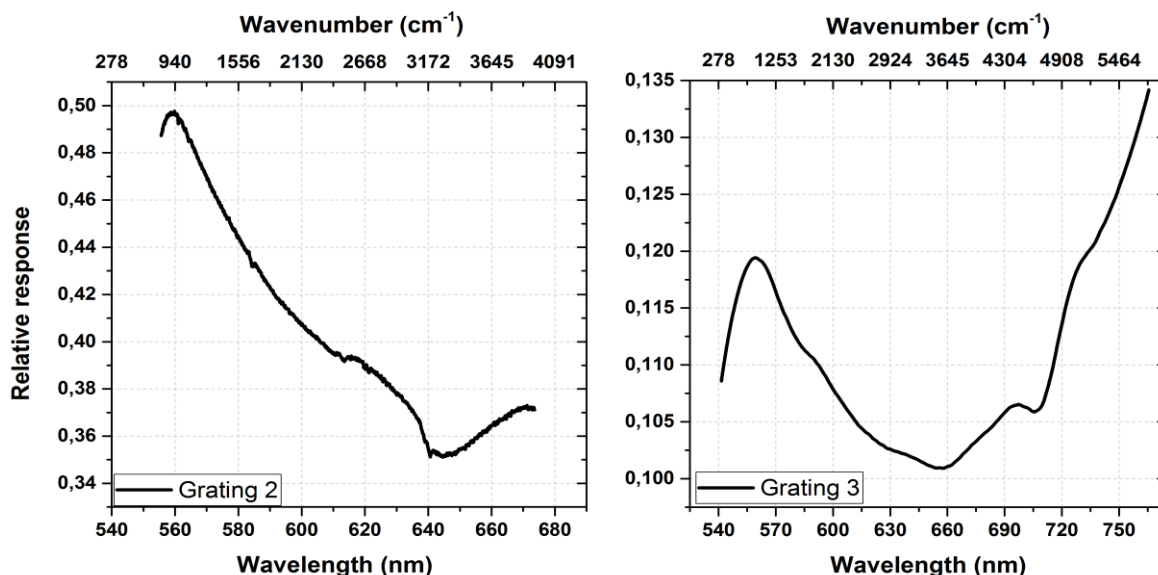


Fig. 3.3. Spectral responses of the experimental instruments as a function of wavelength.

This sensitivity curve can be measured with a calibration source. In our case, a blackbody source was used to correct Raman spectra for the instrumental spectral response. With the placement of the blackbody output at the Raman sample position, the product of through-put, collection efficiency, and quantum efficiency could be assessed. This product is related to a spectrometer figure of merit providing a quantitative comparison of spectrometer sensitivity and signal to noise ratio. The instrumental curves are shown in Fig. 3.3 corresponding to grating 2 and grating 3 of the spectrometer. In cases we only considered Raman signals of carbon-based materials, the grating 2 was mainly used. Otherwise, when we measured Raman spectra of the mixtures of samples and water, we used the grating 3 whose range covers from Raman region of carbonaceous materials to O – H stretching Raman band of water.

## 3.4. Results and discussion

### 3.4.1. Observations

#### 3.4.1.1. Raman spectra of samples in form of powder

Before measurement of DRCS, we obtained Raman spectra of various carbon-based materials in form of powder. The laser power on the samples was 200 mW with the beam diameter of about 2 mm ( $6.4 \text{ W/cm}^2$ ). Typical data acquisition time for each spectrum was 5

minutes and the 1200g/mm grating was used to disperse the selected light. Their spectra are presented in Fig. 3.4.

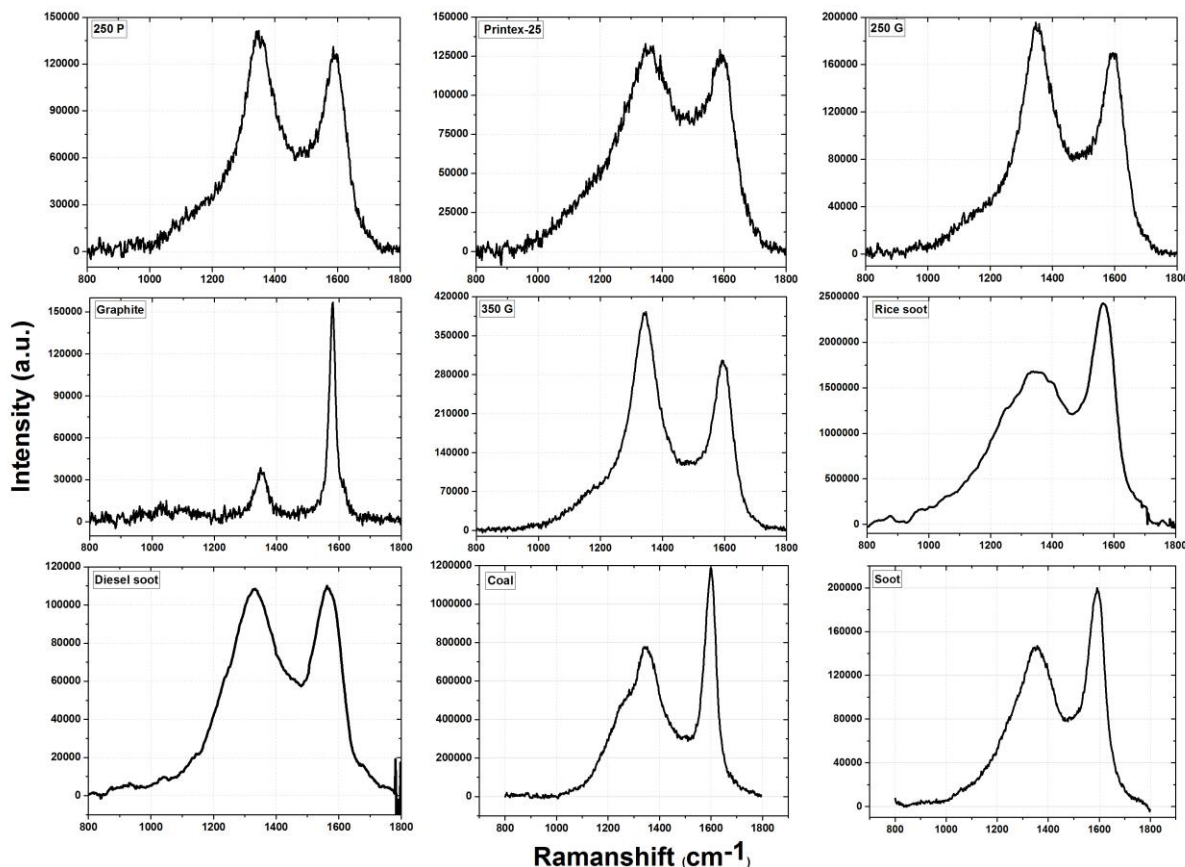


Fig. 3.4. Raman intensities of several carbon-based materials as a function of Raman shift.

In comparison, at first glance the spectra look quite similar because they consist of two main bands at  $\sim 1350 \text{ cm}^{-1}$  (*D* band) and  $\sim 1600 \text{ cm}^{-1}$  (*G* band). However, there are some significant differences. Apart from graphite, the intensity ratio of *D* and *G* bands varies from  $\sim 0.24$  with rice soot to  $\sim 1.3$  with 350G. Fig. 3.4 also allows us to take a closer look at the width, shape, and position bands of these materials where we can see differences. These Raman spectra will be used for comparison with their spectra in water.

### 3.4.1.2. Raman spectra of samples in water

Transmission of the laser beam through air led to the contribution of scattered photons from  $\text{O}_2$  and  $\text{N}_2$  to the Raman spectra of our water or samples. Therefore, before measuring Raman spectra of the mixtures of powder samples in water, we considered Raman spectra of air and Millipore water. The laser power was 200 mW and data acquisition time was about 17 minutes. Firstly, the curve in Fig. 3.5 is the Raman spectrum of air which was measured with the grating 2 of the spectrometer. It contains Raman bands of  $\text{O}_2$  and  $\text{N}_2$  located at 1555 and  $2331 \text{ cm}^{-1}$ , respectively [16].



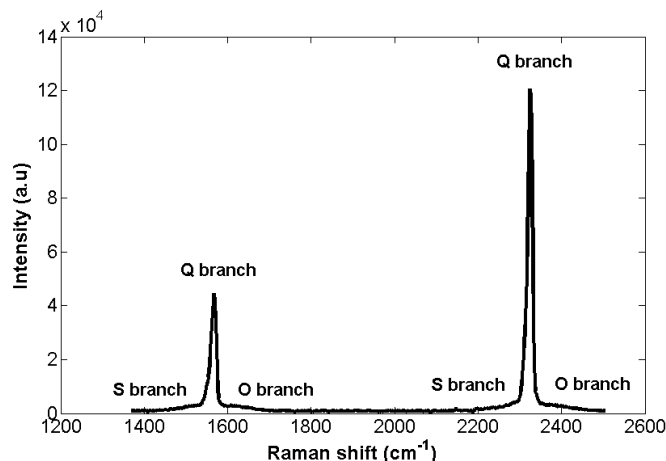


Fig. 3.5. Raman spectrum of  $O_2$  and  $N_2$  in the air with  $2\text{ cm}^{-1}$  as resolution.

Secondly, Fig. 3.6 shows Raman scattering intensity of water as a function of Raman shift when integrated over the Raman shift range from  $500$  to  $5000\text{ cm}^{-1}$  when the exciting laser operates at  $532\text{ nm}$  and we used grating 3 of the spectrometer. In this range, Raman spectrum of water consists of two predominant modes: the bending mode at  $1636\text{ cm}^{-1}$  and the intense stretching mode at  $3400\text{ cm}^{-1}$ . Note that the contribution of the Raman signals of air was subtracted. One can see that Raman scattering from water exhibits a convenient, harmless and photo-stable reference.

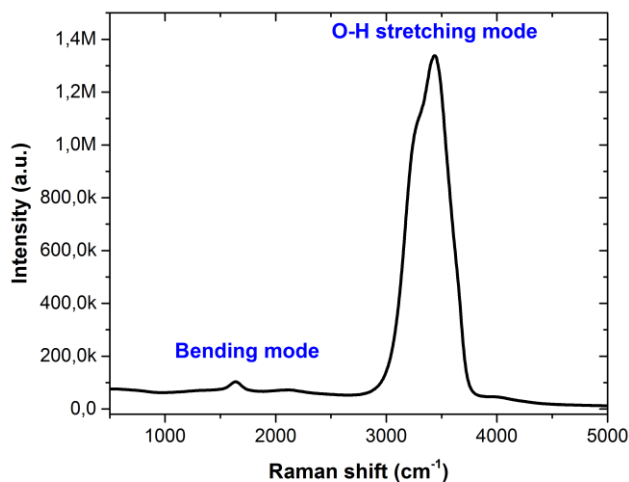


Fig. 3.6. Raman spectrum of pure water

Raman spectra of mixtures of our samples in water were measured. Almost all their Raman signals were weak and it was difficult to separate Raman signals from fluorescence signal, so we only present a selection of spectra in Fig. 3.7. All Raman spectra of the mixtures were achieved using the grating 3.

There are two remarks from this figure. The first point here is the contamination by the Raman spectra of  $O_2$  in the atmosphere (at  $1555\text{ cm}^{-1}$ ) and that of the bending mode of water (at  $1640\text{ cm}^{-1}$ ), superimposed on the Raman spectra of the carbonaceous samples. Because we used the same experimental set up, the path of the laser in the air was unchanged. The Raman signals of  $O_2$  and  $N_2$  were constant and thus could be rather easily removed. The contribution of the bending mode of water, measured for the pure water, could also be subtracted. The second point is the background of the mixtures changing from one to the others because of fluorescence. Reminding that soot may contain a large amount of PAH or possess an oxidized surface, fluorescence is expected [17]. In addition, Raman spectra of Nanograins soot, graphite, Ensaco 250G, Ensaco 250P, Printex-25 in the mixture were too weak compared to fluorescence and could not be extracted. Therefore, in the rest of this chapter, we only focused on determining DRCS of coal, CB Ensaco 350G and diesel soot whose Raman signals could be separated from their backgrounds. The data treatments were more or less different for all samples. Then, every pure Raman spectra of samples in water were overlapped with their spectra in form of powder to estimate the corrections of data treatment and water effect. After that, we could evaluate their DRCS.

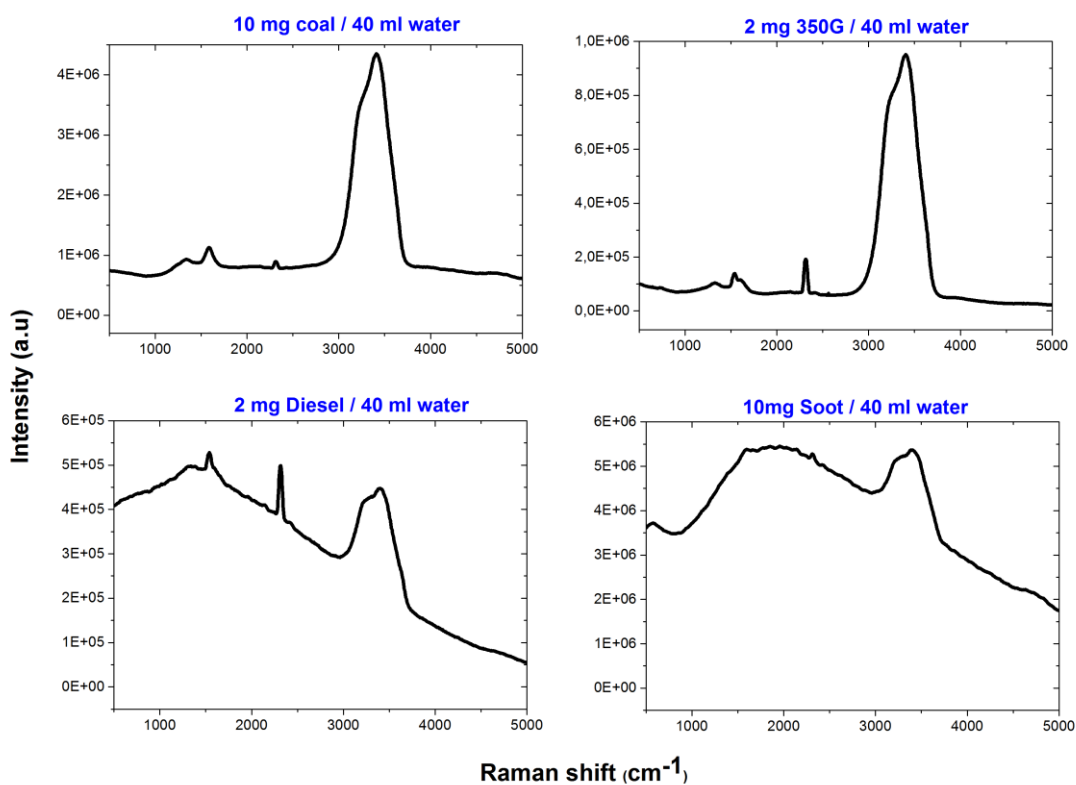


Fig. 3.7. Raman spectra of various carbonaceous particles in water as a function of Raman shift. The contribution of  $O_2$  and  $N_2$  is stable. The intensity of the Raman O – H stretching mode of water depends on the concentration of the mixture.

### 3.4.2. Measurement of differential Raman cross sections

We determined DRCS of each sample at many different concentrations then averaged them. Each concentrations were prepared several times to check the reproducibility because of the removal of the carbonaceous sample remaining on the water surface. According to the equation 3.4, we need to calculate the number of digital “counts” (photoelectrons) of the *D*, *G* and O – H stretching bands for calibration. From literature, the backscattering DRCS of water for the O – H stretching band reported by Andrew Bray is  $5.74 \times 10^{-30} \text{ cm}^2 \cdot \text{sr}^{-1} \cdot \text{molecule}^{-1}$  [18].

#### 3.4.2.1. Anthracite coal from Vietnam

After corrections, all obtained Raman spectra of coal and water stretching band of the mixtures at different concentration are plotted in Fig. 3.8. Because the O – H stretching band is much higher than *D* and *G* bands, they are separated into two figures. In comparison, the spectra of coal in water had the same shape with that that of the Raman spectrum of coal in form of powder, as shown in Fig. 3.9. This proved that there was no water effect on the Raman spectra of coal powder in water. It is clear that the higher the concentration of the mixture is, the higher Raman signal of coal is attained. An opposite trend in the O – H stretching band is observed because the probe volume decreases with the increase of the optical density of the solution. Note that the legends in Fig. 3.8 are the mass of coal in 40 ml water.

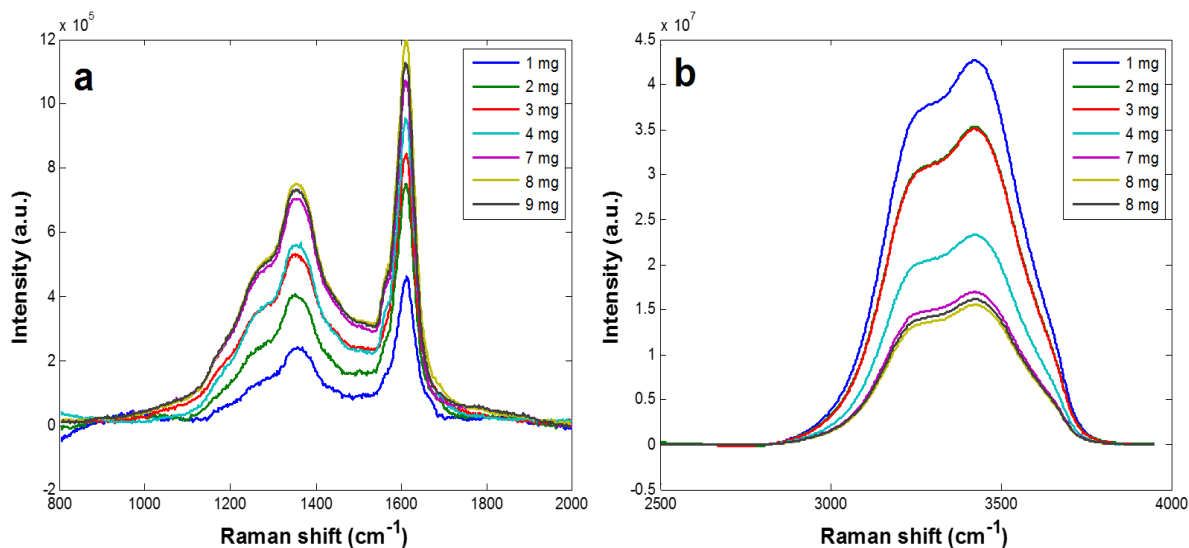


Fig. 3.8. Raman spectra of the coal mixtures at different concentrations. a) shows *D* and *G* band of coal in the mixtures; b) shows O – H stretching band of water in the mixtures.

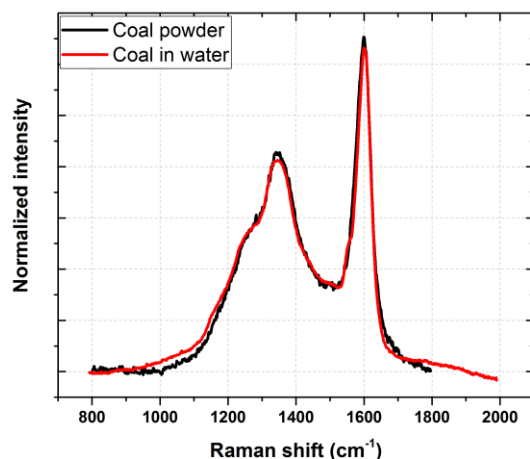


Fig. 3.9. Comparison of the Raman spectra of coal in form of powder and that of coal after mixing in water.

The ratio between the observed Raman signals of *D* and *G* bands and O-H stretching band of the solvent are shown in Fig. 3.10 a. *D* band signal was taken by summing the photoelectron counts from 1000 to 1500  $\text{cm}^{-1}$  and *G* band the counts from 1500 to 1700  $\text{cm}^{-1}$ . The experimental data are well fitted by straight lines whose slopes are 0.0025 and 0.0015, respectively. From the slopes, we can evaluate the DRCS of *D* and *G* bands. Note that carbon accounting for 92% mass of coal, from equation (3.4), DRCS of *D* and *G* peaks are found to be  $(4.1 \pm 1.0) \times 10^{-28} \text{ cm}^2 \cdot \text{sr}^{-1} \cdot \text{atom}^{-1}$  and  $(2.7 \pm 0.5) \times 10^{-28} \text{ cm}^2 \cdot \text{sr}^{-1} \cdot \text{atom}^{-1}$  as shown in Fig. 3.10 b.

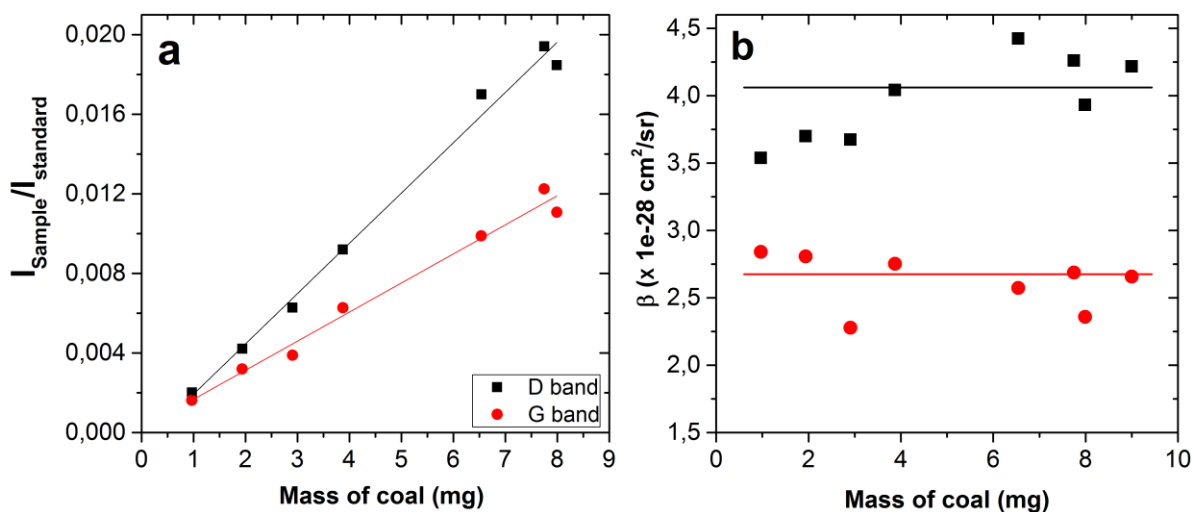


Fig. 3.10. a) Ratios of Raman intensities of *D* and *G* peaks with such intensity of water measured in coal / water mixtures at different concentration. b) Differential Raman cross section of *D* and *G* peaks of coal.

### 3.4.3.2. Carbon black Ensaco 350G

Raman spectra of Ensaco 350 G mixed with water were more complicated than that of coal. While the *D* peak appeared clearly, the overlapping band between the *G* peak, O<sub>2</sub> and the bending mode of water from 1555 to 1620 cm<sup>-1</sup>, respectively, was quite complex. Subtraction of the bending mode contamination could not be performed: the measured water signal was evidently weaker than expected from the pure water measured ratio and the measured intensity of the stretching mode of the solution. It should be noticed that the change in bending/stretching mode intensity ratio is sensitive to the concentration of 350G, the higher the concentration is the lower the relative intensity of the bending mode is. It traces an interaction of the nanoparticles with the solvent, their shape offering a much higher solvation surface than the coal microparticles. This effect also suggests a rather good dispersion of the CB nanoparticles. A comparison of the shapes of the water stretching band at different concentrations shows that no changes are observed. It underlines a weak effect for this mode and suggests that, at present, no changes for its intrinsic intensity can be assumed. The same comparison for the bending mode was not performed because the poorer signal/noise ratio prevented from a clear conclusion. In the present case, in order to overcome the above-mentioned difficulty, data treatment was then slightly different from that of the previous sample and assumed that the water stretching mode cross section was unchanged.

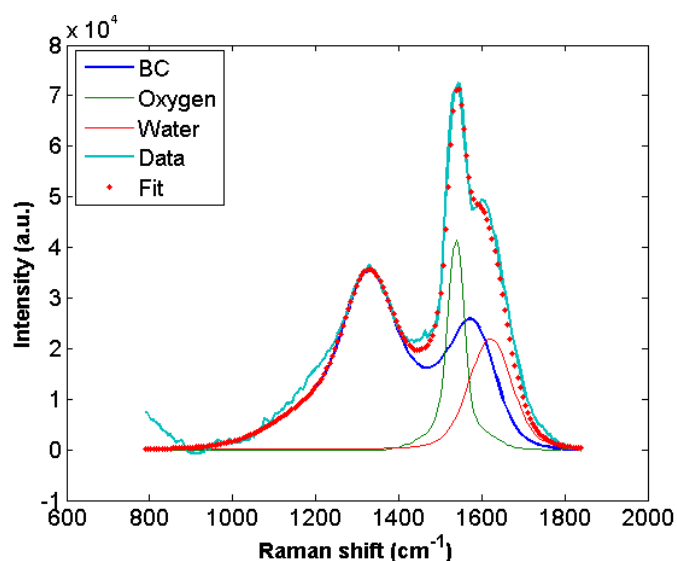


Fig. 3.11. Deconvolution of the Raman spectrum of Ensaco 350 G powder. The bright blue line is the experimentally observed Raman spectrum; The blue solid line is the Raman spectrum of sample in form of powder; The green solid line is the Raman signal of O<sub>2</sub>; The red solid line is the bending band of water; The red dot line is fitted spectrum from the three components contributing to the experimental data.

Raman spectrum of Ensaco 350 G in water consists of three components: Raman spectrum of 350 G in form of powder, Raman spectrum of O<sub>2</sub> and that of the bending mode of water. To fit the experimental spectrum, we summed them up with constraints only on the *D* band of CB powder Raman spectrum and using the O<sub>2</sub>/N<sub>2</sub> Raman signals to determine the

strength of the O<sub>2</sub> Raman band independently. The shape of the water bending mode was taken from the pure water Raman data. This reproduced spectrum nearly merges with the real spectrum. The blue curve was then taken as the Raman spectrum of Ensaco 350G in water. We carried out this measurement at various concentrations. The ratios of the observed Raman signals of *D*, *G* band and O – H stretching band is plotted in Fig. 3.12a and their DRCS are shown in Fig. 3.12 b. By using equation 3.4 and noting that carbon accounting for ~100% mass of Ensaco 350G, we got the average DRCS for the *D* band  $(5.1 \pm 0.8) \times 10^{-28} \text{ cm}^2 \cdot \text{sr}^{-1} \cdot \text{atom}^{-1}$  and for the *G* band  $(2.9 \pm 0.5) \times 10^{-28} \text{ cm}^2 \cdot \text{sr}^{-1} \cdot \text{atom}^{-1}$ .

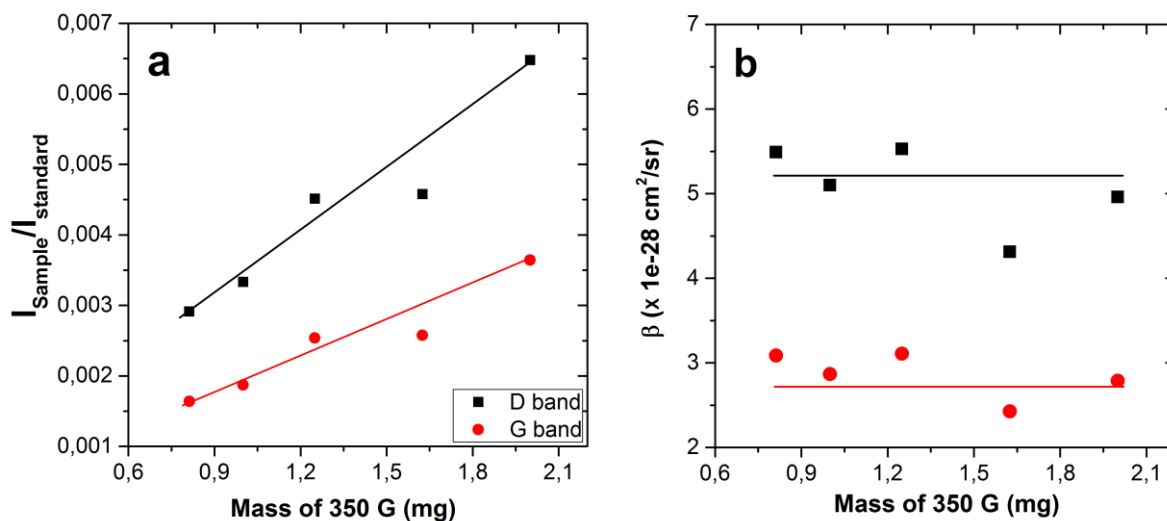


Fig. 3.12. a) Ratios of Raman intensities of *D* and *G* peaks with water measured in Ensaco 350G / water mixtures at different concentration. b) Differential Raman cross section of *D* and *G* peaks of Ensaco 350G.

### 3.4.3.2. Diesel soot SRM 2975 (NIST)

Similar to the data treatment of BC Ensaco 350 G, with diesel soot, the measurement was done at two different concentrations: 9 mg and 5.4 mg diesel soot in 40 ml water. We finally obtained its differential Raman cross sections:  $\beta_D = (8.8 \pm 2.0) \times 10^{-28} \text{ cm}^2 \cdot \text{sr}^{-1} \cdot \text{atom}^{-1}$  and  $\beta_G = (1.1 \pm 0.5) \times 10^{-27} \text{ cm}^2 \cdot \text{sr}^{-1} \cdot \text{atom}^{-1}$  corresponding to DRCS of *D* and *G* bands, respectively. Fig. 3.13 is the deconvolution of Raman spectrum of diesel soot at the concentration of 9 mg soot in 40 ml water. In that case, the signal to noise ratio was worse compared to CB Ensaco 350G.

Noted that in the Raman spectra of Ensaco 350G and Diesel soot in Fig. 3.11 and Fig. 3.13 the fluorescence contamination was subtracted.

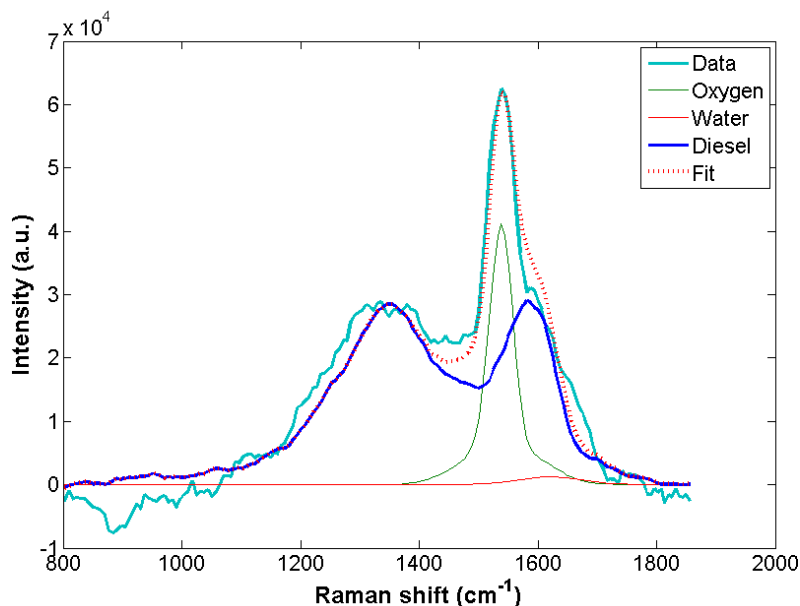


Fig. 3.13. Deconvolution Raman spectrum of Diesel soot SRM 2975 (NIST). The bright blue line is the experimentally observed Raman spectrum; The blue solid line is Raman spectrum of sample in form of powder; The green solid line is Raman signal of O<sub>2</sub> and water; the red denoted line is the sum of the 3 components.

### 3.4.4. Discussion

#### 3.4.4.1. Comparison of the DRCS of coal, carbon black and soot

Obviously, there is no large difference between the DRCS of the three various samples, which are on the order of few  $10^{-28}$   $\text{cm}^2 \cdot \text{sr}^{-1} \cdot \text{atom}^{-1}$  although Raman signals of coal is stronger and easier to obtain than that of others (Fig. 3.4). In order to explain this point, we could look at the images of each drop of the mixtures after evaporation via transmission optical microscopy (Fig. 3.14). Although we did not measure directly the distribution of particle size in water, these images are worth providing a qualitative observation. Ensaco 350 G and diesel soot particles in water are in the form of clusters of nanoparticles (not resolved). The size and shape of the clusters depend on the concentrations of nanoparticles and phase (aerosol or in the water), they appear on the image more or less micrometric. The coal particles are found in the form of more compact micrometric particles.

In nature, anthracite is the highest rank of coal which is solid and brittle with black lustrous features. Therefore, after being smashed up by manual handling in an agate mortar, the piece of coal was broken into few micrometer diameter solid particles. The effective densities of the coal particles are thus expected to be higher than for the porous clusters of soot and carbon black nanoparticles [19], although such cluster morphology may differ in water than after evaporation on the substrate. It should be noted here that ball milling was used as well for coal and similar size distribution was obtained. Therefore, for the same mass of particles, the resulting optical densities of the solutions were smaller and the probe volume of coal solution was higher. It may be seen from the stronger water Raman signal.



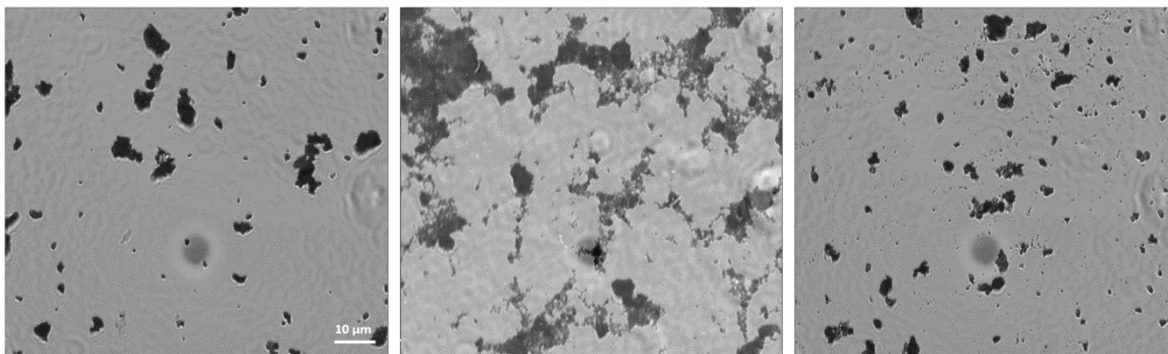


Fig. 3.14. Distribution of coal, Ensaco 350G and diesel soot particles in drops of the mixtures after evaporation via transmission optical microscopy (from left to right, respectively)

Diesel soot is found to exhibit larger cross sections than those of coal and carbon black 350G although uncertainties on the measurements may limit these differences. That the  $D$  band differs from one material to another is not surprising because it involves the specific defects. The  $G$  band, related to the  $sp^2$  stretching bond, may be compared quantitatively. The cross sections are given per carbon atoms, assuming that the scattering process is only dependent of the quantity of  $sp^2$  carbon. However, the size and shape are also involved in the scattering properties and the images showing smaller clusters of diesel soot point to possible differences in the water solution. Smaller clusters than the coal micrometric particles may behave differently as optical depth of the coal particles would have to be taken into account to relate more precisely the cross section to the mass of coal. The DCRS are effective and cannot be transferred to other size and (more compact) shapes of particles.

#### 3.4.4.2. Comparison of the obtained DRCS to other carbonaceous materials

The obtained DRCS of our samples are given per carbon atom while those of molecules in literature are per molecule. To be compared, DRCS from the literature will be converted into per carbon atom by dividing the obtained values to a factor of the number of carbon atoms in each molecule. Table 3.1 shows DRCS from literature and our study of some carbonaceous materials and molecules in the liquid phase excited at a wavelength ranging from 488 nm to 532 nm, except for  $C_{60}$  which excited at 752.5 nm. This study shows that DRCS of our samples are approximately 100 times larger than that of the breathing mode of benzene at nearly the same laser excitation wavelength. It is also higher than that of diamond. The reason probably is the appearance of resonance Raman effect in our samples leading to the enhancement of Raman signals [20]. In general, Raman scattering is extremely weak. However, BC materials have strong optical absorbance. The incident laser frequency is always close in energy to an electronic transition in BC, enhancing the intensity of the Raman signals.

The achieved DRCS of coal, 350 G, diesel soot are found in between other polyaromatic materials shown in table 3.1, lower than graphite and higher than nanographites. For those bulky materials, the variations cannot involve the particle shapes scattering properties. Size distribution of the clusters of diesel soot, 350 G and coal particles are not be the same and their phase function of the Raman scatter should not be the same.



Table 3.1. Differential Raman cross sections for some carbon-based materials from literatures.

Label	Laser excitation $\lambda$ (nm)	Raman shift $\nu$ (cm <sup>-1</sup> )	DRCS $\beta$ (cm <sup>2</sup> sr <sup>-1</sup> molecule <sup>-1</sup> )	DRCS $\beta$ (cm <sup>2</sup> sr <sup>-1</sup> atom <sup>-1</sup> )	Reference
N <sub>2</sub> gas	514.5	2331	$0.43 \times 10^{-30}$		[16]
O <sub>2</sub> gas	514.5	1555	$0.58 \times 10^{-30}$		[16]
Benzene	488	992 (ring breathing mode)	$(3.25 \pm 0.10) \times 10^{-29}$	$5.42 \times 10^{-30}$	[21]
	514		$(3.51 \pm 0.02) \times 10^{-29}$	$5.85 \times 10^{-30}$	[22]
Toluene	488	1002	$(1.83 \pm 0.10) \times 10^{-29}$		[21]
C <sub>60</sub>	752.5	1469	$(2.09 \pm 0.06) \times 10^{-29}$	$3.48 \times 10^{-31}$	[11]
Graphene	514.5	1580		$2.27 \times 10^{-28}$	[23]
Graphite	514.5	1585		$4.57 \times 10^{-28}$	[24]
				$7.2 \times 10^{-28}$	[25]
Nano graphite	514.5	1350 (breathing mode)		$L_a=20$ nm, $\beta= 2.0 \times 10^{-29}$ $L_a=35$ nm, $\beta= 1.3 \times 10^{-29}$ $L_a=65$ nm, $\beta= 0.7 \times 10^{-29}$	[6]
		1580 (stretching mode)		$L_a=20$ nm, $\beta= 2.0 \times 10^{-29}$ $L_a=35$ nm, $\beta= 2.8 \times 10^{-29}$ $L_a=65$ nm, $\beta= 3 \times 10^{-29}$	
Ia natural diamond	514.5	1332		$(3.42 \pm 0.48) \times 10^{-30}$	[26]
	785			$(2.15 \pm 0.48) \times 10^{-30}$	[12]
Coal (anthracite from Vietnam)	532	1357 (breathing mode)		$(4.1 \pm 1.0) \times 10^{-28}$	Our work
		1610 (stretching mode)		$(2.7 \pm 0.5) \times 10^{-28}$	
Ensaco 350G	532	1344 (breathing mode)		$(5.1 \pm 0.8) \times 10^{-28}$	Our work
		1596 (stretching mode)		$(2.9 \pm 0.5) \times 10^{-28}$	
Diesel soot SRM 2975 (NIST)	532	1348 (breathing mode)		$(8.8 \pm 2.0) \times 10^{-28}$	Our work
		1582 (stretching mode)		$(1.1 \pm 0.5) \times 10^{-27}$	

It implies that an enhancement of the backward scattering due to an anisotropic distribution (Mie regime) would lead to much greater differences between the micrometric coal particles and the (expected) much smaller diesel soot clusters, in particular operating the ultrasonic cleaning unit.

The literature data on graphite Table 3.1. are fluctuating over a factor of 2 and that of graphene are rather close [23]. In the investigation of Cançado *et al.*, 2007 on nanographites [6], FWHM of *D* and *G* peaks are found to vary inversely with the crystallite size ( $L_a$ ) ranging from 20 to 65 nm. The correlation was recently revisited and confirmed [27]. The FWHM of the *D* and *G* bands of our samples are much larger than that of nano-graphites in Cançado *et al.* (2007). For the nano-graphite,  $\Gamma_D$  and  $\Gamma_G$  range from ten to 50  $\text{cm}^{-1}$  while in our case, they are about several tens to two hundred. It shows that the polyaromatic units  $L_a$  of our samples are much smaller than that of nano-graphite. Diesel soot have usually  $L_a$  of about 2 nm, carbon black around 1-2 nm and the Nui Beo anthracite coal exhibits fringes under HRTEM (not shown) between 1-2 nm as well. They are about the same range. i.e. 1-2 nm. With such differences, the electronic structure as traced by the optical gap will differ between these materials. It implies that resonance effects should be different if the cross sections are confirmed. Correlation of the optical gap with the Raman properties in term of *G* band positions for instance was already shown [20], [28]. The relation to the intensities is less clear, although very sensitive to the resonance effects. We tentatively assign the differences to the polyaromatic units themselves, their sizes modulating the resonance effects at a fixed wavelength of 532 nm. In order to progress on these questions, DCRS would have to be measured at several wavelengths in order to probe the resonant effects up to the UV.

### 3.5. Conclusions

The fundamental advantage of our method is that it permits the measurement of differential cross sections throughout fewer input parameters than other methods. Furthermore, water allows us to use long integration times and large laser power because it vapors much slower than other solvents, such as ethanol or cyclohexane. Although water has many strong points, such as safety, cheap, strong O – H stretching band whose DRCS is well-known and absence of resonance, it is not the best reference for all carbonaceous samples because Raman shift of the bending mode contamination locates close to Raman shift of *D* and *G* bands. It caused a difficulty in our data analysis process. Other solvent such as DCM or heavy water may be exploited in the future to overcome spectral congestion problems. It should be recall that until this work, no data were obtained on the DRCS database of BC or soot exhausted from incomplete combustion because of the difficulty of experimental data.

General applications to other carbonaceous nanoparticles may not be possible. The fluorescent contribution of PAH which are found on combustion products may overwhelms Raman signals. Extraction may be an issue to address the DCRS of the remaining BC. In LIDAR measurement, because water was considered as the standard substance, spectral analysis of backscattering of light from the ocean may be used to characterize concentrations of suspended constituents at the surface of the ocean water. This potentially applies to the marine investigations.

An important point in this investigation is that it rigorously reveals that DRCS of BC are huge. In particular, DRCS of *D* and *G* peaks of coal are  $\beta_D = (4.1 \pm 1.0) \times 10^{-28} \text{ cm}^2 \cdot \text{sr}^{-1} \cdot \text{atom}^{-1}$

and  $\beta_G = (2.7 \pm 0.5) \times 10^{-28} \text{ cm}^2.\text{sr}^{-1}.\text{atom}^{-1}$ ; those of Ensaco 350G are  $\beta_D = (5.1 \pm 0.8) \times 10^{-28} \text{ cm}^2.\text{sr}^{-1}.\text{atom}^{-1}$  and  $\beta_G = (2.9 \pm 0.5) \times 10^{-28} \text{ cm}^2.\text{sr}^{-1}.\text{atom}^{-1}$  and finally  $\beta_D = (8.8 \pm 2.0) \times 10^{-28} \text{ cm}^2.\text{sr}^{-1}.\text{atom}^{-1}$  and  $\beta_G = (1.1 \pm 0.5) \times 10^{-27} \text{ cm}^2.\text{sr}^{-1}.\text{atom}^{-1}$  corresponding to DRCS of *D* and *G* bands of Diesel soot SRM 2975 (NIST). These are found close to that of graphite and nearly 2 orders of magnitude higher than other carbonaceous solid (diamond) or molecules ( $\text{N}_2$ , benzene...) commonly at the focus of atmospheric research, thanks to their polyaromatic structures. We believe a proper determination of the order of magnitude of DRCS of carbon-based materials will contribute to the feasibility of detection of BC emission in the atmosphere using Raman spectroscopy.

## References

- [1] A. Sadezky, H. Muckenhuber, H. Grothe, R. Niessner, and U. Pöschl, “Raman microspectroscopy of soot and related carbonaceous materials: Spectral analysis and structural information,” *Carbon N. Y.*, vol. 43, no. 8, pp. 1731–1742, 2005.
- [2] D. S. Knight and W. B. White, “Characterization of diamond films by Raman spectroscopy,” *J. Mater. Res.*, vol. 4, no. 2, pp. 385–393, 1989.
- [3] T. P. Mernagh, R. P. Cooney, and R. A. Johnson, “Raman spectra of Graphon carbon black,” *Carbon N. Y.*, vol. 22, no. 1, pp. 39–42, 1984.
- [4] A. Ferrari and J. Robertson, “Interpretation of Raman spectra of disordered and amorphous carbon,” *Phys. Rev. B*, vol. 61, no. 20, pp. 14095–14107, 2000.
- [5] L. G. Cançado, a. Jorio, E. H. M. Ferreira, F. Stavale, C. a. Achete, R. B. Capaz, M. V. O. Moutinho, a. Lombardo, T. S. Kulmala, and a. C. Ferrari, “Quantifying defects in graphene via Raman spectroscopy at different excitation energies,” *Nano Lett.*, vol. 11, no. 8, pp. 3190–3196, 2011.
- [6] L. G. Cançado, A. Jorio, and M. A. Pimenta, “Measuring the absolute Raman cross section of nanographites as a function of laser energy and crystallite size,” *Phys. Rev. B*, vol. 76, no. 6, pp. 1–7, 2007.
- [7] F. Tuinstra and J. L. Koenig, “Raman Spectrum of Graphite,” *J. Chem. Phys.*, vol. 53, p. 1126, 1970.
- [8] P. Delhaes, *Carbon-based Solids and Materials*. John Wiley & Sons, Ltd, 2011.
- [9] R. Brunetto, T. Pino, E. Dartois, A. T. Cao, L. D’Hendecourt, G. Strazzulla, and P. Bréchnignac, “Comparison of the Raman spectra of ion irradiated soot and collected extraterrestrial carbon,” *Icarus*, vol. 200, no. 1, pp. 323–337, 2009.
- [10] C. Casiraghi, A. C. Ferrari, and J. Robertson, “Raman spectroscopy of hydrogenated amorphous carbons,” *Phys. Rev. B*, vol. 72, no. 8, p. 85401, 2005.
- [11] J. D. Lorentzen, S. Guha, J. Menéndez, P. Giannozzi, and S. Baroni, “Raman cross section for the pentagonal-pinch mode in buckminsterfullerene C<sub>60</sub>,” *Chem. Phys. Lett.*, vol. 270, no. 1–2, pp. 129–134, 1997.
- [12] R. L. Aggarwal, L. W. Farrar, S. K. Saikin, X. Andrade, A. Aspuru-guzik, and D. L. Polla, “Measurement of the absolute Raman cross section of the optical phonons in type Ia natural diamond,” *Solid State Commun.*, vol. 152, no. 3, pp. 204–209, 2012.
- [13] J. E. Bohn, P. G. Etchegoin, E. C. L. Ru, R. Xiang, S. Chiashi, and S. Maruyama, “Estimating the Raman Cross Sections of Single Carbon Nanotubes,” *ACS Nano*, vol. 4, no. 6, pp. 3466–3470, 2010.
- [14] M. Fryling, J. C. Frank, and L. R. McCreery, “Intensity calibration and sensitivity comparisons for CCD/Raman spectrometers,” *Appl. Spectrosc.*, vol. 47, no. 12, pp. 1965–1974, 1993.

- [15] R. L. McCreery, *Photometric Standards for Raman Spectroscopy*. John Wiley & Sons, Ltd, 2006.
- [16] H. W. Schrotter and H. W. Klackner, *Raman scattering cross sections in gases and liquids*. Springer-Verlag Berlin Heidelberg, 1979.
- [17] L. G. Rojas, A. R. Peraza, and F. Ruetter, "Aging Oxidation Reactions on Atmospheric Black Carbon by OH Radicals . A Theoretical Modeling Study Aging Oxidation Reactions on Atmospheric Black Carbon by OH Radicals . A Theoretical Modeling Study," *J. Phys. Chem.*, vol. 119, no. 52, pp. 13038–13047, 2015.
- [18] A. Bray, R. Chapman, and T. Plakhotnik, "Accurate measurements of the Raman scattering coefficient and the depolarization ratio in liquid water," *Appl. Opt.*, vol. 52, no. 11, pp. 2503–2510, 2013.
- [19] F.-X. Yon, J.; Bescond, A.; Ouf, "A simple semi-empirical model for effective density measurements of fractal aggregates," *J. Aerosol Sci.*, vol. 87, pp. 28–37, 2015.
- [20] A. C. Ferrari and J. Robertson, "Resonant Raman spectroscopy of disordered, amorphous, and diamondlike carbon," *Phys. Rev. B*, vol. 64, no. 7, p. 75414, 2001.
- [21] Y. Kato and H. Takuma, "Absolute Measurement of Raman-Scattering Cross Sections of Liquids," *J. Opt. Soc. Am.*, vol. 61, no. 3, p. 347, 1971.
- [22] M. O. Trulson and R. A. Mathies, "Raman cross section measurements in the visible and ultraviolet using an integrating cavity: Application to benzene , cyclohexane , and cacodylate Raman cross section measurements In the visible and ultraviolet using an Integrating cavity : Application t," *J. Chem. Phys.*, vol. 84, p. 2060, 1986.
- [23] P. Klar, E. Lidorikis, A. Eckmann, I. A. Verzhbitskiy, A. C. Ferrari, and C. Casiraghi, "Raman scattering efficiency of graphene," *Phys. Rev. B - Condens. Matter Mater. Phys.*, vol. 87, no. 20, pp. 1–12, 2013.
- [24] N. Wada and S. A. Solin, "Raman efficiency measurements of graphite," *Phys. B+C*, vol. 105, no. 1–3, pp. 353–356, 1981.
- [25] K. Sinha and J. Menendez, "First-and second-order resonant Raman scattering in graphite," *Phys. Rev. B*, vol. 41, no. 15, pp. 845–847, 1990.
- [26] A. K. McQuillan, W. R. L. Clements, and B. P. Stoicheff, "Stimulated Raman emission in diamond: spectrum, gain, and angular distribution of intensity," *Phys. Rev. A*, vol. 1, no. 3, p. 628, 1970.
- [27] P. Mallet-Ladeira, P. Puech, C. Toulouse, M. Cazayous, N. Ratel-Ramond, P. Weisbecker, G. L. Vignoles, and M. Monthieux, "A Raman study to obtain crystallite size of carbon materials: A better alternative to the Tuinstra-Koenig law," *Carbon N. Y.*, vol. 80, no. 1, pp. 629–639, 2014.
- [28] M. A. Tamor and C. H. Wu, "Graphitic network models of 'diamondlike' carbon," *J. Appl. Phys.*, vol. 67, no. 2, pp. 1007–1012, 1990.

# Chapter 4

## *Results II:*

# Raman scattering: spectral analysis and structural information of deposited soot

## Contents

---

<b>4.1. Introduction .....</b>	<b>71</b>
<b>4.2. Experiment .....</b>	<b>74</b>
4.2.1. Soot production .....	74
4.2.2. Raman and HRTEM measurements .....	75
<b>4.3. Results and analysis.....</b>	<b>75</b>
4.3.1. Raman spectra of soot produced by various flame conditions.....	75
4.3.2. Spectral analysis by curve fitting .....	77
<b>4.4. Discussion of soot structural information .....</b>	<b>90</b>
4.4.1. Spectral analysis.....	90
4.4.2. Indices of aromatization .....	94
4.4.3. The second order .....	99
4.4.4. The sp hybridized bond.....	102
<b>4.5. Conclusions .....</b>	<b>102</b>
<b>References .....</b>	<b>104</b>

---

During flaming process, soot goes through different structures even at the molecular scale. In this chapter, Raman spectra of soot, collected under several flame conditions at different flame heights, are analyzed in regard to their structural properties. On one hand, Raman spectral characteristics of our samples reveal a dominant disordered polyaromatic structure in the particles via the  $D_1$ ,  $D_2$  and  $G$  bands. On the other hand, these spectra show some amorphous carbon properties via the presence of  $D_3$  band at  $\sim 1500 \text{ cm}^{-1}$  and polyene-like structures via the assignment of  $D_4$  band at  $\sim 1200 \text{ cm}^{-1}$ . Another interesting point is the existence of sp hybridized structure in some soot samples, showing a rich diversity of carbon hybridization within soot. In our study, several soot samples have the  $I_{D1}/I_G$  ratio much higher than 2, for which relations that can be found in the literature between  $I_{D1}/I_G$  and  $L_a$  are no more available. Other materials showing very intense  $D$  band are defected graphene [1]. Alternative analyses of this structural index, the polyaromatic unit mean size, are explored.

## 4.1. Introduction

*Soot* is any black, blackish or brown aggregate which contains polyaromatic layers and is generated by the incomplete combustion [2]. The polyaromatic layers are a characteristic of soot, thus soot particles can be easily distinguished from other carbonaceous aerosol particles which lack this distinctive feature [3]. Soot exists in the atmosphere as clusters or chains aggregated by tens to hundreds of spherules. Each spherule is called a primary soot particle whose size in diameter mostly lies between 10 to 30 nm comprising crystalline and amorphous domains [4]. The crystalline domains typically consist of 3 – 4 stacked polyaromatic layers, with average lateral extensions ( $L_a$ ) of up to 3 nm and interlayer distances of about  $3.55 \text{ \AA}$  [3,4]. The amorphous domains contain isolated cross-linked polyaromatic units and other organic and inorganic components adsorbed or embedded (PAHs, sulfate, aliphatics, metal oxides, etc.). The ratio between these domains depends on the initial fuels, burning condition, pyrolysis process, etc. The kinetics of soot formation was detailed in chapter 1.

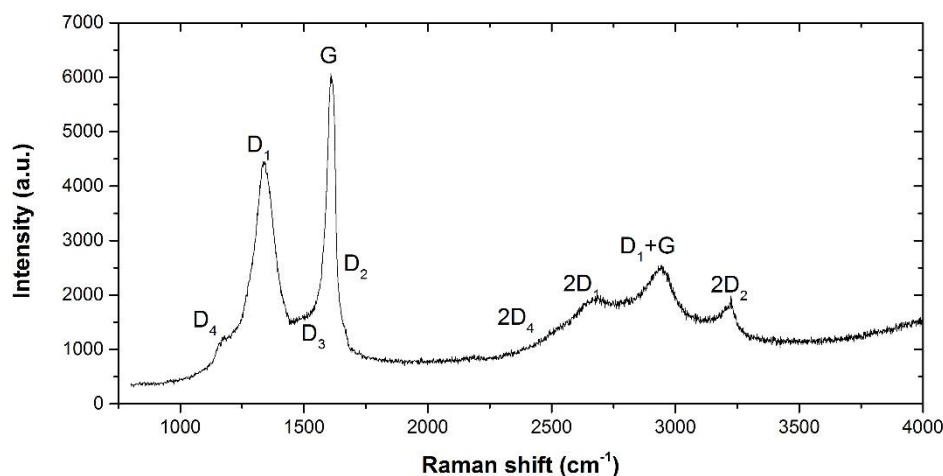


Fig. 4. 1. Raman spectrum of flame soot

For highly disordered materials such as soot, Raman spectroscopy is considered as a powerful tool in investigation of the vibrational properties because it is sensitive not only to crystal structures but also to molecular structures [4]. Fig. 4.1 shows the first and second orders in typical Raman spectrum of soot. From various types of industrial soot, diesel soot and flame soot that were studied in literature [4], [6], [7], we can summarize the general characterization in Raman spectra of soot excited by visible wavelength.

The most prominent features in the first order of soot Raman spectra are the so-called *D* and *G* bands, which lie at around 1350 and 1590  $\text{cm}^{-1}$  respectively. The detailed analysis of *D* and *G* bands reveals the presence of several bands. It was thoroughly presented by Sadezky et al. (2005) and their nomenclature is used thereafter, for instance the *D* band is called *D*<sub>1</sub> after detailed spectral decomposition to take into account the other defect induced bands. It should be recalled here that either a solid-state physics [8], [9] or a molecular approach [9], [10] are used to discuss these modes. For disordered material like soot with no long-range order, the molecular approach is more suitable. However for comparison, available interpretations in the literature or historical purpose, we used both descriptions.

The *G* peak, centered at 1590  $\text{cm}^{-1}$ , was originally assigned to an ideal graphitic lattice vibration mode with  $E_{2g}$  symmetry in the crystalline structure of graphite [11]. This mode occurs at all  $\text{sp}^2$  pairs and does not require the presence of sixfold rings [8]. If we see the *G* band in the Raman spectra, we can say that the sample contains  $\text{sp}^2$  carbon networks and these will dominate the Raman spectra because of resonance effects [12]. The *D*<sub>1</sub> peak appears at 1350  $\text{cm}^{-1}$  and corresponds to a breathing mode of  $A_{1g}$  in a graphitic lattice vibration. This mode is forbidden in perfect lattice and only becomes active in the presence of defects. Its intensity is strictly connected with the presence of sixfold aromatic rings [8]. Another first order band accounting for structural disorder is the *D*<sub>2</sub> peak at  $\sim 1620 \text{ cm}^{-1}$  which can be observed as a shoulder of the *G* band. The frequency of *D*<sub>1</sub> and *D*<sub>2</sub> modes shift to higher energy with increasing excitation energy [4], [13] and these two peaks are defect-induced Raman features. There is also a contribution of very broad *D*<sub>3</sub> peak at  $\sim 1500 \text{ cm}^{-1}$  originating from the amorphous carbon fraction of soot ( $\text{sp}^2$  fraction of the amorphous network). In addition, the *D*<sub>1</sub> band may exhibit a shoulder peak at  $\sim 1200 \text{ cm}^{-1}$  which we label as *D*<sub>4</sub>. Dippel and Heintzenberg proposed tentatively that it could come from  $\text{sp}^2 - \text{sp}^3$  bond or C–C and C=C stretching vibrations of polyene-like structures [14].

Raman spectra of soot also contain the second order bands in the range of about 2300 to 3300  $\text{cm}^{-1}$ , in which two pronounced peaks at  $\sim 2700$  and  $2900 \text{ cm}^{-1}$  have been assigned to the  $2D_1$  overtone and  $D_1+G$  combination bands. The  $2D_1$  mode is an overtone of the *D*<sub>1</sub> peak where the electron is backscattered by a second phonon instead of a defect [13]. This peak exists even when no *D*<sub>1</sub> peak is present [8], i.e. without any kind of disorder as it involves ring breathing.  $D_1+G$  peak is a combination of the *D*<sub>1</sub> and *G* modes. There are also the first overtone of the *D*<sub>2</sub> and *D*<sub>4</sub> modes at 3240 and 2450  $\text{cm}^{-1}$  which are named  $2D_2$  and  $2D_4$  respectively.



Besides of using Raman spectroscopy to identify vibrational properties of carbonaceous materials in general and of soot in particular, it is also an experimental technique to determine the defect quantity in these materials.

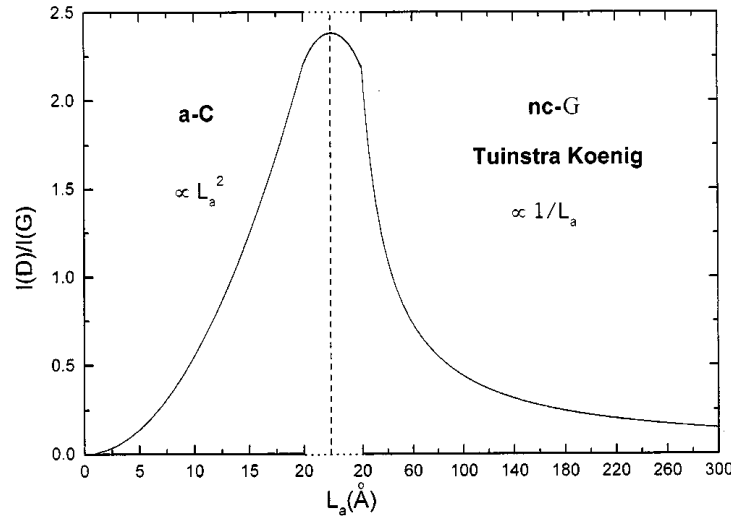


Fig. 4. 2. Variation of the  $I_D/I_G$  ratio with  $L_a$  [8].

In 1970, Tuinstra and Koenig reported an empirical relationship (called TK relationship) between the average crystallite size obtained from X-ray diffraction and the intensity ratio of the two major Raman bands ( $I_D/I_G$ ). The crystallite size can be viewed as the average lateral extension ( $L_a$ ) of the polyaromatic units including the isolated ones or the average interdefects distances in defected graphite or graphene. Knight and White took the dependence on laser wavelength  $\lambda_L$  into account and postulated the following correlation between  $L_a$  and the ratio  $I_D/I_G$ ,

$$\frac{I_D}{I_G} = \frac{C(\lambda_L)}{L_a} \quad (4.1)$$

where  $C(\lambda_L)$  is the wavelength dependent pre-factor [11] and  $C(\lambda_L) \sim 2.4 \times 10^{-10} \lambda^4$  [15]. Lespade et al. provided the first theoretical explanation of this relationship based on the finite size of the crystallites [16]. However, this linear relationship between  $1/L_a$  and the  $I_D/I_G$  ratio breaks down for crystallite sizes below  $\sim 2$  nm because for small  $L_a$  the D band strength, being proportional to the probability of finding a sixfold aromatic ring in the carbon cluster, is proportional to the  $sp^2$  cluster area and vanishes with the number of  $sp^2$  available carbon [8]. For crystallite sizes below 2 nm, Ferrari and Robertson proposed that

$$\frac{I_D}{I_G} = C'(\lambda_L) L_a^2 \quad (4.2)$$

where  $C'(\lambda_L)$  represents a wavelength dependent pre-factor. Imposing continuity between (4.1) and (4.2), Ferrari & Robertson found  $C'(514 \text{ nm}) \approx 0.0055$  [17]. Overall, the schematic evolution of the intensity ratio of D and G bands in Raman spectra of carbon materials as a function of the crystalline size is sketched in Fig. 4. 2, in which a clear increase at small  $L_a$  with a maximum at  $L_a \approx 2 \text{ nm}$  was inferred, followed by a continuous decrease of  $I_D/I_G$ . Note that there is an ambiguity concerning  $I_D/I_G$  ratio: should it be the ratio of the peak heights

or peak areas. The difference is not so important for disorder graphite with  $L_a \gg 2$  nm when the peak widths are similar. However, for nearly or amorphous carbon the broadening of the  $D$  peak is correlated to a distribution of clusters with different orders and dimensions, leading to more Gaussian like peaks and area are more often used. The information about the less distorted aromatic rings is in the intensity maximum [8]. Another point is that  $L_a$  in our soot is defined as the average size of polyaromatic unit.

As mentioned above, Raman spectroscopy has been used popularly in study of carbonaceous materials during several decades. In the present study, besides of Raman spectroscopy, we also use far ultraviolet to mid infrared (FUV-IR) spectroscopy and high resolution transmission electronic microscope (HRTEM) images as efficient tools to discriminate structural information of soot produced by various premixed ethylene flames at low pressure using Nanograins reactor at ISMO as well as the structural evolution of soot films along the flame or the height above the burner (HAB). Although the results of FUV-IR spectroscopy are not presented in detail in this dissertation, they will be added to the appendix and be used to supply and compare to the obtained Raman spectra results.

This chapter is organized as follows. In section 4.2 we briefly describe the experimental setups and sample preparation. In section 4.3 we present the results of spectral analysis. Soot structural information will be discussed in section 4.4 and we present in section 4.5 our conclusion.

## 4.2. Experiment

### 4.2.1. Soot production

Soot samples were produced in ethylene premixed flames using the Nanograins reactor in ISMO. The detailed information of sampling conditions was presented in section 2.2 of chapter 2, particularly in table 2.1. Soot was prepared under varying flame conditions and HAB ranging from 18 to 50 mm. We use the following C/O ratios and pressures: 0.82 (60 mbar), 1 (28 mbar), 1.05 (40 mbar), 1.3 (40 mbar). The soot was deposited on NaCl / KBr / MgF<sub>2</sub> substrate windows. The deposition time of the films varied from few seconds to about 20 minutes. All these parameters gave combustion regimes that could make a wide variety of soot.

Our flame conditions were chosen based on the soot characteristics and the convenience of the sampling process. The aim of the sampling step was to produce various deposited soot whose thickness could vary from thin to thick depending on each type of measurements. The flame C/O = 1.3 at 40 mbars is a special burning condition, in which soot exhibit a strong aromatic hydrogenation. Their Raman spectra show a strong fluorescence contamination. The distinction between Raman and fluorescence signals was described in 16<sup>th</sup> page of chapter 1. Flame C/O = 1.05 at 40 mbars is a convenient condition which can sample both thin and thick deposited soot in a short time. The others just turn around the C/O=1.05 flame conditions.

### 4.2.2. Raman and HRTEM measurements

The first and second orders in Raman spectra of soot were acquired by a Renishaw inVia confocal Raman microspectrometer at the Laboratoire de Géologie de l'École Normale Supérieure (Paris, France). This instrument includes: a 514 nm Ar ion laser (150mW) and a 785 nm diode laser (300 mW); 1024 × 256 pixels CCD detector achieving a spectral resolution of 0.5 cm<sup>-1</sup> using an 1800 line/mm spectrographic grating; the sampling platform is a Leica microscope that we mostly used with a 50x objectives lens. This spectrometer is shown in Fig. 2.7 of chapter 2.

The conditions of measurement were: a continuous Ar (514 nm) laser beam was used as exciting radiation; the excitation laser power was set to 0.28 mW to avoid modification of the carbon structure due to laser-induced heating effects; laser beam had circular polarization and was focused to a ~ 1 μm spot; the Raman shift was measured from 400 to 4000 cm<sup>-1</sup> and acquisition time was 180 sec.

Some samples were deposited on amorphous carbon lacey covering a copper mesh, either directly by insertion of the grid in the molecular flow or by wet transfer in ethanol from the samples deposited on substrate for spectroscopic studies. Then their HRTEM images were acquired on a JEOL 2011 electron microscope operating at 200 kV using a LaB<sub>6</sub> filament.

## 4.3. Results and analysis

### 4.3.1. Raman spectra of soot produced by various flame conditions

Raman spectra of four selected soot samples are presented in Fig. 4. 3. All such spectra have a thing in common which is the presence of *D* and *G* bands located at 1350 and 1600 cm<sup>-1</sup> respectively in the first order and the broad second order spreading from 2200 to 3700 cm<sup>-1</sup>. However, they also exhibit many differences in shape of backgrounds, in the intensity ratio between *D* and *G* bands as well as FWHMs of peaks although their sampling distances are 30 mm. This point illustrates the wide variety of soot that can be produced by tuning the burning conditions.

The most observable difference between the four spectra is the presence (for C/O = 1.3) or the absence (for the others) of a fluorescence continuum and a shoulder peak on the *D<sub>I</sub>* band at ~ 1269 cm<sup>-1</sup>. The second remarkable point is the appearance of a minor peak observed at ~ 2150 cm<sup>-1</sup> for C/O = 1.05. This peak provides new information on soot structure, it has not been mentioned before in soot Raman spectra studies to our knowledge. To discriminate more soot structural properties, spectral analysis will be detailed in the following sections.

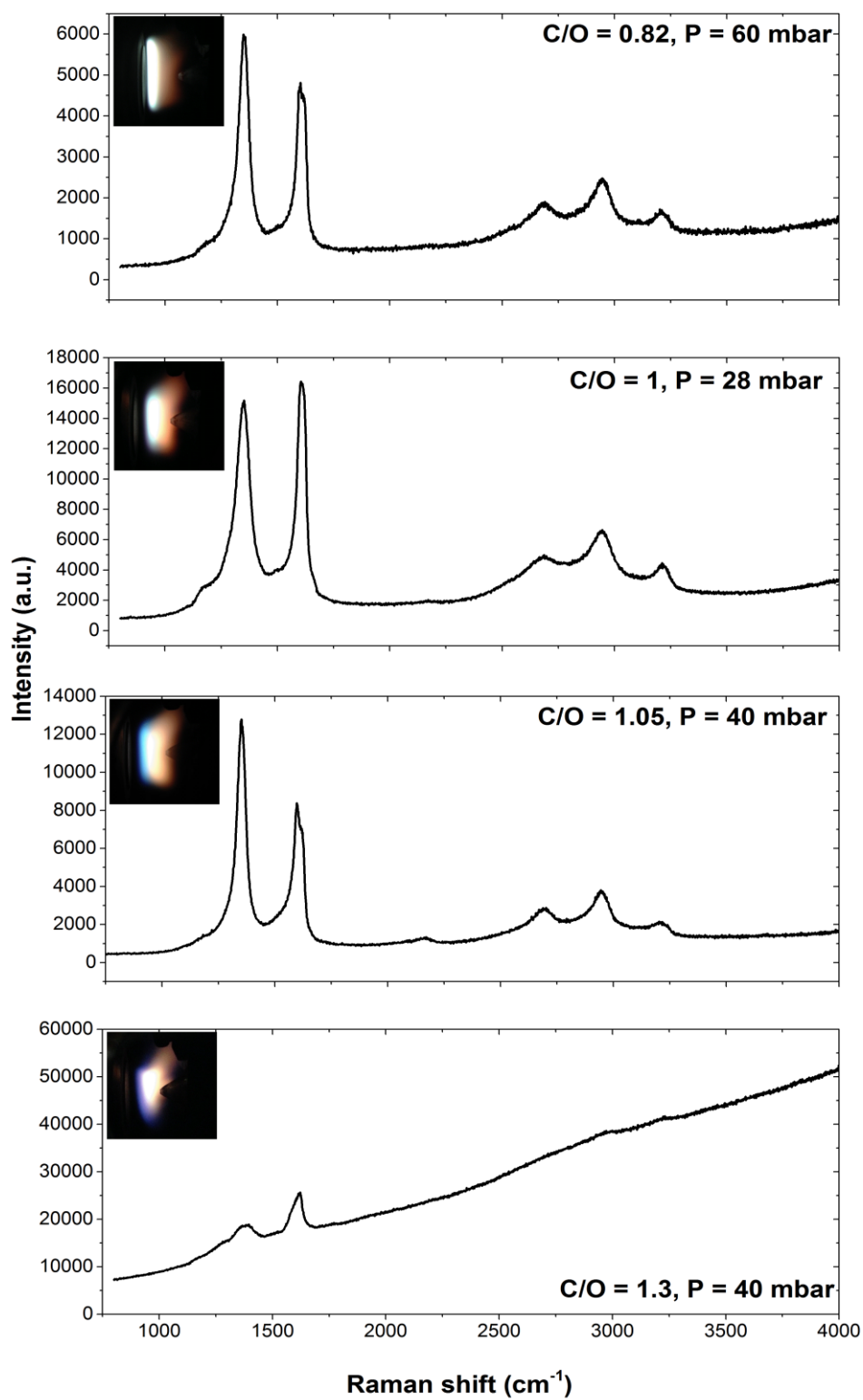


Fig. 4. 3. Raman spectra of soot produced by various flame conditions at HAB = 30 mm.

### 4.3.2. Spectral analysis by curve fitting

In order to determine spectral parameters, we used cftool toolbox of the software program Matlab R.2013a for spectral decomposition. The first order Raman band are successfully fitted by a combination of four Lorentzian ( $D_4$ ,  $D_1$ ,  $G$ ,  $D_2$ ) and one Gaussian ( $D_3$ ) peaks, as proposed by Sadezky et al. (2005). For soot produced by C/O = 1.3 flame, an extra  $D'_1$  peak is added at  $\sim 1269 \text{ cm}^{-1}$  to achieve a better fit with the experimental data [18]. The second order band was done using only a combination of four Lorentzian bands assigned to the  $2D_4$ ,  $2D_1$ ,  $D_1+G$  and  $2D_2$  peaks. These correspond to overtones and combinations of the first order band. In addition, a linear function is also considered as baseline. The goodness of the fit could be estimated by the value of the R-square. It is defined as the ratio of the sum of squares of the regression to the total sum of squares. This value can take any value between 0 and 1, with a value closer to 1 indicating that a greater fit is accounted for by the model. In our case, R-square values are always higher than 0.99 proving a good job.

In comparison, Raman spectra of our soot are quite similar to those of soot produced in Sadezky et al 2005, Brunetto et al 2009 and Carpentier et al 2012's references. From previous studies on soot produced with Nanograins [6], [7], we classified our soot samples into two types: "aromatic-rich soot" and "aliphatic-rich soot". They named "aromatic-rich soot" the samples with  $R_{\text{arom}} > 0.6$ , and "aliphatic-rich soot" the samples with  $R_{\text{arom}} < 0.3$ , in which the CH stretching mode integrated absorbance ratio in the mid-IR,  $R_{\text{arom}}$ , is equal to aromatic C-H / (aliphatic C-H + aromatic C-H). This value is obtained from infrared spectroscopy. However, it is important to note that  $\text{sp}^3$  carbon account for less than 1% of the total carbon (thus mostly  $\text{sp}^2$ ) in all soot samples [18]. But this very small amount was found to strongly influence soot structure. All information about IR spectra of our samples could be found in [Appendix A](#). In this chapter, we focus mainly on Raman spectroscopy and HRTEM information.

Let us turn now Raman to spectral information. Soot produced from C/O = 1.3 flame are aromatic-rich soot while soot produced from C/O = 0.82, 1 and 1.05 flames are aliphatic-rich soot or mixed. Regarding the C/O = 1.3 flame, the fluorescence continuum is probably due to a higher PAH content of these soot [19]. The appearance of  $D'_1$  in the  $D$  band could originate from the merging of sub-bands characteristic of the individual polyaromatic sub-units [20]. In this case, the substructure of the  $D$  band may suggest the presence of mostly polyaromatic units poorly linked together as the intimate soot structure [18], as suggested by the strong fluorescence. For each flame condition, soot particles were extracted at several HAB, in particular sampling distances of the C/O = 1.05 flame ranged from 14 to 50 mm. Fig. 4. 4, Fig. 4. 5, Fig. 4. 6, Fig. 4. 7 plot the first and second orders Raman spectral deconvolution for soot prepared with C/O = 0.82, 1, 1.05 and 1.3 flames. It should be noticed that the acquisition time and power excitation were the same but the quantity of soot on each substrates were different. For all investigated soot samples, spectral parameters were determined by curve fitting with the same set of bands. The complete data set with mean values of the first and second order band positions, FWHMs and peak areas are given in table 4.1. Their characteristic features will be outlined below.

-  $C/O = 0.82$ ,  $P = 60$  mbar

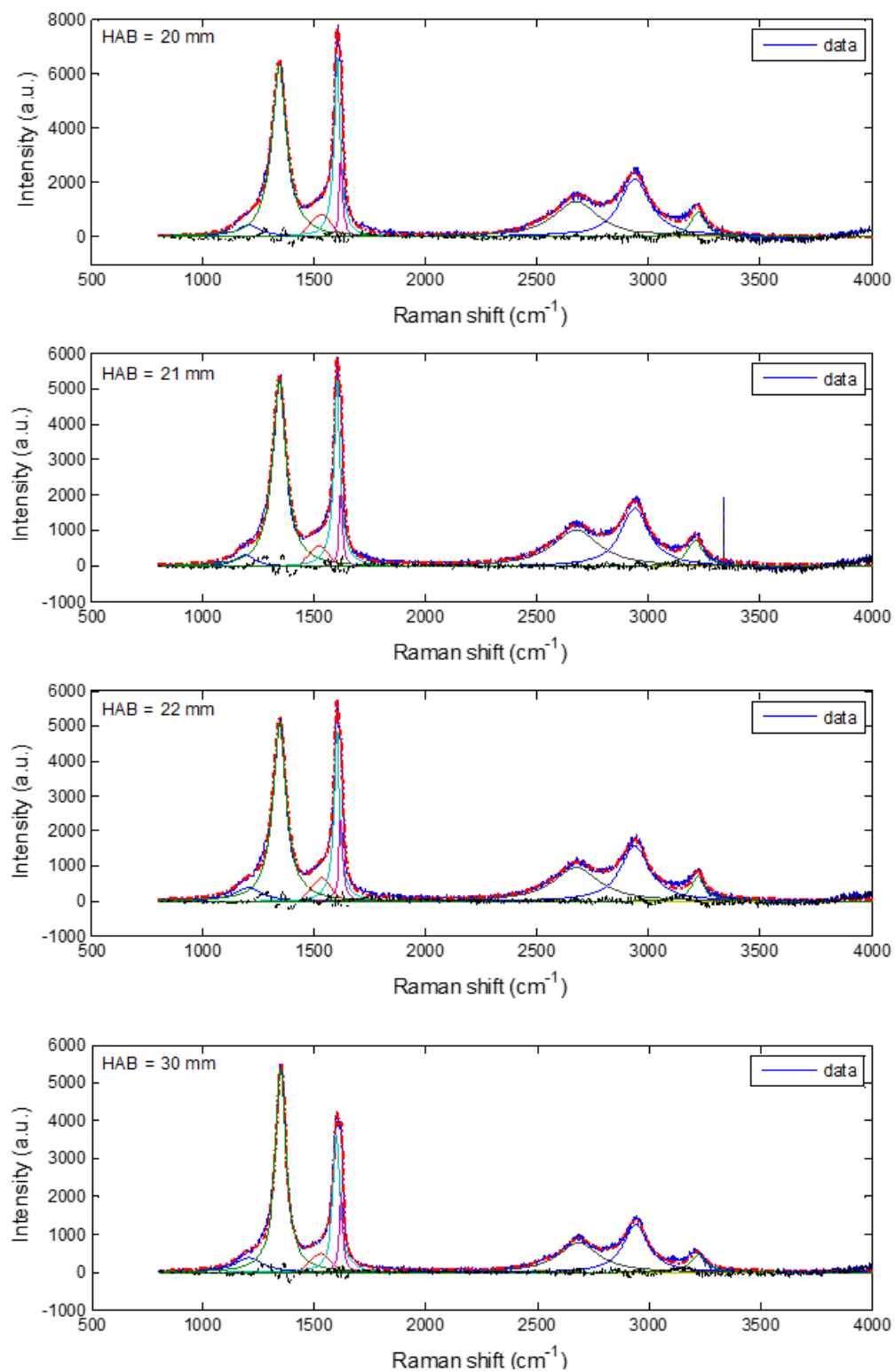
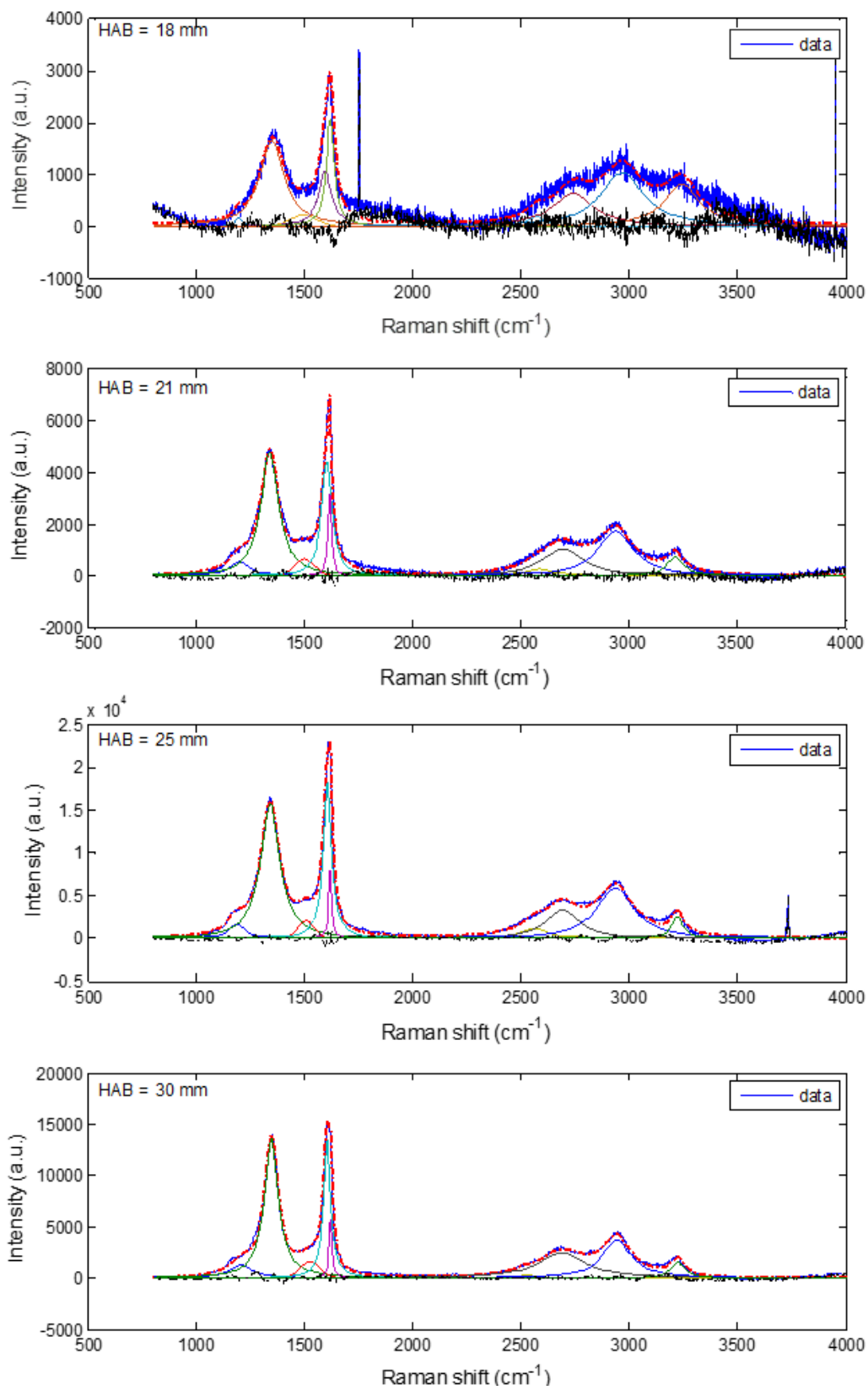


Fig. 4. 4. First and second order spectral deconvolution of soot produced by  $C/O = 0.82$  flame collected at varying HAB (in mm). Blue line is experimental data, red dot line is fit curve, black dot line is the difference between fit and real data.

-  $C/O = 1, P = 28 \text{ mbar}$



-  $C/O = 1$ ,  $P = 28$  mbar (continuous)

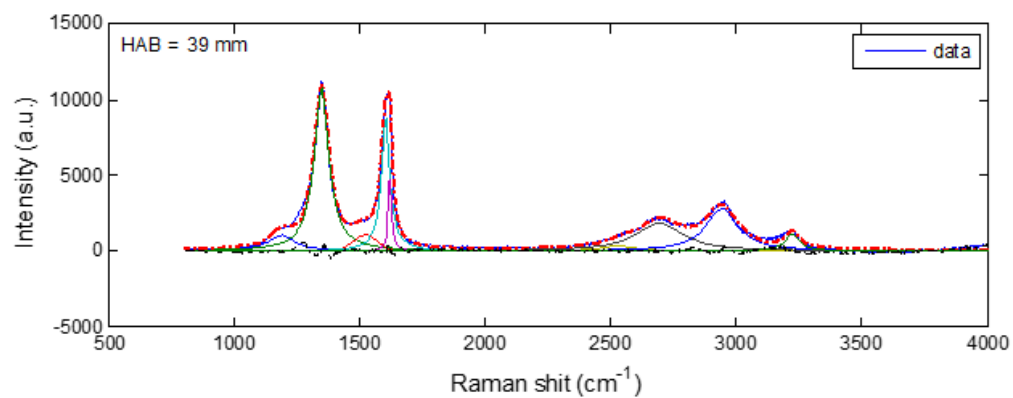
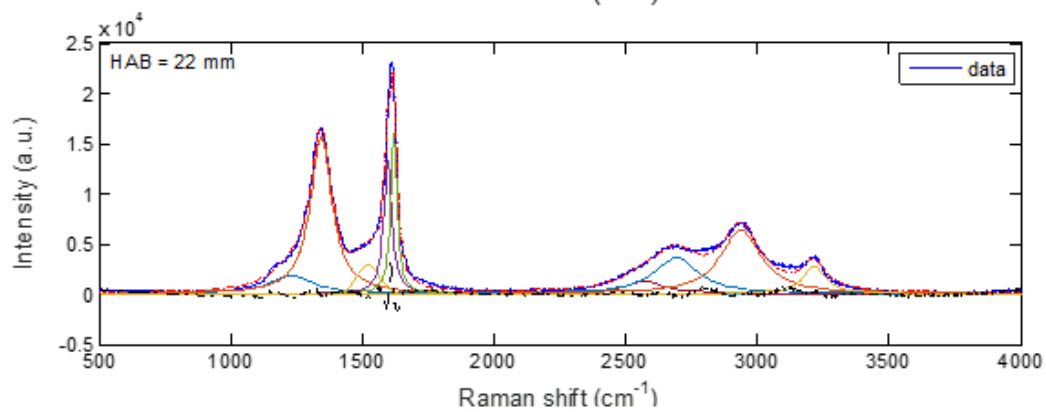
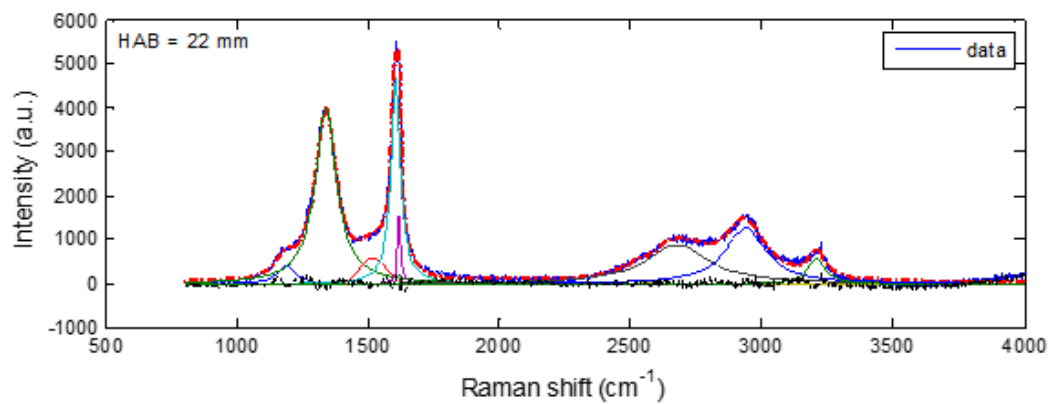
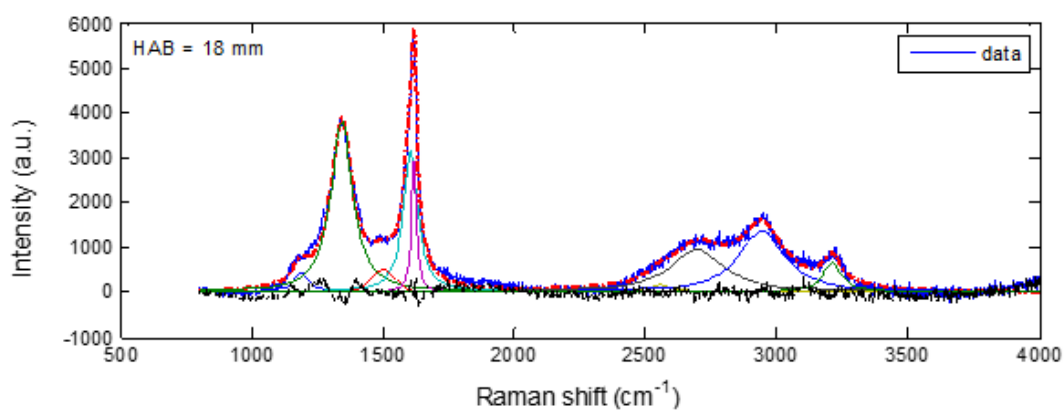
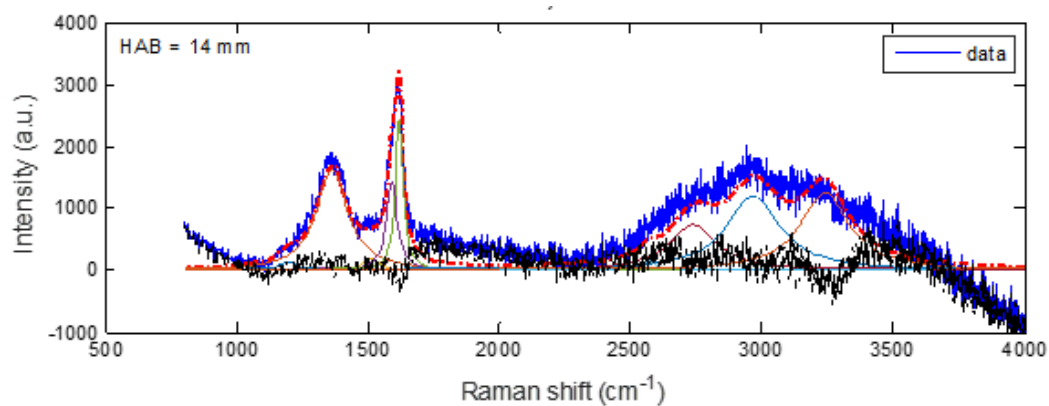


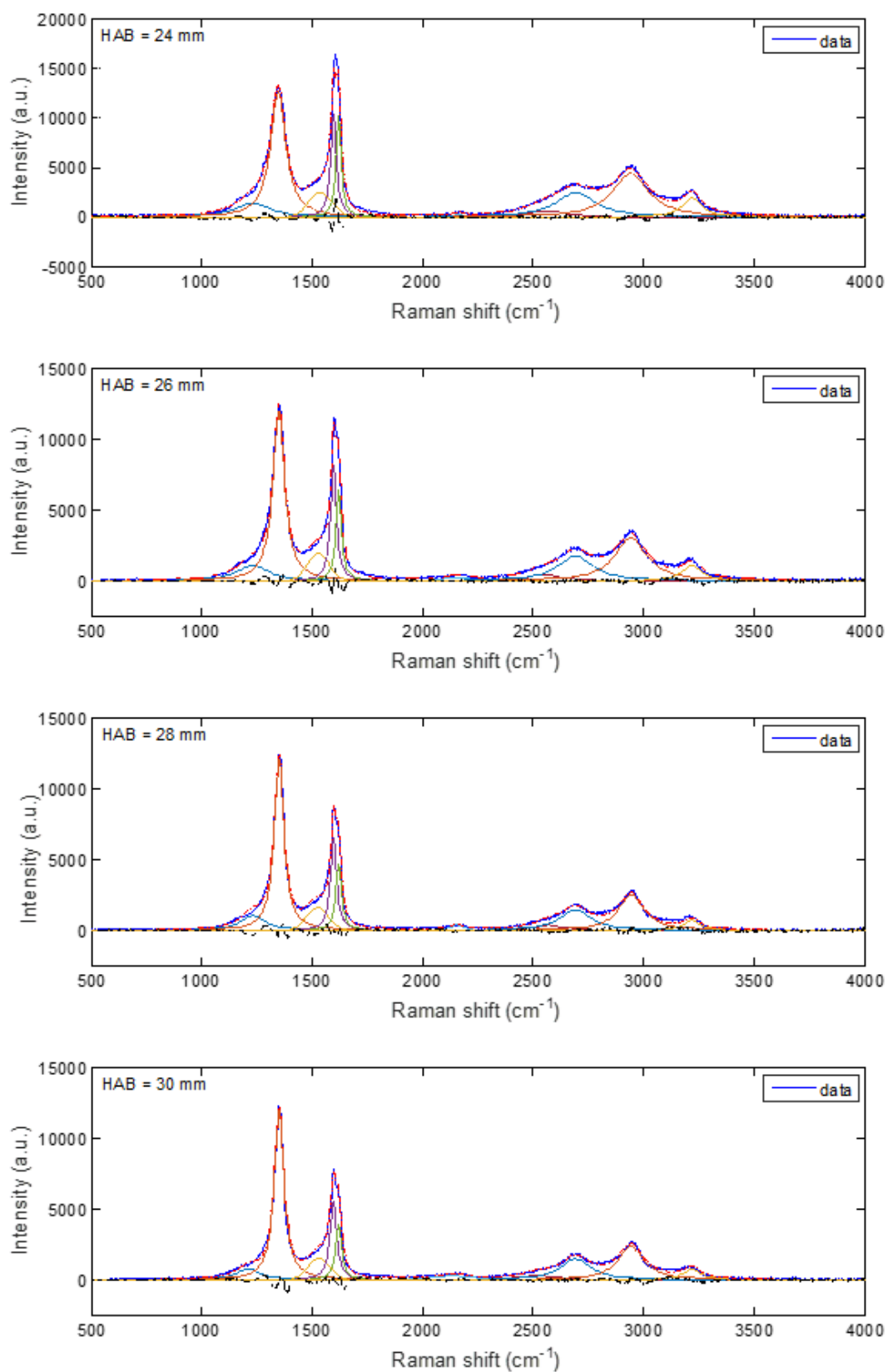
Fig. 4. 5. First and second order spectral deconvolution of soot produced by  $C/O = 1$  flame collected at varying HAB (in mm). Blue line is experimental data, red dot line is fit curve, black dot line is the difference between fit and real data.



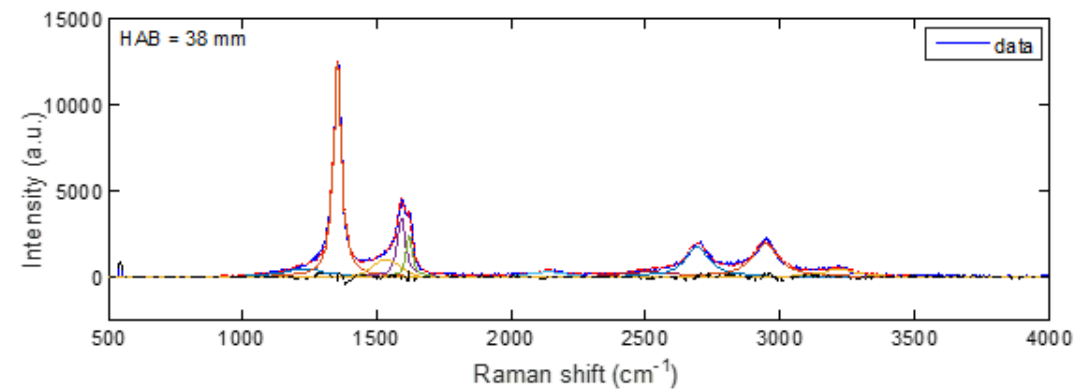
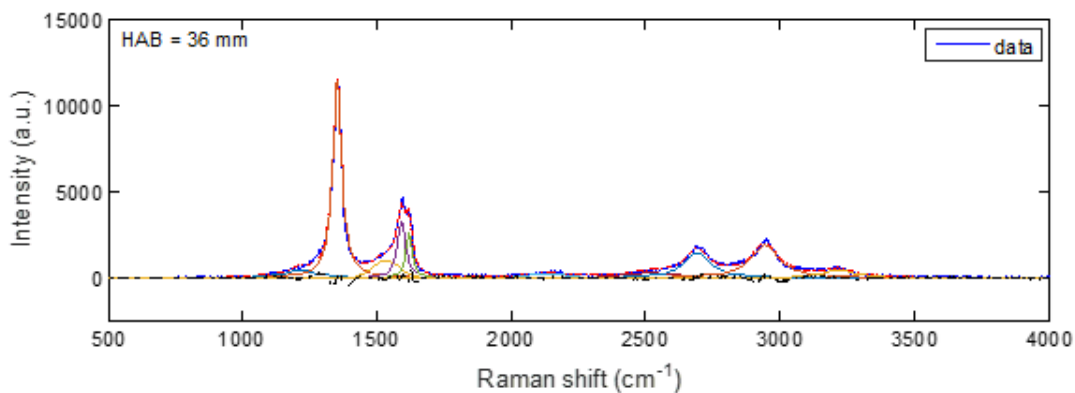
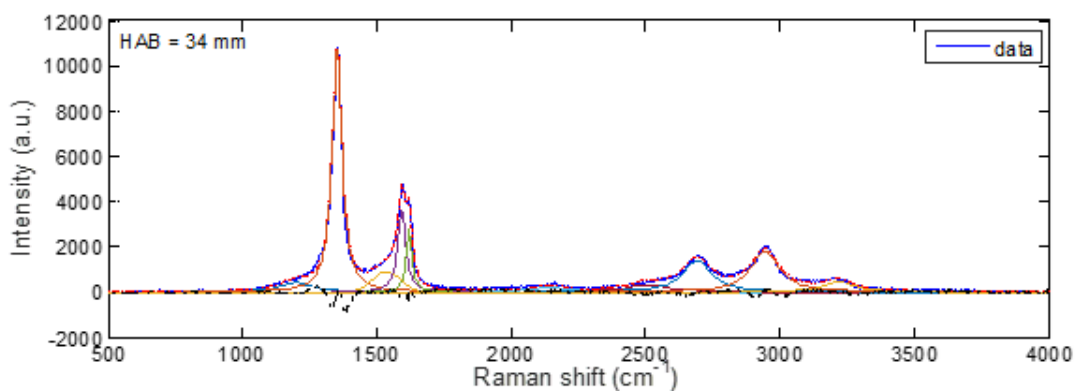
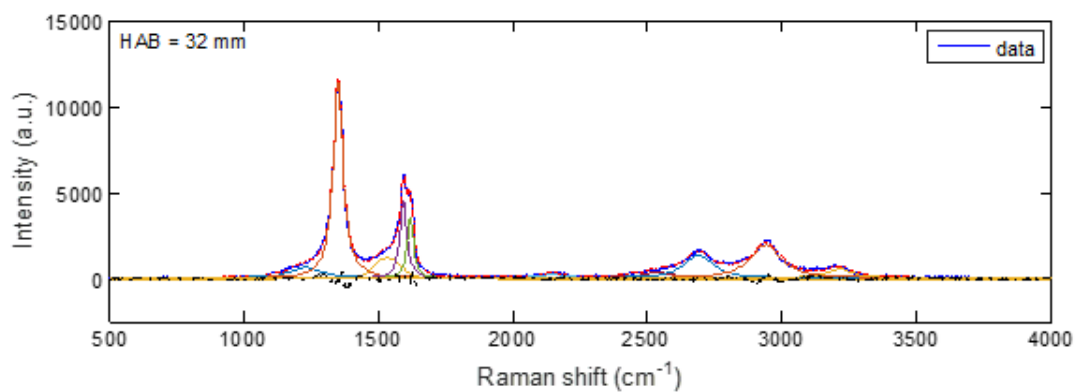
-  $C/O = 1.05$ ,  $P = 40$  mbar



-  $C/O = 1.05$ ,  $P = 40$  mbar (continuous)



-  $C/O = 1.05$ ,  $P = 40$  mbar (continuous)



-  $C/O = 1.05$ ,  $P = 40$  mbar (continuous)

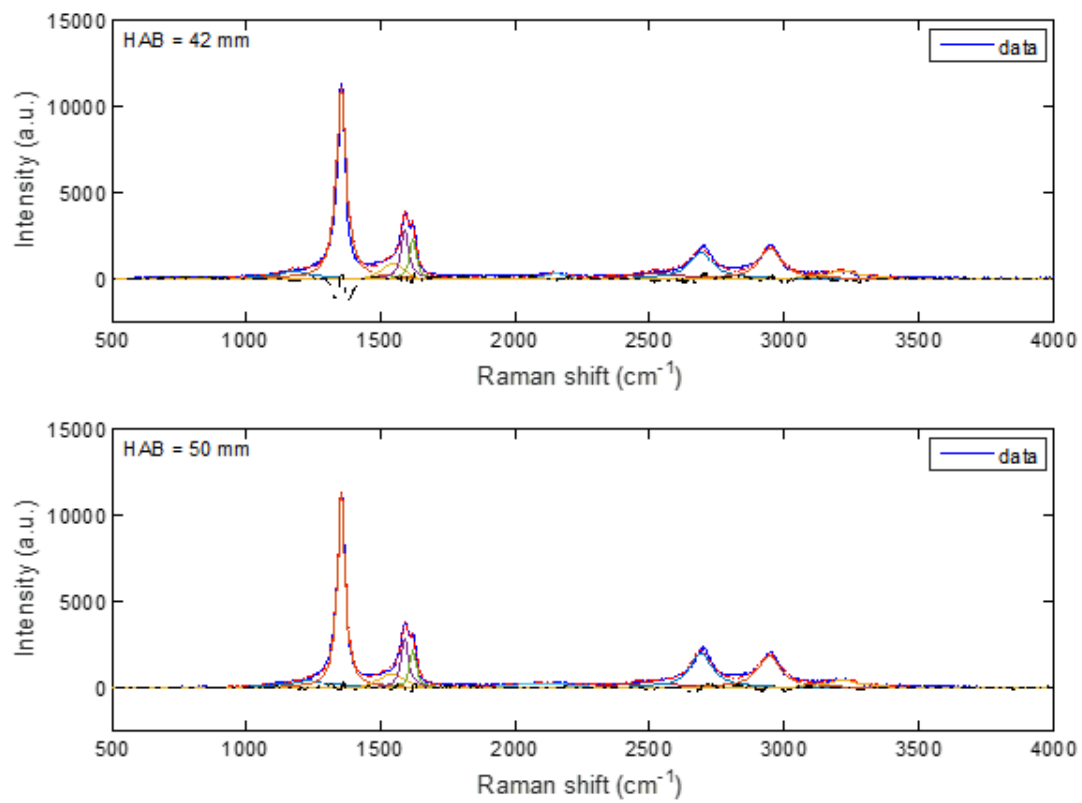
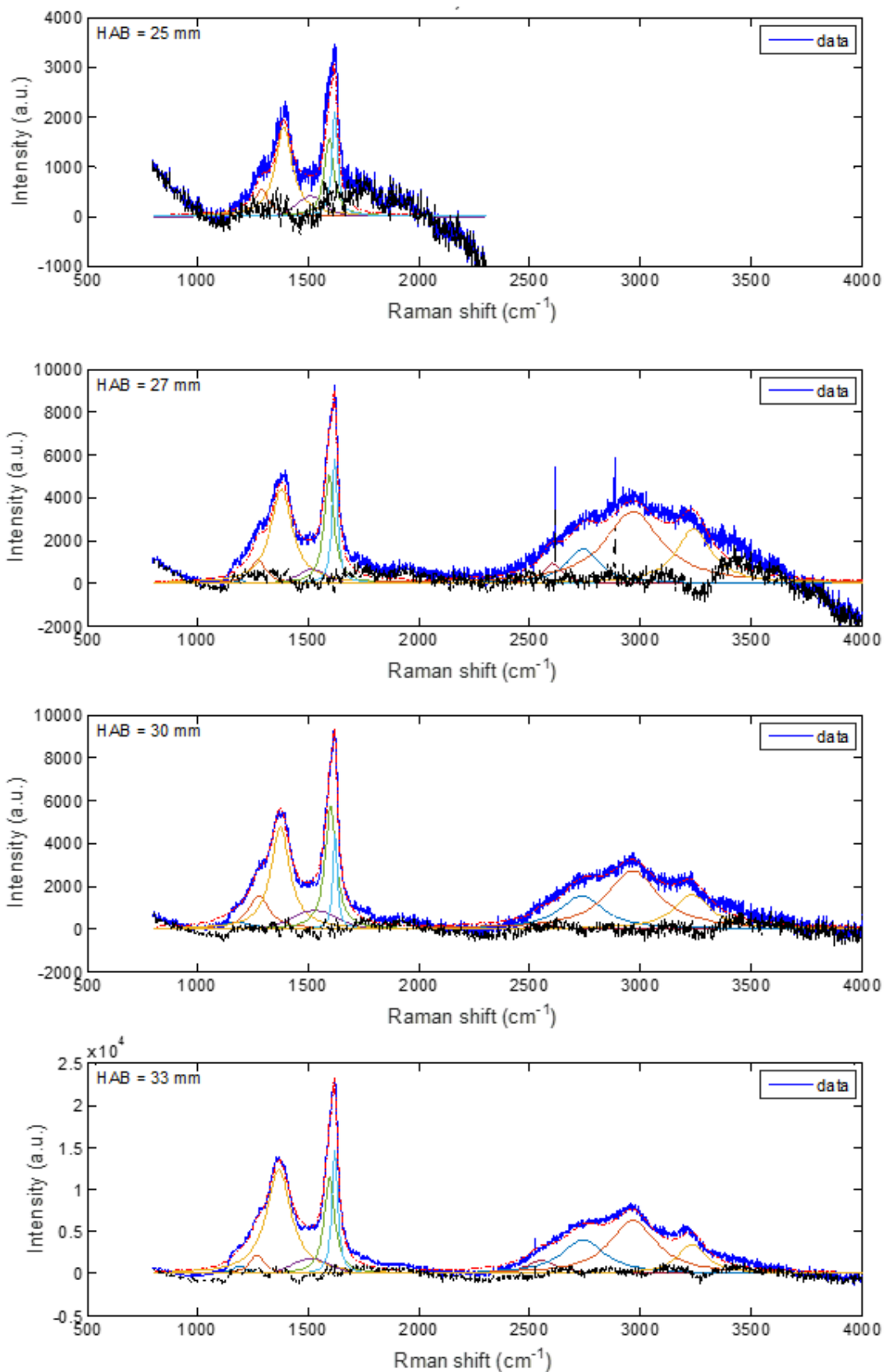


Fig. 4. 6. First and second order spectral deconvolution of soot produced by  $C/O = 1.05$  flame collected at varying HAB (in mm). Blue line is experimental data, red dot line is fit curve, black dot line is the difference between fit and real data.

-  $C/O = 1.3$ ,  $P = 40$  mbar



-  $C/O = 1.3$ ,  $P = 40$  mbar (continuous)

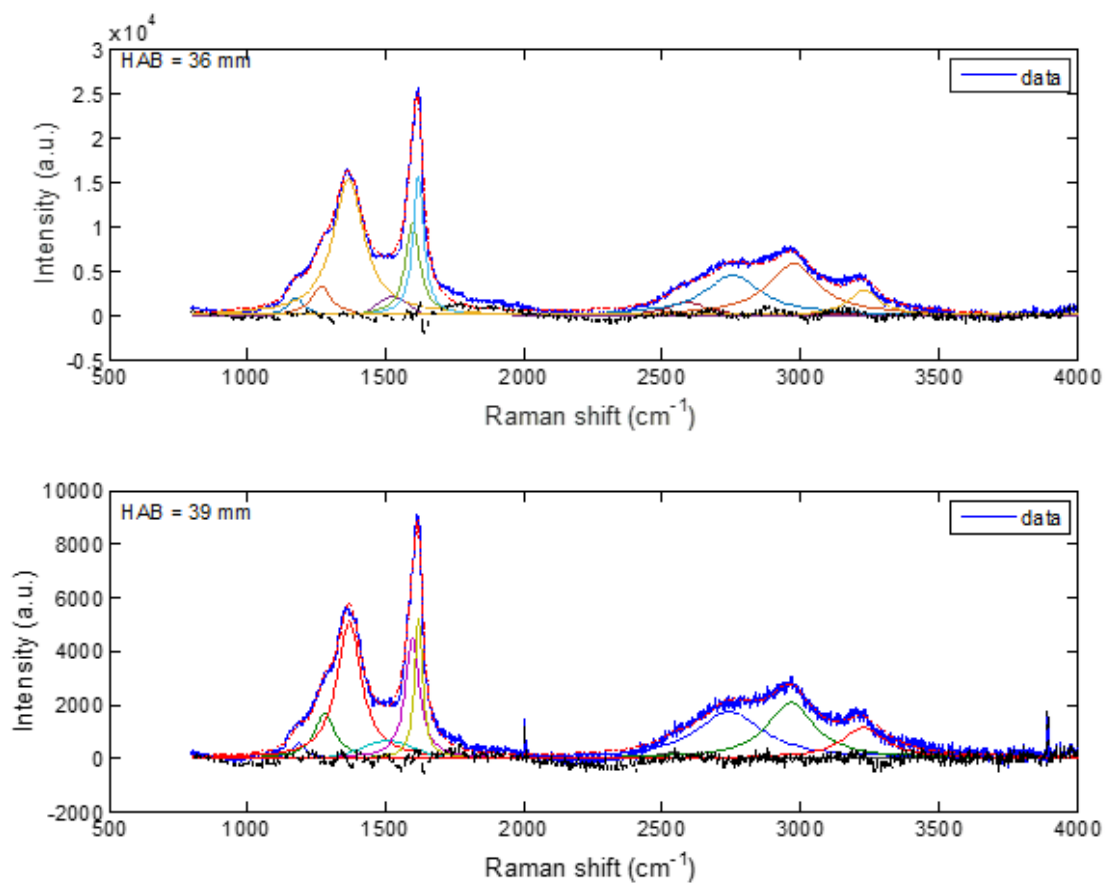


Fig. 4. 7. First and second order spectral deconvolution of soot produced by  $C/O = 1.3$  and collected at varying HAB (in mm). Blue line is experimental data, red dot line is fit curve, black dot line is the difference between fit and real data.

Table 4.1. Fit parameters of spectral decomposition, with  $d$  [mm],  $\omega$  [ $\text{cm}^{-1}$ ],  $\gamma$  [ $\text{cm}^{-1}$ ],  $A$  are HAB, peak position, FWHM and Area of peaks respectively. Note that the uncertainty of the peak position is lower than 10% of its peak width.

*The first order*

C/O	$d$	$\omega_{D_4}$	$\omega_{D'_4}$	$\omega_{D_1}$	$\omega_{D_3}$	$\omega_G$	$\omega_{D_2}$	$\gamma_{D_4}$	$\gamma_{D'_1}$	$\gamma_{D_1}$	$\gamma_{D_3}$	$\gamma_G$	$\gamma_{D_2}$	$A_{D_4}$	$A_{D'_1}$	$A_{D_1}$	$A_{D_3}$	$A_G$	$A_{D_2}$
0.82	20	1203		1344	1530	1603	1621	132		81	110	35	19	95493		807841	95727	365322	84368
	21	1188		1345	1520	1602	1621	103		75	100	36	18	50000		618653	59656	295400	58432
	22	1203		1346	1530	1602	1621	146		72	101	33	21	85470		583339	68965	251692	76839
	30	1203		1350	1529	1600	1621	150		58	108	38	19	86873		492542	54550	214086	62974
1	18	1195		1350	1493	1596	1619	43		139	139	69	39	10650		372900	41640	145700	119500
	21	1175		1342	1500	1604	1619	72		123	88	58	21	142884		2.199E6	115904	975553	284498
	25	1186		1342	1505	1605	1619	91		107	90	47	17	239909		2.644E6	199903	1.349E6	216101
	30	1203		1347	1524	1604	1621	126		80	110	40	16	250000		1.698E6	180838	849516	147295
	30	1200		1348	1520	1602	1621	105		72	100	36	19	50000		447114	41071	196368	60257
	39	1188		1348	1518	1603	1621	128		73	113	42	17	200000		1.229E6	123285	583736	126440
1.05	14	1195		1364	1512	1592	1620	84		141	80	48	34	17800		366300	14830	108700	131300
	18	1188		1344	1500	1606	1619	72		100	110	66	22	50000		598548	59074	328426	101441
	22	1230		1344	1522	1597	1620	198		99	98	37	28	557712		2.423E6	299361	767211	705190
	24	1230		1347	1537	1597	1620	200		83	129	31	27	438551		1.647E6	338840	495548	435467
	26	1230		1350	1528	1597	1620	171		64	117	32	30	300359		1.203E6	239788	408586	296834
	28	1230		1351	1524	1597	1620	136		53	117	33	31	226699		1.004E6	199426	341257	228602
	30	1211		1351	1529	1596	1620	134		54	117	37	33	165796		1.003E6	193615	316851	202968
	32	1230		1352	1534	1594	1620	156		44	116	31	28	155683		793486	151035	219221	153106
	34	1198		1353	1534	1593	1620	148		45	124	35	25	99872		754149	118755	201972	109858
	36	1223		1351	1534	1591	1620	189		44	98	35	28	101490		604130	115770	170880	95610
	38	1230		1354	1534	1592	1620	169		36	124	36	27	132624		692614	128810	192499	104300
	42	1176		1354	1541	1590	1620	148		44	102	32	28	99840		753980	92691	143708	106757
50	1230		1354	1540	1590	1620	193		35	126	31	29	115709		609615	98585	140852	98165	
1.3	25	1191	1289	1390	1509	1594	1620	50	77	93	148	51	30	2204	64750	260600	62530	127600	99510
	27	1191	1272	1379	1516	1594	1620	35	80	118	148	53	29	9041	141000	819000	102100	420500	260500
	30	1172	1277	1374	1525	1601	1621	164	113	102	236	60	23	79400	274800	763800	218400	535000	161300
	33	1189	1268	1367	1511	1596	1620	76	79	134	202	57	30	116000	275500	2.607E6	381300	1.028E6	696700
	36	1176	1268	1367	1524	1598	1619	67	86	135	122	62	45	204200	430000	3.251E6	273000	1.01E6	1.11E6
	39	1186	1280	1369	1505	1598	1620	57	89	106	223	62	34	50970	233700	850400	151200	438200	278200

Table 4.1. Fit parameters of spectral decomposition, with  $d$  [mm],  $\omega$  [ $\text{cm}^{-1}$ ],  $\gamma$  [ $\text{cm}^{-1}$ ],  $A$  are HAB, peak position, FWHM and Area of peaks respectively. Note that the uncertainty of the peak position is lower than 10% of its peak width. (*continuous*)

*The second order*

C/O	$d$	$\omega_{2D_4}$	$\omega_{2D_1}$	$\omega_{G+D_1}$	$\omega_{2D_2}$	$\gamma_{2D_4}$	$\gamma_{2D_1}$	$\gamma_{G+D_1}$	$\gamma_{2D_2}$	$A_{2D_4}$	$A_{2D_1}$	$A_{G+D_1}$	$A_{2D_2}$
0.82	20	2518	2671	2937	3220	87	242	165	81	12488	504895	555182	119460
	21	2516	2672	2936	3207	84	245	148	86	8204	391888	384201	97286
	22	2510	2672	2937	3220	91	239	155	74	7370	359438	378939	80149
	30	2516	2684	2941	3220	93	210	132	79	10996	259524	260878	55563
1	18	2563	2737	2965	3238	132	222	233	198	46530	236700	393200	254000
	21	2559	2690	2940	3220	160	226	155	110	132217	987646	993544	318336
	25	2556	2687	2933	3220	160	193	213	68	300000	1000000	2,00E+06	271291
	30	2520	2684	2940	3220	106	258	160	72	42727	1000000	936803	180619
	30	2516	2680	2939	3208	67	248	138	72	6204	274072	238499	52778
	39	2524	2689	2939	3220	160	220	153	70	80968	636304	661656	120191
1.05	14	2567	2737	2966	3240	69	220	248	228	15390	255000	467100	447800
	18	2555	2695	2942	3211	100	250	209	89	27738	371208	452501	89897
	22	2570	2690	2937	3215	197	202	183	104	361392	1,00E+06	2,00E+06	444502
	24	2557	2690	2939	3215	194	223	197	108	202348	856244	1,00E+06	334611
	26	2546	2688	2940	3215	190	195	174	108	132739	541943	830093	188082
	28	2566	2689	2942	3215	166	172	140	90	97281	395220	544959	98084
	30	2516	2690	2941	3215	190	167	144	102	100995	395711	532844	121770
	32	2535	2690	2941	3215	194	134	139	121	99568	282278	432278	106435
	34	2503	2689	2943	3215	196	132	127	138	99586	285508	360598	103291
	36	2516	2689	2942	3215	196	117	130	138	99528	272992	383782	100304
	38	2514	2690	2943	3215	196	106	117	139	99454	285955	353056	97930
	42	2521	2689	2946	3215	178	106	100	139	99779	258255	278979	99732
	50	2489	2690	2943	3215	200	97	102	150	97480	309820	296417	98229
1.3	25												
	27	2599	2739	2965	3239	99	177	313	191	142900	444200	2,00E+06	764100
	30	2555	2732	2963	3231	90	236	284	200	39510	578800	1,00E+06	502100
	33	2549	2739	2964	3231	159	236	252	160	396700	2,00E+06	3,00E+06	870900
	36	2585	2752	2972	3226	154	247	226	134	357600	2,00E+06	2,00E+06	585200
	39	2540	2740	2963	3224	115	292	208	195	44040	799300	680400	348400



The mean value of the  $G$  peak positions was observed from different types of soot ranging from 1590 to 1606  $\text{cm}^{-1}$ . Almost all  $G$  peak positions for the  $C/O=0.82$  and 1 flames are higher than 1602  $\text{cm}^{-1}$  while those for  $C/O=1.05$  and 1.3 are lower than 1597  $\text{cm}^{-1}$ . The mean values of the  $G$  peak FWHMs ranged from 31 to 69  $\text{cm}^{-1}$ . In these fit, the  $D_2$  band was systematically introduced, with a position at about 1620  $\text{cm}^{-1}$ , although poorly constraints apart for some HAB for the  $C/O=1.05$  flame where it could be seen clearly. The choice was to keep it for consistency and most gave a weaker  $D_2$  band than the  $G$  one. However, for few small HAB where the signal/noise was much worse of for the  $C/O = 1.3$  flame, the fitted  $D_2$  was rather strong. The mean values of the  $D_2$  peak FWHMs fluctuate from 16 to 39  $\text{cm}^{-1}$ . The  $A_{D_2}/A_G$  is variable from 0.1 to 1.1. It may thus introduce a dispersion of the values. Therefore, only when specified, the  $D_2$  band was mostly not considered in the fit except when it is clearly separated from the  $G$  band.

The  $D_1$  peak positions locate at 1342 to 1390  $\text{cm}^{-1}$  and their FWHMs are 53 to 141  $\text{cm}^{-1}$ . In particular, with  $C/O$  1.3 flame,  $D_1$  peak positions shift towards higher frequencies and their widths increase. For the different types of soot  $A_{D_1}/A_G$  is highly variable from 1.4 to 5.2.

The mean values of the  $D_3$  peak position range from 1493 to 1530  $\text{cm}^{-1}$  with the FWHMs are 80 to 236  $\text{cm}^{-1}$ . In addition,  $D_4$  peak position range from 1172 to 1230  $\text{cm}^{-1}$  and their FWHMs are 43 to 200  $\text{cm}^{-1}$ . The  $A_{D_3}/A_G$  and  $A_{D_4}/A_G$  vary in the ranges from 0.1 to 0.7 and from 0.02 to 0.7 respectively. For  $C/O$  1.3 flame, the mean values of  $D_1$  range from 1268 to 1289  $\text{cm}^{-1}$  and its FWHM are 77 to 113  $\text{cm}^{-1}$ .

In the second order,  $2D_1$  peak positions vary from 2732 to 2752  $\text{cm}^{-1}$  and its FWHMs are 97 to 292  $\text{cm}^{-1}$ . The  $2D_1$  band is an overtone of the  $D_1$  band. When the  $D_1$  area increases, the  $2D_1$  area is found to increase too. The mean values of  $D_1+G$  peak positions locate from 2936 to 2972  $\text{cm}^{-1}$  and their FWHMs vary over the range of 100 - 313  $\text{cm}^{-1}$ . For  $2D_2$  peaks, the former values change from 3215 to 3240  $\text{cm}^{-1}$  and the later values are 68 to 228  $\text{cm}^{-1}$ . Finally,  $2D_4$  peak positions vary from 2500 to 2599  $\text{cm}^{-1}$  and their FWHMs are 67 to 197  $\text{cm}^{-1}$ .

The appearance of C peak in  $C/O = 1.05$  flame range from 2131 to 2163  $\text{cm}^{-1}$  and their FWHMs are 63 to 198  $\text{cm}^{-1}$ . This peak indicates the existence of sp hybridization in form of polyynes. Taking a quick look in Fig. 4 in Sadezky (2005) and Fig. 1 in Brunetto (2009), in fact, this peak was recorded but it was not discussed.

Overall, the result clearly indicates that all five bands in the first order ( $G$ ,  $D_1$ ,  $D_2$ ,  $D_3$ ,  $D_4$ ) and four bands in the second order ( $2D_1$ ,  $D_1+G$ ,  $2D_2$ ,  $2D_4$ ) should be taken into account for a complete analysis and interpretation of soot Raman spectra in the range of 900 – 4000  $\text{cm}^{-1}$ . The recorded soot spectra were fitted successfully with a combination of eight Lorentzian shaped bands and only one Gaussian shaped band for  $D_3$  peak. At some samples, there is a contribution of sp hybridized bond which could be fitted by a Lorentzian peak. The detailed structural information will be analyzed in the next sections.

## 4.4. Discussion of soot structural information

### 4.4.1. Spectral analysis

#### 4.4.1.1. Raman spectral parameters from the first order

Our FWHM( $G$ ) values, varying from 30 to 70  $\text{cm}^{-1}$ , are larger than those of graphite in Sadezky's results, particularly  $G$  peak FWHMs of graphite bars are measured to be 20-22  $\text{cm}^{-1}$  and those of the highly-oriented pyrolytic graphite are 15-16  $\text{cm}^{-1}$ , the lower limit being a single Lorentzian band of 14  $\text{cm}^{-1}$  FWHM [4]. However, our FWHM( $G$ ) are much narrower than FWHMs of amorphous carbons (100-300  $\text{cm}^{-1}$ ) presented in Casiraghi's review (2005) [21]. Clearly the  $D$  and  $G$  bands remain narrow compared to amorphous carbon, indicating disordered carbons rather than true amorphous carbons although there is a clear appearance of the  $D_3$  peak.

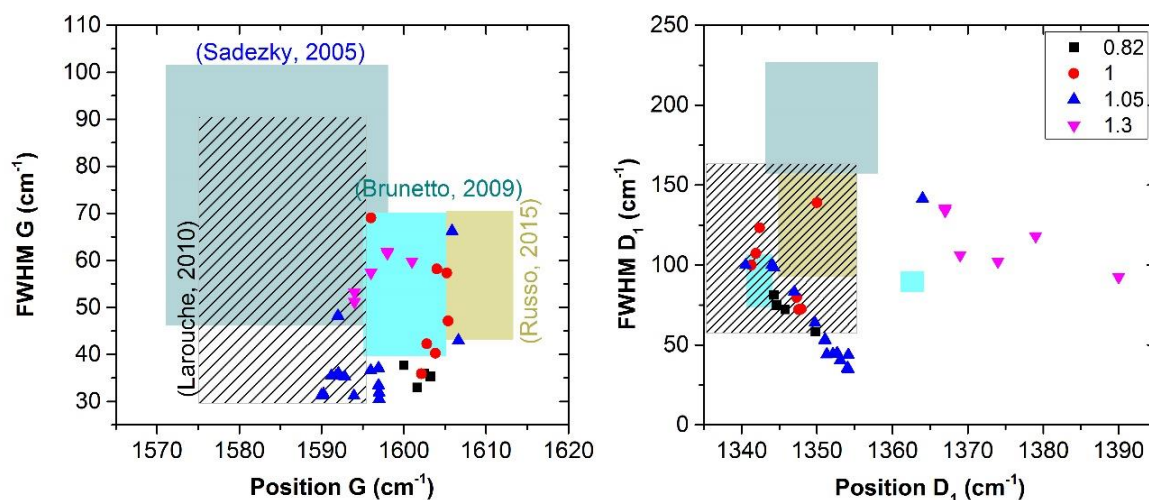


Fig. 4. 8. FWHMs and peak positions of  $D_1$  and  $G$  peaks of our spectra and a selection of soot data from the literature. Dark sky blue, vivid sky blue flaxen yellow and diagonal stripe areas correspond to references [3], [6], [17] and [18], respectively. Noted that these soot were produced at different sampling conditions.

The  $G$  peak positions reported for all soot samples are found well above the 1590  $\text{cm}^{-1}$  up to 1606  $\text{cm}^{-1}$  in Fig. 4. 8. The high position of  $G$  peak can be attributed to the presence of shorter  $\text{sp}^2$  C=C bonds featuring a possible contribution of olefinic chains and/or more probably small polyaromatic units [22]. The  $D_1$  peak position of aliphatic soot varies from 1340 to 1365  $\text{cm}^{-1}$  while that of aromatic soot is above 1365  $\text{cm}^{-1}$ .

Fig. 4. 8 shows the value of FWHM and position of  $D_1$  and  $G$  peaks in our soot Raman spectra compared with those of other premixed flaming and industrial soot. The polyaromatic unit sizes in these materials vary from 1 to 4 nm. In particular,  $L_a$  increases with soot aging moving from 1.12 to 1.17 nm, from 1.21 to 1.22 nm for ethylene soot and from 1.25 to 1.30 nm for benzene soot [22], from 2 to 4 nm for Larouche's samples (e.g. rubber grade carbon black, acetylene soot, plasma blacks, etc.) [23], less than 4 nm for

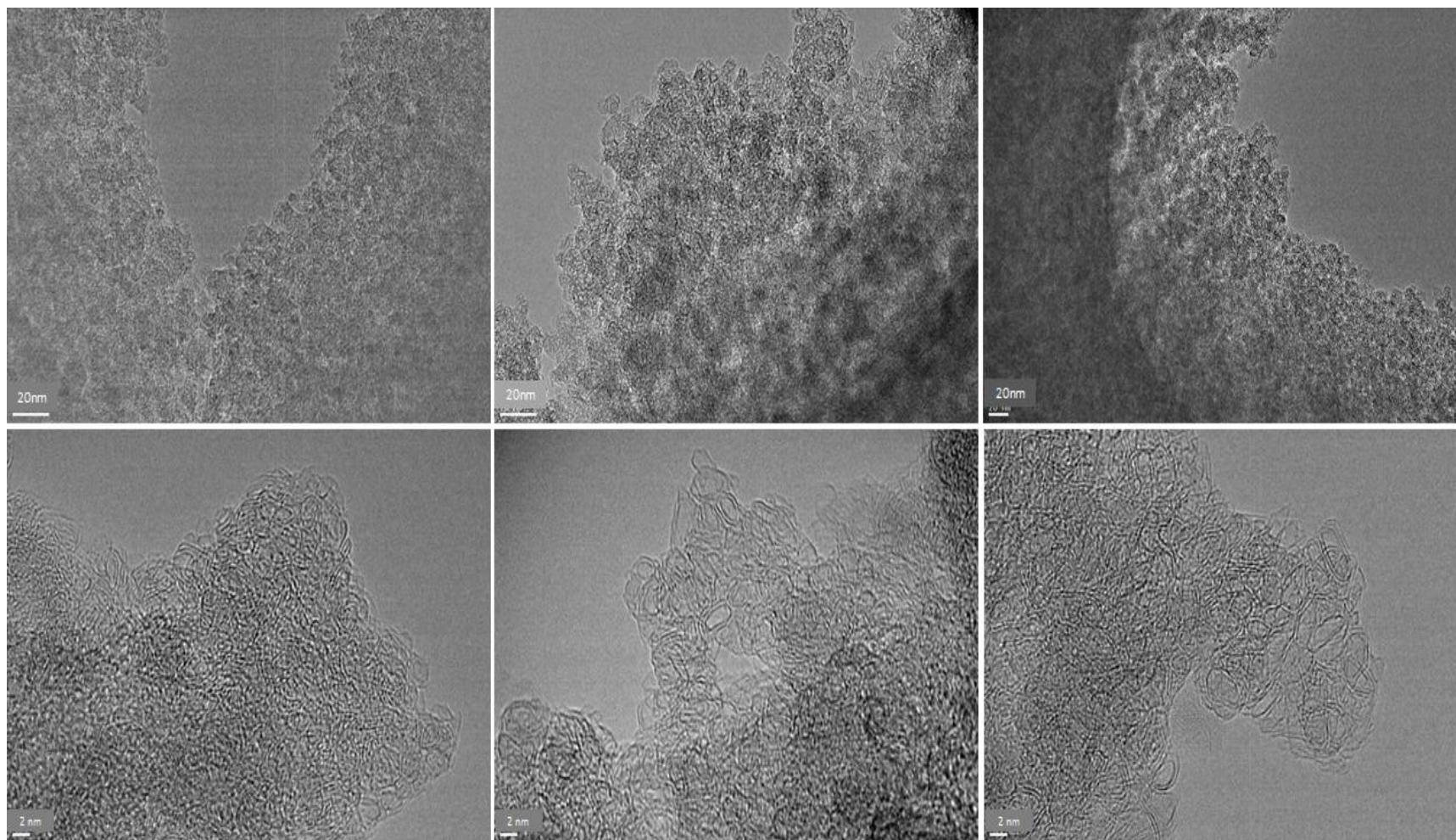


Fig. 4. 9. HRTEM images of C/O 1.05 soot at 24, 36 and 50 mm of HAB corresponding to three columns (from left to right side).

aliphatic soot and from 3 to 4 nm for aromatic soot [7]. In comparison, our FWHM and position peak values are not too different from the published data.

Combining the  $I_{D1}/I_G$  ratio and  $\text{FWHM}(G)$  allows stages 1 or 2 types of structure (see Fig. 4.2), proposed by Ferrari and Roberston [8], to be discriminated, because samples in stage 1 and 2 could have the same  $I_{D1}/I_G$ , but not the same  $\text{FWHM}(G)$ , being this much bigger in stage 2 [24], [25]. We can anticipate that our soot samples vary from the end of stage 1 to the beginning of stage 2. This could be confirmed from HRTEM images of soot.

HRTEM images of soot produced by C/O 1.05 flame at 24, 36 and 50 mm from the burner are plotted in Fig. 4. 9. The HRTEM images have not been quantitatively analyzed yet, but approximate polyaromatic unit size can be observable. It is clear that the average polyaromatic unit size of soot is around 2 nm or lower. However curvature is very pronounced and requires a dedicated examination.

#### 4.4.1.2. Comparison of the positions of $D_1$ and $G$ peaks in Raman spectra to that of the $\text{sp}^3$ defect and C=C stretching bands in IR spectra.

The  $\text{sp}^3$  defect band observed in IR absorption spectra is assigned to edge defects that can occur as aliphatic cross-linking or to non-hexagonal rings carbon defects within the polyaromatic units [18], because of their mixed  $\text{sp}^2$ - $\text{sp}^3$  character and consistency with  $\text{sp}^3$  C-C stretching mode frequency. For our samples, this band appears to vary between 1190 and 1280  $\text{cm}^{-1}$  in IR spectra, probably depending on the nature of the defects (Appendix A). Because of its origin, we question the correspondence to the  $D_1$  band in Raman spectroscopy. This Raman “defect activated” mode involves hexagonal ring breathing activated by edge effects or defects within the polyaromatic unit, all leading to size limitation of the aromatic domain. The mode around 1600  $\text{cm}^{-1}$  in IR spectra is the C=C ( $\text{sp}^2$ ) stretching modes. The  $G$  band relates also to the aromatic  $\text{sp}^2$  C=C stretching mode. Fig. 4. 10 shows the position relation between the defect and C=C stretching modes in IR and Raman spectra. One can see that a trend is well identified for the  $D_1$  band, their frequencies inversely changing. It should be recalled here that no IR  $\text{sp}^3$  defect band can be identified for “aromatic” soot produced in the C/O = 1.3 flame. For the  $G$  band, no  $D_2$  was added to extract the  $G$  band position except for those where the  $G$  and  $D_2$  bands are clearly separated. A tendency is observed and they span a roughly similar range of values.  $G$  band in such disordered material is mostly dictated by the vibrational density of states. Because of the absence of molecular symmetry, the IR activity may thus closely follow that of the Raman one as indeed observed. While the nature of the mode for the  $G$  mode is similar to the IR active one, that of the  $D$  band is possibly different and would require a deeper investigation in a molecular approach [10].



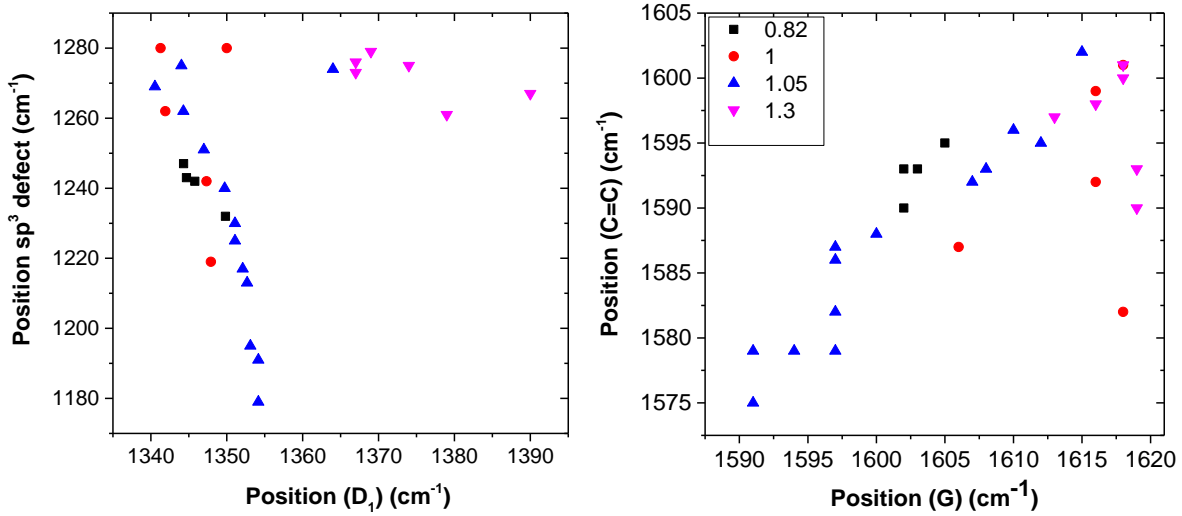


Fig. 4. 10. Position relation of  $D_1$  and  $G$  peaks in Raman spectra with  $sp^3$  defect and C=C stretching bands in IR spectra.

In addition, the relation between the  $I_{D_1}/I_G$  ratio and the IR active C=C stretching and  $sp^3$  defect bands were also considered via their positions (in Fig. 4. 11). It should be recalled that the variation of the position of the C=C stretching mode in the IR spectra was related to the cross-linkage constraints on the polyaromatic layers, the more cross-linked the lower the frequency of the IR mode. In addition, both IR modes exhibit a clear relation as well (see Fig. 5 in appendix A). A clear relation is found for both. Two regimes are found: a region where no clear relation is found for the smallest values of  $I_{D_1}/I_G$ , and one where the  $I_{D_1}/I_G$  changes linearly with the C=C position. The role of the defect in the position of the IR modes is thus clearly consistent with the Raman spectra. Such behavior is shown for the first time to our knowledge.

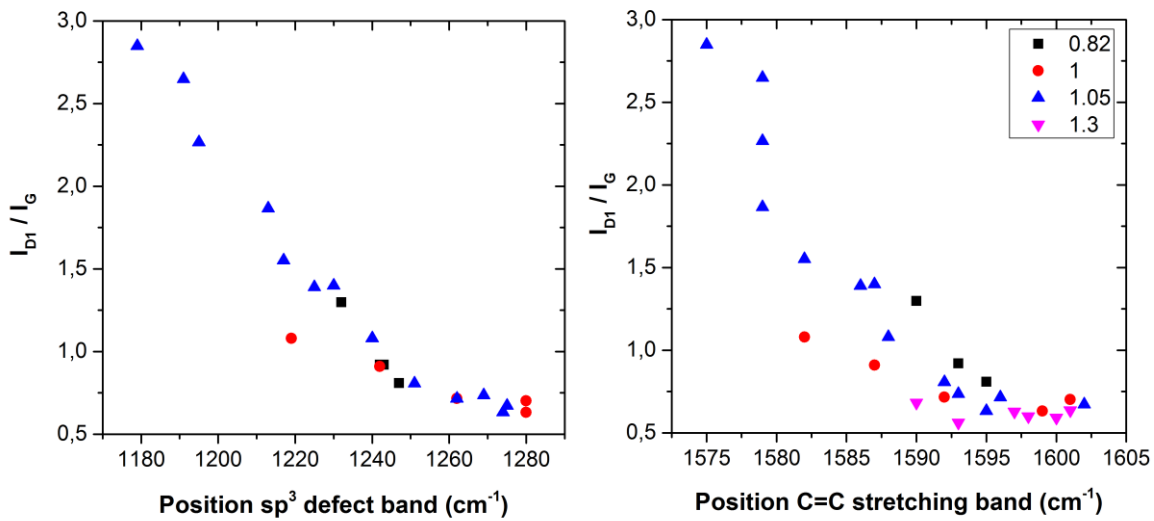


Fig. 4. 11. Relation of the  $I_{D_1}/I_G$  ratio with position of C=C stretching and  $sp^3$  defect bands.

#### 4.4.2. Indices of aromatization

In this part, we will attempt to quantify usual indices relating to soot structural properties, such as the poly-aromatic unit average size or optical Tauc gap using the Raman fit parameters. In order to obtain these indices, the  $I_{D1}/I_G$  ratio plays an important role.

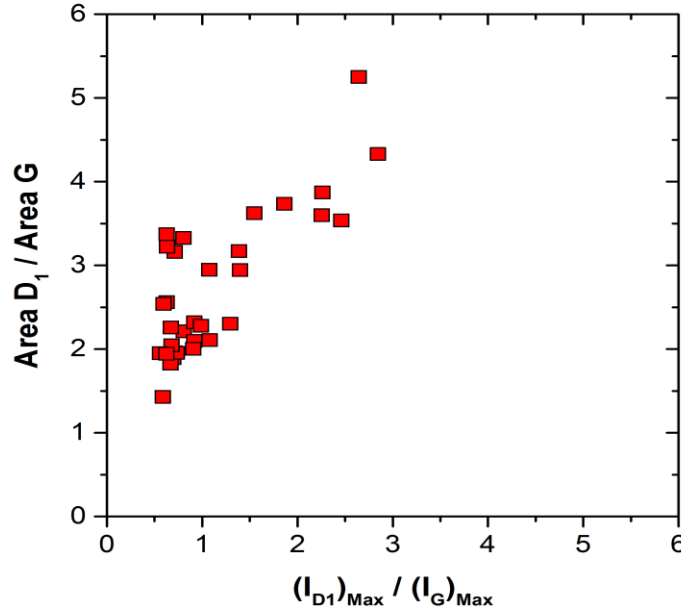


Fig. 4. 12. Comparing the peak height ratio and the peak area ratio in our spectra.

From literature, it is not always clear if the  $I_{D1}/I_G$  ratio should be the ratio of the peak heights or peak areas. According to the review of Ferrari et al. (2000), the difference is not so important for disordered graphite structure, as the peak widths are similar, but this is not so clear for amorphous carbons. In the latter case, the broadening of the  $D$  peak is correlated to a distribution of aromatic domain with different stacking orders and dimensions, and thus the information about the less distorted aromatic rings is in the intensity maximum and not in the width, which depend on the disorder. With our spectra, the peak height ratio and the peak area ratio are not too different as shown in Fig. 4. 12. In this study, we thus denote the  $I_{D1}/I_G$  ratio for the intensity maximum ratio.

##### 4.4.2.1. Polyaromatic unit size

The size is usually derived from  $I_{D1}/I_G$  ratio following the original work of Tuistra and Koenig (1970) [11]. The Fig. 4. 13 reports the plot of the bandwidths  $FWHM(D_1)$  and  $FWHM(G)$  with the  $I_{D1}/I_G$  ratio. It outlines one clear relation, the narrowing of  $D_1$  as the  $I_{D1}/I_G$  ratio rises for the  $C/O=1.05$  flame. As we can see the  $I_{D1}/I_G$  ratio ranges from 0.5 to 3 while the limit value of  $I_{D1}/I_G$  in the three stage classification proposed by Ferrari is 2. The  $I_{D1}/I_G$  ratio which is above 2 belongs to  $C/O$  1.05 flame. This type of soot Raman spectra has never been analyzed in literature.

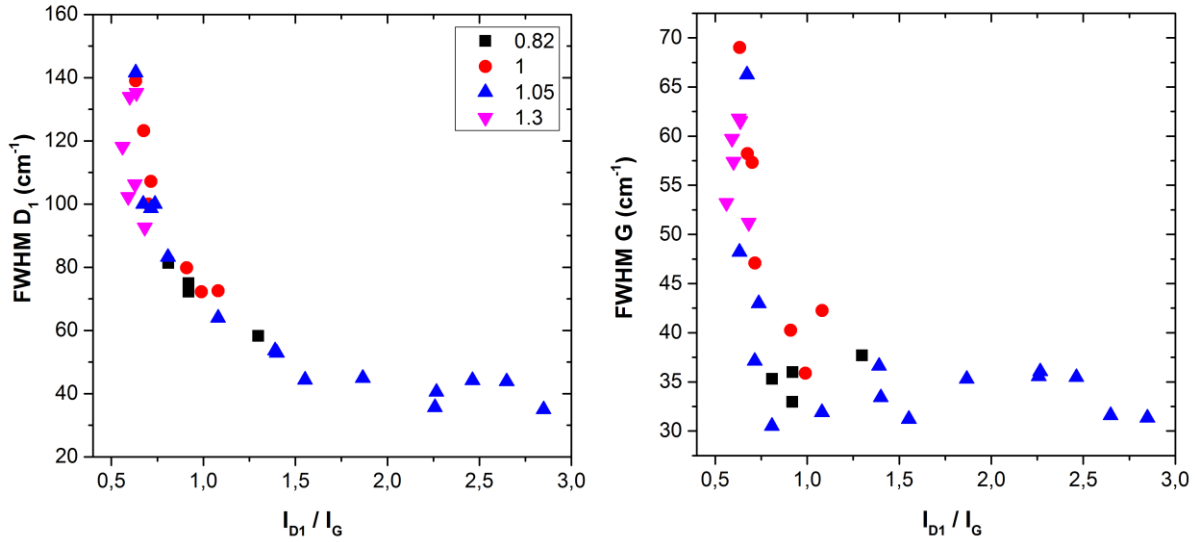


Fig. 4.13. FWHM( $D_1$ ) and FWHM( $G$ ) as a function of  $I_{D1}/I_G$ .

Using equation 4.2 which is available only for  $L_a < 2$  nm, the polyaromatic unit size is accessed and shown in Fig. 4.14. With the  $I_{D1}/I_G$  ratio lower than 2, the obtained  $L_a$  values are consistently found below  $< 2$  nm. The TK relation for the  $I_{D1}/I_G$  ratio above 2 is not adapted as well. However the maximum  $L_a$  found is equal to 2.4 nm, which is acceptable because the limit of validity is not that strict. We consider these  $L_a$  as effective ones that may be used to describe our soot. Quantitative analyses of the HRTEM images will be performed in the future to provide better estimates of the polyaromatic units average sizes.

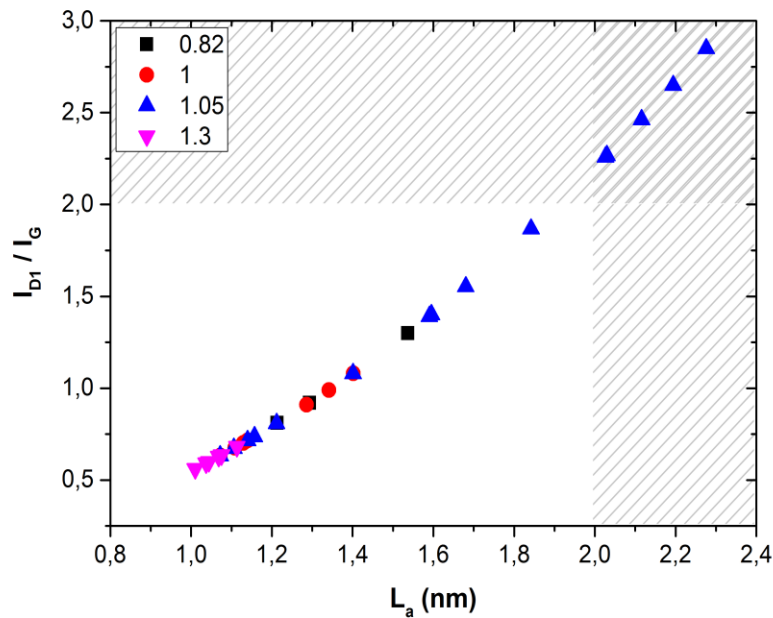


Fig. 4.14. Evaluating  $L_a$  from  $I_{D1}/I_G$ .

### Comparing $L_a$ obtained by Raman spectroscopy and the visible transmission spectroscopy

In our study, not only was Raman spectroscopy and HRTEM used but VUV-IR transmission spectroscopy was also applied to explore soot properties. VUV spectroscopy has allowed us to identify the electronic transition. Moreover, we used the visible spectral range to determine the Tauc gap ( $E_g$ ), then the average coherence length ( $L_a$ ) and the number of six-fold aromatic rings ( $N_R$ ) that can be derived from the empirical relation between  $L_a$  and  $E_g$  (proposed by Robertson 1991) and a similar relation between  $N_R$  and  $E_g$  (proposed by Robertson & O'Reilly, 1997). All this information is detailed in [Appendix A](#).

In this content, we would like to compare  $L_a$  obtained from Raman spectra to that from visible spectroscopy. Fig. 4. 15 exhibits values of  $L_a$  achieved from the  $I_{D1}/I_G$  ratio (Fig. 4. 14) to these corresponding values from the visible transmission spectra in [Appendix A](#). A roughly linear relationship (no uncertainties are reported yet in the data analysis) is found, underlying the qualitative agreement between the two approaches. In comparison, there is about a factor of 2 between the 2 values.

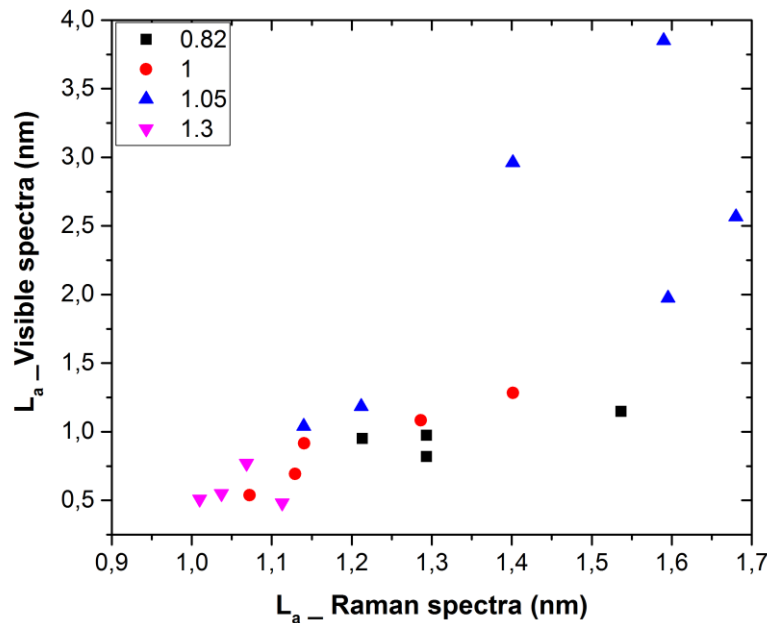


Fig. 4. 15. Comparing  $L_a$  obtained via Raman and visible transmission spectroscopy.

#### 4.4.2.2. Tauc gap and Raman spectral parameters

The optical gap, also ascribed to the Tauc gap ( $E_g$ ) [26], is a phenomenological measure of the energy difference between the top of the valence band and the bottom of the conduction band in amorphous material [27]. From the VUV-visible absorption spectra of soot, we used the visible range (350 – 1000 nm) to determine the Tauc gap using Tauc's relation. The value can be estimated by plotting  $\sqrt{\alpha E}$  as a function of energy (E) then extrapolating the linear region of the graph to zero absorption, where  $\alpha$  is the absorption



coefficient obtained from the optical depth and assuming a thickness of 50 nm for all samples. Note that the uncertainty on the Tauc gap is strongly dependent on the energy range chosen for the linear fit and weakly on the thickness uncertainty.  $E_g$  is abscissa of the linear line at zero absorption. The Tauc gap  $E_g$  and the polyaromatic unit mean size  $L_a$  estimations are detailed in Appendix A.  $E_g$  values of our samples vary from 0 to 1.60 eV.

Looking at our spectra in Fig. 4. 4 to Fig. 4. 7, with C/O = 0.82, 1, 1.3 flames and C/O = 1.05 (HAB < 28 mm), the appearance of  $D_2$  is not clear, we therefore neglect the existence of  $D_2$ . In this case, FWHM( $G$ ) is FWHM of the band at 1600  $\text{cm}^{-1}$ . With C/O = 1.05 (HAB > 28 mm),  $D_2$  peak could be distinguished clearly from  $G$  peak so the existence of  $D_2$  should be considered. It means that the FWHM( $G$ ) is the FWHM of  $G$  peak.

Fig. 4. 16a shows that when the Tauc gap  $E_g$  increases, the  $G$  peak position shifts towards higher frequency. The evolution of  $G$  peak as a function of  $E_g$  could be fit by a polynomial function:

$$\omega_G = (1594 \pm 1.5) + (17 \pm 1.7)E_g \quad (4.3)$$

The width of  $G$  peak is a good tracer of disorder [8]. Fig. 4. 16b plots the inverse  $G$  width against the optical gap for soot samples. No clear relation can be found. It shows that the Tauc gap is more sensitive to the nature of the polyaromatic unit and their defects rather than their organization.

In contrast to the increase of  $E_g$ , the reciprocal of ( $I_{D1}/I_G$ ) ratio decreases with  $E_g$  and nicely shows a unexpected relation:

$$I_{D1}/I_G = 0.76/\sqrt{E_g} \quad (4.4)$$

This expression is not expected since from equation 1.2 and 4.2, one should find  $I_{D1}/I_G \propto 1/E_g^2$ . Such a relation implies, if equation 4.2 is used:

$$E_g(\text{eV}) = 1.9/L_a^4 \quad (4.5)$$

This is strongly different from equation 1.2. This was based on a modeling of the band gap in amorphous carbon based on the size of the polyaromatic units [28]. It appears as not being adapted to soot electronic structure, as long as the relation 4.2 is considered valid. The model relied on small PAH and defected PAH electronic structure calculations and do not take into account the effect on the stacking, the curvature or the cross-linkage in perturbing the electronic structure. Effectively a much faster decrease is found for the gap with  $L_a$  below 2 nm. On the contrary, if one considers equation 1.2 as a good hypothesis, then one would find  $I_{D1}/I_G \propto \sqrt{L_a}$ . Larger  $L_a$  would be then inferred for our soot. Progresses on the polyaromatic analysis from HRTEM may help to provide a size distribution which could help to improve these empirical models.

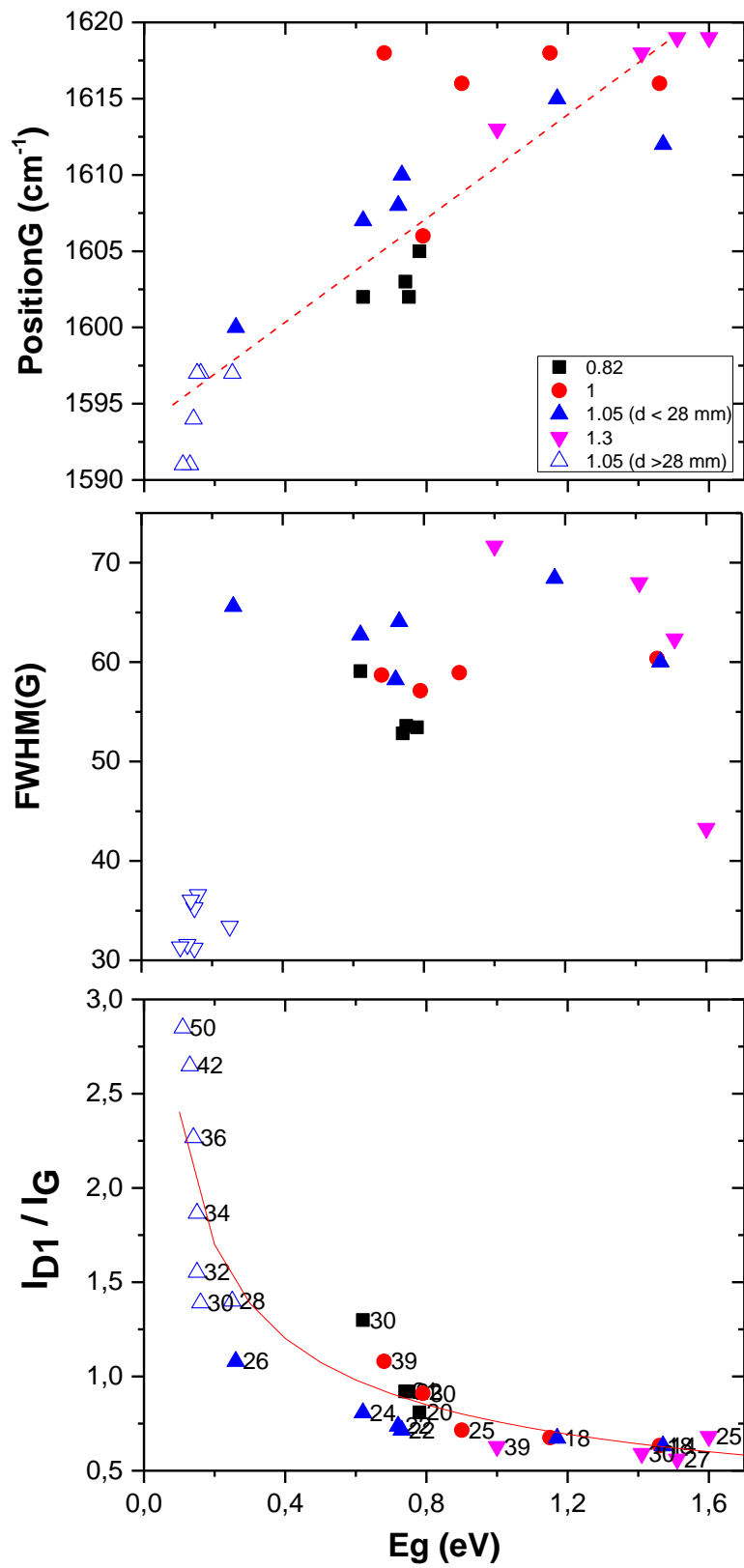


Fig. 4. 16. The relation between G peaks and the Tauc gap  $E_g$ . Label is denoted HAB (mm).

### 4.4.3. The second order

In the second order of Raman scattering, overtones and combination modes with strong band intensities are observable at 2700 and 2940  $\text{cm}^{-1}$ .  $2D_1$  peak properties are structure sensitive and give information about the degree of graphitization of the sample. In Fig. 4.17 the scattering signal of  $2D_1$  peak increases following the rise of scattering signal of  $D_1$  peak. In average, the normalized area of  $2D_1$  peak with  $G$  peak is approximately a half of the normalized area of  $D_1$  peak with  $G$  peak. The linear relation is also held between  $\text{FWHM}(D_1)$  and  $\text{FWHM}(2D_1)$ . Lespades et al. (1984) proposed a graphitization trajectory for carbon materials using the FWHM of these two peaks when a double peak for  $2D_1$  is observed. It is not the case here.

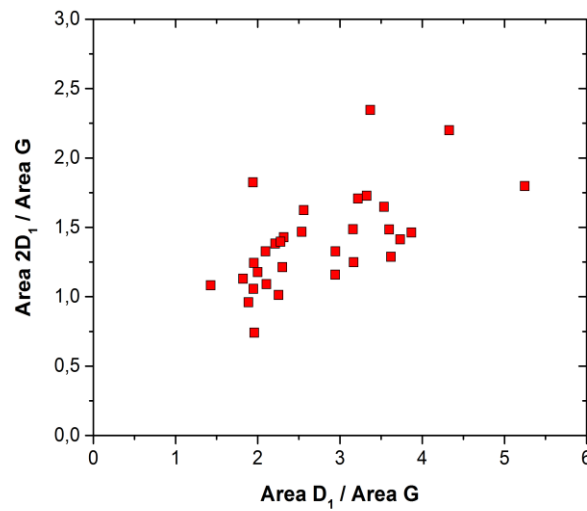


Fig. 4.17. Integrated area under  $2D_1$  Raman peak ( $\sim 2740 \text{ cm}^{-1}$ ) as a function of the integrated area under  $D_1$  Raman peak ( $\sim 1355 \text{ cm}^{-1}$ ).

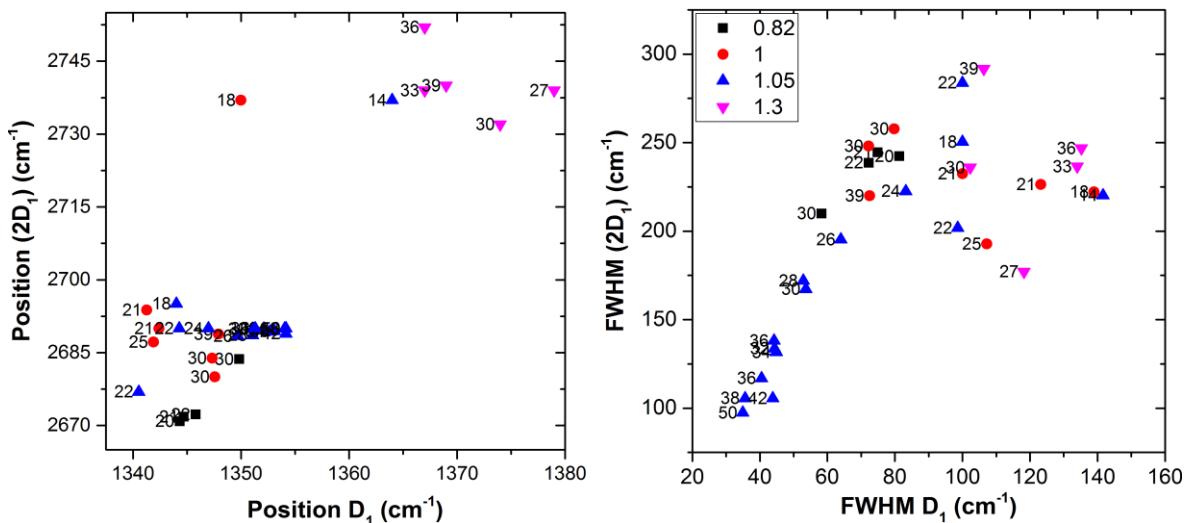


Fig. 4. 18. Relation of position and FWHM between  $2D_1$  and  $D_1$  peaks.

Besides the area of  $D_I$  and its overtone  $2D_I$  peaks, we also considered their position and width peak relations. The relation is explored in Fig. 4. 18. The position of the overtone  $2D_I$  is found to be, in consistency, nearly two times higher than that of  $D_I$  and the two peak position in Raman spectra of aromatic soot shift up toward higher frequency compared to those of aliphatic soot. The width of  $2D_I$  is also two times larger than that of  $D_I$ . Nevertheless, the evolution of  $D_I$  and  $2D_I$  via their FWHMs is also exploited, in which the larger HAB is, the narrower FWHM( $D_I$ ) becomes.

- *The tortuosity ratio ( $R_{Tor}$ )*

Larouche and coworker defined a new ratio called the tortuosity ratio ( $R_{Tor}$ ) [23]. It could be determined by the formula:

$$R_{Tor} = D(\lambda) \cdot \left( \frac{2A_{2D}}{A_G} \right) \quad (4.5)$$

where  $D(\lambda)$  is a normalization parameter, in which  $D(\lambda) = 1$  for a wavelength of 514.5 nm. This ratio is a Raman tracer that may classify in a practical way nanostructured carbon having different curvature of the graphene layers. Fig. 4. 19 plots  $R_{Tor}$  as a function of FWHM( $D$ ), well tracing the defects as illustrated in Fig. 4.13.

In Fig. 4. 19, additional carbonaceous materials were included. These include carbon blacks, nanodiamonds, graphite, coals, glassy carbon, all taken from Jean-Noël Rouzaud private collection. Some were heated up to 2700°C [29]. They were chosen because they all exhibit various curvature of the polyromatic unit and served to explore this effect. It can be seen that a trend is observed, the higher the  $R_{Tor}$ , the narrower the FWHM( $D$ ) although curvature is more pronounced. The soot follows approximately the rough tendency. Analyses of the HRTEM images have to be performed to quantify this and develop this new tracer.

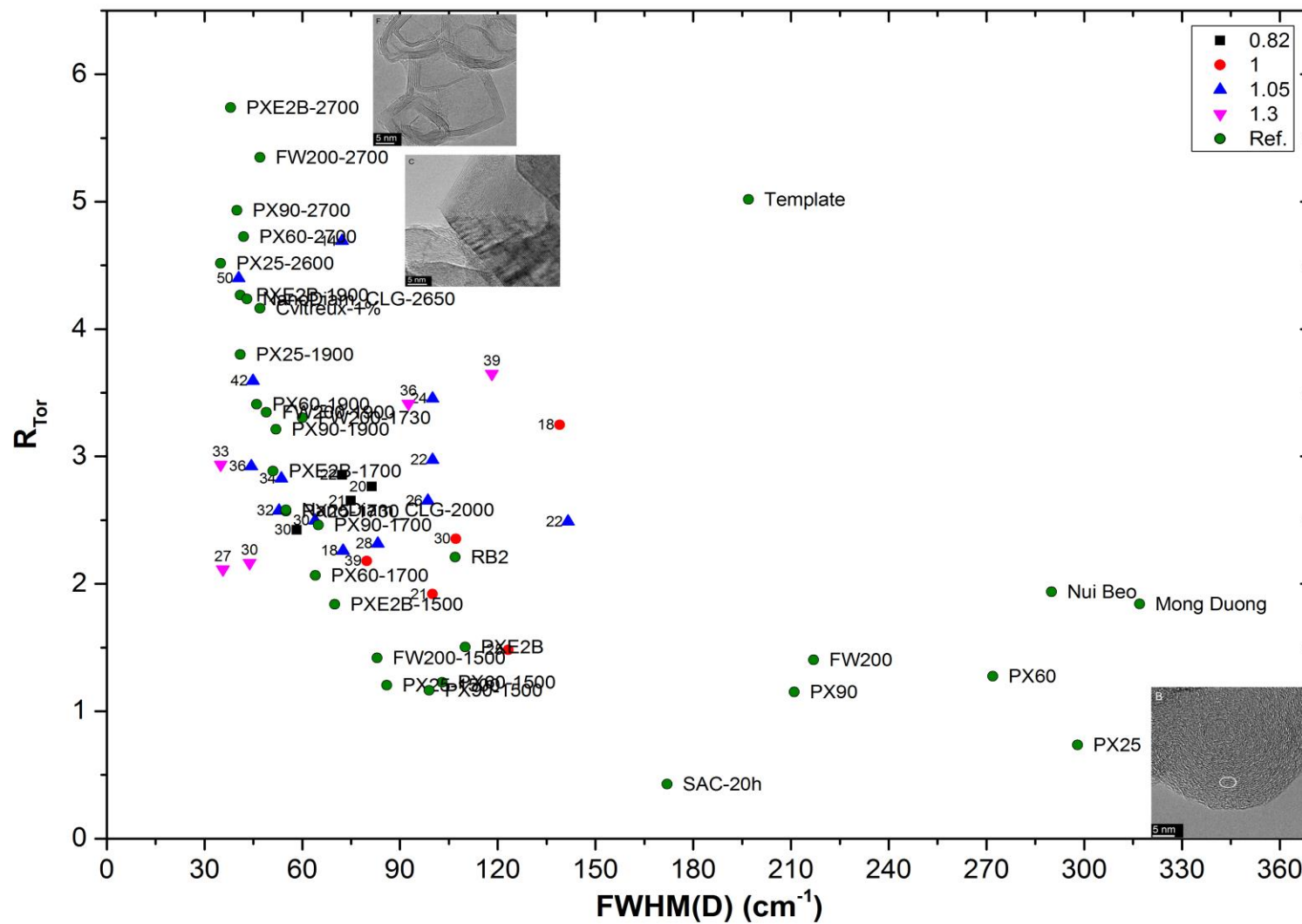


Fig. 4. 19. Classification of our soot in various carbonaceous materials.[29]

#### 4.4.4. The $sp$ hybridized bond

The occurrence of a small peak at  $\sim 2100 \div 2160 \text{ cm}^{-1}$ , called C peak, in Raman spectra of  $C/O = 1.05$  soot is a new information in our observation. This is the fingerprint of  $sp$  chains, particularly polyynes which are defined as a sequence of alternating single and triple bonds ( $-C \equiv C -$ ) [30]. Fig. 4. 20a presents the HAB dependence of  $sp$  peak position. There is a frequency blue shift of the peak position proving a decreasing chain length [31], [32] when HAB increases. In other words, the more the residence time of soot particles in the flame is, the shorter the polyynes chain length is.

From the integrated intensity ratio between C band and ( $D_I + G$ ) band and the ratio  $\alpha$  between Raman cross section of  $sp$  and  $sp^2$  bonds [33], we could determine the absolute amount of  $sp$  bond in these deposited soot shown in Fig. 4. 20b. Along HAB, the amount of  $sp$  bond comparing to  $sp^2$  bond increase from 1% to 12%. In fact, C peak not only appears in Raman spectra of soot formed by  $C/O = 1.05$  flame but they can be also seen in that of other flames. However, the S/N ratio is often not good enough to discriminate C peak from the background.

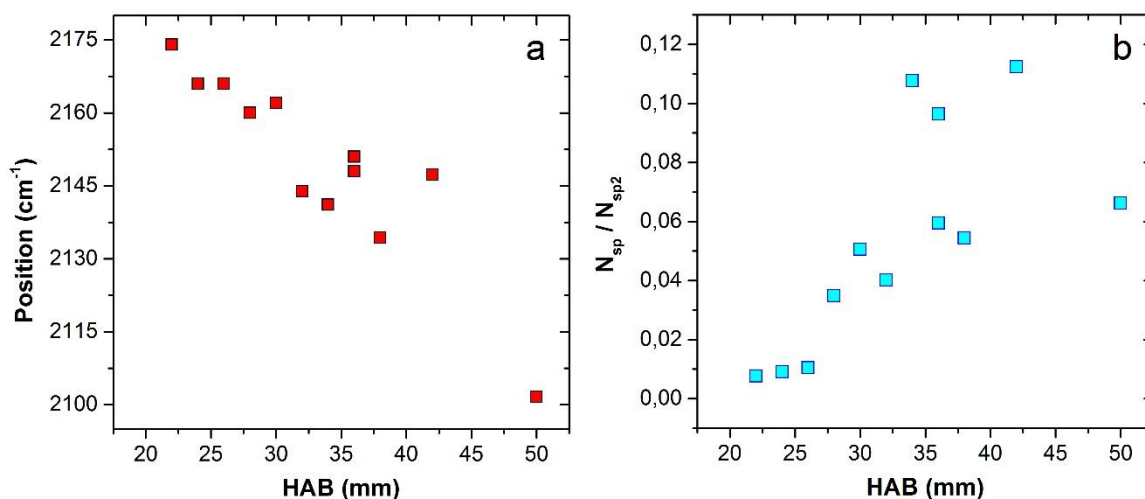


Fig. 4. 20. The evolution of  $sp$  bond vs HAB (mm).

## 4.5. Conclusions

By changing the  $C/O$  ratio and burning pressure, we produced a wide variety of soot samples. Under the 514 nm wavelength laser excitation, a continuum fluorescence background and a shoulder  $D'_I$  peak ( $\sim 1269 \text{ cm}^{-1}$ ) occurs in Raman spectra of aromatic rich soot. Position of  $D_I$  peak clearly upshifts in cases of aliphatic rich soot and downshifts in case of aromatic rich soot towards the same position around  $1350 - 1360 \text{ cm}^{-1}$  when we increase HAB. This suggests that aliphatic rich soot undergoes an aromatization process as it ages.

In aliphatic sooting flames, the C/O = 1.05 flame exhibits the existence of sp hybridization in their structure, in which the amount of sp bond compared to sp<sup>2</sup> bond increase from 1% to 12% and the polyynes length decreases along the HAB. In addition, this is the only condition where the  $I_{D1}/I_G$  ratio above 2 was observed. The empirical formulae have been shown to not take into account the evolution of the electronic structure for these disordered nanoparticles and rather small  $L_a$ . A new dependency is found between Tauc gap and effective  $L_a$  that should be confirmed in the future.

Regarding the data, we have shown that analysis performed in the visible-UV range, the IR and by Raman spectroscopy are all consistent. They allow to gain information in the nature of the vibrational modes and to relate these to the structure. The evolution along the height of the flames can thus be used to decipher the intimate structure of the soot and guide the interpretation of soot evolution in flames.

## References

- [1] A. Jorio, M. M. Lucchese, F. Stavale, E. H. M. Ferreira, M. V. O. Moutinho, R. B. Capaz, and C. a Achete, “Raman study of ion-induced defects in N-layer graphene.,” *J. Phys. Condens. Matter*, vol. 22, no. 33, p. 334204, 2010.
- [2] M. O. Andreae and A. Gelencsér, “Black carbon or brown carbon? The nature of light-absorbing carbonaceous aerosols,” *Atmos. Chem. Phys.*, vol. 6, pp. 3131–3148, 2006.
- [3] P. R. Buseck, K. Adachi, A. Gelencsér, É. Tompa, and M. Pósfai, “Ns-Soot: A Material-Based Term for Strongly Light-Absorbing Carbonaceous Particles,” *Aerosol Sci. Technol.*, vol. 48, no. 7, pp. 777–788, 2014.
- [4] A. Sadezky, H. Muckenhuber, H. Grothe, R. Niessner, and U. Pöschl, “Raman microspectroscopy of soot and related carbonaceous materials: Spectral analysis and structural information,” *Carbon N. Y.*, vol. 43, no. 8, pp. 1731–1742, 2005.
- [5] K. H. Homann, “Fullerenes and soot formation - New pathways to large particles in flames,” *Angew. Chemie, Int. Ed. English*, vol. 37, no. 18, pp. 2435–2451, 1998.
- [6] T. Pino, E. Dartois, A.-T. Cao, Y. Carpentier, T. Chamaillé, R. Vasquez, A. P. Jones, L. d’Hendecourt, and P. Bréchnignac, “The 6.2  $\mu\text{m}$  band position in laboratory and astrophysical spectra: a tracer of the aliphatic to aromatic evolution of interstellar carbonaceous dust,” *Astron. Astrophys.*, vol. 490, no. 2, pp. 665–672, 2008.
- [7] R. Brunetto, T. Pino, E. Dartois, A. T. Cao, L. D’Hendecourt, G. Strazzulla, and P. Bréchnignac, “Comparison of the Raman spectra of ion irradiated soot and collected extraterrestrial carbon,” *Icarus*, vol. 200, no. 1, pp. 323–337, 2009.
- [8] A. Ferrari and J. Robertson, “Interpretation of Raman spectra of disordered and amorphous carbon,” *Phys. Rev. B*, vol. 61, no. 20, pp. 14095–14107, 2000.
- [9] M. A. Pimenta, G. Dresselhaus, M. S. Dresselhaus, L. G. Cançado, A. Jorio, and R. Saito, “Studying disorder in graphite-based systems by Raman spectroscopy,” *Phys. Chem. Chem. Phys.*, vol. 9, no. 11, pp. 1276–1291, 2007.
- [10] C. Castiglioni, C. Mapelli, F. Negri, and G. Zerbi, “Origin of the D line in the Raman spectrum of graphite: A study based on Raman frequencies and intensities of polycyclic aromatic hydrocarbon molecules,” *J. Chem. Phys.*, vol. 114, no. 2, pp. 963–974, 2001.
- [11] F. Tuinstra and J. L. Koenig, “Raman Spectrum of Graphite,” *J. Chem. Phys.*, vol. 53, p. 1126, 1970.
- [12] A. C. Ferrari and J. Robertson, “Resonant Raman spectroscopy of disordered, amorphous, and diamondlike carbon,” *Phys. Rev. B*, vol. 64, no. 7, p. 75414, 2001.
- [13] S. Reich and C. Thomsen, “Raman spectroscopy of graphite,” *Philos. Trans. R. Soc. A Math. Phys. Eng. Sci.*, vol. 362, no. 1824, pp. 2271–2288, 2004.
- [14] B. Dippel, H. Jander, and J. Heintzenberg, “NIR FT Raman spectroscopic study of flame soot,” *Phys. Chem. Chem. Phys.*, vol. 1, no. 20, pp. 4707–4712, 1999.
- [15] L. G. Cançado, K. Takai, T. Enoki, M. Endo, Y. A. Kim, H. Mizusaki, A. Jorio, L. N. Coelho, R. Magalhães-Paniago, and M. A. Pimenta, “General equation for the determination of the crystallite size  $l_a$  of nanographite by Raman spectroscopy,” *Appl. Phys. Lett.*, vol. 88, no. 16, pp. 1–4, 2006.
- [16] P. Lespade, R. Al-Jishi, and M. S. Dresselhaus, “Model for Raman scattering from



- incompletely graphitized carbons,” *Carbon N. Y.*, vol. 20, no. 5, pp. 427–431, 1982.
- [17] A. C. Ferrari, “Raman spectroscopy of graphene and graphite : Disorder , electron – phonon coupling , doping and nonadiabatic effects,” *Solid State Commun.*, vol. 143, pp. 47–57, 2007.
- [18] Y. Carpentier, G. Féraud, E. Dartois, R. Brunetto, E. Charon, A.-T. Cao, L. d’Hendecourt, P. Bréchnignac, J.-N. Rouzaud, and T. Pino, “Nanostructuring of carbonaceous dust as seen through the positions of the 6.2 and 7.7  $\mu$  m AIBs,” *Astron. Astrophys.*, vol. 548, p. A40, 2012.
- [19] Yvain Carpentier, “De la flamme de laboratoire au milieu interstellaire : signatures spectrales d’entités aromatiques libres ou assemblées,” 2009.
- [20] F. Negri, C. Castiglioni, M. Tommasini, and G. Zerbi, “A computational study of the Raman spectra of large polycyclic aromatic hydrocarbons: Toward molecularly defined subunits of graphite,” *J. Phys. Chem. A*, vol. 106, no. 14, pp. 3306–3317, 2002.
- [21] C. Casiraghi, A. C. Ferrari, and J. Robertson, “Raman spectroscopy of hydrogenated amorphous carbons,” *Phys. Rev. B*, vol. 72, no. 8, p. 85401, 2005.
- [22] C. Russo and A. Ciajolo, “Effect of the flame environment on soot nanostructure inferred by Raman spectroscopy at different excitation wavelengths,” *Combust. Flame*, vol. 162, no. 6, pp. 2431–2441, 2015.
- [23] N. Larouche and B. L. Stansfield, “Classifying nanostructured carbons using graphitic indices derived from Raman spectra,” *Carbon N. Y.*, vol. 48, no. 3, pp. 620–629, 2010.
- [24] a. C. Ferrari, S. E. Rodil, and J. Robertson, “Resonant Raman spectra of amorphous carbon nitrides: The G peak dispersion,” *Diam. Relat. Mater.*, vol. 12, no. 3–7, pp. 905–910, 2003.
- [25] L. G. Cançado, A. Jorio, E. H. M. Ferreira, F. Stavale, C. A. Achete, R. B. Capaz, M. V. O. Moutinho, A. Lombardo, T. S. Kulmala, and A. C. Ferrari, “Quantifying defects in graphene via Raman spectroscopy at different excitation energies,” *Nano Lett.*, vol. 11, no. 8, pp. 3190–3196, 2011.
- [26] J. Tauc, R. Grigorovici, and a Vancu, “Optical Properties and Electronic Structure of Amorphous Germanium,” *Phys. Status Solidi*, vol. 15, no. 2, pp. 627–637, 1966.
- [27] M.-L. Theye and V. Paré, “Spatial organization of the sp<sup>2</sup>-hybridized carbon atoms and electronic density of states of hydrogenated amorphous carbon films,” *Carbon N. Y.*, vol. 40, pp. 1153–1166, 2002.
- [28] J. Robertson and E. O’Reilly, “Electronic and atomic structure of amorphous carbon,” *Phys. Rev. B*, vol. 35, no. 6, pp. 2946–2957, 1987.
- [29] M. Pawlyta, J.-N. Rouzaud, and S. Duber, “Raman microspectroscopy characterization of carbon blacks: Spectral analysis and structural information,” *Carbon N. Y.*, vol. 84, pp. 479–490, 2015.
- [30] L. Kavan, “Carbyne forms of Raman shift,” *Carbon N. Y.*, vol. 32, no. 8, pp. 1533–1536, 1994.
- [31] A. Milani, M. Tommasini, and G. Zerbi, “Carbynes phonons: A tight binding force field,” *J. Chem. Phys.*, vol. 128, no. 6, 2008.
- [32] M. Tommasini, A. Milani, D. Fazzi, M. Del Zoppo, C. Castiglioni, and G. Zerbi, “Modeling phonons of carbon nanowires,” *Phys. E Low-Dimensional Syst. Nanostructures*, vol. 40, no. 7, pp. 2570–2576, 2008.

- [33] L. Ravagnan, G. Bongiorno, D. Bandiera, E. Salis, P. Piseri, P. Milani, C. Lenardi, M. Coreno, M. de Simone, and K. C. Prince, “Quantitative evaluation of sp/sp<sup>2</sup> hybridization ratio in cluster-assembled carbon films by in situ near edge X-ray absorption fine structure spectroscopy,” *Carbon N. Y.*, vol. 44, no. 8, pp. 1518–1524, 2006.

# Chapter 5

## *Results III:*

# Detection of soot in the gas phase

## Contents

---

<b>5.1. Introduction.....</b>	<b>108</b>
<b>5.2. Experimental arrangement.....</b>	<b>109</b>
5.2.1. Experimental setup.....	109
5.2.2. Flame conditions .....	112
<b>5.3. Results .....</b>	<b>114</b>
5.3.1. Data summary .....	114
5.3.2. The flame with 1.05 C/O ratio at 40 mbar .....	122
5.3.3. Properties of C/O 1.05 soot in the gas phase via Raman spectroscopy .....	133
<b>5.4. Conclusions and remarks.....</b>	<b>147</b>
<b>References.....</b>	<b>148</b>

---

Soot properties and soot formation mechanisms are still not fully understood. There are several critical gaps, for instance the nucleation mechanism and soot nuclei properties, at the transition between molecules and nanoparticles. This is one of the less understood steps because of the difficulty in collecting experimental data. In addition, exporting the knowledge gained on soot for the analysis of black carbon in the atmosphere is also not trivial because of the changes of their properties via ageing. We decided to focus our attention on the Raman scattering as a tool to investigate soot.

In our work, soot particles in the gas phase were investigated using a 532 nm continuous laser excitation for Raman scattering measurements. We focused on low pressure ethylene flames. The obtained Raman spectra of soot particles extracted from different combustion conditions in a premixed flame provided new information, with measurements probably across the nucleation zone. Due to the overlap with fluorescence, the interpretation of the Raman bands appeared to be difficult. They are found to be clearly different from the soot sampled within the same conditions on substrate and analyzed ex situ.

## 5.1. Introduction

The formation of soot in combustion is kinetically controlled and occurs in short times (1 – 10 msec to reach particle diameters of 30 nm) [1], but it is a complex process involving gas phase chemical kinetics, heterogeneous reactions on the particle surface and particle dynamics [2]. Research has made significant advances and helps us to increase our knowledge of these processes in combustion as well as properties of their products.

Over a half past century, there have been a considerable number of experimental and modeling researches aiming to understand the main steps of soot formation in combustion flames. Soot inception processes in the early regions of low pressure rich premixed flames have been studied employing molecular beam sampling followed by electron microscopy [3], mass spectrometry [4], [5] gas chromatography [6]. These processes in low and atmospheric pressure rich flames have also been considered via ultraviolet-visible absorption spectra [7], laser light scattering and laser induced fluorescence [8]–[10], absorption, fluorescence and scattering measurements [11].

During the recent two decades, significant advances have been achieved in optical diagnostics for PAHs and soot in flames and their precursors formation [12]. Soot formation processes have been extensively investigated. For example, in 1997, Xu, F. et al. studied soot volume fractions by laser extinction and gravimetric methods, soot structure by thermophoretic sampling and transmission electron microscopy, major gas species concentrations by sampling and gas chromatography [13]. Then their volume fraction was monitored by light-attenuation based methods [14]–[16] and laser induced incandescence (LII) [17]. The first observation of inner core and outer shell of primary soot particles was also shown in the year of 1997 by Ishiguro, T. et al. [18]. Selective and quantitative PAH

measurement was obtained by extraction methods from condensed phase as reviewed by Ciajolo et al. [19]. There are numerous investigations of PAH and soot particle properties (optical properties, morphology, and soot volume fraction) which one could find in more detail in the review of P. Desgroux et al. (2013) [12].

Parallel to the experimental methods, modeling of these processes in combustion environments has received great attention. In the early reaction models, soot was considered as the only kind of particle present in a flame and its mass was calculated as the total amount of aromatic species above a certain molecular mass [20]. In recent years, along with the development of diagnostic techniques, our knowledge of particle inception, growth and coagulation has increased. Many kinetics models assume clusters of PAHs to form the first soot nuclei [21]–[23]. The nuclei grow via surface growth reaction involving  $C_2H_2$  through the hydrogen-abstraction-carbon-addition (HACA) mechanism was proposed by Flenklach and Wang in 1991 [24] and the global surface growth rates are extracted from soot mass increase with reaction time [25]. The mass evolution and hydrogen content in combustion-formed particles could be predicted by Sirignano, M. et al. (2010) [2]. Despite of the large number of studies on soot nucleation, crucial step from the molecular phase leading to nascent soot particles is still speculative.

Raman spectroscopy is a powerful tool for the characterization of carbon materials and nanostructures due to its sensitivity to the vibration of C – C bonds. For example, strong electron-phonon coupling and resonance effects allow for the measurement of single carbon nanostructures and together with confinement effects, provides information on their structure, hybridization state, defects, functionalization and doping [26]. In the present work, we focused on the use of Raman spectroscopy to provide information on the structural properties of soot. In particular, we used Raman spectroscopy to probe soot particles in an ethylene premixed flame. With our online gas phase diagnostics, the evolution of particles formed along the flame appeared “visually” via their Raman spectra. This method is able to analyze the main combustion products.

## 5.2. Experimental arrangement

In this section, we will detail the optical diagnostics used to detect soot extracted from the flames. The approach used various flame conditions ranging from slightly sooting flames to strongly sooting flames.

### 5.2.1. Experimental setup

In this experiment, the excitation source, wavelength selector and detector were the same equipment which was used in DRCS measurement. All instrumental details are mentioned in subsection 3.3.2 in chapter 3. The configuration is sketched in Fig. 5.1a. The laser beam was directed through a viewport and a pinhole before entering into the center of the deposition chamber. Combustion products produced by the flame were extracted by a

## 5.2. Experimental arrangement

water-cooled quartz cone (hole diameter 1 mm) which was inserted into the flame at controlled distances from the burner (mentioned in chapter 2).

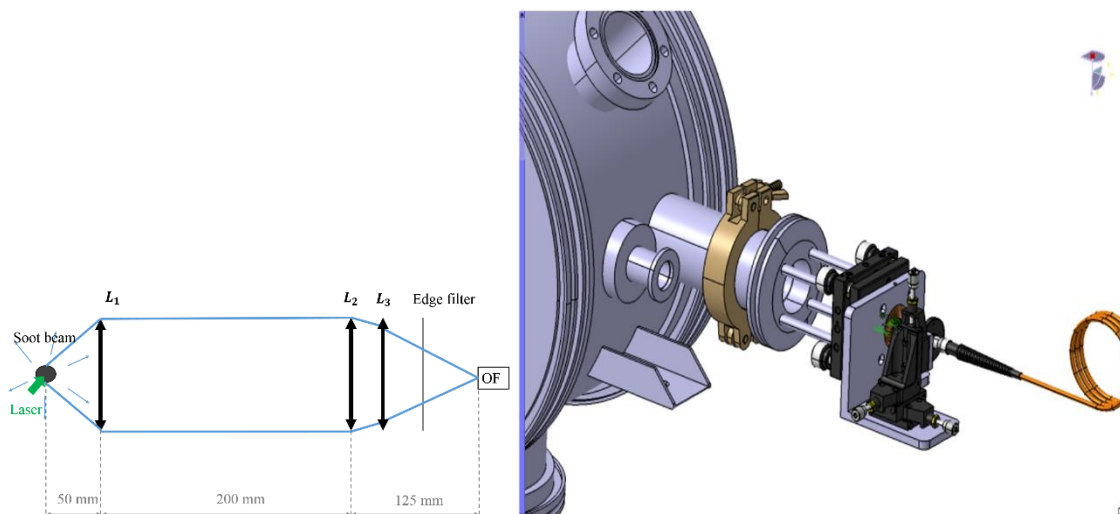
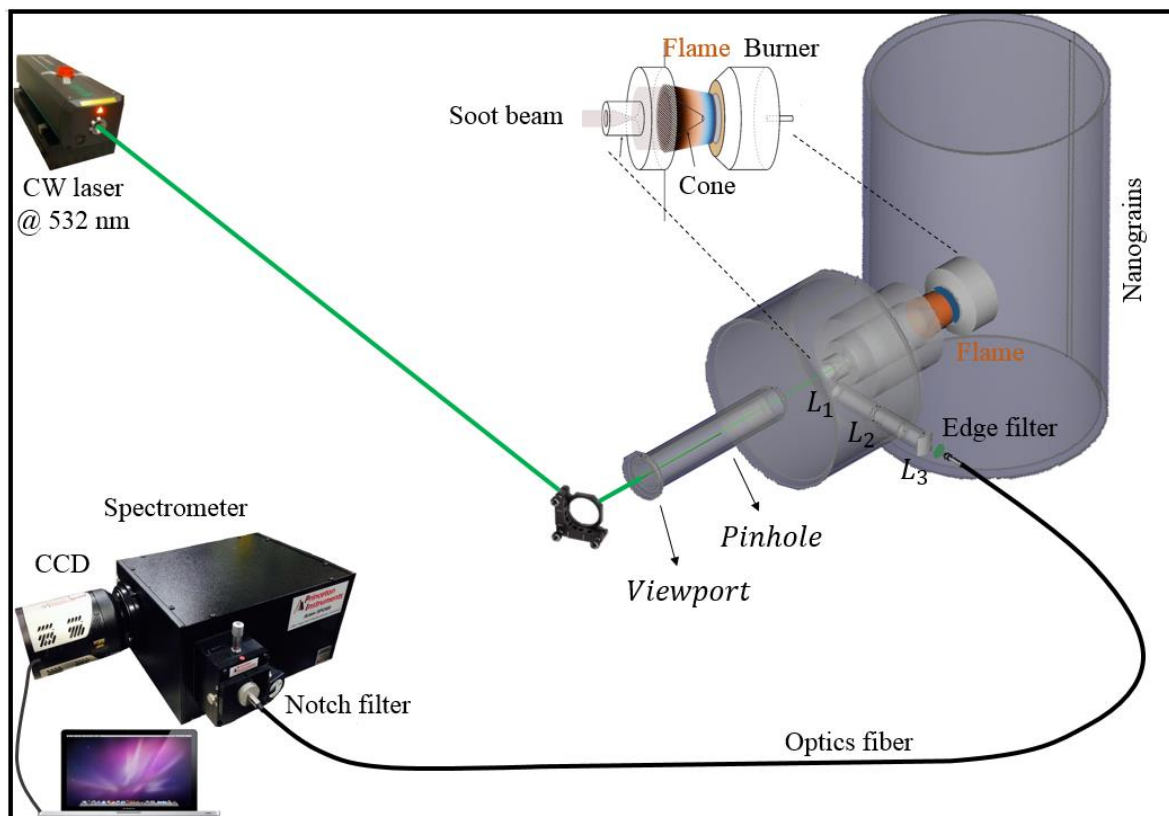


Fig. 5.1. Scheme of online measurement of soot in the gas phase; b. The collection optics scheme, in which the distances from the source to  $L_1$ ,  $L_1$  to  $L_2$ ,  $L_2$  to the optical fiber are 50, 200, 125 mm, respectively; c. The entrance of optical fiber coupled to the collection optics.

## 5.2. Experimental arrangement

The byproducts then flowed through the Laval nozzle into the sampling chamber at  $\sim 10^{-1}$  mbar. Argon was added before the Laval nozzle (few  $10^{-1}$  l.min $^{-1}$ ) to shape the molecular flow with the nozzle and to concentrate the soot beam on the axis. This soot beam was excited by the cw laser. Scattered photons were collected by a lens system inserted into the deposition chamber at the angle 90 degree relatively to the incident beam and then entered into the optical fiber located on a 3 axis translation positioning stage (shown in Fig. 5.1c). The optical fiber was connected with a spectrometer coupled with a CCD camera. Raman signals were acquired by a computer. Note that the incident laser beam was vertically polarized in the direction perpendicular to the scattering plane.

The collection optics is schemed in Fig. 5.1b. After colliding with soot beam, scattered photons were collected by a spherical lens  $L_1$  ( $f_1 = 50$  mm). The collimated photons were then focused on the optics fiber by the second spherical lens  $L_2$  ( $f_2 = 125$  mm) and cylindrical lens  $L_3$ . Because the scattering source was a horizontal line, the cylindrical lens played a role in focusing the incoming light in the horizontal dimension, improving the efficiency of the collection.

There was air flow inserted between the viewport and the pinhole to prevent the viewport from soot deposition on it. In addition, a  $N_2$  gas flow was also injected in front of the first spherical lens to keep its surface free from soot deposition. These gas flows were low enough to not influence the soot beam shape.

The main point in this work was to detect Raman spectra of soot in the gas phase. The flame emission background is much too strong to enable detection of a weak Raman signal. In some experiments focusing on the most abundant (molecular) components, pulsed lasers are used. Our strategy relies on the extraction of the flame products to detect online the Raman spectra on a background free source. Rather than using a pulsed laser, a CW laser was used to avoid competing processes like fragmentation or strong laser heating that are attained with the necessary high laser power. This was the way to obtain Raman spectra measurable in the gas phase, online, of nascent soot for the first time.

In addition, we also surveyed the polarization of scattered photon by inserting a Polaroid filter in front of the entrance of the optical fiber. By rotating the polarization axis of the filter by 90 degree, we obtained scattered signals in vertical and horizontal (the scattering plane) dimensions. It is noteworthy that we only used vertically polarized laser for all results presented here. Moreover, the power excitation dependence of Raman spectra was also done, in which the laser power increased from 0.01 to 5 W. Overall, all spectra were achieved at 90 degree configuration. All attempts for forward or backward scattering were unsuccessful because the signal was always dominated by air and optics Raman signal as well as fluorescence for the optics even if special care was taken for their choice to minimize such contributions (materials, laser and UV grade).

### **5.2.2. Flame conditions**

Soot particles were produced at ISMO using the Nanograins setup. The fuel was ethylene ( $C_2H_4$ ) premixed with oxygen, flowed through the burner at a total of  $4 \text{ l}\cdot\text{min}^{-1}$  flow rate.  $N_2$  gas shield around the burning region was applied at two controlled flow rates 0.2 and  $3 \text{ l}\cdot\text{min}^{-1}$ . We inserted Argon gas flow into the region between the cone and Laval nozzle to control the molecular beam shape and cool its temperature down to room temperature. The velocity of Argon was optimized from 0.1 to  $0.5 \text{ l}\cdot\text{min}^{-1}$  in order to reach the maximum overlap of soot beam and incident laser beam in front of the optical collection. Soot particles were detected directly from the soot beam without deposition.

The main purpose in our study was to measure evolution of soot particles formed in the flames. Another target was to detect soot at minimum possible equivalent ratios of flames, at the distance as short as possible. The idea was triggered by the study on the nucleation flame and the soot formation threshold leaded by Pascale Desgroux and Per-Erik Bengtsson's groups. Particularly, the nucleation flames is defined as conditions in which particle size is stable with HAB. In such a flame, recently nucleated particles have undergone marginal surface growth and coagulation [27], [28]. In [29], Sgro et al. define the soot formation threshold as C/O value where light absorption in the visible and LII are detected. In [30], Faccinetto et al. marked the beginning of the soot inception as corresponding to the very first LII detected signals with laser excitation at 1064 nm, and found it consistent with the appearance of yellow luminosity. The lowest equivalent ratio where we start to see soot nanoparticles Raman signal was 2.22 corresponding to C/O ratio is equal to 0.74 at 100 mbar and the shortest distance in this flame condition was 15 mm. This could be similar to the soot formation threshold obtained at 100 mbar in ethylene/oxygen premixed flame detected by Raman technique in our group.

Varying the different flame conditions, the shortest distances where Raman signals of soot started to be seen are remarked by read color in the table 5.1 where the photos are images of flames at various flame conditions with HAB of 21 mm. The obtained Raman spectra of soot varied from weakly sooting flame to strongly sooting flame as shown in this table. In this study, we used two different quartz cones whose diameters are one and two millimeters. The cooling efficiency passing through the Laval nozzle was much less efficient with the 2 mm cone because smaller argon flux had to be used due to the larger extracted (and hot) burnt gas from the flame.



Table 5.1: Summary of flame conditions where soot Raman spectra detected successfully.

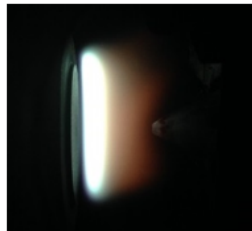
C/O	0.74	0.78	0.82	0.9	0.92	0.95		1		1.05	1.1	1.3	1.6				
$\phi$	2.22	2.34	2.46	2.7	2.76	2.85		3		3.15	3.3	3.9	4.8				
P (mbar)	100	80	60	28	40	28	40	28	40	40	40	40	80				
$d_{Fuel}$ (l.min <sup>-1</sup> )	4	4	4	4	4	4	4	4	4	4	4	4	4				
$d_{N_2}$ (l.min <sup>-1</sup> )	3	3	0.2	3	3	3	3	3	3	3	3	3	3				
d (mm)	15, 18, 24, 30, 36, 42, 48	6, 9, 21, 27, 33, 42	6, 7, 9, 12, 15, 18	18	9, 12, 21, 30	18	12, 30	14, 21, 22, 25, 30, 39	18 21	12, 21, 30	18, 22, 24, 36	6, 8, 9, 10, 11, 12, 13, 24, 18, 19, 10, 22, 24 26, 30, 36, 42, 50	8, 9, 10	28, 40	4, 6, 11, 14, 18, 24, 30, 39, 45, 50	21	30, 50
d <sub>cone</sub> (mm)	2	2	2	2	2	2	1	2	0.2	1	2	1	2	1	1		

C/O = 0.82

C/O = 1.05

C/O = 1.3

d = 21 mm



P : Pressure in the reactor chamber

 $d_{Fuel}$ ,  $d_{N_2}$  : Flow rates of fuel and N<sub>2</sub> gas flows

d: Distance from the burner to the top of the quartz cone. The red values are the distances when we start to see Raman signals.

## 5.3. Results

Raman spectra of soot in the gas phase are very interesting results containing new information on soot. It is necessary to analyze the evolution of Raman spectra of soot along the flames. The content is separated into two main parts. Firstly, we present the data summary in the following subsection, then we focus on the flame condition with  $C/O = 1.05$ .

### 5.3.1. Data summary

This part presents the initial observation consisting in Raman scattering spectra dependence on flaming conditions, sampling distance and polarization as well as power excitation of the incident light. The purpose of this work is to provide an overview of Raman spectra of soot produced in a premixed flame.

#### 5.3.1.1. Spectral response

As mentioned in subsection 3.3.4 of chapter 3, the spectrometer was calibrated by a Neon Mercury lamp. The instrumental response was then measured by the blackbody source. In this scheme shown in Fig. 5.1, the scattering source was located inside the sampling chamber so it was difficult for the blackbody radiation to be inserted at the scattering source position. Therefore, it was installed outside the vacuum chamber, opposite to the collection optics in order to have a source mimicking the scattering source.

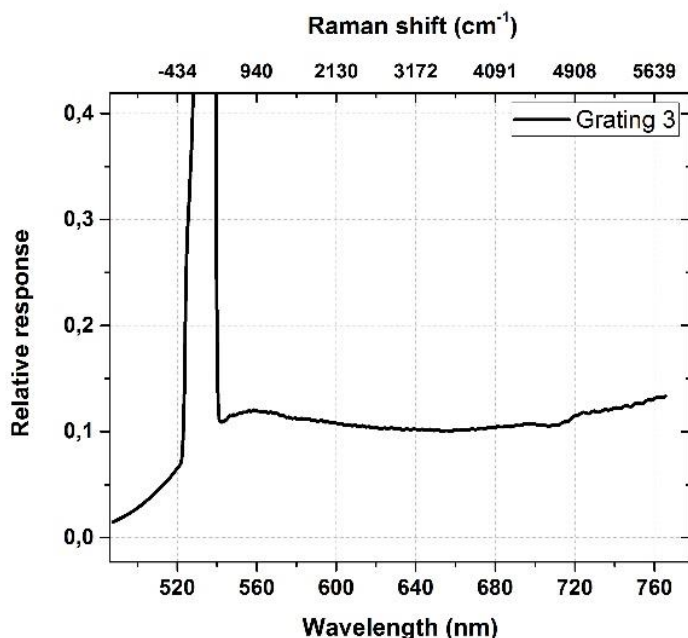


Fig. 5.2. Spectral response of the instruments as a function of wavelength using grating 3 of the spectrometer.

In this case, the instrumental response reflected the transmission coefficient of the collections optics, the optical fiber bundle, the Notch filter, the spectrometer, and CCD camera. The spectral response is shown in Fig. 5.2. A high peak appearing in Fig. 5.2 at ~ 525 to 540 nm was caused by the StopLine notch filter which has OD > 6 blocking around 532 nm. The spectral response from 540 to 760 nm was found quite flat pointing out that no much change in the shape and relative intensities of Raman spectra after transmitting these instruments. Only a small dip is observed at about 700 nm and small interferences fringes are observed above 680 nm probably due to interferences within the interferential filter. Therefore, no corrections were applied to the raw spectra concerning the spectral response of the whole optical system. It should be noticed that this spectral response is very similar to that measure for grating 3 in the DCRS experiments, where the observed variations of about 15% had to be taken into account to improve the cross sections uncertainties.

### 5.3.1.2. Raman scattering spectra dependence on polarization

Polarization effects may be observed for crystalline and highly structured materials where symmetry is evident. Soot is fortuitously constructed of more or less spherically symmetric spherules. There are the spherules formed by polyaromatic units consisting of small layers of graphite, more or less stacked to create structures forming the nanoparticles. Therefore soot should not exhibit polarization dependence because no symmetry can be found at the atomic scale.

In our study, the scattered light was detected at 90 degrees relatively to the incident beam. A Polaroid (rejection ratio about 100) was inserted in front of the entrance of the optical fiber to select either the vertical-vertical (I<sub>vv</sub>) or vertical-horizontal (I<sub>vh</sub>) configurations. The results obtained on spectra of the flames with C/O ratio of 1.05 (P = 40 mbar), 1 (P = 28 mbar) and 1.6 (P = 80 mbar) at some different sampling distances are shown in Fig. 5.3. These reveal several components. A broad fluorescence background is observed at all HAB with varying overall intensities and shapes. The typical Raman bands of soot are superimposed onto this background, with the first order composed of the *G* band located at about 1600 cm<sup>-1</sup>, the *D* band at about 1300 cm<sup>-1</sup> and a weak and broad second order at about 3000 cm<sup>-1</sup>, as usually found for such carbonaceous nanoparticles [32, 35]. These are observed for the first time in the gas phase, to our knowledge.

The shapes of their spectra of vertical and horizontal components were found unchanged; only their absolute intensities seemed slightly different. However, the transmission coefficients differ (very) slightly with the polarization as revealed by a measurement using a calibrated blackbody light source. It should be recalled here that the fibers are not polarization maintaining and that the overall response of the optics and spectrometer acquisition system (including a grating) was checked for both polarization and measured not sensitive.

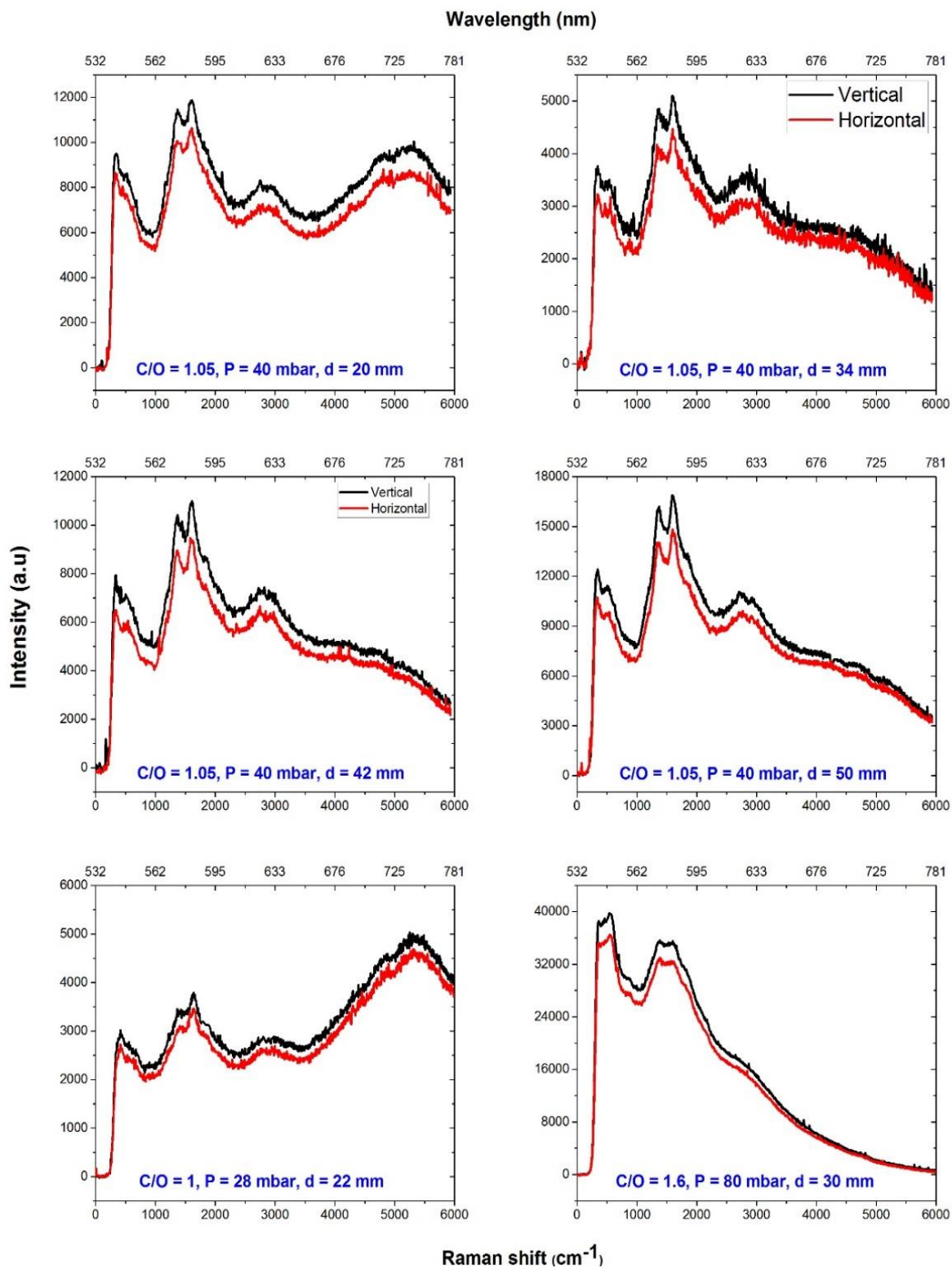


Fig. 5.3. Vertical and horizontal polarization components in spectra of various flame conditions. The acquisition time is 200 sec.

Soot particles are constructed of nearly spherical nanoparticles with disordered nanostructure. These primary particles are formed in the early stage of soot growth. Therefore, the Raman spectra of isolated soot primary particles should not exhibit polarization dependence. This has been observed for the first time measuring the depolarization ratio  $I_{VH}/I_{VV}$  of the Raman bands of soot upon polarized laser irradiation. It is found to be 1 for all soot measured. This property could be used to discriminate between large molecular compounds in the form of PAH, where molecular symmetry could lead to polarization effects, and the soot nuclei. Raman scattering could thus be used to probe the transition between the suspected PAH precursors and the soot nuclei.

### 5.3.1.3. Raman scattering spectra dependence on flame condition

#### *a. Soot Raman spectra dependence on burning conditions*

We have explored the dependence of Raman signals on soot on flaming pressure. For low pressure flames, the pressure has a huge incidence on soot kinetic [31]. At 42 mm from the burner, 1.05 C/O ratio flame was operated under 33 and 48 mbar flaming pressure, and the polarization of excitation light is horizontal. The Raman spectra are shown in Fig. 5.4. From this figure, it can be seen that the pressure has a strong effect in the recorded spectra by changing the background and the superimposed Raman band shapes. This parameter is controlled with a precision better than 1 mbar in our experiment, hence making the conditions more reproducible because our acquisition time may increase up to nearly 1 hour for some spectra.

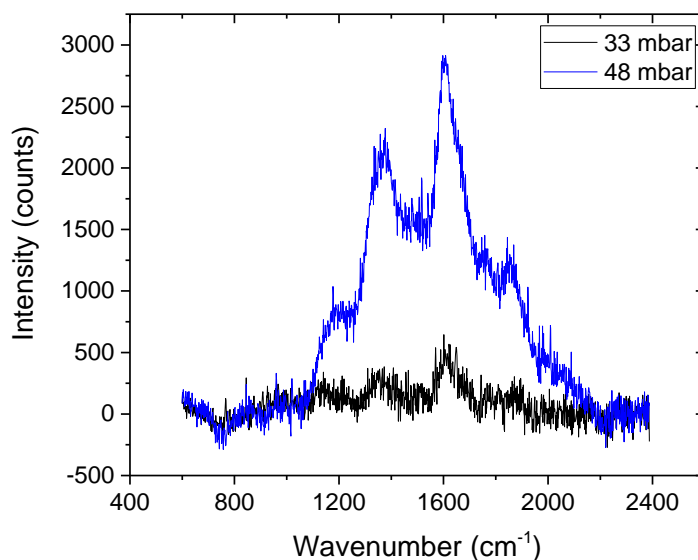


Fig. 5.4. Raman spectra of soot produced by 1.05 C/O ratio flame at 33 and 48 mbar.

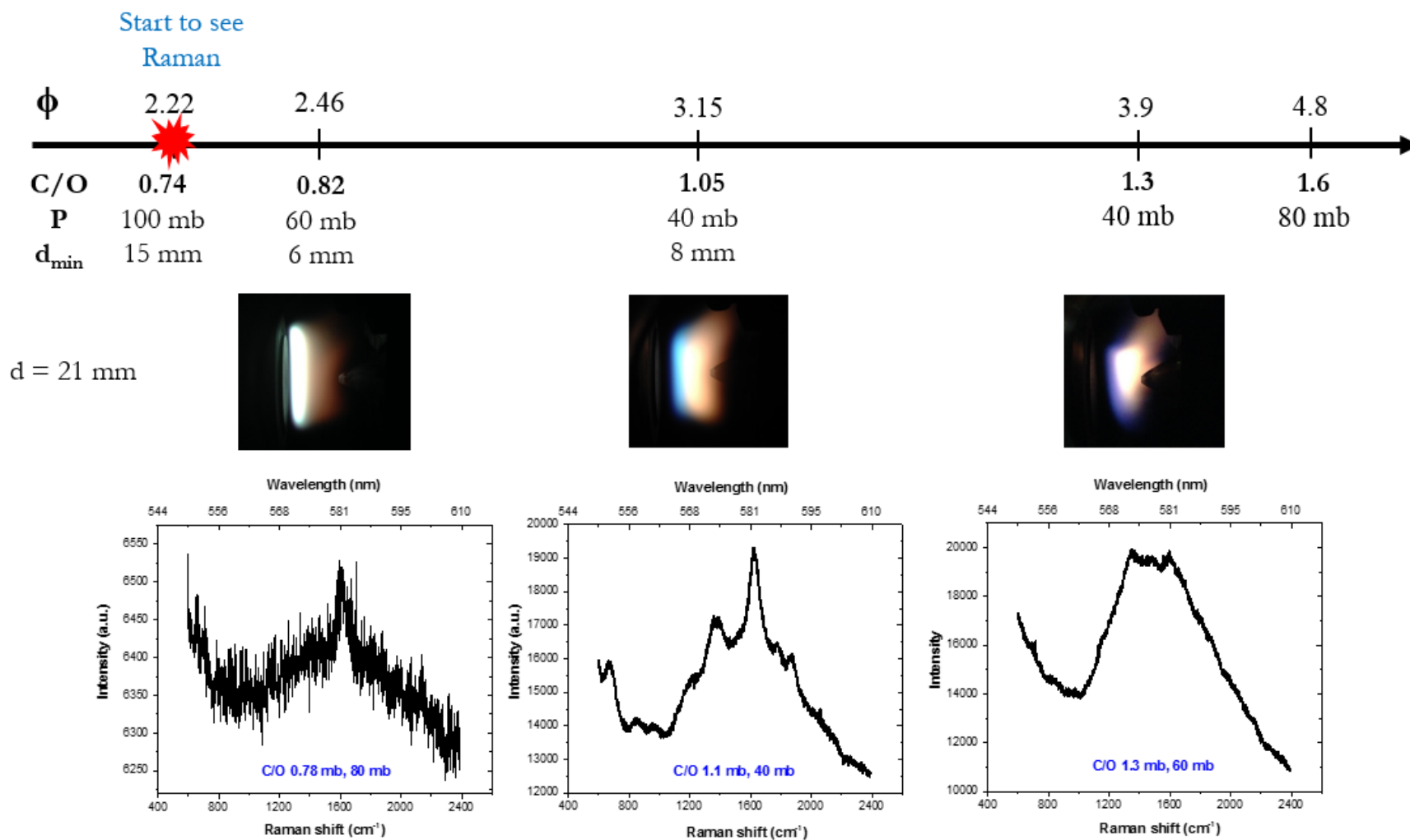


Fig. 5.5. From the left to the right, gas phase Raman spectra of flames whose C/O ratios are respectively 0.78, 1.1 and 1.3 as a function of Raman shift. The acquisition time is 200 sec.

We tried to detect soot nanoparticles at minimum possible equivalent ratio of flames and at the HAB as short as possible. The pressure could be adjusted to obtain an observable Raman signal, although the lowest value was searched for each condition. The explored flames varied from weakly to strongly sooting flames as shown in Fig. 5.5. The lowest equivalent ratio where we start to see Raman signals is 2.22 corresponding to a  $C/O = 0.74$  at 100 mbar and the shortest HAB is 15 mm (mentioned in table 5.1). It should be recalled that for rich flames, the threshold between non-sooting and sooting flame is found in the 1.8-2 equivalent ratio range.

In order to show the variability of the Raman spectra, we also monitored different flame conditions at 21 mm from the burner. They were totally different although their sampling distances (HAB) were the same. In particular, the shapes of *D* and *G* bands in the two first figures were obtained for soot classified as “aliphatic rich soot” when analyzed ex situ while in the last figure, sampled soot belongs to the “aromatic rich soot” classification, as explained in chapter 4.

All these spectra proved that structures and mechanism of soot evolution are strongly dependent on flame conditions such as pressure, HAB and C/O ratio. It is consistent with the findings from ex situ analysis that their structures and their optical properties vary with the HAB and burning conditions as well. It confirms the pertinence of measuring online Raman spectra to analyze soot structures during the soot birth and growth.

#### 5.3.1.4. The excitation power dependence of scattered intensity

Soot was mainly excited by a continuous laser at power of 5 W. This power is very high which might cause heating of the soot by multiphoton absorption and lead to temperature dependence effects of the spectra and even to fragmentation of soot particles. If this effect happens, the structure of soot may also be changed leading to the change of their Raman spectra. By decreasing the laser power from 5 W to 0.01 W, Raman spectra of soot produced by the same flame condition and HAB were explored. From obtained spectra in Fig. 5.6, it is clear that when the power is higher than 0.1W, there is the simultaneous increase of the whole spectral intensity with the power of exciting laser, but the shape of spectra is maintained. It is worth noting that 5 W of exciting laser still locates in the limit where soot structure is not influenced. This study reveals that neither heating effects nor structural changes are observed.

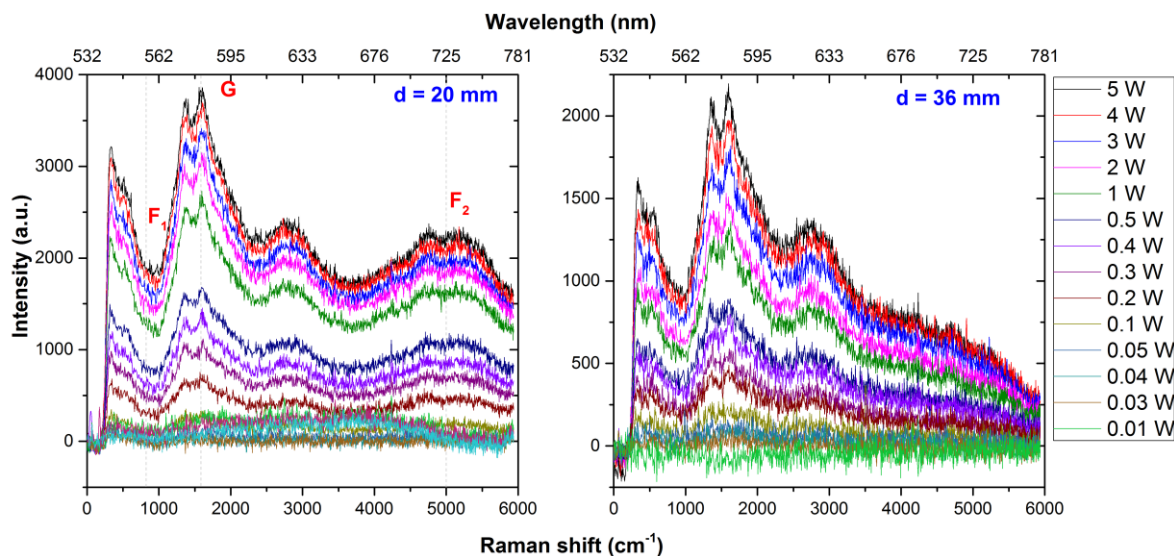


Fig. 5.6. Effect of the excitation power on spectra measured for Flame ( $C/O = 1.05$ ,  $P = 40$  mbar) at 20 and 36 mm with 200 sec for acquisition time.

It is noteworthy that the molecular flow velocity is in the range of 100 m/s ( $\sim 400$  m/s in the supersonic flow conditions, not attained here) and this is approximately the soot particles velocity as well. It implies that each soot experiences laser heating during only about 1 ms (upper estimation) in our experimental configurations. At 5W, it corresponds to a pulse of about 1 ms duration (upper estimation) with about  $0.15 \text{ J/cm}^2$ . Although such energy density is similar to that used in laser induced incandescence with nanosecond pulse duration, here the heating is lasting for 1 ms and is in competition with the collisional cooling in the flow of argon and the radiative cooling. It appears that it is not enough to efficiently heat the particles. It should be mentioned that we explored the cooling effect of the argon flow by varying it from 0 to  $1 \text{ l.min}^{-1}$ . No effects could be observed, pointing out that already collisions with the wall of the chamber after extraction and before flowing through the nozzle already thermalize the gas extracted and the soot to a temperature closer to room temperature rather than to the flame temperature.

For the  $HAB=20 \text{ mm}$ , area of the broad fluorescence observed at a Stokes shift of about  $5000 \text{ cm}^{-1}$ , area of the underlying fluorescence measured at a Stokes shift below  $1000 \text{ cm}^{-1}$  and the difference of the amplitudes between the maximum of the  $G$  band at about  $1600 \text{ cm}^{-1}$  and the dip between the  $G$  and  $D$  Raman bands are reported in Fig. 5. 7 as a function of laser power. The choice for this tracer of the Raman band intensities allows discriminating these from their underlying background without any hypothesis on the shapes of the fluorescence, as discussed in the following sections. They all follow the same trend, i.e. a typical saturation curve. This result is expected for fluorescence because it is a linear process with the power and saturation is expected for the absorption step. In the case of Raman, no saturation should be observed as long as the process is non-resonant. It is not the case here, as discussed in chapter 3 for the high DCRS values measured, and thus a



saturation curve is expected as the Raman scattering process is resonant for the soot nanoparticles. If molecules like small PAHs would be observed, their first electronic excited states would be higher in energy than the photon energy used here (2.33 eV) and resonant effects would not be at work. For those types of species saturation curves should not be observed.

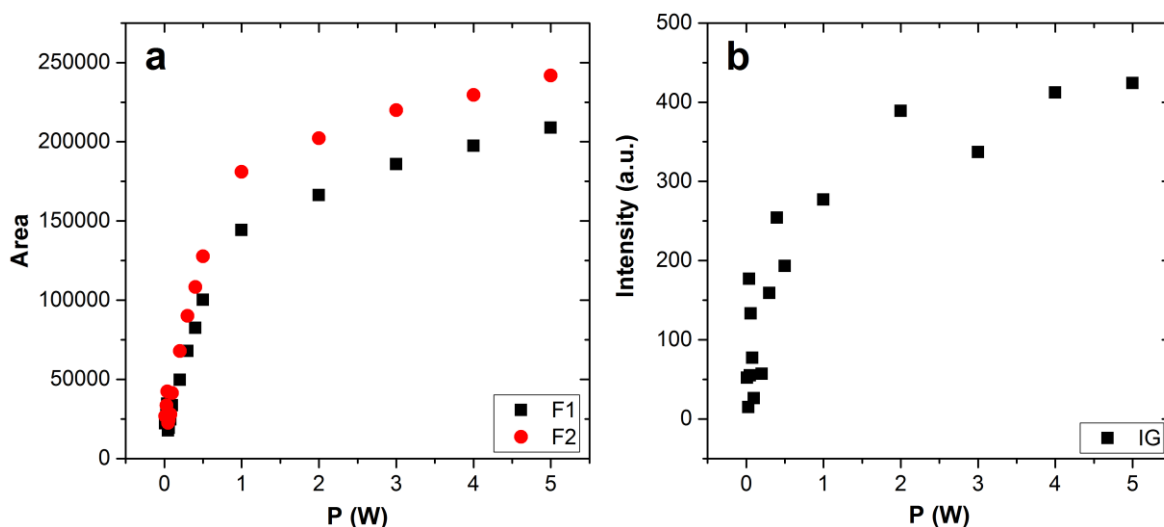


Fig. 5. 7. Power excitation dependence of fluorescence (a) and Raman (b) signals of C/O = 1.05 flame at HAB = 20 mm. (a) F1 and F2 denote areas of the underlying fluorescence measured at (900-1000  $\text{cm}^{-1}$ ) and (4700-4800  $\text{cm}^{-1}$ ). (b)  $I_G$  is the difference of the amplitudes between the maximum of G peak and the valley between D and G bands.

### 5.3.1.5. The evolution of Raman spectra of soot from the blue zone to the orange zone of flames

When the HAB was increased gradually, we succeeded in obtaining Raman spectra of flaming products from the blue zone to the orange zone of the flames. Whatever flame conditions were, when the sampling distances increased, we always saw a general trend in which the signal intensities grown up and reached the maximum value then went down and finally recovered. The distances where the maximum signals were seen depended on the flame conditions. Fig. 5. 8 shows the evolution of Raman spectra of soot in four different flames. With the first two flames, we only monitored the first order of Raman spectra spectral region, then the observation was broaden to consider the second order of spectra and further signals at longer wavelength.

These spectra contain both Raman scattering and fluorescence signals. The main difficulty which we had to face with in treating the data was how to separate each component. The more detailed analysis will be presented in the following sections.

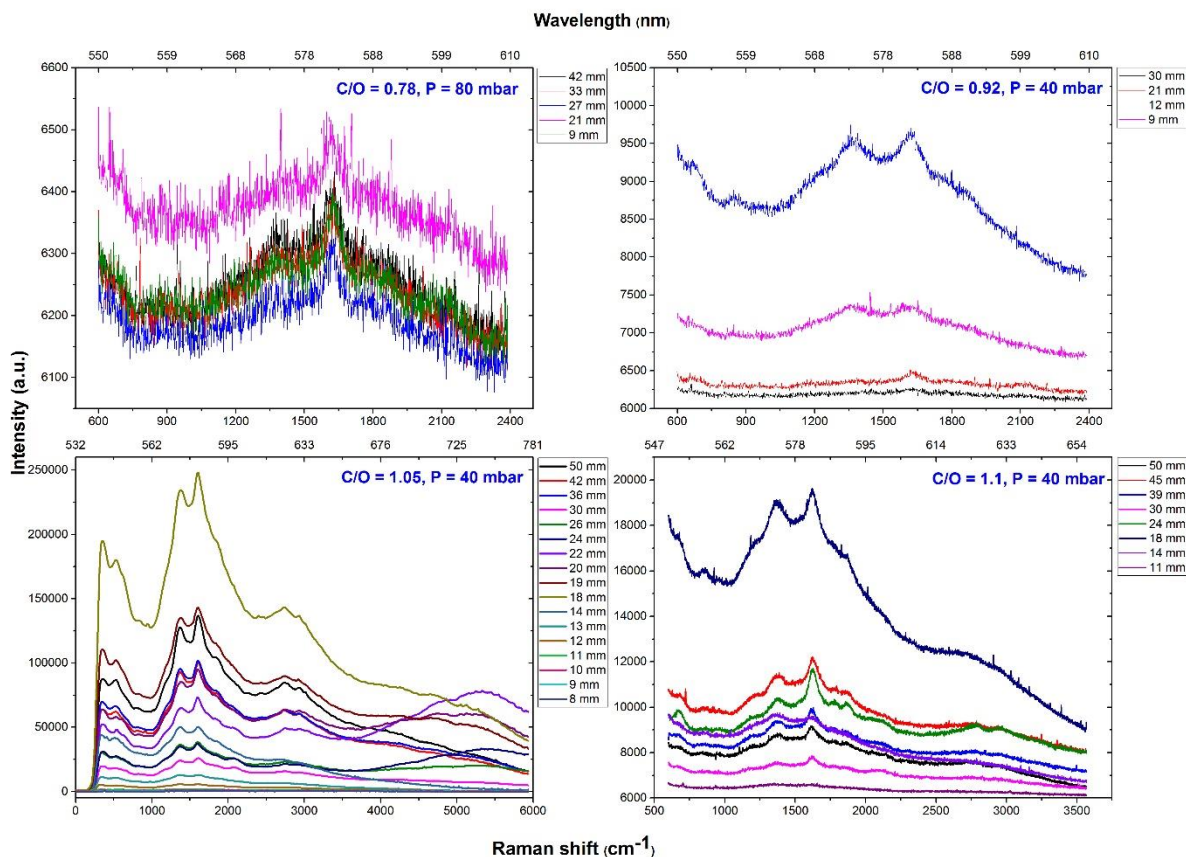


Fig. 5. 8. The evolution of spectra of including the gas phase Raman of soot from the blue zone to the orange zone for a series of the flame conditions. With  $C/O = 0.78$  and  $C/O = 0.92$  flames, we plot the first order Raman spectra as a function of Raman shift and their acquisition times were 500 sec. With  $C/O = 1.1$  flame, we considered the first and second order of their Raman spectra and the acquisition time was 500 sec. With  $C/O = 1.05$ , Raman spectra as a function of Raman shift were considered from the first order to the end of visible range and the acquisition time was 1000 sec.

### 5.3.2. The flame with 1.05 C/O ratio at 40 mbar

In the previous section, we described several flame conditions concerning the evolution of Raman spectra in those flames. We will now focus only on the 1.05 C/O ratio at 40 mbar flame condition. There was a set of measurements of spectra of soot at various sampling distances. This study has enabled detailed investigation of the evolution of soot in a premixed flame by online Raman, in the gas phase, for the first time.

#### 5.3.2.1. Raman measurement and spectral analysis

Fig. 5. 9 reports the evolution of spectra of soot during flame combustion, as a function of HAB. On the left of Fig. 5. 9, from the top to the bottom, there are several images of the quartz cone inserted into the flame at 50, 40, 22, and 14 mm from the burner

surface. Next to the images, spectra of soot at various sampling distances were vertically translated, the arrangement following the sampling distances. All are unscaled and monitored with the same conditions, laser power and acquisition time. Thus relative intensities are real. It should be recalled that the hole diameter of the sampling cone is 1 mm, giving an effective sampled volume having a similar radius thus a spatial resolution for the HAB about 2 mm or slightly less. This should be kept in mind when regarding the spectral evolution as a function of HAB.

There are several remarkable points in these spectra. The first point is the appearance of Raman symmetric stretching band of ethylene (the precursor) at  $3025\text{ cm}^{-1}$  at the close distances from 6 to 11 mm from the burner. The Raman band intensity of ethylene decreases while the HAB increases. Then it disappears simultaneously with the appearance of a Raman signal showing bands with characteristics close to the *G* and *D* bands, thus probably those of the first soot particles. The second point is a broadband visible emission at 750 nm. This emission band appears clearly in spectra at some sampling distances, from 18 to 36 mm. This band at 750 nm builds-up then reduces and red shifts when the sampling distance increases. The final point is the appearance of shoulder peaks at approximately  $1900$  and  $2100\text{ cm}^{-1}$  at the first order, close to the typical *G* and *D* bands in Raman spectra of soot. In order to observe clearly the evolution of the emission, the spectra are normalized to the *G* peaks in Fig. 5. 10 for all sampling distances from 11 to 50 mm. At the shortest sampling distances, the signal to noise ratio of spectra is too low so we don't plot them in this figure.

One key step in data treatment is to obtain pure Raman signals of soot from these spectra, i.e. to remove the emission contribution without additional information. The protocol for this step starts from the normalized spectra in Fig. 5. 10. Based on the appearance of a broadband visible emission at 750 nm, these spectra could be classified into two groups: the first one for soot produced at lower HAB than 14 mm with the absence of the broadband and the second one for that at further distances with the observation of this emission band. The spectrum of products extracted at shorter 14 mm sampling distances contains Raman signals spreading from  $920$  to  $3700\text{ cm}^{-1}$  and the contribution of their fluorescence. We do not know the fluorescence spectra of the products extracted from our flame. However, we know that fluorescence is expected from the population of PAH that should be present in the flame [32], [33].

Regarding the strength of the signal, it is clear that this fluorescence is weak because it does not overwhelm the Raman signal. In addition it has been shown that the shape of this fluorescence may not change much with HAB [34]. Therefore, a straight line segment is used between two points whose abscissas are  $920$  and  $3700\text{ cm}^{-1}$  on the spectra and enabled to extract the Raman spectra of the soot. It should be noted that background in Raman spectroscopy is always an issue and most of the time a simple linear background is used for simplicity. Here, it is done in an unusual way because the straight line covers the first and second order range. This is due to the presence of bands at higher energies than the

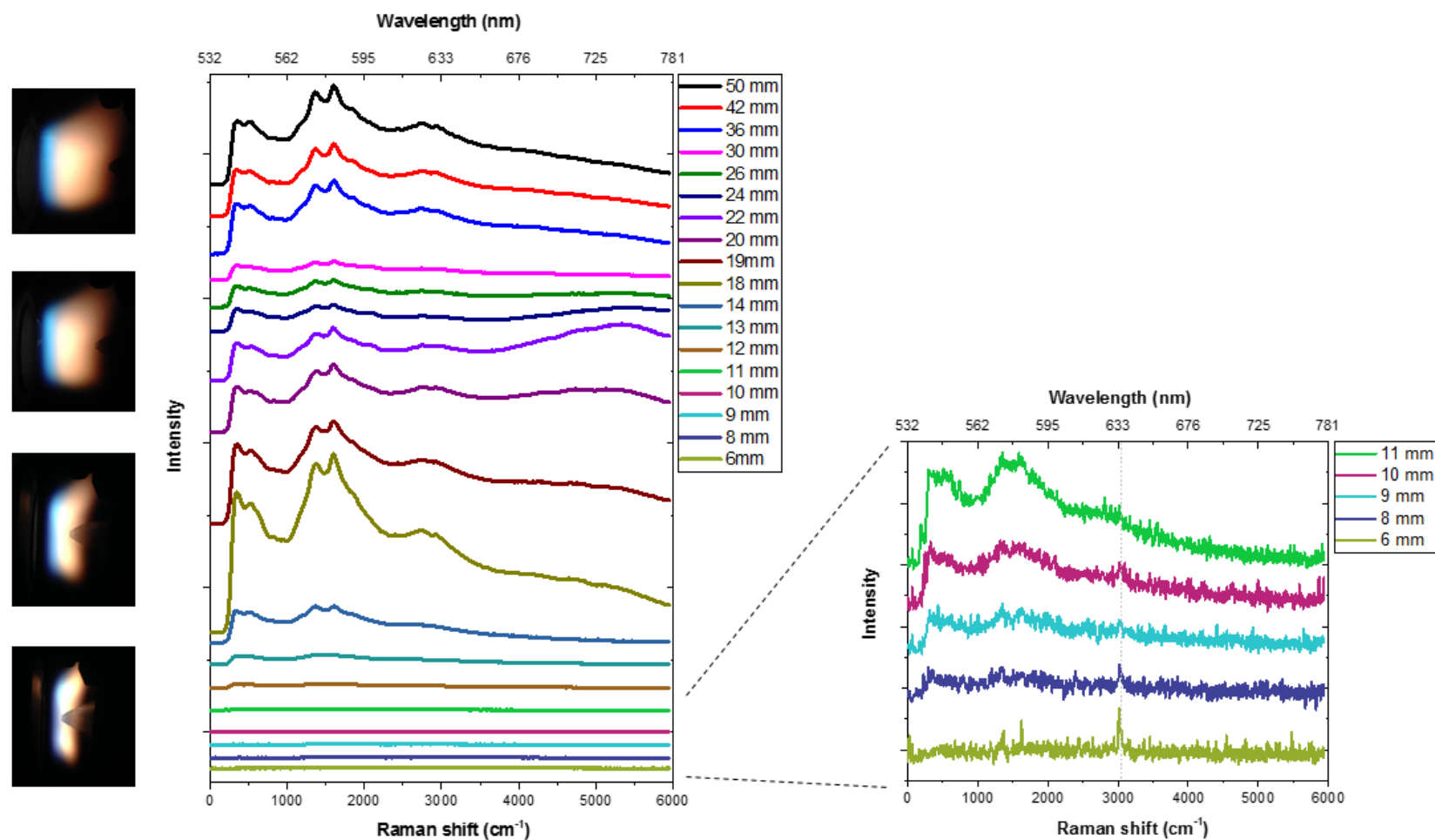


Fig. 5. 9. The evolution of gas phase Raman spectra of soot produced by 1.05 C/O ratio flame at the sampling distances from 6 to 50 mm. On the left, the photos show the images of the quartz cone inserted in the flame at different positions. All are unscaled and monitored with the same conditions, laser power and acquisition time. Thus relative intensities are real and comparable.

G band ( $\sim 1600\text{ cm}^{-1}$ ) whose assignments will be provided in the following sections. The purple area in Fig. 5. 11a is considered as the first fluorescence component. At further sampling distances, in addition to these two components, there is also the appearance of the broad red emission band (shown in Fig. 5. 11b).

In summary, we could separate each spectrum into three components: the contribution of fluorescence considered as the background (called 1<sup>st</sup> fluorescence), the broadband red emission (called 2<sup>nd</sup> fluorescence) and the appearance of Raman spectra of soot containing the first and second orders. Note that the shape of fluorescence of soot at 14 mm is used as the reference of the first fluorescence component in all spectra. In particular, this fluorescence curve is rescaled with a factor corresponding to the intensity difference between this curve and other spectra at position around  $920\text{ cm}^{-1}$ . After subtracting the first fluorescence component, a linear line segment connect between two points whose abscissas are  $920$  and  $3700\text{ cm}^{-1}$  on the rest of each spectrum to separate this region into Raman signal and the emission band. It should be emphasized that the second fluorescence component appears at longer wavelength range where almost no contribution of the first fluorescence component is found. The former refers to emission a small shift relative to the excitation wavelength and the latter measures the contribution at long wavelength, stating that it does not imply that there have to be different emitters at a given HAB.

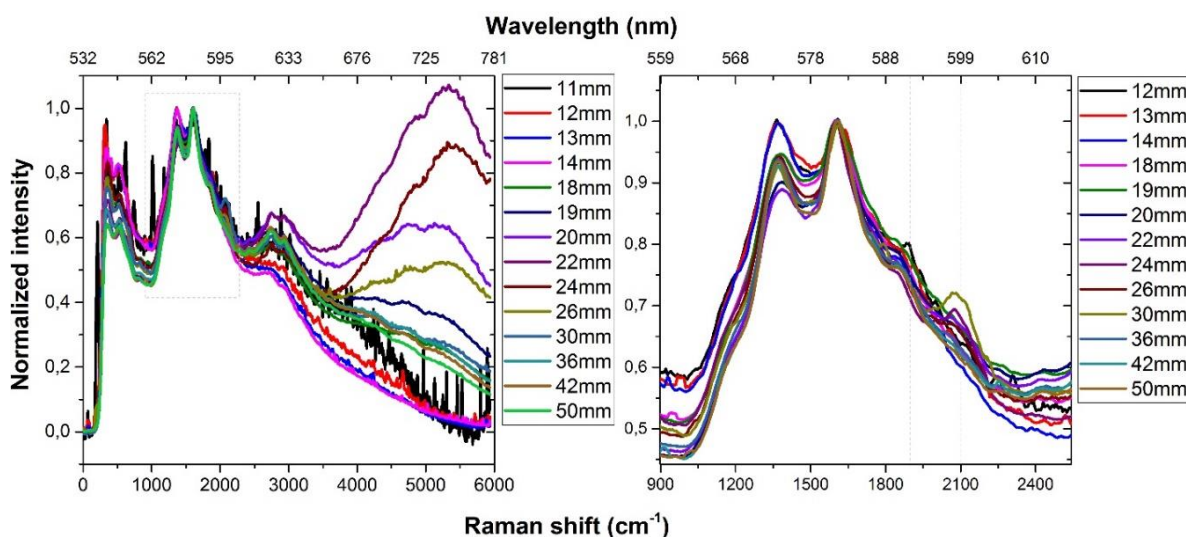


Fig. 5. 10. Normalized gas phase spectra of soot produced by 1.05 C/O ratio flame at the sampling distances from 11 to 50 mm. The first order Raman of soot range is zoomed in on the left figure.

In summary the measurements in ethylene premixed flame indicate that the spectra of flame products excited by CW laser at 532 nm is composed of Raman and fluorescence signals which seem to be directly connected to soot formation process. By dividing each full spectrum into three components, spectra of soot have become less complicated. In the following sections, these components will be analyzed alternatively.

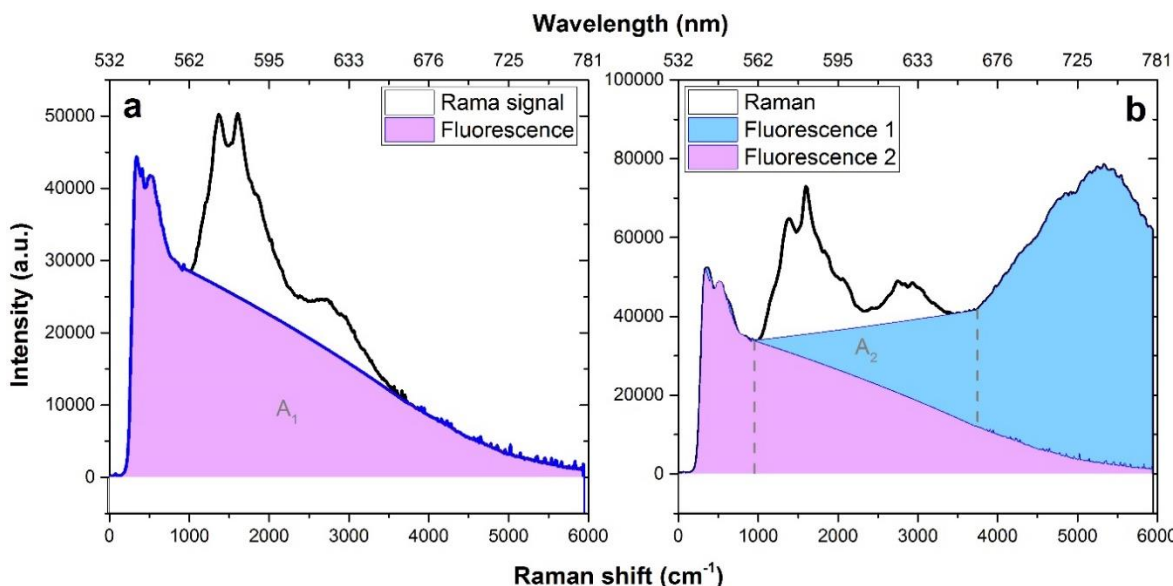


Fig. 5.11. Fluorescence and Raman signal in spectra of soot produced at 14 mm (a), and 22 mm (b). A simple linear background is assumed under the Raman signal from soot nanoparticles. The emission in purple is then used to decompose and extract the broad emission at longer wavelength (in blue).

### 5.3.2.2. Deconvolution of Raman spectra of soot in the gas phase

After fluorescence subtraction, Raman spectra of soot are plotted in Fig. 5.12. They contain the first and second orders of vibrational modes of soot extracted directly from the flame. Curve fitting for the determination of spectral parameters was performed with cftool toolbox of software program Matlab R2013a. The R-square value computes the coefficient of determination value from actual data and model data. First and second orders were fitted simultaneously with fixing and limiting the range of FWHM of  $D_1 + G$  and  $2D_1$  peaks was 1 to 2 times larger than that of  $D_1$  and  $G$  peaks, alternatively. The first order Raman band of soot in the gas phase generally exhibit two broad and strongly overlapping peaks with intensity maxima at  $\sim 1370$  cm<sup>-1</sup> and at  $\sim 1610$  cm<sup>-1</sup>. In addition, as mentioned above, the appearance of two shoulder peaks at  $\sim 1900$  cm<sup>-1</sup> and  $\sim 2100$  cm<sup>-1</sup>. Because of the overlapping and broad form of  $D$  and  $G$  bands, instead of decomposing the first order band into five typical bands ( $D_1$ ,  $D_2$ ,  $D_3$ ,  $D_4$ ,  $G$ ) as Raman spectra of soot films in chapter 4, we only use the combination of  $D_1$ ,  $D_4$ ,  $G$  and  $C_1$ ,  $C_2$  (for the shoulder peaks). Fig. 5.13 sketches four different combinations of Raman spectra of soot obtained at 50 mm from the burner. The line shapes of peaks are detailed detail in Table 5.2.



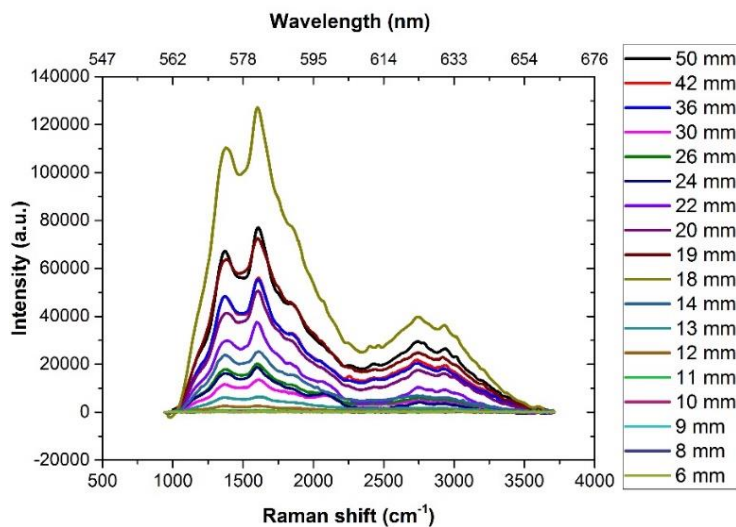


Fig. 5. 12. Gas phase Raman spectra of soot from the as a function of Raman shift after subtracting the first and second fluorescence components.

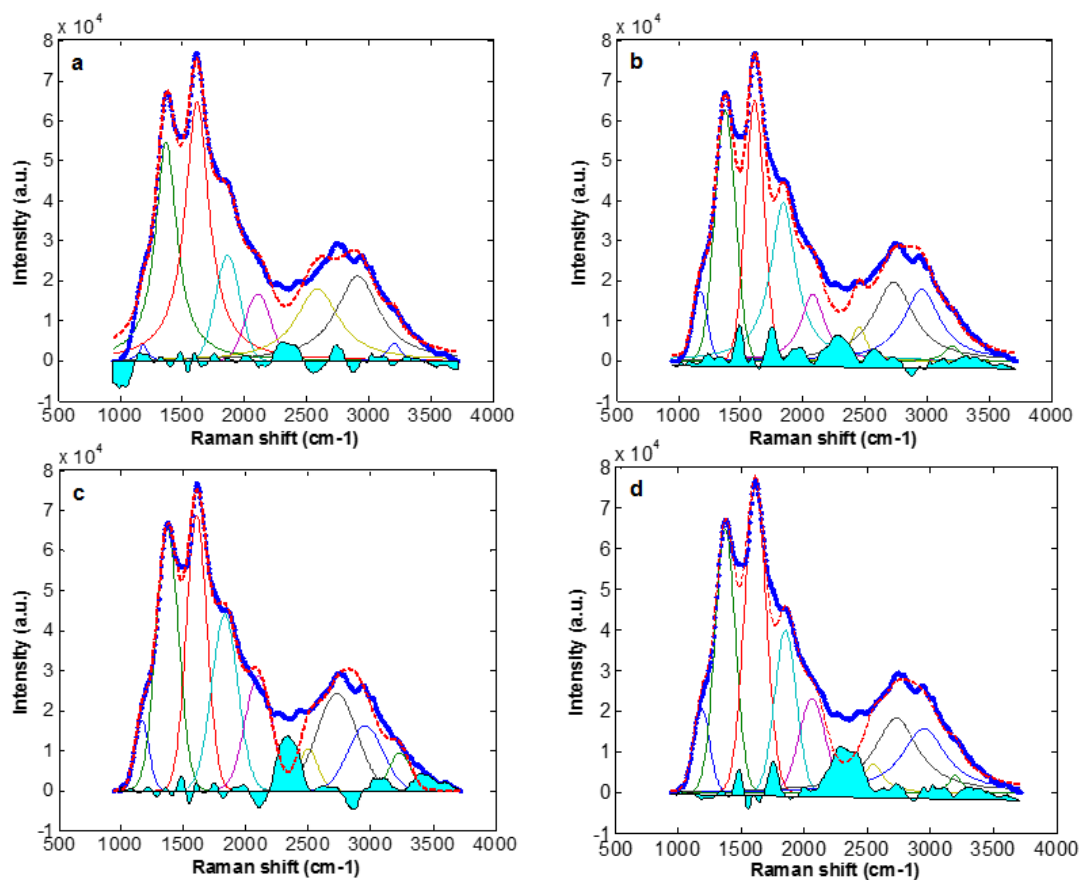


Fig. 5. 13. Deconvolution of Raman spectra of soot in the gas phase with HAB = 50 mm, in which: blue dot line is data, red dot line is fit curve, bright blue filled area is the difference between data and fit data.

Table 5.2: Band combinations tested for curve fitting of the first and second order Raman spectra of soot in the gas phase (L = Lorentzian, G = Gaussian)

Band	D <sub>4</sub>	D <sub>1</sub>	G	C <sub>1</sub>	C <sub>2</sub>	2D <sub>4</sub>	2D <sub>1</sub>	D <sub>1</sub> +G	2D <sub>2</sub>	R-squared
Initial position (cm <sup>-1</sup> )	1180	1370	1609	1850	2058	2550	2750	2950	3200	
a	L	L	L	G	G	-	L	L	L	0.988
b	G	G	G	L	L	L	L	L	L	0.981
c	G	G	G	G	G	G	G	G	G	0.961
d	G	G	G	G	G	L	L	L	L	0.965

After testing various fitting ways, it is clear that something misses between the first and the second order. Therefore, we propose that a second order polynomial function could be added as the background (Fig. 5. 14), in which the maximum of this background is located at around 2200 - 2300 cm<sup>-1</sup>. This approach will help to test the robustness of the choice of band modeling using C<sub>1</sub> and C<sub>2</sub> bands, and to explore the effects of the unknown background shapes.

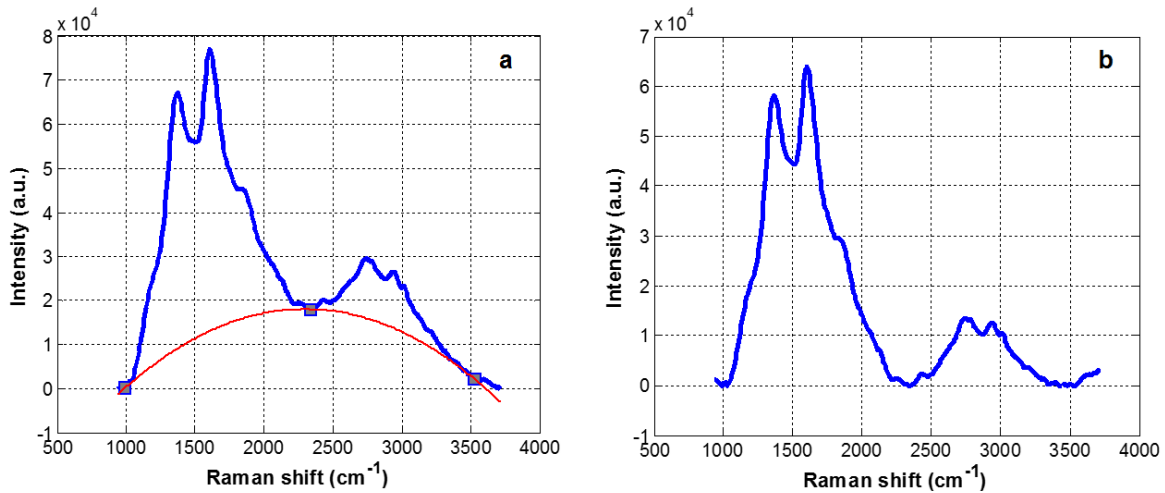
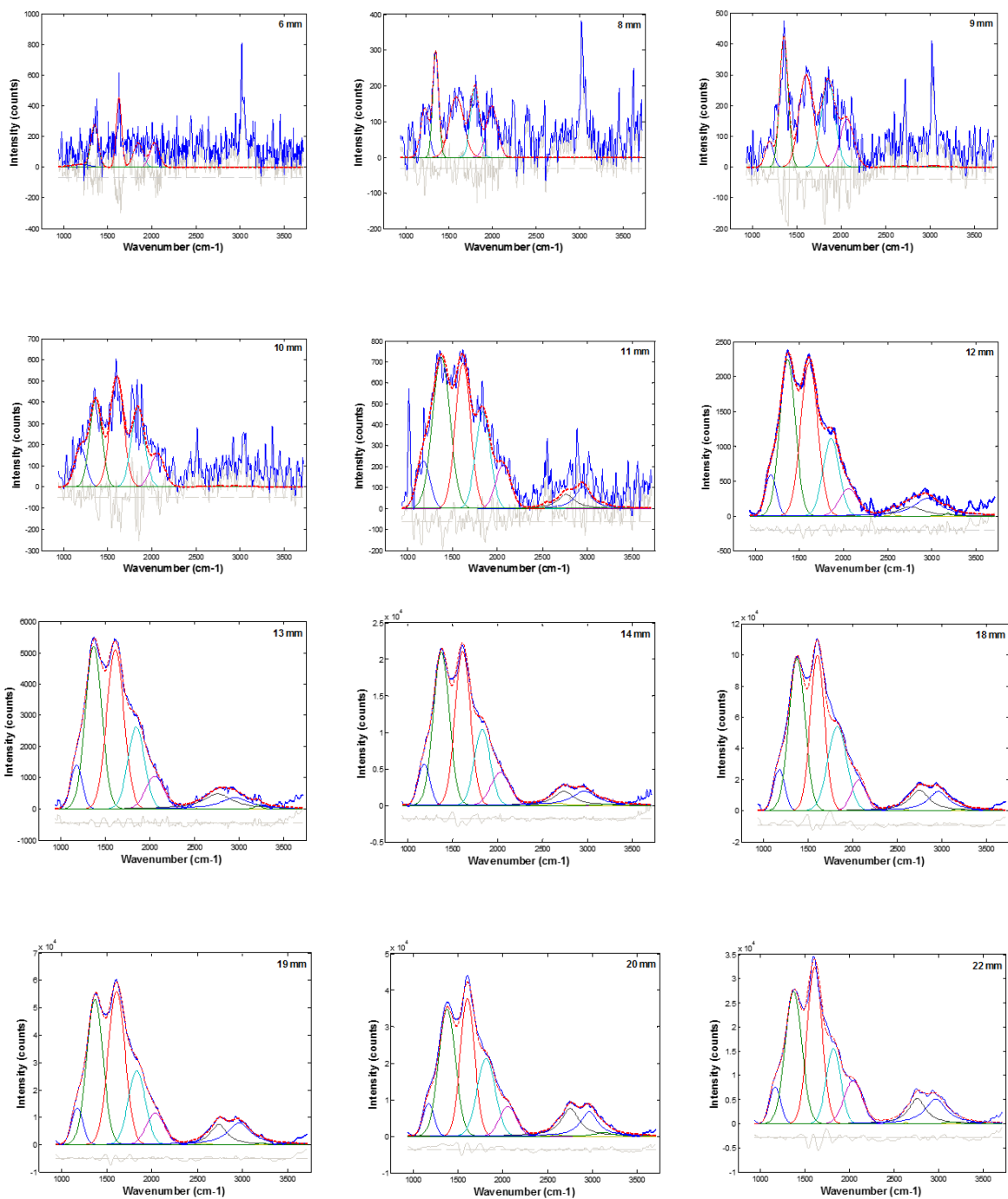


Fig. 5. 14. a) Raman spectrum of soot at HAB = 50 mm before subtracted background. b) Raman spectrum of soot at HAB = 50 mm after subtracted background

Moreover, although the first order requires Gaussian function for the bands to provide a better fit, those of the second order should be fitted by Lorentzian function rather than Gaussian function.





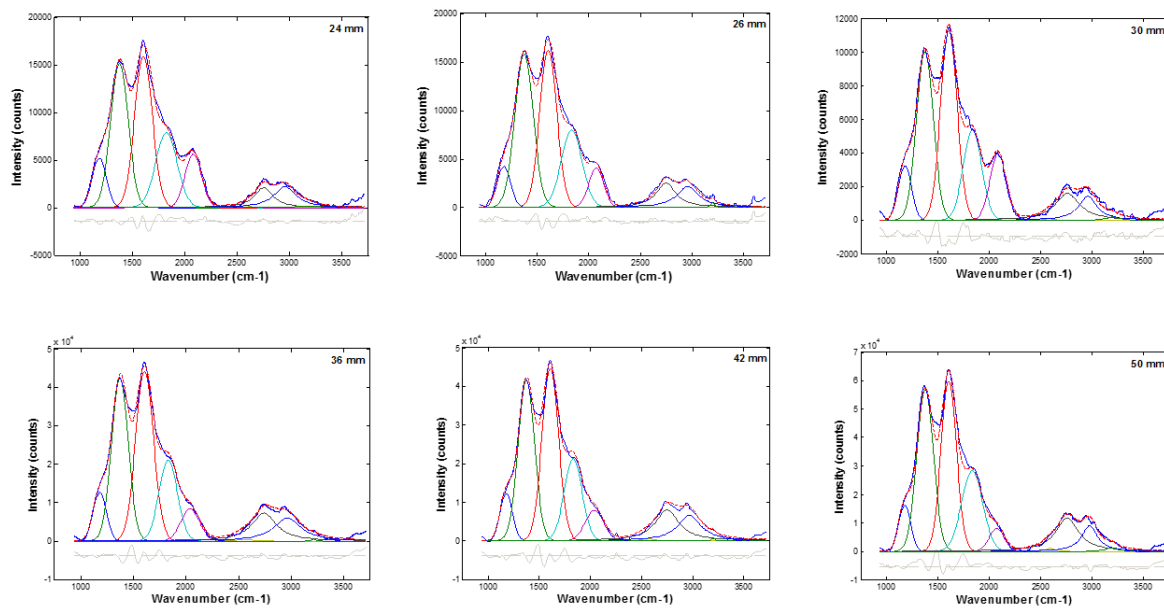


Fig. 5. 15. Curve fit with band combination for the first and second order of online Raman spectra of soot produced by 1.05 C/O Ethylene flame. The blue dot lines are Raman spectra, the red dot lines are fitted curves, grey curves are the difference of fit and data curves.

Overall, Raman spectra of soot in the gas phase could be decomposed by five Gaussian for the first order and four Lorentzian for the second order as shown in Fig. 5. 15.

Table 5.3: Raman fit parameters. Note that the uncertainty of the peak position is lower than 10% of its peak width.

*The first order*

d [mm]	$\omega_{D_4}$ [cm <sup>-1</sup> ]	$\omega_{D_1}$ [cm <sup>-1</sup> ]	$\omega_G$ [cm <sup>-1</sup> ]	$\omega_{C_4}$ [cm <sup>-1</sup> ]	$\omega_{C_2}$ [cm <sup>-1</sup> ]	$\gamma_{D_4}$ [cm <sup>-1</sup> ]	$\gamma_{D_1}$ [cm <sup>-1</sup> ]	$\gamma_G$ [cm <sup>-1</sup> ]	$\gamma_{C_1}$ [cm <sup>-1</sup> ]	$\gamma_{C_2}$ [cm <sup>-1</sup> ]	$A_{D_4}$	$A_{D_1}$	$A_G$	$A_{C_1}$	$A_{C_2}$
6	1181	1350	1627	1845	2031	286,1	100	69,86	127,3	125,2	5615	29210	33740	21620	21320
8	1220	1345	1586	1799	1992	108	80	193,8	120	150	16000	25000	34980	24990	23000
9	1193	1356	1607	1854	2066	104	110	189,6	182,3	182,2	9214	49750	60180	54580	30070
10	1190	1364	1603	1842	2067	151,2	159,7	180	175	182	29990	71040	99950	69970	30070
11	1175	1373	1616	1839	2064	171	230	196,2	192,2	195,7	41010	176600	144700	94430	43580
12	1175	1364	1611	1859	2058	142,8	207,4	226,5	215,6	243,3	90370	496900	530500	256000	101400
13	1178	1368	1613	1847	2053	146,9	216,4	226,3	217,1	238,6	218600	1,201E6	1,225E6	605600	265100
14	1180	1372	1612	1830	2030	149	210,3	201	207,6	244,1	900200	4,703E6	4,525E6	2,309E6	1,168E6
18	1178	1375	1605	1828	2068	144	212,5	186,2	248,8	192,2	4,052E6	2,213E7	1,979E7	1,434E7	4,033E6
19	1174	1367	1608	1831	2036	143,6	213	220,4	220,9	232,8	2,032E6	1,204E7	1,313E7	6,356E6	2,835E6
20	1170	1375	1604	1813	2056	140,3	222,2	187,5	237,7	218,7	1,331E6	8,244E6	7,546E6	5,409E6	1,908E6
22	1169	1372	1611	1821	2042	142,3	220	195	188,5	238,5	1,145E6	6,409E6	6,719E6	3,125E6	2,256E6
24	1181	1372	1604	1822	2079	154,8	199,4	199,8	240,5	184,2	857000	3,209E6	3,377E6	2,013E6	1,101E6
26	1176	1371	1607	1833	2072	149,2	210,5	195	237	168,7	665400	3,54E6	3,371E6	2,018E6	726000
30	1182	1374	1608	1837	2085	146,1	193,4	188,9	209,9	185,1	501900	2,068E6	2,268E6	1,201E6	774900
36	1181	1372	1608	1832	2041	145,5	187,4	200,3	204,9	206,9	1,945E6	8,441E6	9,409E6	4,593E6	1,837E6
42	1179	1374	1609	1831	2039	137,5	188,5	190,5	204,1	211,6	1,792E6	8,351E6	9,057E6	4,636E6	1,776E6
50	1179	1376	1607	1834	2072	133,9	190,8	176,2	240,3	169,1	2,306E6	1,155E7	1,123E7	7,245E6	1,458E6

Table 5.4: Raman fit parameters. Note that the uncertainty of the peak position is lower than 10% of its peak width (*continuous*).*The second order*

d [mm]	$\omega_{2D_4}$ [cm <sup>-1</sup> ]	$\omega_{2D_1}$ [cm <sup>-1</sup> ]	$\omega_{D_1+G}$ [cm <sup>-1</sup> ]	$\omega_{2D_2}$ [cm <sup>-1</sup> ]	$\gamma_{2D_4}$ [cm <sup>-1</sup> ]	$\gamma_{2D_1}$ [cm <sup>-1</sup> ]	$\gamma_{D_1+G}$ [cm <sup>-1</sup> ]	$\gamma_{2D_2}$ [cm <sup>-1</sup> ]	$A_{2D_4}$	$A_{2D_1}$	$A_{D_1+G}$	$A_{2D_2}$
6	--	--	--	--	--	--	--	--	--	--	--	--
8	2500	2758	2941	3198	100,5	108,88	210,3	251,3	12,38	10,56	10,81	10,61
9	2526	2712	3030	3312	142,3	104	110	106,2	483,2	562,6	1269	759
10	2529	2760	2951	3205	135,7	174,4	180	170	189,5	1046	1093	200,7
11	2543	2764	2952	3191	65,72	230	196,2	101,4	1425	24180	32730	1244
12	2556	2759	2950	3184	33,04	352,6	306,1	72,67	2631	73070	146000	5066
13	2518	2760	2952	3210	2,411	389,5	384,7	66,31	379	294500	217500	13740
14	2667	2739	2967	3227	143,7	265,4	324	144,4	74860	808400	997200	36710
18	2601	2747	2960	3183	55,86	259,5	276,5	102,5	68680	5,408E6	5,369E6	170300
19	2568	2737	2960	3205	100,7	216	299,5	53,28	63570	2,504E6	3,737E6	55150
20	2599	2751	2964	3129	69,94	237,1	228	191,3	78530	2,857E6	2,417E6	336700
22	2629	2759	2966	3137	51,05	225,7	279,6	139,2	20980	1,855E6	2,265E6	84350
24	2619	2754	2957	3176	39,11	209	255,7	185,4	10090	691300	872300	57900
26	2618	2748	2959	3200	50	220,4	249,8	38,89	6565	891300	850100	29460
30	2580	2760	2957	3198	120,5	286,8	212,9	148,5	15980	717300	475600	44470
36	2560	2745	2966	3219	144,3	208,9	308,9	37,82	96060	3,209E6	2,893E6	31650
42	2559	2748	2966	3199	147,7	278,2	272,6	39,86	116700	3,5E6	2,816E6	39520
50	2589	2756	2974	3189	117,9	268,8	182,2	124,1	184700	4,938E6	2,597E6	270600

### 5.3.3. Properties of C/O 1.05 soot in the gas phase via Raman spectroscopy

#### 5.3.3.1. Raman symmetric stretching band of Ethylene at close distances to the burner

In the blue zone of the flame, the precursor gas was seen via its Raman stretching band at  $3025\text{ cm}^{-1}$  in Raman shift. As shown in Fig. 5. 16, Raman intensity of ethylene decreases with the increase of HAB. When HAB is larger than 11 mm, ethylene signal disappears simultaneously with the gradual appearance of *D* and *G* peaks in Raman spectra of soot. Raman spectra of soot at these distances are probably across the nucleation zone.

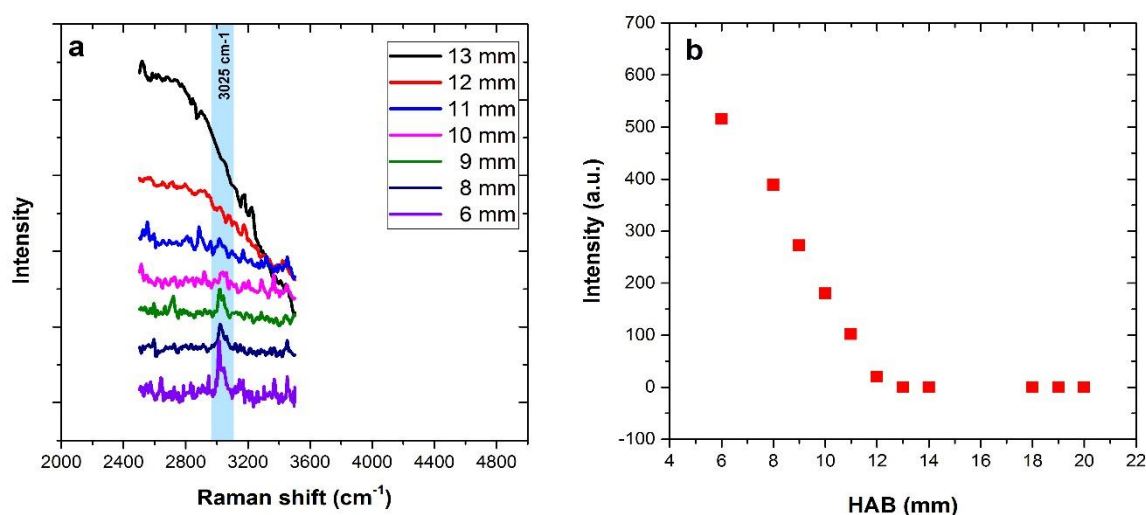


Fig. 5. 16. Raman spectra (a) and Raman signal intensity (b) of ethylene versus HAB

#### 5.3.3.2. Characterization of $\text{sp}^2$ bonds in Raman spectra of soot in the gas phase

Raman spectra of soot in the gas phase are different from those of soot films although the sampling conditions were the same. In this content, we focus on the presence of the so-called *D* and *G* bands, at about  $1370$  and  $1608\text{ cm}^{-1}$  respectively and their second order. The appearance of two shoulder peaks (from  $1900$  to  $2100\text{ cm}^{-1}$ ) will be considered later.

##### a. Comparison between Raman spectra of soot in the gas phase and those of soot films

When comparing Raman spectra of soot in the gas phase to those of deposited soot, the significant feature is the difference of *D*<sub>1</sub> and *G* peaks position and FWHM, as well as the ratio of *D*<sub>1</sub> and *G* intensities. Indeed, as shown in Fig. 5. 17 while *D*<sub>1</sub> peak position of soot deposition ranges from  $1330$  to  $1355\text{ cm}^{-1}$ , in the gas phase it shifts upwards  $\sim 1365$  to  $1375\text{ cm}^{-1}$ . In general, the *D* peak position will increase with increasing disorder [35].

Moreover, the position of  $G$  peak also locates above  $1600\text{ cm}^{-1}$  compared to the range from  $1590$  to  $1620\text{ cm}^{-1}$  of soot films. The  $G$  peak is due to the bond stretching of all pairs of  $\text{sp}^2$  atoms in both ring and chains [36]. As demonstrated for  $229\text{ nm}$  excitation wavelength, in those with only  $\text{sp}^2$  rings, the  $G$  dispersion saturates at  $1600\text{ cm}^{-1}$ , for those consisting of  $\text{sp}^2$  chains,  $G$  rises past  $1600\text{ cm}^{-1}$  [37]. Although the  $G$  band does show a slight dispersion with excitation energy, we expect large shift toward higher energy as due to an increasing concentration of  $\text{sp}^2$  chains. If such hypothesis is true, the  $\text{sp}^2$  chains may be an important component in the structure of soot in the gas phase (even if  $\text{sp}^2$  rings are present). We need to supply more evidences to confirm this information.

When HAB increases gradually, the evolution in structure of soot films via peak dispersion and FWHM as well as the ratio  $I_{D_1}/I_G$  changed in an orderly manner (shown in Fig. 5. 17 and Fig. 5. 18a), whereas the values for soot in the gas phase vary randomly. Note that  $I_{D_1}$  and  $I_G$  are the intensity maxima of  $D_1$  and  $G$  peaks instead of integrated areas. Starting from  $14$  to  $50\text{ mm}$  above the burner, we could see a rapid and exponential increase from  $0.5$  to  $3$  in the intensity ratio of  $D_1$  and  $G$  peaks with soot film Raman spectra. However, with soot in the gas phase, this ratio fluctuates around  $1$ .

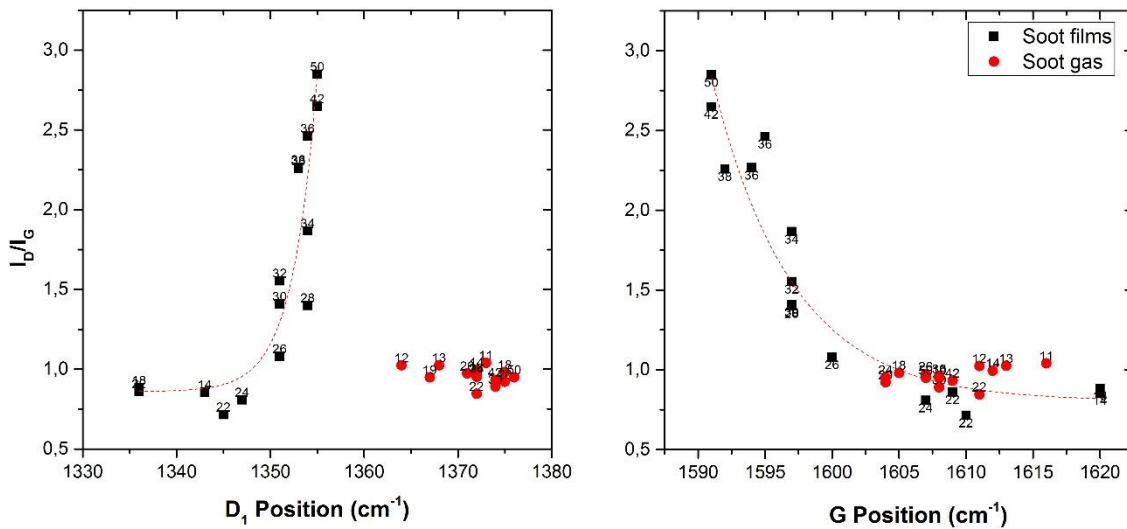


Fig. 5. 17. Dispersion of the ratio intensity of  $D_1$  and  $G$  peaks versus their positions. The label at each point is denoted its HAB.

FWHMs of  $D_1$  and  $G$  peaks indicate the disorder of carbonaceous materials. In general, we find that the  $D$  and  $G$  lines observed in spectra of our soot films are narrow and much narrower than those of hydrogenated amorphous carbon (HAC) [38], [39]. However, these values seen in the gas phase are very large, around  $200\text{ cm}^{-1}$ . It shows that soot in the gas phase are much more disordered than those within the soot films. It reveals also that sampled soot properties may be altered during the sampling process by impaction on a

substrate: bias of sticking soot, temperature effect altering the structures after sampling... These effects are expected to be more important for young soot rather than for mature soot and clearly plead for gas phase diagnostics in situ or in line!

*b. Tracing the evolution of soot structure in the ethylene flame*

From the appearance and development of *D* and *G* peaks in Raman spectra, we would like to separate the measured spectra into two periods: before and after 11 mm of HAB. As mentioned above, at 11 mm from the burner, the Raman line of ethylene disappears simultaneously with the clear appearance of *D* and *G* bands of soot.

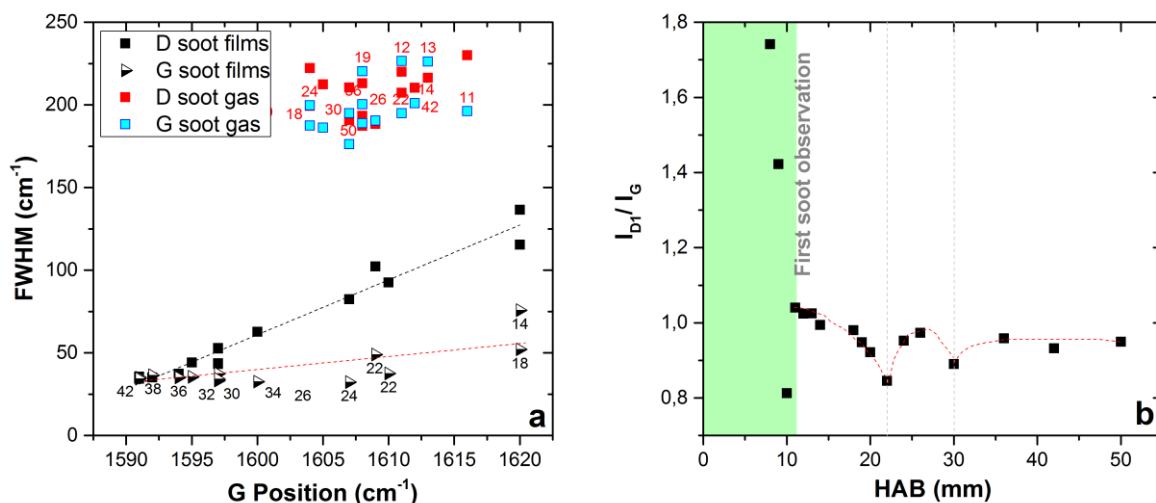


Fig. 5. 18. a) FWHMs of  $D_1$  and  $G$  peaks versus  $G$  position. The label at each points is denoted its HAB. The label denotes HAB in mm. b) Intensity ratio of  $D_1$  and  $G$  peaks, in gas phase, vs HAB.

The FWHMs of the  $G$  and  $D$  bands do not show a clear dependence with HAB. The large widths may preclude from any evolution as long as they still show the  $G$  and  $D$  bands and not the sole broad  $D_3$  band like in truly amorphous carbon. Thus these nanoparticles do contain an appreciable amount  $\text{sp}^2$  carbon in the form of polyaromatic unit. From the  $I_{D1}/I_G$  evolution with HAB, 3 regions appear: 11-22, 22-30 and above 30 mm. We already provide here a tentative explanation of the regimes to guide the readers for the following. The first one starts with the soot inception, which then grow in number and size. Then clustering of these soot nuclei and then surface accretion should take place (around the transition of second regime). Then mass growth of the soot occurs together with aging of the intimate structure (second regime). After 30 mm, the cone start to be out of the inner flame mixing burnt gas from the chamber (convection is at work and distorts the flame structure) and flame by-products, stability of the spectra (Fig. 5. 10) suggest that we are not only probing the evolution of soot within the flame.

### 5.3.3.3. The appearance of sp hybridization in soot structure in the gas phase

A new spectral feature is the appearance of shoulder peaks in the region  $1800 - 2100 \text{ cm}^{-1}$  in Raman spectra of soot in the gas phase. The presence of Raman features in the  $1800 - 2300 \text{ cm}^{-1}$  region are the fingerprint of sp chains which are related to the stretching vibrations of sp hybridized CC bonds (carbynoid species) [40]. In fact, sp hybridized bonds were seen in Raman spectra of soot films presented in chapter 4, but in the gas phase their intensities are much higher.

The structure of sp carbon species are linear structure with two possible electronic structures with either a sequence of double bonds only ( $= \text{C} = \text{C} =$ ), called cumulenes, or alternating single and triple bonds ( $-\text{C} \equiv \text{C} -$ ), called polyynes [41]. It must be noticed that ideal polyynes are energetically more stable than cumulenes due to Peierls distortion [42]. This spectral region is particular to sp carbon chains, since none of the other carbon nanostructures have peaks in this region (Fig. 5. 19). From the density functional theory calculations on molecular systems for the infinite model of sp linear structures, there is the frequency red shift of the most intense Raman line with increasing chain length [43], [44].

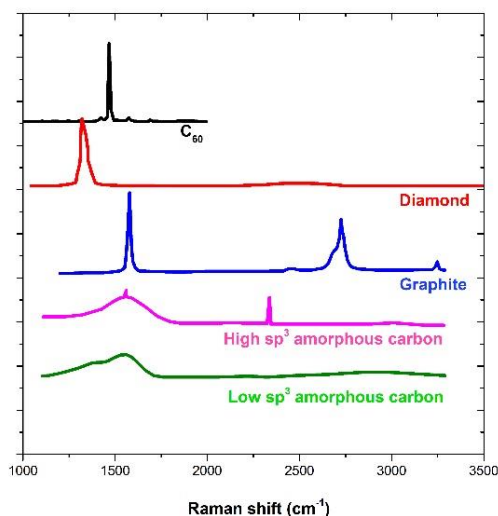


Fig. 5. 19. Experimental Raman spectra of some carbon solids and nanostructures [36].

#### a. The difference in Raman spectra of soot in the gas phase and that of deposited sample

In this content, we would like to compare soot in the gas phase and soot deposited on a substrate. Fig. 5. 20 shows a spectrum of soot produced at 18 mm from the burner of 1.05 C/O ratio flame conditions measured directly in the gas phase and that of a soot film deposited on NaCl substrate measured immediately after deposition and kept in vacuum at about  $10^{-2}$  mbar. Fig. 5. 20a shows the raw spectra and Fig. 5. 20b their normalized spectra after subtracted background spectra.



Fig. 5. 21 shows the comparison the deconvoluted Raman spectrum in the gas phase and that in deposited phase. FWHM of *D* and *G* peaks in the gas phase decrease when soot is deposited on the substrate. In particular, in the gas phase, they are  $220$  and  $280$   $\text{cm}^{-1}$  while after deposition they are  $157$  and  $120$   $\text{cm}^{-1}$ , respectively. It indicates that soot structure after deposition is less disordered than that in the gas phase. Immediately after deposited on the NaCl window, the *sp* structure, called carbynoid structures, decreased quickly in Raman spectrum of soot and almost vanished when soot was exposed in the air (see chapter 4). This was only observed for amorphous carbon produced in plasma and deposited under vacuum, in the group of Milani et al [39].

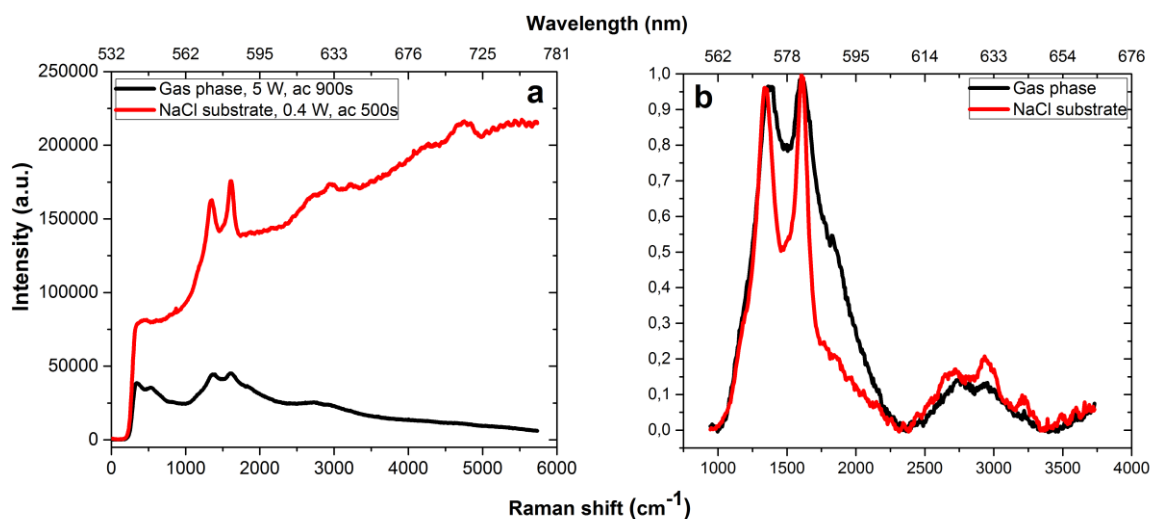


Fig. 5. 20. Raman spectra of soot produced by 1.05 C/O flame at 18 mm excited by the continuous laser in the gas phase and deposited substrate. (a) Raw data, (b) normalized Raman signal after subtracting fluorescence.

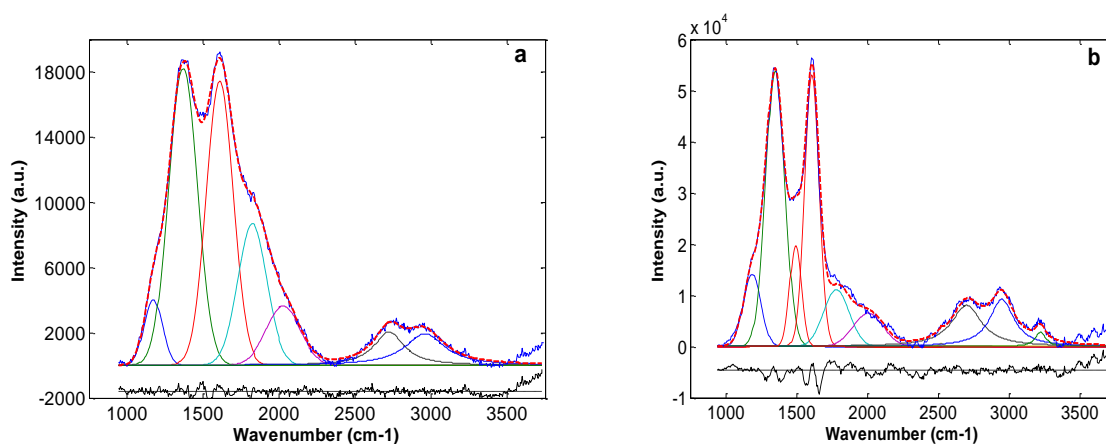


Fig. 5. 21. Decomposition of Raman spectra of soot in the gas phase (a) and in the deposited phase (b).

If the ratio  $\alpha$  between Raman cross section of  $sp$  and  $sp^2$  bonds is known, the absolute amount of  $sp$  bonds could also be determined. In the result of Ravagnan et al (2006) [45], by comparing in situ NEXAFS and Raman spectra of cluster-assembled films, they estimated the value of  $\alpha$  is equal to 1.2. However their value stands for polyynes dominated structures embedded in an amorphous carbon. Assuming this value is a good approximation for more cumulenic structures as well, we found that, in the gas phase, the  $sp / sp^2$  bond ratio is about 31% and this value decreases quickly to 19% in the soot film. This could be explained by the instability of the carbon chains and in the solid state they tend to form in fact  $sp^2$  and  $sp^3$  carbon atoms from the original  $sp$  hybridized carbon atoms [46]. Remarkably, after deposition, cumulenes decrease by 50% while the attenuation of polyynes is only 30% because cumulenes are expected to be less stable than ideal polyynes due to the occurrence of Peierls distortion [40].

b. *The evolution of  $sp$  hybridized bond in Raman spectra of soot in the gas phase*

Let us turn now to the Raman spectra of  $sp$  hybridized CC bonds in our gas phase measurement. The C band has a remarkably strong intensity and appears to be structured and composed of two peaks. According to decomposed spectra in Fig. 5. 15, the two Gaussian fits ( $C_1$  and  $C_2$ ) of the C band are found at  $1800 - 1870 \text{ cm}^{-1}$  ( $C_1$ ) and  $1980 - 2100 \text{ cm}^{-1}$  ( $C_2$ ) ranges, respectively (Fig. 5. 22).

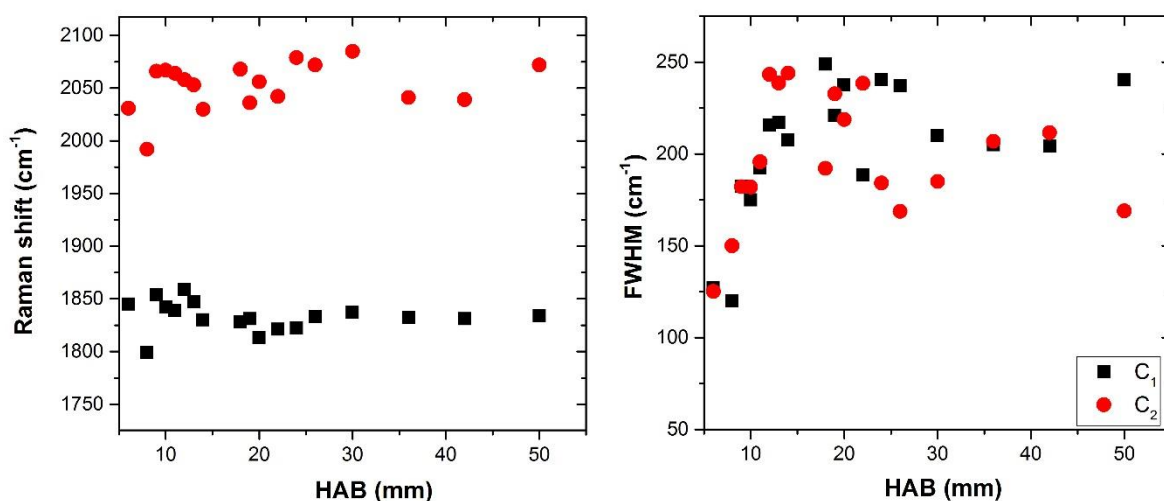


Fig. 5. 22. FWHM and position of two peaks  $C_1$  and  $C_2$  appearing along the flame.

These  $C_1$  and  $C_2$  peaks are located nearby the D and G bands which are typical of  $sp^2$  carbon and related to vibrational modes of  $sp^2$ -hybridized sites (between  $1170$  and  $1620 \text{ cm}^{-1}$ ) [35]. The Raman feature observed in the  $1980 - 2100 \text{ cm}^{-1}$  region can be interpreted as due to the stretching modes of polyynes, with a contribution that has been attributed to cumulenes in the  $1800 - 1870 \text{ cm}^{-1}$  range [47], [48]. The stability of these peak positions in

Fig. 5. 22 points to stable chain length distributions. Their FWHMs are although found quite similar. They increase from  $\sim 125 \text{ cm}^{-1}$  to  $250 \text{ cm}^{-1}$  when HAB rises to 15 mm, then get stable at further distances to the burner. It suggests an evolution of the size distribution toward broader distributions.

c. The evolution of  $sp$  and  $sp^2$  bonds in structure of soot in the gas phase

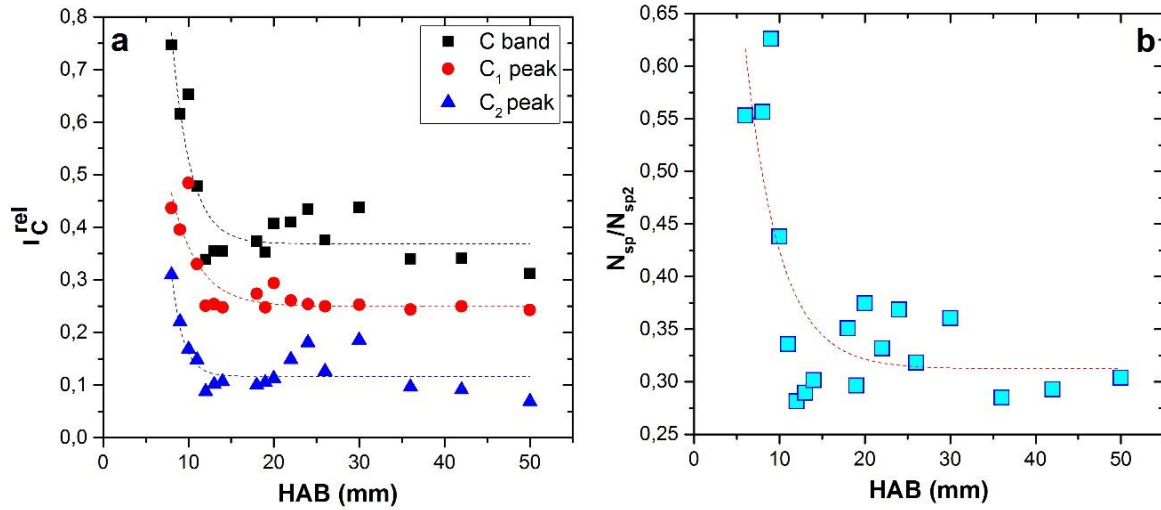


Fig. 5. 23. a) The ratio between the integrated intensity of the C band and of the (D + G) band versus HAB. b) The evolution of the  $sp$  -  $sp^2$  ratio versus HAB.

The relative C band and the (D + G) band intensities, expressed by the ratio between their integrated intensities  $I_C^{rel} = I_C/I_{D+G}$ , is roughly 75% at close HAB down to 34% at further HAB as shown by black points in a. This value can be used to quantify the evolution of  $sp/sp^2$  bond ratio in the film and it can be defined also for the  $C_1$  ( $I_{C_1}^{rel} = I_{C_1}/I_{D+G}$ ) and  $C_2$  ( $I_{C_2}^{rel} = I_{C_2}/I_{D+G}$ ) band, respectively. The integrated intensity of the carbyne peak  $I_{C_1}^{rel}$  is directly related to the cumulene amount in the network and was thus chosen as the main parameter relating to their evolution. If the ratio  $\alpha$  between Raman cross section of  $sp$  and  $sp^2$  bonds is known, the absolute amount of  $sp$  bonds could also be determined. In the result of Ravagnan, L. et al (2006) [45], by comparing in situ NEXAFS and Raman spectra of cluster-assembled films, they estimated the value of  $\alpha$  is equal to 1.2. However their value stands for polyynes dominated structures embedded in an amorphous carbon. Assuming this value is a good approximation for more cumulenic structures as well, we found that at closest distances from HAB, the amount of the atoms  $sp$  hybridized are making up more than 50 % of that of  $sp^2$  hybridization. Then it falls down rapidly to 30% when HAB increases up to 15mm and keeps a slightly stable trend at further distances. Thus the shorter HAB is, the more the amount of  $sp$  hybridization is. This value decreases following an exponential decay function as shown in Fig. 5. 23. a) The ratio between the

integrated intensity of the C band and of the (D + G) band versus HAB. b) The evolution of the  $sp - sp^2$  ratio versus HAB. Fig. 5. 23b. Combining  $I_{C_1}^{rel}$  and  $I_{C_2}^{rel}$  values indicate that within  $sp$  hybridization, the average account of cumulenes bond is always dominant (approximately 63 %) assuming equal Raman efficiency. However, at closest distances, this absolute ratio is a little bit lower (around 60%). It means the amount of polyynes decreases more quickly than that of cumulenes when HAB is shorter than 15 mm. In summary, the present results show the existence of  $sp$  hybridization in structure of soot in the gas phase, in which the major part is in the form of cumulenes.

By comparing Raman spectra of soot in the gas phase and in deposited phase which were detailed in the chapter 4, we can state that there is the existence of  $sp$  carbon chains in structure of our soot. However, after depositing on substrates and store in the ambient condition,  $C_1$  peak disappeared and the intensity of  $C_2$  peak strongly decrease. Linear carbon chains can be produced in the gas phase at high temperature, however they are very fragile and unstable under ambient conditions and they undergo cross-linking reactions leading to aromatisation when condensed in a solid phase.

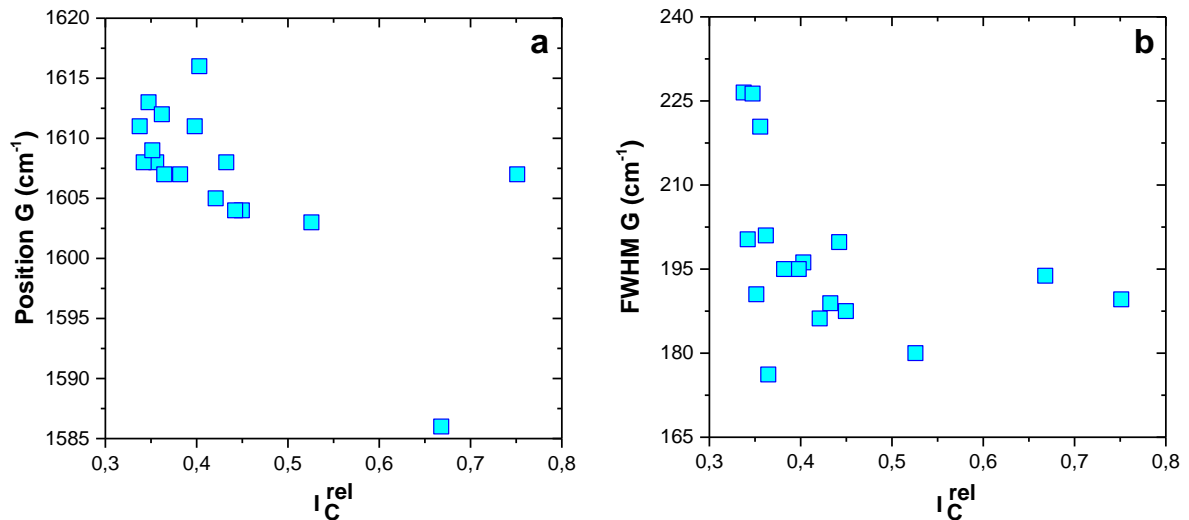


Fig. 5. 24. a) Blue-shift of the G peak versus  $I_C^{rel}$  for different HAB. b) Relation of FWHM of G peak and  $I_C^{rel}$

In Fig. 5. 24a, we show the relation between  $G$  peak position and  $I_C^{rel}$ . It can be observed that the decrease of the  $I_C^{rel}$  corresponds to a shift of the  $G$  peak towards higher frequency indicating a slight isomerisation of the  $sp$  network into polyenic  $sp^2$  chains and/or cyclisation. In addition, Fig. 5.24 shows a potential increase of  $I_D/I_G$  when the  $I_C^{rel}$  decreases, but additional work has to be performed to confirm this.

In summary, during the downtrend of  $I_C^{rel}$ , a slight blue-shift (in Fig. 5. 24a) and a slight narrowing of  $G$  peak (in Fig. 5. 24b) (these trends are not so clear) and an increase in the  $I_D/I_G$  were obtained (in Fig. 5. 25). Although these changes are not dramatic, they may suggest a possible small trend towards ordering of the  $sp^2$  phase [35]. Analyses of the Raman spectra from the other flames may help to investigate further these trends if confirmed.

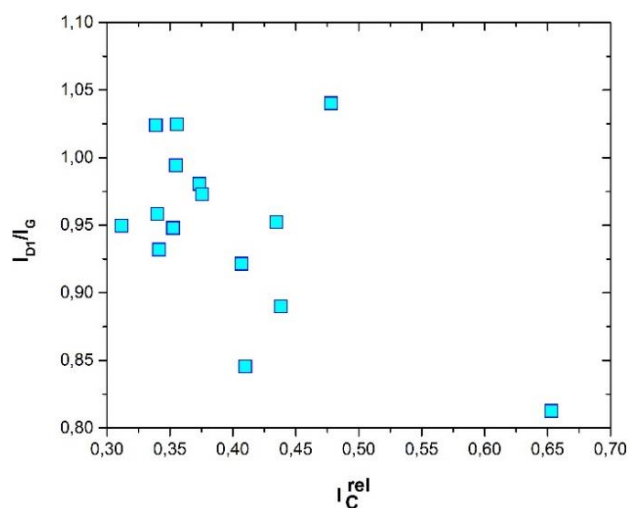


Fig. 5. 25. The relation of  $I_D/I_G$  versus the  $I_C^{rel}$ .

We have investigated the appearance of  $sp$  hybridization in structure of soot in the gas phase, in which the amount of cumulenes is two times more higher than of polyynes. We also demonstrated that polyynes are more stable than cumulenes. However, both of them vanish quickly when they are deposited on a substrate and stored in the ambient air. As shown in chapter 4, cumulenes totally disappear and the remnants of polyynes is a tiny peak at around  $2100\text{ cm}^{-1}$ . This is the strong different feature of in situ measurement of soot in the gas phase comparing to ex situ measurement of soot films. Furthermore, by looking the details of the Raman spectra of soot in the gas phase and right after deposition, we outlined that structure of soot on substrate is more ordered than the other. These are the first experimental results of soot in the gas phase.

### 5.3.3.3. The evolution of soot via fluorescence

These fluorescence components we obtained upon visible excitation wavelengths are challenging to interpret. As reported in Fig. 5. 26 and Fig. 5. 27, the first fluorescence component does not vary much in shape with HAB while the second emission spectra shift slightly toward higher wavelength.

### The first fluorescence component

Fig. 5. 26 reports the evolution of the first fluorescent component along the height of the flame. This component is compared with laser induced fluorescence (LIF) spectra of Bejaoui et al. (2014) on a premixed methane flame. It was measured directly in the flame and thus on hot species while in our case all are cooled within the Laval nozzle flow. The main point is that no shape variations were observed. In our case, the razor-edge filters block the wavelength lower than 539 nm. A quick check revealed (not shown) that no emission could be observed in the anti-Stokes region in our experiment by removing this filter. Considering Stokes emission spectra, our spectra show a similar trend with LIF spectra, i.e. no noticeable variation apart from its intensity.

These spectra could come from the emission of free-flying PAH or PAHs adsorbed on the soot particles. However, the use of visible wavelengths only restricts to excitation of PAHs with low-lying electronic excited states. This may happen for big sizes or with defects (for instance five-membered ring) within the polyaromatic carbon skeleton [32].

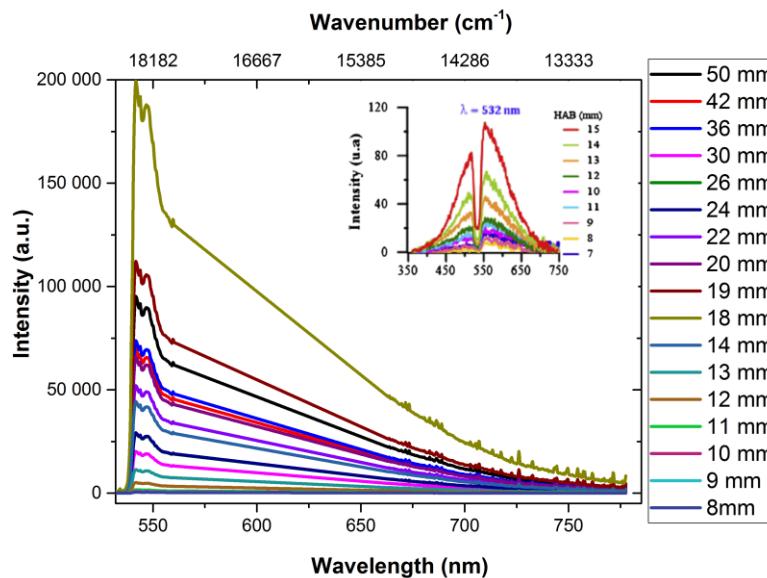


Fig. 5. 26. The evolution of the first fluorescent component vs HAB. The attached figure on the right corner shows LIF spectra measured with visible 532 nm excitation in the premixed flame of methane by Bejaoui et al. (2014) [32].

### The second fluorescence component

This component just appears when HAB is higher than 18 mm as shown in Fig. 5. 27. Its intensity grows up rapidly from HAB = 20 mm and reach the maximum value at HAB = 22 mm then decreases and do not change after HAB = 36 mm. The fluorescence at 750 nm could be from accretion on the surface of the gas phase molecular component leading to mass growth of the soot grains after nucleation. These must then lead to

fluorophore or chromophore of soot grains when their sizes increase. A fluorophore may imply there is an electronic energy transfer between the soot grain and the molecules attached (similar to functionalization for examples) on the surface due to surface accretion. This is not clear if it may happen and electronic relaxation within the soot particle should be much more efficient than electronic energy transfer to the surface. Chromophore means that they are absorbing themselves the incoming light and fluoresce with yields competing with non-radiative electronic relaxation. Basically, species that are able to fluoresce at such long wavelength with such a "low" excitation energy may be rarely molecules (PAHs here) in the gas phase. There is the proposition of the PAHs with at least one pentagonal cycle in the polyaromatic unit, which may be at work, like for fluorescence 1 indeed. But the clear appearance of the soot slightly before and the large Stokes-shift of the fluorescence suggests that it may happen on their surface as well, or originate from the particular soot structures. In particular it may be similar to nano-organic compounds suggested by D'Alessio and co-workers to be mostly aliphatic, oxygen containing, and considered as the soot nuclei that would thus be poorly aromatic [19]. In our case, the Raman spectra indicate clearly the presence of  $sp^2$  aromatic carbon in abundance, but do not exclude a vanishingly small fluorescence quantum yield for these particles. While these could carry the fluorescence during their mass growth, they may not resemble exactly the suggestion of d'Alessio. In addition, one has to remember that the hole the cone, about 1 mm, implies that the sampled volume is probably more than 1 mm diameter. Thus what we see at 19 mm may in fact come from "20 mm" and the extent of the fluorescing zone may be just about 1 mm as well.

If this broad component is fitted by a Gaussian function, the maximum peak position as a function of HAB is present in Fig. 5. 28. The peak of the spectra is red shifted  $\sim 25$  nm when the burner moves from 18 to 25 mm from the cone.

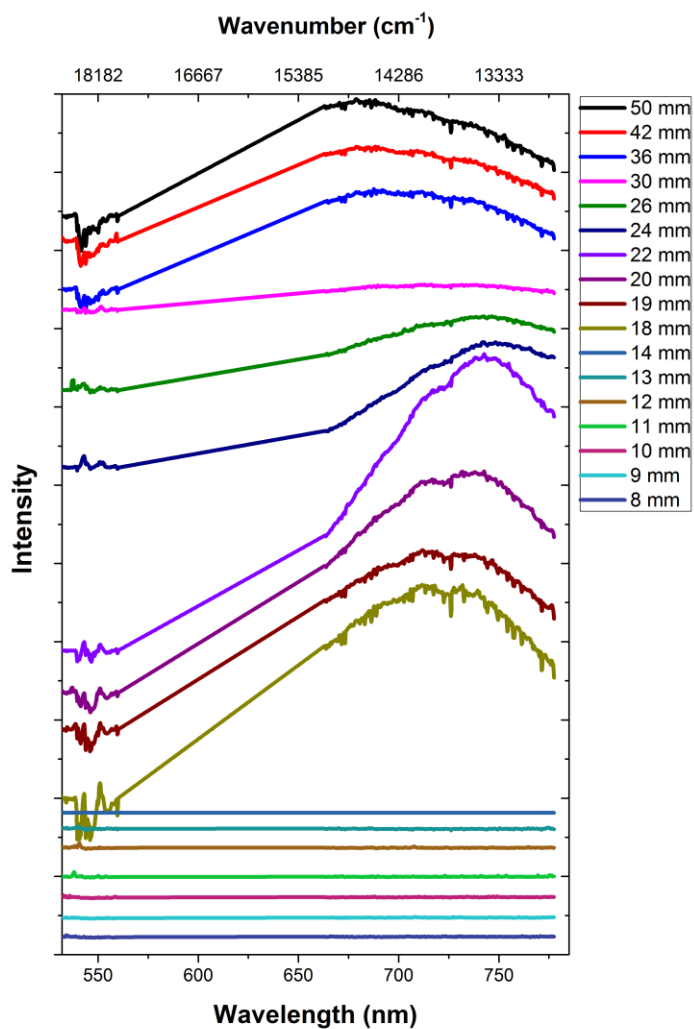


Fig. 5.27. The evolution of second fluorescent component vs HAB.

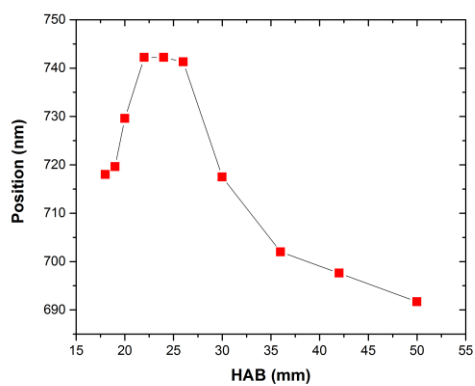


Fig. 5.28. The maximum peak position of 750 nm emission band vs HAB.



#### 5.3.3.4 The evolution of soot via fluorescence and Raman measurements

In summary, Fig. 5. 29 provides a view of the soot structure evolution that traces the evolution in the flame. We could separate the evolution of soot in the flame region into four stages corresponding to HAB:

The first stage (HAB = 6  $\rightarrow$  11 mm) is signed by the existence of the precursor fuel (ethylene). Its signal decreases gradually and disappears when the burner go further than 11 mm. The birth of Raman spectra of carbonaceous particles is observed in this region. The *G* and *D* bands are seen and quite narrow. They might be more molecular. The Raman spectra show a high content of sp hybridized bond compared to sp<sup>2</sup> hybridized bond.

The second stage (HAB = 11  $\rightarrow$  22 mm) is marked by the appearance of clear Raman signal of *D* and *G* bands of soot. There is no ethylene fingerprint any more (It is possible that ethylene still remains but its concentration is too weak to detect). The existence of soot become clearer and clearer indicating by the decrease of signal/noise ratio. The first one started with the soot inception, which then grow in number and size by probably adsorbing or accreting gas phase molecules and PAHs on soot particles (exhibited by the appearance of the first fluorescent component) then clustering of these soot nuclei and then surface accretion should take place (around 22mm). The gas phase molecular component leading to mass growth of the soot grains may then cause to fluorophore or chromophore (the second fluorescent reason). The  $I_D/I_G$  ratio decreases in that range (Fig. 5.18). In addition, decrease of the sp phase is observed simultaneously in this stage.

The third stage (HAB = 22  $\rightarrow$  30 mm), trace by an increase of the  $I_D/I_G$  ratio, a slight decrease of fluorescence 1 and Raman signal. Fluorescence 2 clearly decreases. These may trace aging of the soot toward mature soot. However that geometrical differences in the soot beam may be responsible of this decrease cannot be excluded.

With the last stage (HAB above 30 mm), the cone start to be out of the inner flame mixing burnt gas from the chamber (convection is at work and distorts the flame structure) and flame by-products, stability of the spectra suggest that we are not only probing the evolution of soot within the flame.

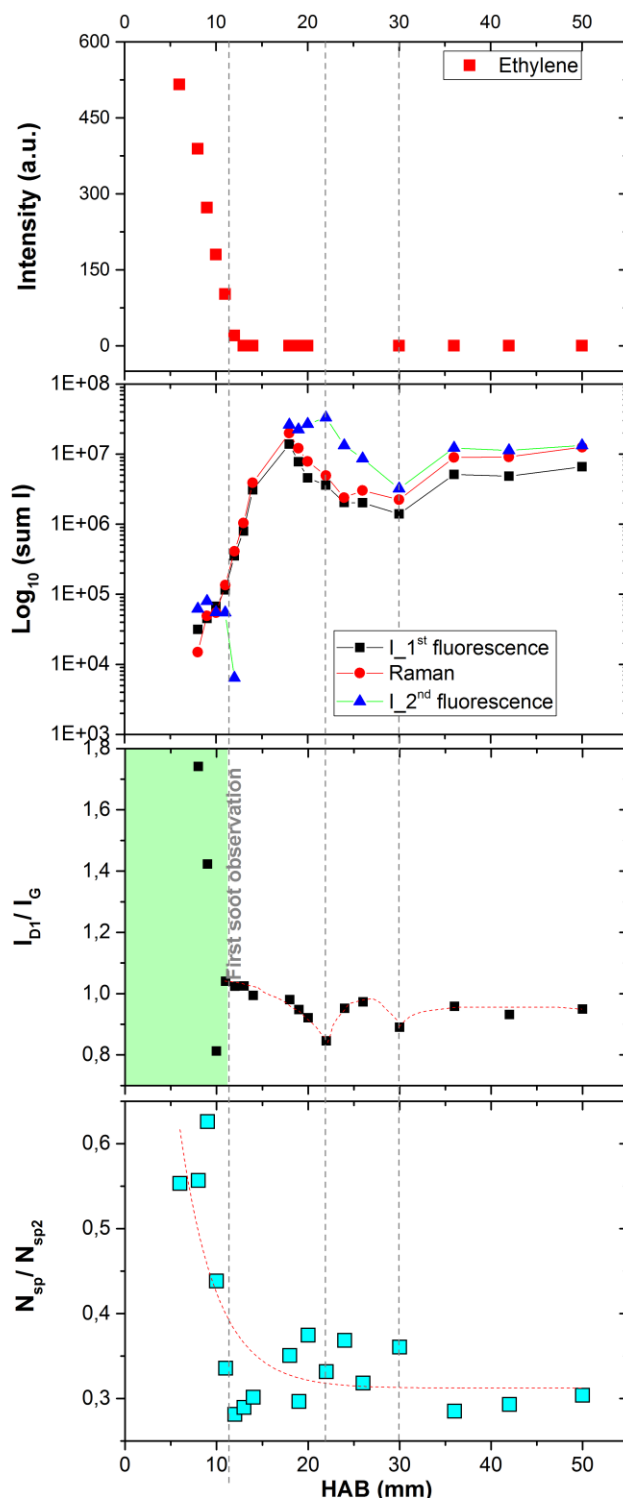


Fig. 5. 29. The evolution of soot along the height above the burner (HAB) in a C/O = 1.05 ethylene premixed flame. From the top to the bottom: evolution of the precursor concentration (ethylene), the integrated intensity of Raman and fluorescent components in semi-logarithmic scale, the  $I_D/I_G$  ratio and the evolution of  $N_{sp}/N_{sp^2}$  ratio versus HAB.

## 5.4. Conclusions and remarks

Aging process of soot in the air changes soot structure from our low pressure flame. Almost all Raman spectra of soot were obtained previously by ex-situ measurements. In our study, this is the first time that soot was detected in the gas phase using Raman spectroscopy. It involves many interesting and new information of soot formation pathways in low pressure combustion and soot properties.

- (a) Structure of soot strongly dependent on flaming condition, such as C/O ratio, pressure and HAB.
- (b) Raman spectra of soot are un-polarized because soot is constructed of nanoparticles with disordered nanostructuration.
- (c) Soot structure in the gas phase is more disorder than deposited soot.
- (d) The existence of sp hybridization in soot structure in which cumulenes, although dominant, are less stable than polyyenes. They quickly decrease and vanish when soot is deposited on a substrate and store in the ambient air.
- (e) The ethylene signal's disappearance in conjunction with the emergence of *D* and *G* bands at HAB = 10 mm, probably from the soot nuclei. It is thus the first spectral information on these nanoparticles.
- (f) Starting from HAB = 10 mm, we could see the development of the first fluorescence component. When HAB < 28 mm, beside of Raman bands and the first fluorescence component, there is a contribution of the emission band at ~ 750 nm. This already gives some clues on the evolution of the nature of the carrier of the bands tracing the soot growth.

We have not fully and systematically studied yet all data because of the limited time in my PhD period. In the near future, these observations may be extended to the other flames and provided some general trends of soot birth and growth in low pressure flames.

## References

- [1] H. G. Wagner, "Soot formation in combustion," *Symp. Combust.*, vol. 17, no. 1, pp. 3–19, 1979.
- [2] M. Sirignano, J. Kent, and A. D'Anna, "Detailed modeling of size distribution functions and hydrogen content in combustion-formed particles," *Combust. Flame*, vol. 157, no. 6, pp. 1211–1219, 2010.
- [3] B. L. Wersborg, J. B. Howard, and G. C. Williams, "Physical mechanisms in carbon formation in flames," *Symp. Combust.*, vol. 14, no. 1, pp. 929–940, 1973.
- [4] J. D. Bittner and J. B. Howard, "Composition profiles and reaction mechanisms in a near-sooting premixed benzene/oxygen/argon flame," *Symp. Combust.*, vol. 18, no. 1, pp. 1105–1116, 1981.
- [5] P. Gerhardt, K. H. Homann, S. Löffler, and H. Wolf, "Large ionic species in sooting acetylene and benzene flames," in *Proc. PEP Symp. Chania, Crete, Agard*, 1987, p. 22.1-11.
- [6] H. Bockhorn, F. Fetting, and H. W. Wenz, "Article Investigation of the Formation of High Molecular Hydrocarbons and Soot in Premixed Hydrocarbon-Oxygen Flames," *Berichte der Bunsengesellschaft für Phys. Chemie*, vol. 87, no. 11, pp. 1067–1073, 1983.
- [7] A. M. Weiner and S. J. Harris, "Optical detection of large soot precursors," *Combust. Flame*, vol. 77, no. 3–4, pp. 261–266, 1989.
- [8] A. D. Alessio, A. Di Lorenzo, A. F. Sarofim, and S. Masi, "Soot formation in methane-oxygen flames," *Combust. Inst.*, vol. 15, no. 1, pp. 1427–1438, 1975.
- [9] A. Di Lorenzo, A. D'Alessio, S. Masi, P. Menna, and C. Venitozzi, "UV absorption, laser excited fluorescence and direct sampling in the study of the formation of polycyclic aromatic hydrocarbons in rich CH<sub>4</sub>/O<sub>2</sub> flames \*," *Combust. Inst.*, vol. 18, no. 1, pp. 485–491, 1981.
- [10] B. S. Haynes, H. Jander, and H. G. Wagner, "Optical Studies of Soot-Formation Processes in Premixed Flames," *Berichte der Bunsengesellschaft für Phys. Chemie*, vol. 84, no. 6, pp. 585–592, 1980.
- [11] A. D'Alessio, A. D'Anna, A. D'Orsi, P. Minutolo, R. Barbella, and A. Ciajolo, "No Title," *Proc. Combust. Inst.*, vol. 24, p. 973, 1992.
- [12] P. Desgroux, X. Mercier, and K. A. Thomson, "Study of the formation of soot and its precursors in flames using optical diagnostics," *Proc. Combust. Inst.*, vol. 34, no. 1, pp. 1713–1738, 2013.

- [13] F. Xu, P. B. Sunderland, and G. M. Faeth, "Soot formation in laminar premixed ethylene / air flames at atmospheric pressure," *Combust. Flame*, vol. 108, pp. 471–93, 1997.
- [14] T. C. Williams, C. R. Shaddix, K. A. Jensen, and J. M. Suo-Anttila, "Measurement of the dimensionless extinction coefficient of soot within laminar diffusion flames," *Int. J. Heat Mass Transf.*, vol. 50, no. 7–8, pp. 1616–1630, 2007.
- [15] J. Zerbs, K. P. Geigle, O. Lammel, J. Hader, R. Stirn, R. Hedef, and W. Meier, "The influence of wavelength in extinction measurements and beam steering in laser-induced incandescence measurements in sooting flames," *Appl. Phys. B Lasers Opt.*, vol. 96, no. 4, pp. 683–694, 2009.
- [16] F. Migliorini, K. A. Thomson, and G. J. Smallwood, "Investigation of optical properties of aging soot," *Appl. Phys. B Lasers Opt.*, vol. 104, no. 2, pp. 273–283, 2011.
- [17] C. Schulz, B. F. Kock, M. Hofmann, H. Michelsen, S. Will, B. Bougie, R. Suntz, and G. Smallwood, "Laser-induced incandescence: Recent trends and current questions," *Appl. Phys. B Lasers Opt.*, vol. 83, no. 3, pp. 333–354, 2006.
- [18] T. Ishiguro, Y. Takatori, and K. Akihama, "Microstructure of diesel soot particles probed by electron microscopy: First observation of inner core and outer shell," *Combust. Flame*, vol. 108, no. 1–2, pp. 231–234, 1997.
- [19] A. Ciajolo, "Condensed phases in soot formation process," in *Combustion generated fine carbonaceous particles*, no. October, H. Bockhorn, A. D'Anna, A. F. Sarofim, and H. Wang, Eds. Karlsruhe: KIT scientific publishing, 2009, pp. 333–344.
- [20] M. Frenklach, D. W. Clary, W. C. Gardiner, and S. E. Stein, "Detailed kinetic modeling of soot formation in shock-tube pyrolysis of acetylene," *Symp. Combust.*, vol. 20, no. 1, pp. 887–901, 1985.
- [21] J. Appel, H. Bockhorn, and M. Frenklach, "Kinetic Modeling of Soot Formation with Detailed Chemistry and Physics: Laminar Premixed Flames of C2 Hydrocarbons," *Combust. Flame*, vol. 121, pp. 122–136, 2000.
- [22] J. Singh, R. I. A. Patterson, M. Kraft, and H. Wang, "Numerical simulation and sensitivity analysis of detailed soot particle size distribution in laminar premixed ethylene flames," *Combust. Flame*, vol. 145, no. 1–2, pp. 117–127, 2006.
- [23] S. B. Dworkin, Q. Zhang, M. J. Thomson, N. A. Slavinskaya, and U. Riedel, "Application of an enhanced PAH growth model to soot formation in a laminar coflow ethylene/air diffusion flame," *Combust. Flame*, vol. 158, no. 9, pp. 1682–1695, 2011.
- [24] B. Apicella, X. Wang, M. Armenante, A. Bruno, and N. Spinelli, "Picosecond and

- nanosecond laser ionization for the on-line analysis of combustion-formed pollutant,” in *Proceedings of the 32nd Meeting on Combustion*, 2009, p. I-12.
- [25] H. Bockhorn, F. Fetting, A. Heddrich, U. Meyer, and G. Wannemacher, “Particle sizing of soot in flat pre-mixed hydrocarbon oxygen flames by light scattering,” *J. Aerosol Sci.*, vol. 19, no. 5, pp. 591–602, 1988.
- [26] A. Milani, M. Tommasini, V. Russo, A. L. Bassi, A. Lucotti, F. Cataldo, and C. S. Casari, “Raman spectroscopy as a tool to investigate the structure and electronic properties of carbon-atom wires,” *Beilstein J. Nanotechnol.*, vol. 6, pp. 480–491, 2015.
- [27] T. Mouton, X. Mercier, M. Wartel, N. Lamoureux, and P. Desgroux, “Laser-induced incandescence technique to identify soot nucleation and very small particles in low-pressure methane flames,” *Appl. Phys. B Lasers Opt.*, vol. 112, no. 3, pp. 369–379, 2013.
- [28] H. Bladh, N.-E. Olofsson, T. Mouton, J. Simonsson, X. Mercier, A. Faccinetto, P.-E. Bengtsson, and P. Desgroux, “Probing the smallest soot particles in low-sooting premixed flames using laser-induced incandescence,” *Proc. Combust. Inst.*, vol. 35, pp. 1843–1850, 2015.
- [29] L. A. Sgro, A. C. Barone, M. Commodo, A. D’Alessio, A. De Filippo, G. Lanzaolo, and P. Minutolo, “Measurement of nanoparticles of organic carbon in non-sooting flame conditions,” *Proc. Combust. Inst.*, vol. 32 I, no. 1, pp. 689–696, 2009.
- [30] A. Faccinetto, P. Desgroux, M. Ziskind, E. Therssen, and C. Focsa, “High-sensitivity detection of polycyclic aromatic hydrocarbons adsorbed onto soot particles using laser desorption/laser ionization/time-of-flight mass spectrometry: An approach to studying the soot inception process in low-pressure flames,” *Combust. Flame*, vol. 158, no. 2, pp. 227–239, 2011.
- [31] P. Desgroux, X. Mercier, B. Lefort, R. Lemaire, E. Therssen, and J. F. Pauwels, “Soot volume fraction measurement in low-pressure methane flames by combining laser-induced incandescence and cavity ring-down spectroscopy: Effect of pressure on soot formation,” *Combust. Flame*, vol. 155, no. 1–2, pp. 289–301, 2008.
- [32] S. Bejaoui, X. Mercier, P. Desgroux, and E. Therssen, “Laser induced fluorescence spectroscopy of aromatic species produced in atmospheric sooting flames using UV and visible excitation wavelengths,” *Combust. Flame*, vol. 161, no. 10, pp. 2479–2491, 2014.
- [33] F. Beretta, A. D’alessio, A. D’Orsi, and P. Minutolo, “U.V. and Visible Laser Excited Fluorescence from Rich Premixed and Diffusion Flames,” *Combust. Sci. Technol.*, vol. 85, no. 1–6, pp. 455–470, 1992.
- [34] S. Bejaoui, X. Mercier, P. Desgroux, and E. Therssen, “Laser induced fluorescence

- spectroscopy of aromatic species produced in atmospheric sooting flames using UV and visible excitation wavelengths,” *Combust. Flame*, 2014.
- [35] A. Ferrari and J. Robertson, “Interpretation of Raman spectra of disordered and amorphous carbon,” *Phys. Rev. B*, vol. 61, no. 20, pp. 14095–14107, 2000.
- [36] A. C. Ferrari, “Raman spectroscopy of graphene and graphite : Disorder , electron – phonon coupling , doping and nonadiabatic effects,” *Solid State Commun.*, vol. 143, pp. 47–57, 2007.
- [37] L. G. Cançado, A. Jorio, E. H. M. Ferreira, F. Stavale, C. A. Achete, R. B. Capaz, M. V. O. Moutinho, A. Lombardo, T. S. Kulmala, and A. C. Ferrari, “Quantifying defects in graphene via Raman spectroscopy at different excitation energies,” *Nano Lett.*, vol. 11, no. 8, pp. 3190–3196, 2011.
- [38] R. Brunetto, T. Pino, E. Dartois, A. T. Cao, L. D’Hendecourt, G. Strazzulla, and P. Bréchnignac, “Comparison of the Raman spectra of ion irradiated soot and collected extraterrestrial carbon,” *Icarus*, vol. 200, no. 1, pp. 323–337, 2009.
- [39] G. Ferini, G. a. Baratta, and M. E. Palumbo, “A Raman study of ion irradiated icy mixtures,” *Astron. Astrophys.*, vol. 414, no. 2, pp. 757–766, 2004.
- [40] A. Milani, A. Lucotti, V. Russo, M. Tommasini, F. Cataldo, A. L. Bassi, and C. S. Casari, “Charge transfer and vibrational structure of sp- hybridized carbon atomic wires probed by surface enhanced Raman spectroscopy,” *Sci. Technol.*, pp. 2–5, 2011.
- [41] L. Kavan, “Carbyne forms of Raman shift,” *Carbon N. Y.*, vol. 32, no. 8, pp. 1533–1536, 1994.
- [42] A. Abdurahman, A. Shukla, and M. Dolg, “Ab initio many-body calculations on infinite carbon and boron-nitrogen chains,” *Phys. Rev. B*, vol. 65, no. 11, p. 115106, 2002.
- [43] A. Milani, M. Tommasini, and G. Zerbi, “Carbynes phonons: A tight binding force field,” *J. Chem. Phys.*, vol. 128, no. 6, 2008.
- [44] M. Tommasini, A. Milani, D. Fazzi, M. Del Zoppo, C. Castiglioni, and G. Zerbi, “Modeling phonons of carbon nanowires,” *Phys. E Low-Dimensional Syst. Nanostructures*, vol. 40, no. 7, pp. 2570–2576, 2008.
- [45] L. Ravagnan, G. Bongiorno, D. Bandiera, E. Salis, P. Piseri, P. Milani, C. Lenardi, M. Coreno, M. de Simone, and K. C. Prince, “Quantitative evaluation of sp<sup>2</sup>/sp<sup>3</sup> hybridization ratio in cluster-assembled carbon films by in situ near edge X-ray absorption fine structure spectroscopy,” *Carbon N. Y.*, vol. 44, no. 8, pp. 1518–1524, 2006.

- [46] F. Cataldo, “The role of Raman spectroscopy in the research on sp-hybridized carbon chains: Carbynoid structures polyynes and metal polyynides,” *J. Raman Spectrosc.*, vol. 39, no. 2, pp. 169–176, 2008.
- [47] L. Ravagnan, F. Siviero, C. Lenardi, P. Piseri, E. Barborini, P. Milani, C. S. Casari, A. Li Bassi, and C. E. Bottani, “Cluster-Beam Deposition and in situ Characterization of Carbyne-Rich Carbon Films,” *Phys. Rev. Lett.*, vol. 89, no. 28, p. 285506, 2002.
- [48] J. Kūrti, C. Magyar, A. Balázs, and P. Rajczy, “Vibrational analysis for short carbon chains with alternating and cumulenenic structure,” *Synth. Met.*, vol. 71, no. 1–3, pp. 1865–1866, 1995.



# Chapter 6

## Conclusions and perspectives

### Contents

---

<b>6.1. Conclusions</b> .....	154
<b>6.2. Perspectives</b> .....	156

---

## 6.1. Conclusions

Our study emphasizes one more time the worth of Raman spectroscopy in carbonaceous materials investigation, not only their optical properties or structural information, but also their evolution in combustion. The achieved results contain new information that could be applied in other researches and help us to understand more soot formation processes in the flame.

Indeed, until this work, there were no data on the differential Raman cross section (DRCS) of carbonaceous particles such as black carbon (BC) or soot exhausted from incomplete combustion because of the difficulty of experimental measurements for strongly absorbing particles. The DRCS of BC are rigorously revealed to be huge. Particularly, these are found close to that of graphite and nearly 2 orders of magnitude higher than other carbonaceous solid (diamond) or molecules ( $N_2$ , benzene...) commonly at the focus of atmospheric research. We believe the determination of the order of magnitude of DRCS of carbon-based materials will contribute to demonstrate the feasibility of detection of BC emission in the atmosphere using Raman spectroscopy and its potential application to marine investigations.

Besides DRCS, we gain a larger knowledge on structural properties of soot produced by ethylene premixed flames. New information found in their Raman spectra is the fingerprint of sp hybridized bond at  $\sim 2150\text{ cm}^{-1}$  forming a carbynoid component. We have investigated the appearance of sp hybridization in structure of soot produced in a  $C/O = 1.05$  ethylene flame, monitored in the gas phase and on deposited films, in which the amount of cumulenes is two times higher than of polyynes. We also confirmed that polyynes are more stable than cumulenes. However, both of them vanish quickly when they are deposited on a substrate and stored in the ambient air.

From Raman spectra, the effective polyaromatic unit size of our soot is assessed varying from 1 to slightly higher than 2 nm using the available relation for such small size. This polyaromatic unit size is then compared to that obtained from the visible transmission spectra using other relations. A rough factor of 2 is seen between the two values. Those derived from the visible spectra probably overestimate the values. In addition, the  $C/O = 1.05$  flame is the only condition where the  $I_{D1}/I_G$  ratio above 2 was observed, apart from ion irradiated graphene, in which the relation between  $L_a$  and the  $I_{D1}/I_G$  ratio proposed by Ferrari, Robertson and co-workers is questioned. The empirical formulae have been shown to not take into account the evolution of the electronic structure for these disordered nanoparticles and rather small  $L_a$ . Cross-linkage between polyaromatic units and curvature is tentatively assigned at the source of the much stronger dependence of the gap to the effective  $L_a$  (to the power of 4). This new dependency found between Tauc gap and effective  $L_a$  should be confirmed in the future by quantitative analysis of high resolution transmission electronic microscopy images in collaboration with Pascaline Pr  (Ecoles de Mines de Nantes) and applied for the low optical Tauc gap ( $< 2\text{ eV}$ ).

This is the first time that soot is detected in the gas phase using Raman spectroscopy. It reveals many interesting and new information on soot formation pathways in low pressure combustion and soot properties. Raman spectra of soot are un-polarized because soot is constructed of nanoparticles with disordered nanostructuration. Our spectral data cross the nucleation zone of soot birth in the flame and provides information of soot evolution in the flame. Polyaromatic structure is clearly forming the nascent soot, as seen from the clear *G* and *D* band, but accompanied by a high content of *sp* hybridization. The lack of a fluorescence specific to the soot birth although outline some of its properties. They should not resemble the nano-organic compounds (NOC) of d'Alessio and co-workers because the purely amorphous structure of the NOC is not seen by Raman spectroscopy. In addition, the NOC were assigned to the UV fluorescent species in the flame, indicating almost transparent particles in the visible range. Such properties would severely limit their Raman cross section due to the absence of resonance at 532 nm, preventing their detection in our experiment. The strong component of *sp* hybridized structure suggest that the hot temperature within the flame prevent a purely polyaromatic structure for the particles. To our understanding, this observation suggest that, in the combustion conditions of the measurement, chemical condensation is at work involving polyaromatic units and carbon chains, rather than stacking of PAHs to form dimers. From our observations, three regions are found for the birth and growth. First inception is observed at a rather short height above the burner, probably because of the high equivalent ratio. Then the number of particle increases by more than 3 orders of magnitude. This is accompanied by the appearance of a broad and red emission band (when excited at 532 nm) which we tentatively assigned to trace mass growth by surface accretion. After this, the Raman signal seems to saturate and the evolution of the Raman features is rather small, with for instance the disappearance of the *sp* component bands when reaching this saturation at about 22 mm height in the flame. This last region may then trace evolution of the soot structure toward a more aromatic, at least a high *sp*<sup>2</sup> hybridization content, intimate structure. This scenario has to be proven and examined for other flames in order to check an eventual generality or to check whether Raman probe may help to discriminate chemical condensation versus dimerization or even to definitely exclude this pure cluster channel.

In summary, our study contains much new information on soot properties, connecting vibrational IR and Raman spectroscopy sensitive to the nature of the defects, the electronic structure rationalized through the phenomenological Tauc gap and electronic microscopy imaging the structure at the atomic scale. The success in detecting soot Raman spectra in the gas phase for the first time and their DRCS are very promising for the detection of soot exhausted in the atmosphere. In June 2016, we had a first remote sensing campaign in Lyon, in collaboration with Alain Miffre and Patrick Rairoux from the Institut Lumière Matière (CNRS/Université Claude Bernard Lyon). In this investigation, we try to detect Raman spectra of emitted soot from small butane diffusion flame at ~ 40 meters from the detector. However, we have not obtained Raman signals of soot yet and now we are improving the soot emission source and other optical parameters for new attempts.

## 6.2. Perspectives

As already mentioned, we plan to detect soot emission in the atmosphere developing a Lidar type system dedicated to black carbon. Now we are improving the optical scheme as well as experimental ambient conditions. We will continue also to work on all our data. We have several HRTEM images and many Raman data of soot in the gas phase in different low pressure flames. Progresses on the polyaromatic analysis from HRTEM may help to provide a size distribution which could help to improve these empirical models that relates at present one structural index,  $L_a$ , to the electronic structure through the Tauc gap and to the vibrational band revealing the defects through Raman or IR spectroscopy. Extension of Raman measurement to multi-wavelength Raman spectroscopy may also help to probe resonance effect and detect the  $sp^3$  phase through UV Raman.

For the nucleation zone of soot in the flame: the signal to noise ratio of Raman spectra across the nucleation zone should be improved to better probe their structure. Polarization studies of soot nuclei should be also added. The depolarization ratio  $I_{VH}/I_{VV}$  of the Raman bands of soot upon polarized laser irradiation could be used to discriminate between large molecular compounds in the form of PAH, where molecular symmetry could lead to polarization effects, and the soot nuclei. Raman scattering could thus be used to probe the transition between the suspected PAH precursors and the soot nuclei. These studies may also be extended at other excitation wavelengths to probe the resonance Raman effects.

After approaching an improved understanding of soot structural properties along their evolution in the low pressure, we would like to turn to similar investigations on higher pressure flames. This will question the presence of  $sp$  hybridized form which has only been observed from low pressure gas phase reactor. For instance, their detection in atmospheric pressure flames would put to front their role in the nucleation and growth of soot, reinforcing a dominant chemical condensation scenario. In addition, newly observed nucleation flames in the group of Pascale Desgroux (Laboratoire de Physico-Chimie de la Combustion et de l'Atmosphère, Université de Lille 1) are priority target conditions for our method as it would give access to structural information of the soot nuclei. These flames are found at the transition between sooting and non-sooting flame and mass growth of nascent soot is hindered by the small amount of available carbon,

In conclusion, our study outlines that spectrally resolved online diagnostics, in the gas phase, are of importance to progress on the understanding of combustion. Spectral information provides invaluable knowledge on the process and make Raman spectroscopy a privileged tool for that as excitation wavelength are not so selective. In addition, we have seen that multi-analyses are also powerful to interpret the data on disordered polyaromatic units and should be used whenever possible.

# Appendix A

# Polyaromatic disordered carbon grains as carriers of the UV bump: FUV to mid-infrared spectroscopy of laboratory analogs

L. Gavilan<sup>1,2</sup>, K. C. Le<sup>3</sup>, T. Pino<sup>3</sup>, I. Alata<sup>2,3</sup>, A. Giuliani<sup>4,5</sup>, and E. Dartois<sup>2</sup>

<sup>1</sup> Université Versailles St-Quentin; Sorbonne Universités, UPMC Université Paris 06; CNRS/INSU, LATMOS-IPSL, 78280 Guyancourt, France

<sup>2</sup> Institut d'Astrophysique Spatiale (IAS), CNRS, Univ. Paris Sud, Université Paris-Saclay, F-91405 Orsay, France

<sup>3</sup> Institut des Sciences Moléculaires d'Orsay (ISMO), CNRS, Univ. Paris Sud, Université Paris-Saclay, F-91405 Orsay, France

<sup>4</sup> DISCO beam line, SOLEIL synchrotron, Saint Aubin, France

<sup>5</sup> INRA, UAR1008 CEPIA, F-44316 Nantes, France  
e-mail: lisseth.gavilan@latmos.ipsl.fr

Preprint online version: February 28, 2017

## Abstract

**Context.** A multiwavelength study of laboratory carbons with varying degrees of hydrogenation and  $sp^2$  hybridization is required to characterize the structure of the carbonaceous carriers of interstellar and circumstellar extinction.

**Aims.** We study the spectral properties of carbonaceous dust analogs from the far-ultraviolet to the mid-infrared and correlate features in both spectral ranges to the aromatic/aliphatic degree.

**Methods.** Analogs to carbonaceous interstellar dust encountered in various phases of the interstellar medium have been prepared in the laboratory. These are amorphous hydrogenated carbons (a-C:H), analogs to the diffuse interstellar medium component, and soot particles, analogs to the polyaromatic component. Thin films ( $d < 100$  nm) have been measured in transmission in the vacuum-ultraviolet (VUV; 120 - 210 nm) within the APEX chamber of the DISCO beam line at the SOLEIL synchrotron radiation facility. Spectra of these films were further measured through the UV-Vis (210 nm - 1  $\mu$ m) and in the mid-infrared (3 - 15  $\mu$ m).

**Results.** Tauc optical gaps,  $E_g$ , are derived from the visible spectra. The major spectral features are fitted through the VUV to the mid-infrared to obtain positions, FWHM, and integrated intensities. These are plotted against the  $\pi-\pi^*$  electronic transitions peak position. Unidentified or overlapping features in the UV are identified by correlations with complementary infrared data. A correlation between the optical gap and position of the  $\pi-\pi^*$  electronic transitions peak is found. The latter is also correlated to the position of the  $sp^3$  carbon defect band at  $\sim 8$   $\mu$ m, the aromatic C=C stretching mode position at  $\sim 6$   $\mu$ m, and the H/C ratio.

**Conclusions.** Ultraviolet and infrared spectroscopy of structurally diverse carbon samples are used to constrain the nanostructural properties of carbon carriers of both circumstellar and interstellar extinction, such as the associated coherent lengths and the size of polyaromatic units. Our study suggests that carriers of the interstellar UV bump should exhibit infrared bands akin to the A/B classes of the Aromatic Infrared Bands, while the circumstellar bump carriers should exhibit bands corresponding to the B/C classes.

**Key words.** ISM: dust, extinction - Infrared: ISM - Galaxies: ISM - Methods: laboratory: solid state - Ultraviolet: ISM

## 1. Introduction

The diversity of carbonaceous solids in interstellar and circumstellar environments in our Galaxy and in extra-galactic lines of sight has been the subject of numerous theoretical, observational, and experimental studies (Draine & Lee 1984; Greenberg & Li 1999; Pendleton & Allamandola 2002; Dartois et al. 2005; Pino et al. 2008; Godard & Dartois 2010; Duley & Hu 2012; Jones 2012a,b,c).

Observations of interstellar extinction were first documented by Trumpler (1930). One prominent spectral feature in extinction curves in the Milky Way is a broad ultraviolet absorption bump consistently centered at 217.5 nm (4.6  $\mu$ m<sup>-1</sup>). The UV bump was first observed in the 1960s by Stecher & Donn (1965), but its carrier is still not fully understood, although it has been generally attributed to electronic transitions in carbon. Fitzpatrick & Massa (1986) first parametrized the UV bump using data from the International Ultraviolet Explorer (IUE) toward 45 reddened OB Milky Way stars. They found that the position of the bump was mildly variable while its full width at half maximum strongly variable; the lack of correlation between these parameters suggested that graphite was an improbable car-

rier. In Fitzpatrick & Massa (1988) they included the far ultraviolet (FUV) extinction, finding that a Lorentzian (for the UV bump), a FUV rise, and an underlying linear continuum were necessary components. This study was expanded to 78 stars, published as an atlas (Fitzpatrick & Massa 1990) and further extended to include 329 stars (Fitzpatrick & Massa 2005, 2007). In the latter, stellar atmosphere models were used to eliminate spectral mismatch errors in the curves, and showed that extinction parameters are highly sensitivity to local conditions. The exact origin and variability of interstellar extinction and the nature of the dust carriers across different wavelength ranges is still a central question in cosmic dust research.

Astronomical observations in the infrared also play an important role in dust characterization. Unidentified infrared emission bands (UIBs), also known as Aromatic Infrared Bands (AIBs), are features between 3 and 20  $\mu$ m (3.3, 6.2, 7.7, 8.6 and 11.2  $\mu$ m) widely observed in a range of environments in our Galaxy (Peeters 2014). These bands are attributed to the infrared fluorescence of polyaromatic carriers, associated to the PAH hypothesis (e.g. Rosenberg et al. 2014). However, alternative carriers have also been proposed, such as amorphous organic solids

with mixed aromatic-aliphatic structures due to mixed  $sp^2$  and  $sp^3$  hybridizations. Observations of a single carbon star with a circumstellar disk by Sloan et al. (2007) concluded that its spectra was consistent with hydrocarbon mixtures containing both aromatic and aliphatic bonds. Aceke et al. (2010) suggested that a strong UV flux reduces the aliphatic component and emphasizes the spectral signature of the aromatics in the emission spectra towards Herbig Ae stars. Yang et al. (2013) studied the ratio of the CH stretching modes at 3.3 and 3.4  $\mu\text{m}$  in emission towards UIBs, and argued that their observed emitters are predominantly aromatic nanoparticles.

The spectroscopy of laboratory analogs to interstellar carbon dust has helped to unveil the origin of the UV bump. Draine & Lee (1984) proposed early on that crystalline graphite could fit the UV bump, and later on Jones (1990) argued that hydrogenated amorphous carbons (a-C:H) containing small polyaromatic units may be suitable carriers. Observations of the aliphatic bands at 6.85 and 7.25  $\mu\text{m}$  in absorption later revealed the presence of interstellar hydrogenated amorphous carbons (Pendleton & Allamandola 2002; Dartois et al. 2004). Laboratory hydrogenated carbons have since then been considered realistic carriers of the bump (Colangeli et al. 1997; Schnaiter et al. 1998; Furton et al. 1999; Dartois et al. 2004). Laboratory a-C:Hs at different degrees of hydrogenation have been compared to observed astronomical spectra (Dartois et al. 2007; Duley & Hu 2012). Soot nanoparticles prepared via laser pyrolysis (Jäger et al. 2006, 2008) are also candidates but only following the activation of  $\pi-\pi^*$  transitions by UV irradiation (Gadallah et al. 2011). Indeed, energetic thermal and non-thermal processes can alter carbonaceous dust in the diffuse interstellar medium (ISM). In photo-dissociation regions, photodesorption processes compete with hydrogenation to effectively alter their structure and optical properties. This has been experimentally explored via UV irradiation of thin a-C:H films (Scott & Duley 1996; Mennella et al. 1996, 2002; Alata et al. 2014, 2015), as well as via ion irradiation (Mennella et al. 2003; Godard et al. 2011). Recent optical models of interstellar dust (Jones 2012a,b,c; Jones et al. 2013) have shown that amorphous carbons extending over a wide range of optical gap energies can be used to fit the observed extinction from the FUV to the infrared. Russo et al. (2014) performed a UV study extending from 190 to 1100 nm on molecular weight sorted species prepared by combustion. Bescond et al. (2016) recently studied the optical properties of soots in the visible near-UV from 200-1100 nm and performed an inversion model to extract the size distribution and fractal dimension of soots. Few laboratory spectroscopic studies on carbonaceous dust extending over a wide spectral range exist, due to experimental difficulties to access the vacuum-ultraviolet (VUV). In this range, different techniques have been used including electron energy loss spectroscopy (EELS) (Fink et al. 1984; Zubko et al. 1996) and synchrotron VUV sources (Colangeli et al. 1993; Gavilan et al. 2016).

For this study, we have prepared carbonaceous compounds of mixed aromatic and aliphatic structures at different degrees of hydrogenation, produced in the laboratory. By measuring them over a large spectral range (from the mid-infrared to the VUV) we expect to unveil relations between vibrational modes and electronic transitions, both observable signatures of interstellar dust, extending our previous findings in Gavilan et al. (2016). We also aim to constrain the carbonaceous carriers of the interstellar UV bump and shed light on the spectroscopic decomposition of interstellar extinction based on our laboratory data.

This article is organized as follows. In Section 2 we describe the experimental setups and sample preparation. In Section 3 we

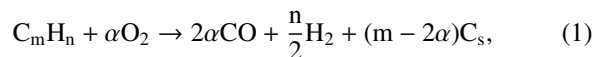
present the analysis of UV and IR bands. In Section 4 we discuss our analysis and astronomical implications and in Section 5 we present our conclusions.

## 2. Experiments

The experimental setups used to prepare the carbonaceous samples have already been described in Gavilan et al. (2016). Here we provide further details relevant to the samples used in this study. Thin carbon films ( $d < 100$  nm) deposited on  $\text{MgF}_2$  windows were used for measurements between 120 - 1000 nm, and thicker carbon films ( $d > 300$  nm) deposited on IR transparent KBr, CsI, KCl windows for measurements in the mid-infrared.

*SICAL-ICP*, a low pressure ( $\sim 10^{-2}$  mbar) radiofrequency (R.F.) plasma reactor was used to prepare the hydrogenated amorphous carbon samples. A 13.56 MHz R.F. power is inductively coupled to the plasma by impedance matching via a copper coil surrounding a glass cylinder (e.g. Dworschak 1990). While the a-C:H sample presented in Gavilan et al. (2016) was prepared using methane ( $\text{CH}_4$ ) as the precursor gas, and an R.F. input power of 100 W, the a-C:H presented in this paper was prepared using a plasma fed by toluene ( $\text{C}_7\text{H}_8$ ), and an R.F. input power of 150 W. Our goal in this study was to produce a more aromatic a-C:H. The higher R.F. power (150 vs 100 W) has an important influence on the structure of the produced solid hydrocarbon. Higher ion energies lead to preferential sputtering of hydrogen due to the lower binding energies of CH with respect to CC bonds.

We used the *Nanograins* combustion flame setup to produce soot nanoparticle films (Carpentier et al. 2012; Pino et al. 2015). In premixed flames, sooting is the result of competition between the rate of pyrolysis, growth of soot precursors and oxidation rate (Mansurov 2005). The formation of soot nanoparticles can be described by the following equation,

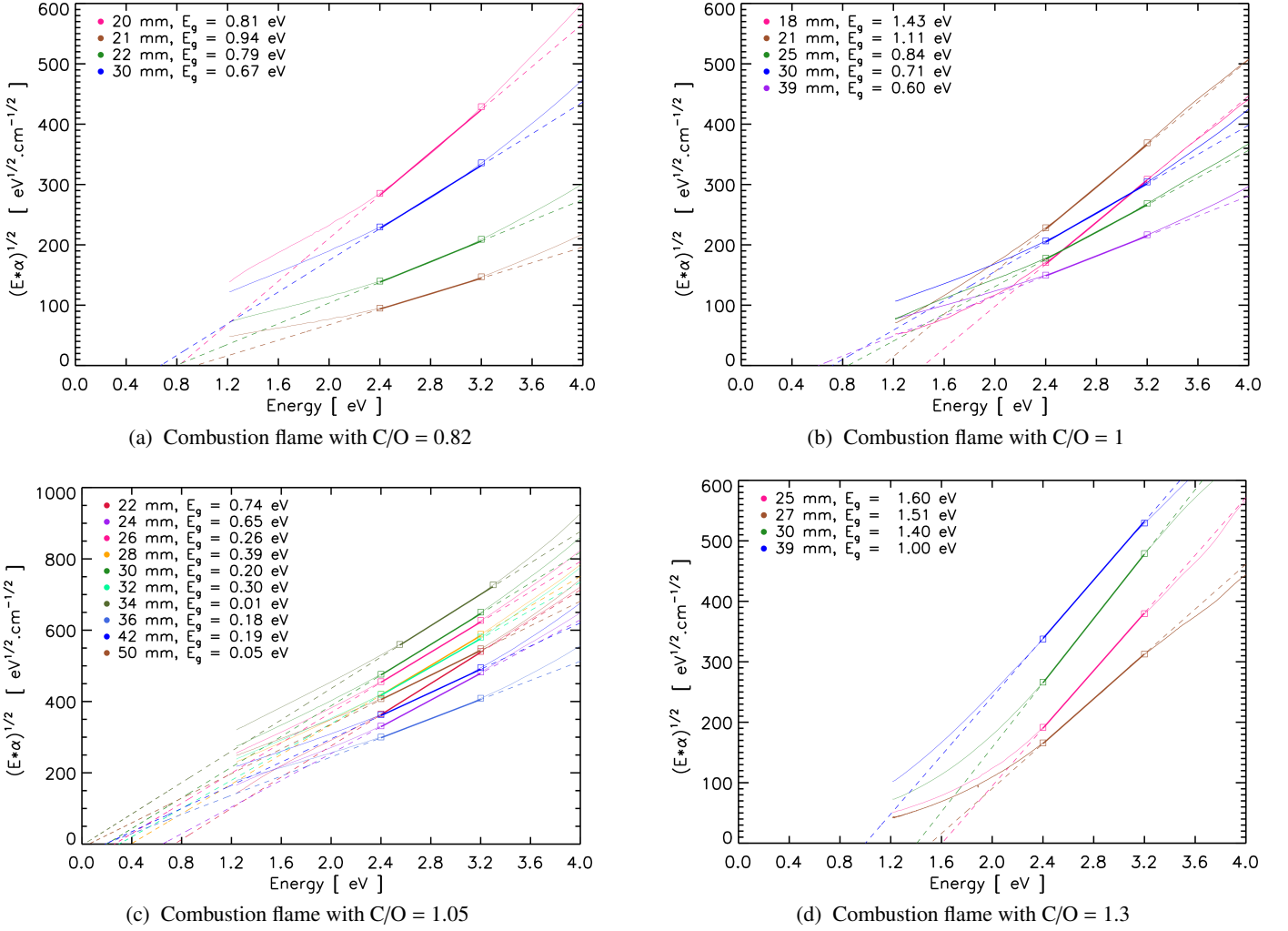


where  $m$  and  $n$  are positive integers related to the hydrocarbon gaz precursor type,  $s$  is a positive integer related to the number of carbon atoms in a solid soot nanoparticle, and  $\alpha$  is a positive rational for the oxidation coefficient. Theoretically, for soots to form in an ethylene flame, eq. 1 imposes  $\text{C}/\text{O} > 1$ . In practice, the sooting regime appears as soon as  $\text{C}/\text{O} \sim 0.7$  at 40 mbar. Soots produced in an ethylene ( $\text{C}_2\text{H}_4$ ) flame, first introduced in Gavilan et al. (2016), were prepared under the following conditions:  $\text{C}/\text{O}$  ratio = 1.05, height above the burner (HAB) = 30 mm. In this paper we present soots prepared under varying flame conditions and HAB ranging from 18 to 50 mm. We used the following  $\text{C}/\text{O}$  ratios and pressures: 0.82 (60 mbar), 1 (28 mbar), 1.05 (33 - 40 mbar), 1.3 (40 mbar). The deposition time of the films varied from  $\sim 1$  - 4 minutes for the closest HAB of 25 mm to 1 to 20 seconds beyond 30 mm.

## 3. UV and IR spectroscopy

VUV spectra of all samples were recorded in the 120 - 250 nm range using the APEX branch of the DISCO beam line at the SOLEIL synchrotron (Giuliani et al. 2009). These spectra were completed in the UV-Vis (210 - 1000 nm) measured with a spectrophotometer (Specord, *Analytikjena*). The overlapping energy range was used to combine the VUV and UV-Vis datasets. Infrared spectra of the same films were measured using an evacuated FTIR spectrometer (Bruker Vertex 80V) equipped with a

**Figure 1.** Tauc optical gap extrapolation using the visible spectra for soot samples prepared with different C/O flame ratios and collected at varying heights above the burner (HAB in mm).



KBr beam-splitter and an (MCT) detector working in the 4000 to 600  $\text{cm}^{-1}$  (2.5 to 15  $\mu\text{m}$ ) at 2  $\text{cm}^{-1}$  resolution. The infrared spectra were corrected with a polynomial baseline to subtract the continuum absorption increasing towards higher wavenumbers due to electronic transitions that extend into the infrared. The spectroscopic analysis involved deconvolution of the main electronic bands for the VUV-UV spectra and for the vibrational modes between 3300 and 600  $\text{cm}^{-1}$  for the infrared spectra using the IDL MPFIT routine based on the Levenberg-Marquardt non-linear least-squares minimization method (Markwardt 2009).

### 3.1. Relationships among the UV fit parameters

UV-VUV spectra with enough S/N were selected and deconvolved using a Lorentzian and three Gaussian functions. We called these the L1, G1, G2 and G3 bands. L1 is the main UV absorption band, falling between 190 to 260 nm and it is in most cases well-fitted by a single Lorentzian. G1 and G2 are neighbouring peaks, appearing around 300 nm and 190 nm respectively. G3 is the large UV absorption at around 110 nm. No additional linear background was required for these fits. The resulting fit UV-VUV parameters are summarized in Table A.1.

#### 3.1.1. Determination of the optical gap

We used the visible spectral range (350 - 1000 nm) to determine the optical gap, also known as the Tauc gap (Tauc et al. 1966). Figure 1 shows the calculated gap values for each film. These were obtained by extrapolating the linear region in an  $(\alpha \times E)^{1/2}$  vs.  $E$  plot, where  $\alpha$  is the absorption coefficient obtained from the relation  $\alpha = \tau/h$ , where  $\tau$  is the optical depth and  $h$  the film thickness and  $E$  is in eV. For disordered carbon materials like those presented in this paper, the empirical linear dependance between  $\alpha$  and  $E$  is expressed by,

$$(\alpha \times E)^{1/2} = B^{1/2}(E - E_g) \quad (2)$$

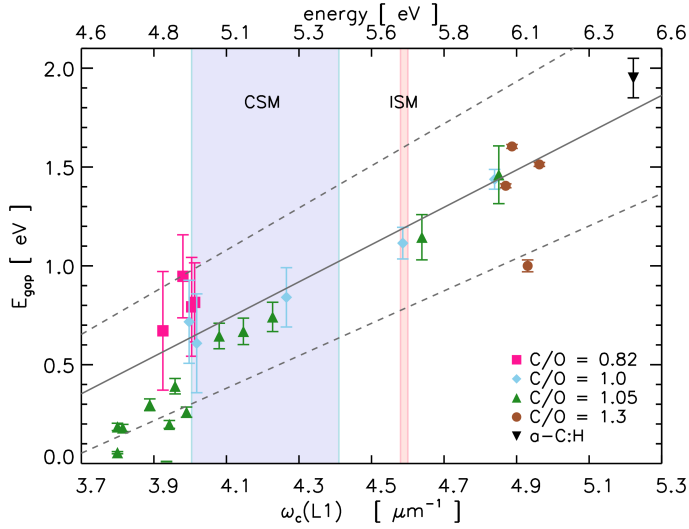
where  $B$  is a constant attributed to their thermal processing (Jones 2012a). To determine the Tauc gap from the visible-ultraviolet spectra we chose the same region in the visible tail of the Tauc spectra where  $2.4 < E$  (eV)  $< 3.2$ , to extract the linear fit extrapolated to zero absorption, and from 2.4-2.7 eV and 2.7 to 3.2 eV to determine the average systematic error bar typically used in soot extinction analysis (Adkins & Miller 2015). Note that, for the soot produced with the C/O = 1.05 flame, HAB = 34 mm, the fitting linear energy range was shifted to 2.5 - 3.3 eV, in order to avoid a negative gap value. While the thickness



of the samples is assumed to be  $\sim 30\text{-}60$  nm as in (Gavilan et al. 2016), this is taken as constant for all samples as it does not significantly affect the gap value determination, whose systematic uncertainty is dominated by the choice of linear energy range. For the prepared samples, the value of the Tauc optical gap ( $E_g$ ) increases from the least hydrogenated soots to the most hydrogenated a-C:H, i.e.  $0 < E_g < 2$  eV. The H/C ratio of each sample is obtained from infrared spectra and discussed in Section 3.4.

For the a-C:H prepared with a toluene precursor, the optical gap was found to be 1.95 eV, lower than the 2.5 eV estimated for the methane-precursor a-C:H of (Gavilan et al. 2016). For the soot samples produced with the C/O = 0.82 flame,  $E_g$  decreases from 0.78 to 0.62 eV as the HAB increases. This is the same trend as for the C/O = 1 flame, where  $E_g$  decreases from 1.46 to 0.68, for the C/O = 1.05 flame with a decrease from 1.47 to 0.01, and for the C/O = 1.3 flame with a decrease from 1.6 to 1 eV. Jones (2012a) sequences the family of amorphous carbons based on the optical gap energy, building on previous work by Robertson (1986). Amorphous carbon that are hydrogen rich, called a-C:H, have  $E_g \approx 1.2 - 2.5$  eV while the hydrogen poor carbons, called a-C, have  $E_g \approx 0.4 - 0.7$  eV. For our soot samples  $E_g < 1.6$  eV, and  $E_g = 1.95$  for our a-C:H. Thus, Robertson's classification can be further improved by our disordered carbon data.

### 3.1.2. $E_g$ vs. $\omega_c(L1)$



**Figure 2.** Tauc optical gap,  $E_g$ , for our laboratory samples versus the center of the  $\pi\text{-}\pi^*$  electronic transition,  $\omega_c(L1)$ . The latter is used as our main spectroscopic parameter in the UV.

In Fig. 2 we display the position of the main UV absorption (fitted by a Lorentzian, called L1) against the optical gap, yielding the relation,

$$E_g[\text{eV}] = 0.76 \pm 0.3 \times \omega_c(L1)[\mu\text{m}^{-1}] - 3.1 \pm 0.5. \quad (3)$$

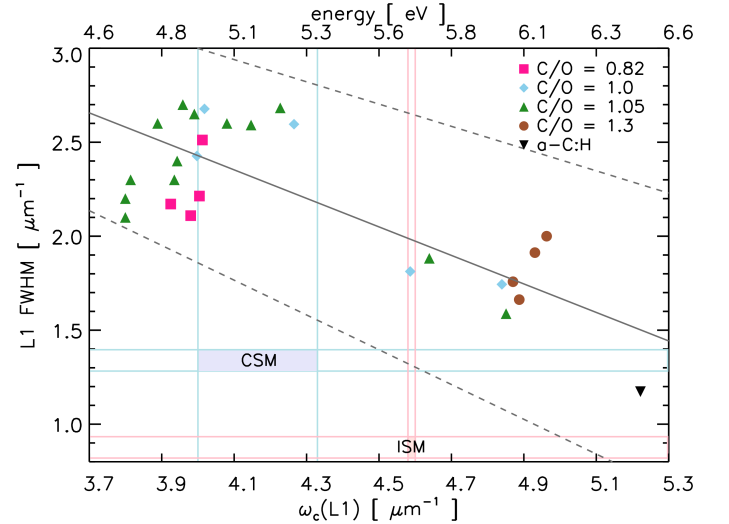
These two parameters have a linear Pearson correlation coefficient  $r = 0.91$ . The wide variations in the position of the L1 peak from  $3.8$  to  $5.2 \mu\text{m}^{-1}$  ( $192$  to  $262$  nm) is consistent with previous experimental works where the UV peak is centered between  $180$  and  $280$  nm (Llamas Jansa et al. 2003). Russo et al. (2014), found that the spectral features in the UV-Visible range

are mainly affected by the higher molecular weight species of combustion flame products. Because L1 is strongly correlated to the optical gap  $E_g$ , variations in the position of L1 can be attributed to changes in the nanostructure due to varying H/C,  $sp^3/sp^2$  and the size of the polyaromatic units, which will be discussed in the following sections. The Tauc optical gap model, which has been used to give a complete description of the optical properties of carbonaceous materials (Robertson & O'Reilly 1987; Robertson 1991; Jones 2012a), appears to be well-suited for our soot samples.

From now on, our fitting parameters will be compared to the parameters of the interstellar  $217.5$  nm UV bump (Fitzpatrick & Massa 2005, 2007), i.e.,  $\omega_c = 4.593 \mu\text{m}^{-1}$  with  $\sigma = 0.0191 \mu\text{m}^{-1}$  and  $\text{FWHM} = 0.77 - 1.29 \mu\text{m}^{-1}$  with  $\sigma = 0.050 \mu\text{m}^{-1}$ . We also compare our parameters to the average position of the circumstellar  $\sim 240$  nm UV bump, as determined by observations of the circumstellar envelopes of C-rich stars like V348 Sagittarii (Drilling et al. 1997). For the average circumstellar medium (CSM) bump,  $\omega_c = 4.12 \mu\text{m}^{-1}$ , limited from  $4 \mu\text{m}^{-1}$  (Blanco et al. 1995) up to  $4.4 \mu\text{m}^{-1}$  (Waelkens et al. 1995), and a  $\text{FWHM} = 1.34 \mu\text{m}^{-1}$  with  $\sigma = 0.06 \mu\text{m}^{-1}$  (Drilling et al. 1997).

The spectral parameters of our samples will be preferably plotted against the position of L1,  $\omega_c(L1)$ , strongly correlated to  $E_g$ , as L1 (rather than  $E_g$ ) is the direct spectroscopic parameter.

### 3.1.3. $\gamma(L1)$ versus $\omega_c(L1)$

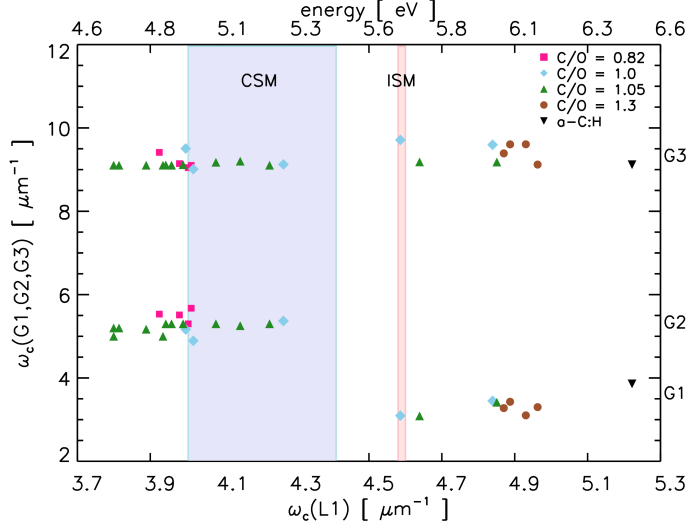


**Figure 3.** FWHM of the  $\pi\text{-}\pi^*$  electronic transition,  $\gamma(L1)$ , versus its center position,  $\omega_c(L1)$ , showing a clear correlation, absent in interstellar extinction curves (Fitzpatrick & Massa 2005).

As seen in Fig. 3, an anti-correlation is found between the FWHM  $\gamma(L1)$  and  $\omega_c(L1)$  ( $r = -0.79$ ), while  $\gamma(L1)$  vs.  $E_g$  is also anti-correlated ( $r = -0.72$ ). This result contrasts with the non-correlation between both parameters in extinction curves found by Fitzpatrick & Massa (2005). The large scatter in FWHM has been suggested to be due to grain clustering broadening (Schnaiter et al. 1998). From all our samples, only one has an L1 peak within the observed ISM FWHM parameter range, the a-C:H prepared with toluene, with  $\gamma(L1) = 1.2 \mu\text{m}^{-1}$ , but is centered at  $5.2 \mu\text{m}^{-1}$  and not at the expected  $4.6 \mu\text{m}^{-1}$ . However, if we consider a different parametrization of the interstellar UV

bump (Sect. 4), two soot samples are more representative,  $C/O = 1$  (HAB = 21 mm) and  $C/O = 1.05$  (HAB = 18 mm).

### 3.1.4. $\omega_c(G1, G2, G3)$ versus $\omega_c(L1)$



**Figure 4.** Positions of the UV and VUV major electronic transitions,  $\omega_c(G1)$ ,  $\omega_c(G2)$ ,  $\omega_c(G3)$ , versus the center of the  $\pi$ - $\pi^*$  electronic transition  $\omega_c(L1)$ . For all samples presented here the positions of these peaks fall at precise energies, with little dispersion, but their relative intensities tend to vary strongly.

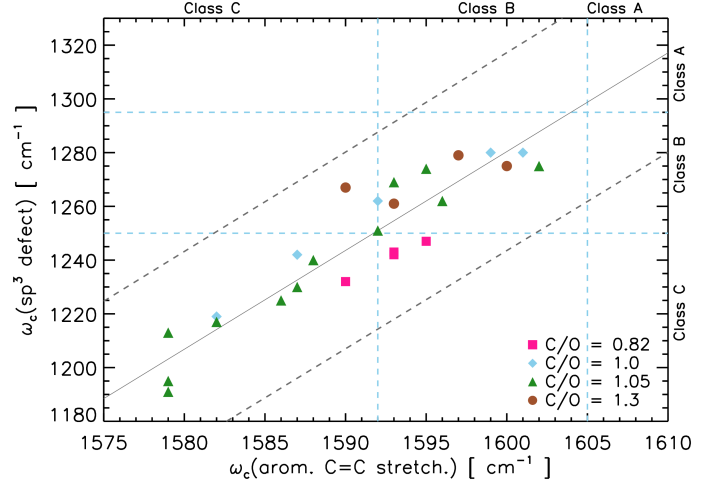
In Fig. 4 we plot the positions of the main electronic transitions measured in the UV and VUV. G1 and G2 are absorption peaks in the neighborhood of L1. We can see that each electronic transition falls within a particular energy range for all samples: G1 peaks are constrained between 4.8 and 5.7  $\mu\text{m}^{-1}$  while G2 peaks fall between 3 and 4  $\mu\text{m}^{-1}$ . The G1 and G2 transitions rarely appear simultaneously. The position of the G3 peak falls consistently at an average of 9  $\mu\text{m}^{-1}$ . The ratio of the integrated G3 band to the L1 feature averages  $2.0 \pm 0.8$ .

## 3.2. Relationships among the UV and mid-IR fit parameters

To complement the UV and VUV fit parameters, a detailed band analysis of the C-H stretching mode region (3100-2700  $\text{cm}^{-1}$ ) and bending mode region (1800-500  $\text{cm}^{-1}$ ) was performed. The Out Of Plane (OOP) bending modes in the 900 to 700  $\text{cm}^{-1}$  (11 to 15  $\mu\text{m}$ ) are generally used for the classification of the aromatic ring edge structures (Russo et al. 2014), but these are only present in the soots prepared in flames with  $C/O = 0.82$  and 1.05. The mid-infrared attributions are found in previous soot studies (Carpentier et al. 2012; Dartois et al. 2007). Generally, the bending mode region is  $\sim 1.5$ -4 times more absorbing than the stretching mode region for the soot samples. In a few cases, the integrated intensities of these modes were normalized to the most intense mode of the respective region for intercomparison between samples, to account for thickness variations between samples. The resulting fitted mid-infrared parameters are summarized in Table A.2.

### 3.2.1. $\omega_c(\text{sp}^3 \text{ defect})$ versus $\omega_c(\text{arom. C=C stretch.})$

In Fig. 5, we show the strong correlation ( $r^2 = 0.89$ ) between the  $\omega_c(\text{aromatic C=C stretch})$  and  $\omega_c(\text{sp}^3 \text{ defect})$  band positions, confirming previous findings (Carpentier et al. 2012). This relation traces differences in shapes and structures of the polyaromatic units in the soot. For polyaromatic carbons, three astrophysical AIB classes are proposed based on their spectra in the 6 to 9  $\mu\text{m}^{-1}$  region (Peeters et al. 2002). According to this classification, our laboratory soots correspond to classes B and C of the AIBs.



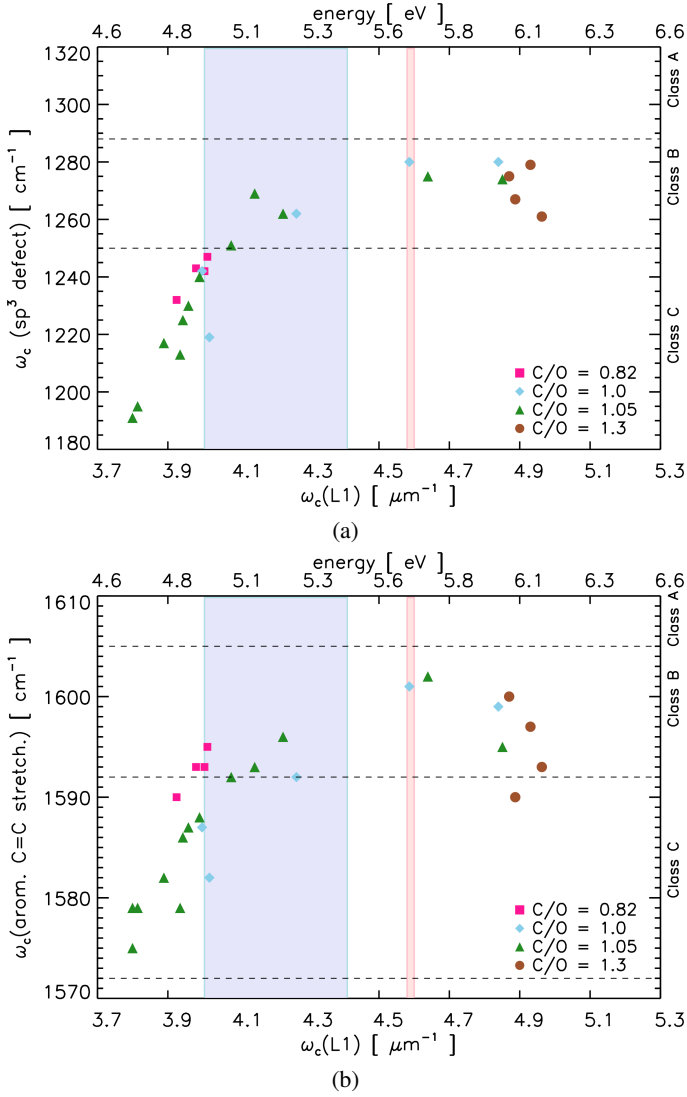
**Figure 5.** Correlation between the carbon defect band,  $\omega_c(\text{sp}^3 \text{ defect})$ , versus the aromatic C=C stretching band,  $\omega_c(\text{C=C})$ , verifying previous findings in other soot samples (Carpentier et al. 2012).

### 3.2.2. $\omega_c(\text{sp}^3 \text{ defect})$ & $\omega_c(\text{arom. C=C stretch.})$ versus $\omega_c(L1)$

The  $\text{sp}^3$  defect band is assigned to edge defects that can occur due to aliphatic cross-linking and as non-hexagonal rings carbon defects (Carpentier et al. 2012) and contribute to electronic intra-band states of the material. For our samples, this band appears between 1190 - 1280  $\text{cm}^{-1}$ .

In Fig. 6(a) we plot the position of the  $\text{sp}^3$  defect band versus the center of the L1 peak which correlates well for all of our samples. From this relation, the L1 position of the CSM bump would correspond to an  $\text{sp}^3$  defect located  $\sim 1260 \text{ cm}^{-1}$  (i.e. class B/C carrier) while for the ISM bump, we expect it to be found  $\sim 1280 \text{ cm}^{-1}$  (i.e. class B carrier).

In Fig. 6(b) we plot the position of the aromatic C=C band versus the center of the L1 peak, also well correlated, as expected from the relation found in Fig. 5. For the a-C:H, the C=C band is found at 1625  $\text{cm}^{-1}$  and for the soot with the highest  $E_g$  it is found at 1590  $\text{cm}^{-1}$ . As the value of  $E_g$  decreases (and the H/C ratio of the sample decreases), the position shifts down to 1575  $\text{cm}^{-1}$ . The correlation is linear up to L1 positions  $\sim 4.7 \mu\text{m}^{-1}$ . At higher energies this correlation shows a larger scatter. For the L1 position of the CSM bump, we would expect the C=C vibrational mode to be located  $\sim 1592 \text{ cm}^{-1}$  while for the ISM bump, we expect the defect to be found near 1600  $\text{cm}^{-1}$ . It is then not surprising that the  $\text{sp}^3$  defect and C=C band positions correlate with the position of L1 as they are all sensitive to the electrons delocalizations in  $\text{sp}^2$  conjugated systems.



**Figure 6.** Aromatic infrared bands (AIBs) in our laboratory soot samples. (a)  $\omega_c(\text{sp}^3 \text{ defect})$  versus  $\omega_c(\text{L1})$ . (b)  $\omega_c(\text{arom. C=C stretch.})$  versus  $\omega_c(\text{L1})$ . The laboratory found band positions for the  $\text{sp}^3$  defect and aromatic C=C band are compared to the classification of AIBs by (Peeters et al. 2002). Our laboratory samples are classified as Class B and Class C AIBs. The inferred CSM UV bump carrier fall within class B/C, and the ISM UV bump carriers approaches the A/B class.

### 3.3. Origin of UV features G1 and G2

#### 3.3.1. $A(\text{G1})/A(\text{C=O})$ versus $\omega_c(\text{L1})$

G1 is a minor peak appearing for some soots ( $\text{C/O} = 1.3$ , for all distances from the burner,  $\text{C/O} = 1.05$  for 14 and 18 mm) and for the a-C:H. To identify the origin of the G1 peak present in some UV spectra (for flames with  $\text{C/O}$  ratios = 1, 1.05 and 1.3), we plotted the Lorentzian position vs the ratio of the areas of  $A(\text{G1})$  to  $A(\text{C=O})$ , showing that this feature appears for a certain type of carbon, whose main  $\pi-\pi^*$  band appears at  $\omega_c(\text{L1}) > 4.6 \mu\text{m}^{-1}$ .

We choose the thickest films, where the carbonyl mode is clearly observed, to identify the origin of G1. These samples correspond to flames with  $\text{C/O} = 1, 1.05$ . The flame with  $\text{C/O} = 1.3$  produced very thin films where oxidation is surface dominated. By plotting the ratio of the G1 feature to the L1 feature

in the UV to the ratio of the integrated C=O to the C=C mode, a weak correlation arises. By following the evolution of the mid-infrared and UV spectra for the flame with  $\text{C/O} = 1$  in the series of Fig. A, as soon as the intensity of  $\text{C=O} \ll \text{C=C}$ , the UV G1 peak disappears. The G1 peak can be assigned to the oxidation of the younger soots produced near the burner, as traced by the C=O infrared intensities.

#### 3.3.2. $A(\text{G2})/A(\text{CH}_{\text{arom.}})$ versus $\omega_c(\text{L1})$

G2 is a minor peak appearing for some soots ( $\text{C/O} = 1$ , beyond 25-39 mm,  $\text{C/O}=1.05$ , beyond 22 mm) at  $\sim 5.3 \mu\text{m}^{-1}$  (180 nm). This peak appears as the soots are collected farther from the burner, i.e. more mature soots with polyaromatic structures or fullerene-like soots (Carpentier et al. 2012). Gadallah et al. (2011) and Llamas Jansa et al. (2003), attributed this peak to carbonyl vibrations. We propose a different attribution. We divided the integrated area of G2 by the integrated area of the aromatic =CH stretching mode, and confirm that G2 appears only when the intensity of the  $\text{sp}^3$  defect  $\gg$  C=C band and for  $\omega_c(\text{L1}) < 4.3 \mu\text{m}^{-1}$ , corresponding to the lower Tauc gap materials, i.e. low H/C soots where defects abound.

### 3.4. H/C ratios

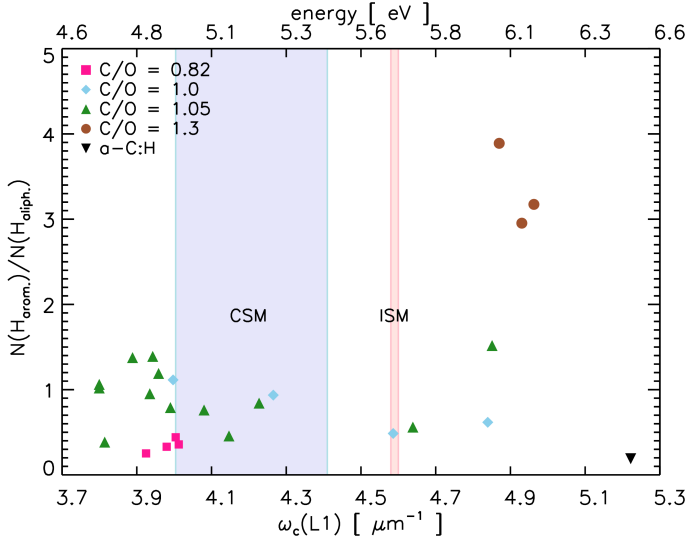
The mid-infrared spectra of different carbonaceous samples reveals the carbon hybridization states and allows us to discriminate between aliphatic and aromatic hydrogen. The C-H stretching peaks in the 3100-2900  $\text{cm}^{-1}$  allow us to determine the aromatic to aliphatic hydrogen ratio. We take the ratio of the integrated  $\text{CH}_{\text{aromatic}}$  ( $\sim 3040 \text{ cm}^{-1}$ ) to the  $\text{CH}_{\text{aliphatic}}$  modes ( $\text{CH}_2$  asymmetric stretching mode,  $\sim 2920 \text{ cm}^{-1}$  including the Fermi resonance and the  $\text{CH}_3$  asymmetric mode at  $\sim 2960 \text{ cm}^{-1}$ ) normalized by their oscillator strengths,  $A(\text{CH}_{\text{arom.}}) = 1.9 \times 10^{-18} \text{ cm/group}$ ,  $A(\text{CH}_{2,\text{as.}}) = 8.4 \times 10^{-18} \text{ cm/group}$ , and  $A(\text{CH}_{3,\text{as.}}) = 1.25 \times 10^{-17} \text{ cm/group}$  (Dartois et al. 2007). With the exception of a single sample ( $\text{C/O} = 1$ ,  $d=18 \text{ mm}$ ) most spectra show a dominance of methylene over methyl groups. The resulting ratio is shown in Fig. 7 plotted against the central position of L1, resulting in a large scatter. This is also the case for the ratio of the areas of  $\text{CH}_{\text{arom.}}$  to the sum of the areas of ( $\text{CH}_{\text{aliph.}} + \text{CH}_{\text{arom.}}$ ). We note in particular the case for soots produced in the  $\text{C/O} = 1.3$  flame, where the aromatic to aliphatic hydrogen ratio is an order of magnitude greater than in most other materials.

Carbonaceous materials containing hydrogen can be classified in terms of the hydrogen to carbon ratio (Robertson & O'Reilly 1987). To find a representative experimental H/C ratio for our samples we have considered different combinations of vibrational modes in the infrared spectra. An empirical parameter of the H/C content in our samples is found by taking the ratios of the integrated intensities of the  $\text{CH}_{\text{arom.}}$  mode to that of the aromatic C=C stretching mode ( $\sim 1600 \text{ cm}^{-1}$ ), (taking  $A(\text{C=C}) \sim 0.175 \times 10^{-18} \text{ cm/group}$  (Joblin et al. 1994)). We call this the aromatic H/C ratio. Using the empirically found aromatic H/C ratios and the aromatic+aliphatic H/C ratio, i.e.  $N(\text{CH}_{\text{arom.}} + \text{CH}_{2,3,\text{as.}})/N(\text{C=C})$ , we calculate  $X_H$ , defined as,

$$X_H = \frac{H/C}{1 + H/C} \quad (4)$$

The result is shown in Fig. 8. Two linear trends are found for the hydrogen poor ( $\text{H/C} \ll 1$ ) carbonaceous samples (soots).

Tamor & Wu (1990) provided an empirical linear relationship between the band gap and the H/C ratios of a-C:H materials with  $E_g = 1.2 - 2 \text{ eV}$ , where,



**Figure 7.** Aromatic to aliphatic hydrogen ratio versus  $\omega_c(L1)$ , determined from the integrated infrared  $=CH$  and  $-CH_{2,3}$  stretching modes, corrected by the ratio of the corresponding oscillator strengths.

$$E_g(eV) \simeq 4.3X_H \quad (5)$$

If only considering the aromatic H/C ratio, the coefficient is about 100 times larger than the one found by Tamor & Wu (1990). If we include the aliphatic contribution, the fitted slope is still  $\sim 4$  times larger. Although eq. 5 is applicable to a-C:H materials with  $E_g = 1.2 - 2$  eV and our soots have gaps between 0.01 to 1.60 eV, our materials show a linear relationship between the H/C ratio and the gap. This demonstrates that not only knowledge of hydrogen bonding but also knowledge of the carbon coordination is essential to understand the physical and chemical structure of carbonaceous materials. For low gap materials, Tamor & Wu's relationship no longer holds. The evolution of the properties between low gap and high gap materials should be taken into account in optical models of astrophysical carbon.

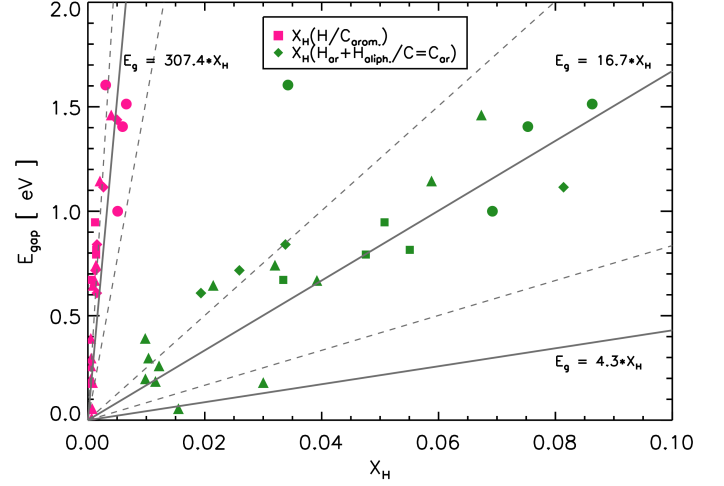
### 3.5. Carbon structure

#### 3.5.1. $L_a$ and $N_{rings}$ versus $\omega_c(L1)$

The  $E_g$  parameter can be used to unveil the structural properties of aromatic absorbers in amorphous carbons (Robertson & O'Reilly 1987; Robertson 1991), including the average coherence length,  $L_a$  (size of the polyaromatic units), and the number of aromatic rings,  $N_R$ , for the largest clusters contributing to the electronic density of states, although not necessarily the most abundant ones (Gadallah et al. 2011). An empirical relation between  $L_a$  and  $E_g$  was proposed by Robertson (1991),

$$L_a(nm) = \left[ \frac{0.77}{E_g(eV)} \right]. \quad (6)$$

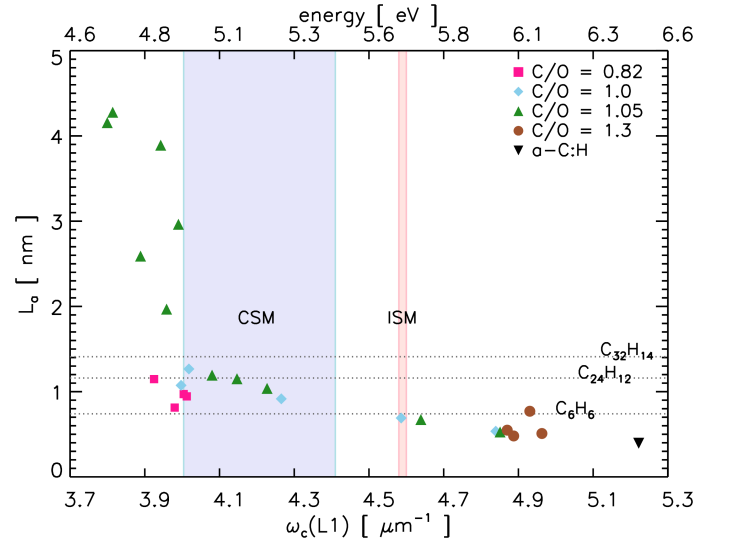
A similar empirical relation was proposed for a single graphene sheet where the number of six-fold aromatic rings,  $N_R$ , can be derived from  $E_g$  according to the model by Robertson & O'Reilly (1987), in which the gap energy decreases as a func-



**Figure 8.** Empirically found  $E_g$  versus  $X_H$ . We used the aromatic H/C ratio and aromatic+aliphatic H/C ratio, presented as two linear fits for the hydrogen poor (low  $E_g$ ) regime (only soots). When both aromatic and aliphatic CH modes are included, our linear fit approaches the coefficient found for amorphous carbon in Tamor & Wu (1990). The shape of the symbols corresponds to those used in Fig. 7.

tion of the size of the graphene layers, via the following relation,

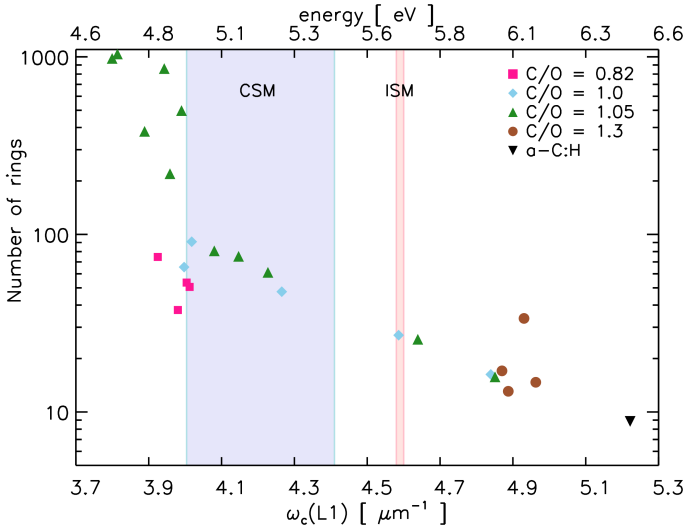
$$N_R = \left[ \frac{5.8}{E_g(eV)} \right]^2. \quad (7)$$



**Figure 9.** Average coherence length,  $L_a$ , of polyaromatic units of selected laboratory carbons ( $L_a < 5$  nm) versus  $\omega_c(L1)$ . For comparison, we included the coherence length of Benzene ( $C_6H_6$ ), Coronene ( $C_{24}H_{12}$ ) and Ovalene ( $C_{32}H_{14}$ ), found in <http://pah.nist.gov>.

We have plotted the  $E_g$  derived  $N_R$  and  $L_a$  values and plotted them against the position of the main UV bump (also strongly correlated to  $E_g$ ) shown in figures 9 and 10. When the position of the L1 peak shifts towards the UV, towards a larger band gap,





**Figure 10.** Number of rings,  $N_R$ , in the polyaromatic units of our laboratory carbons versus  $\omega_c(L1)$  suggesting  $N_R \sim 60$  for the CSM bump and  $N_R \sim 25$  for the ISM bump.

$L_a$  and  $N_R$  decrease. For the interstellar UV bump this would correspond to about 25 rings in a polyaromatic unit, and to 65 rings for the circumstellar bump. For the aromatic coherence length, we infer  $\sim 0.7$  nm for the interstellar bump carrier and  $\sim 1$  nm for the circumstellar bump carrier. Our soots consist of  $L_a = 0.5$  to 3.3 nm nanoparticles with corresponding band gaps of  $E_g = 0.1 - 1.6$  eV. The smallest aromatic length  $L_a = 0.4$  nm was found for the a-C:H with  $E_g = 2$  eV.

### 3.5.2. H/C versus $L_a$ and $N_{rings}$

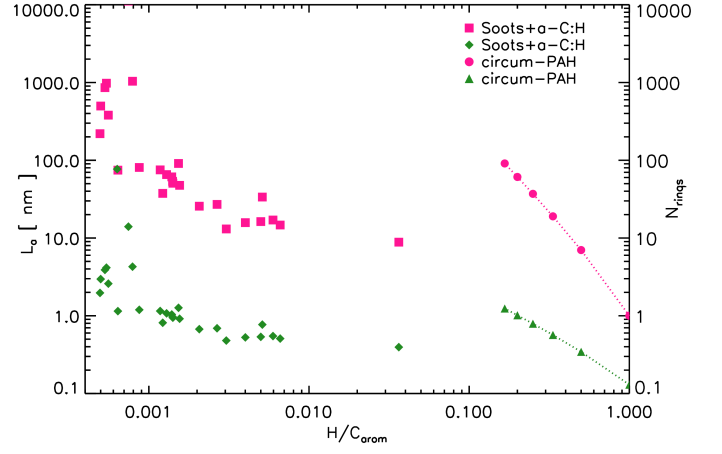
We use empirical relationships between the number of rings and the H/C ratio of our materials and compare them to purely aromatic carbons, i.e. PAHs. In circum-PAHs the number of rings grows in a sequence as follows:  $N_{rings} = 1, 7, 19, 37, 61, 91$ , with corresponding H/C ratios = 1, 0.5, 0.33, 0.25, 0.2, 0.17. To compare the structure of our soots to these PAHs we will use the relation found in Jones (2012b), to evaluate the radius of the most compact aromatic domains, equivalent to  $L_a$  for the circum-PAHs,

$$a_R(nm) = 0.09 * (2 * N_R + \sqrt{N_R} + 0.5)^{0.5} \quad (8)$$

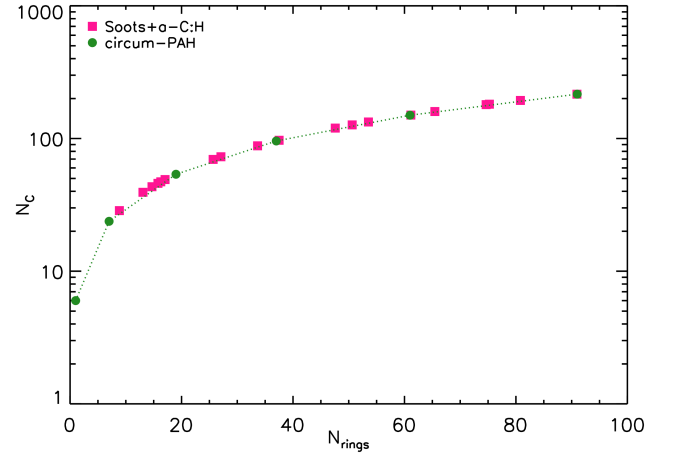
As show in Fig. 11 our samples are, as expected, much less hydrogenated than circum-PAHs. For these soots,  $L_a$  ranges from 0.3 to 10 nm while the number of rings in a polyaromatic unit spans from  $\sim 1$  for the most hydrogenated soot sample to 1000 for the least hydrogenated. Both  $L_a$  and  $N_R$  decay exponentially as a function of the aromatic H/C ratio following the same trend as PAHs. Similarly, to find the number of carbon atoms in these polyaromatic units, we use the following equation from (Jones 2012b),

$$N_C = 2 * N_R + 3.5 * \sqrt{N_R} + 0.5 \quad (9)$$

As shown in Fig. 12 the polyaromatic units in our soot samples contain between 20 and 100 carbon atoms. These are in the same range as those discussed in Steglich et al. (2010), who proposed, in accordance to semi-empirical calculations, that a distribution of large PAH molecules with a mean size of 50-60 carbon atoms can produce a bump centered at  $\sim 217.5$  nm.



**Figure 11.** Average coherence length,  $L_a$ , and number of rings,  $N_R$ , in the polyaromatic units of our laboratory carbons and circum-PAHs versus the corresponding aromatic H/C ratio.

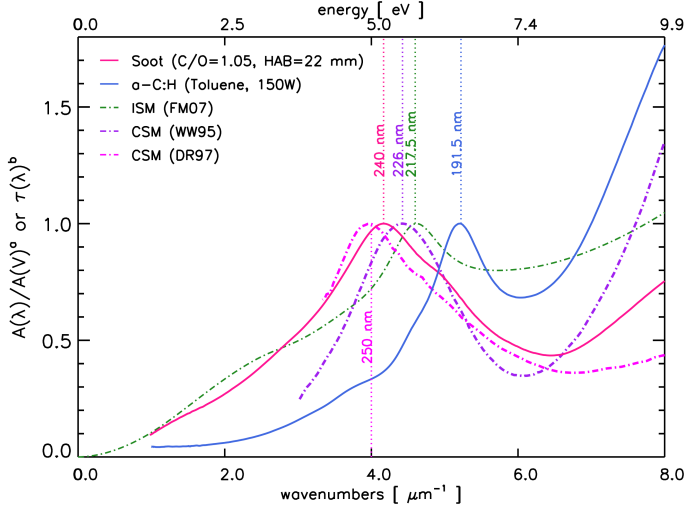


**Figure 12.** Number of carbon atoms ( $N_C$ ) versus the number of rings  $N_R$  in the polyaromatic units of the laboratory samples presented here (soots and a-C:H) and circum-PAHs, using Eq. 9.

## 4. Discussion

The transmission measurements from the VUV to the mid-infrared of several carbonaceous samples have allowed us to perform a large spectroscopic study covering the main electronic and vibrational transitions. We find the following correlations:

- The position of the UV L1 feature ( $\pi-\pi^*$ ) is correlated to the position of the  $sp^3$  carbon defect, and to the position of the aromatic C=C stretching mode. This reveals a relation between electronic and vibrational band positions in soots.
- The Tauc optical gap,  $E_g$ , is correlated to the position of the  $\pi-\pi^*$  band,  $\omega_c(L1)$ . Both  $E_g$  and  $\omega_c(L1)$  are relevant parameters allowing the classification of both soots and a-C:Hs.
- The H/C ratio of these carbonaceous samples is correlated to  $E_g$  and therefore to  $\omega_c(L1)$ . For soots, the empirical relationship between the H/C ratio and the gap differs from that found for highly hydrogenated carbonaceous materials.



**Figure 13.** Normalized laboratory soot and a-C:H visible-VUV spectra compared to the average ISM extinction curve (Fitzpatrick & Massa 2007) (FM07), and the CSM extinction curves of the circumstellar envelope of HD 213985 (Waelkens et al. 1995) (WW95) and V348 Sagittarii (Drilling et al. 1997) (DR97), for which the original spectrum has been heavily filtered. All spectra are re-normalized to the maximum intensity of their  $\pi$ - $\pi^*$  resonance.

The wide variety of our laboratory carbonaceous dust allows us to explore the spectral properties of the observed ISM and CSM extinction curves (e.g. Fig 13), from the VUV to the IR :

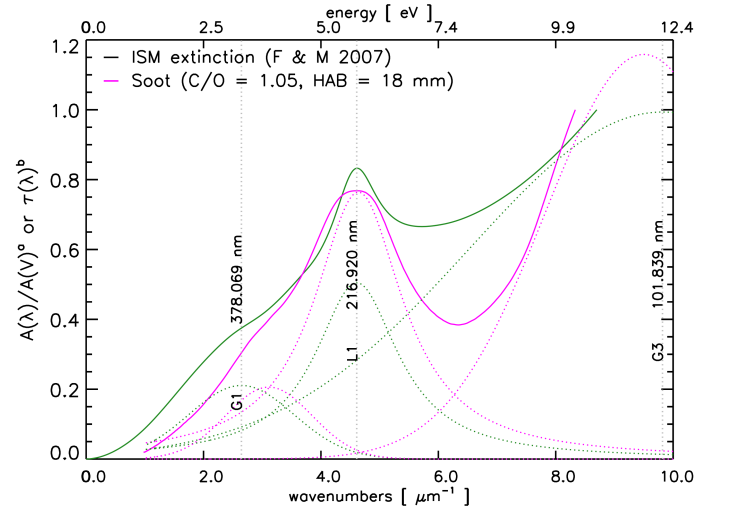
- Spectroscopy in the VUV ( $120 < \lambda < 200$  nm), has allowed us to identify an absorption band in the VUV present in all our samples: the G3 band, with a fitted position centered at  $\sim 9 \mu\text{m}^{-1}$  ( $\sim 110$  nm) and an integrated optical depth ratio of  $\sim 2$  with respect to L1. G3 is attributed to  $\sigma$ - $\sigma^*$  transitions and may contribute to the FUV rise identified in Fitzpatrick & Massa (2007).
- For the average ISM bump, centered at 217.5 nm, we infer the following spectral properties of the carrier:  $E_g \sim 1.2$  eV,  $\omega_c(\text{G3}) \sim 9.5 \mu\text{m}^{-1}$ ,  $\omega_c(\text{sp}^3 \text{ defect}) \sim 1280 \text{ cm}^{-1}$ ,  $\omega_c(\text{C}=\text{C}) \sim 1600 \text{ cm}^{-1}$ .
- For the average CSM bump, centered  $\sim 226$ -250 nm, we infer the following spectral properties of the carrier:  $E_g \sim 0.7$  eV,  $\omega_c(\text{G3}) \sim 9 \mu\text{m}^{-1}$ ,  $\omega_c(\text{sp}^3 \text{ defect}) \sim 1250 \text{ cm}^{-1}$ ,  $\omega_c(\text{C}=\text{C}) \sim 1592 \text{ cm}^{-1}$ .

The connection between ultraviolet extinction data and infrared emission has been possible thanks to early datasets from the IUE and IRAS satellites, observing towards the same lines of sight. Cox & Leene (1987) showed the absence of correlation between the mid-infrared excess and the normalized intensity of the UV bump, but later work by Cardelli et al. (1989) showed that their bump normalization was not appropriate. An extended study by Jenniskens & Desert (1993) and later on by Boulanger et al. (1994) revealed a link between mid-infrared emission bands (AIBs) and the UV bump absorption. In contrast, they found no relation between the AIBs to the FUV rise.

Correlations between the positions of UV and infrared absorption bands are found for the carbonaceous samples presented in this paper. These spectral parameters suggest that the carrier of the ISM bump is likely found at the frontier of class B/A of the AIBs, while the carrier of the CSM bump is found at the fron-

tier of class B/C. Based on the Tauc optical gap and using available empirical formulae for carbons, the structure of the ISM UV bump carrier implies an average polyaromatic unit size  $\sim 0.7$  nm and for the CSM UV bump carrier,  $\sim 1.1$  nm, within nanoparticles.

While the position of the interstellar 217.5 nm bump ( $4.592 \mu\text{m}^{-1}$ ) is stable, its FWHM varies (Fitzpatrick & Massa 2005). The FWHM of the  $\pi$ - $\pi^*$  band of our carbonaceous analogs,  $\gamma(\text{L1})$ , is correlated to the position  $\omega_c(\text{L1})$ . None of our samples fulfill simultaneously the observed constraints on the UV bump (position, FWHM) in interstellar spectra (Fitzpatrick & Massa 2007). In Fig. 14, we take the average interstellar extinction curve and perform a deconvolution as done for our laboratory samples to explore the effect of the deconvolution on the same basis. A direct comparison of the FWHM of a laboratory soot (1.88  $\mu\text{m}^{-1}$ ) to the newly parametrized FWHM (1.78  $\mu\text{m}^{-1}$ ) from the average interstellar extinction curve indicates that laboratory polyaromatic solid carbons can approximate the average carrier of the UV bump. However, it is more likely than more than one kind of carbon is measured towards a line of sight, and that more hydrogenated carbons contribute strongly to the FUV rise as shown in Gavilan et al. (2016) and in Fig. 13, where our laboratory soot and a-C:H spectra are compared to extinction curves in the ISM and CSM.



**Figure 14.** Deconvolution of the average interstellar extinction curve (Fitzpatrick & Massa 2007) ( $^{\circ}$ normalized to its maximum) following the deconvolution procedure of laboratory soots described in Sect. 3.1. The L1 peak is centered at  $\omega_c = 4.609 \mu\text{m}^{-1}$  with a FWHM =  $1.779 \mu\text{m}^{-1}$ . While the position is unchanged with respect to the parametrization of (Fitzpatrick & Massa 2007), the original FWHM value is almost doubled. For comparison, the spectra of a laboratory soot prepared in a flame with C/O = 1.05 and HAB = 18 mm is included, showing a similarly intense and wide  $\pi$ - $\pi^*$  transition, a G1 peak and a slightly less intense FUV rise.

## 5. Conclusions

We have produced laboratory analogs to interstellar carbonaceous dust characterized by their wide degree of hydrogenation and differences in polyaromatic structure. This influences the

spectral signatures, in particular the position of the UV bump, attributed to  $\pi$ - $\pi^*$  electronic transitions. Our carbonaceous analogs consist of soots, characterized by low H/C and  $E_g$  values. A hydrogenated a-C:H with  $E_g \sim 2$  eV was also produced. The UV to mid-infrared spectroscopy has allowed us to find correlations between the electronic transitions and vibrational modes and to deduce structural properties such as the average length ( $\sim 0.7 - 1.1$  nm) of polyaromatic units within nanoparticles.

These laboratory correlations suggest that for the interstellar and circumstellar UV bump carriers, infrared signatures are expected in classes B/A and B/C of the AIBs respectively. More hydrogenated carbons contribute to the FUV rise in agreement with its weak correlation with the UV bump. Observations are then not only sensitive to local environmental conditions but also to the transition of dust from circum- to interstellar environments. As shown by our measurements, disordered polyaromatic carbonaceous grains are viable carriers of the observed UV interstellar and circumstellar extinction.

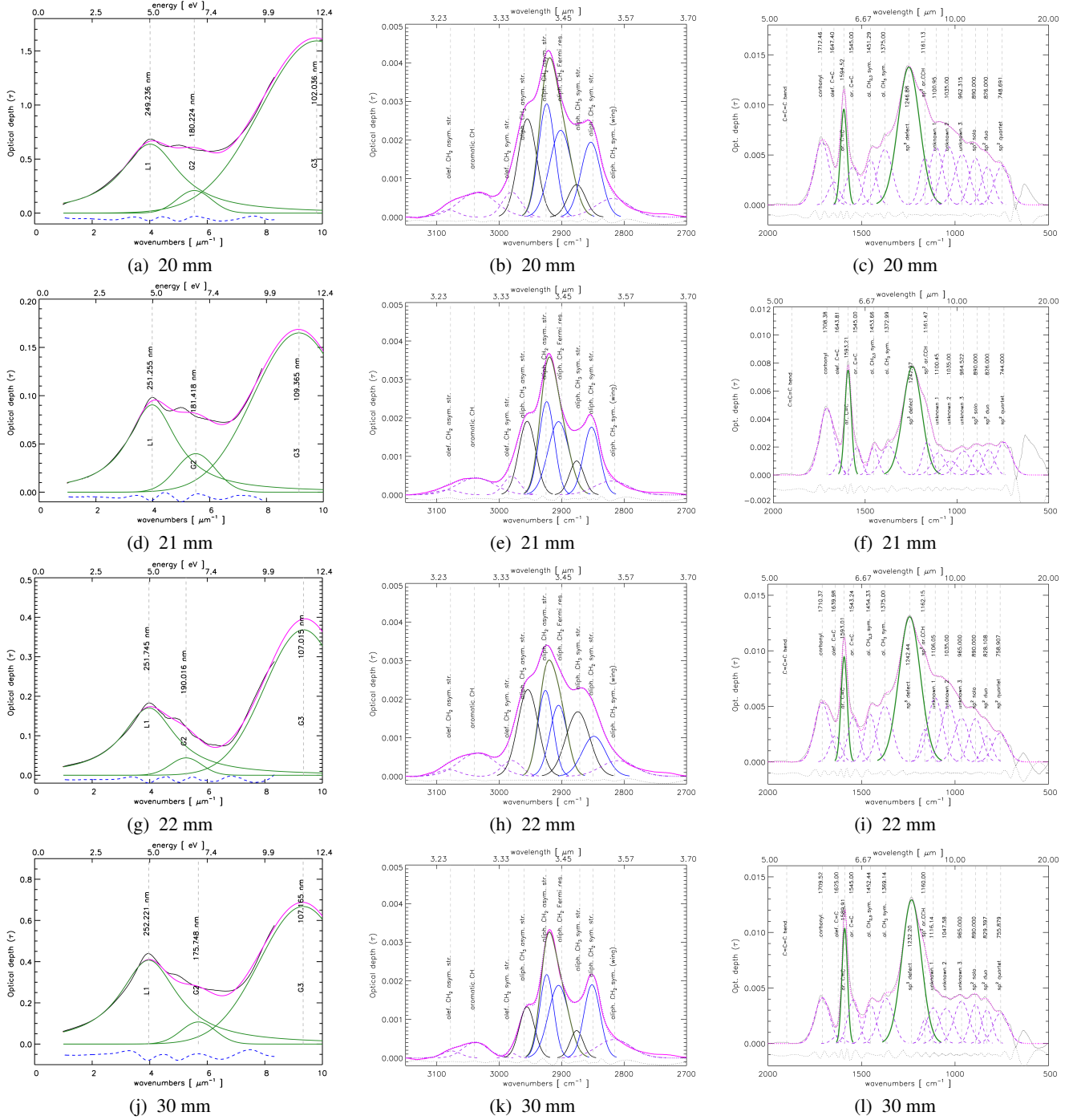
*Acknowledgments.* VUV measurements were performed at the DISCO beamline of the SOLEIL synchrotron radiation facility (projects: 20141074 & 20130778). This work has been supported by the French program PCMI, and the ANR COSMISME project (grant ANR-2010-BLAN-0502). K.C.L. thanks the Vietnamese government for a doctoral scholarship. L.G. thanks the Centre National d'Études Spatiales (CNES) for a post-doctoral fellowship.

## References

- Acke, B., Bouwman, J., Juhász, A., et al. 2010, *ApJ*, 718, 558  
 Adkins, E. M. & Miller, J. H. 2015, *Phys. Chem. Chem. Phys.*, 17, 2686  
 Alata, I., Cruz-Diaz, G. A., Muñoz Caro, G. M., & Dartois, E. 2014, *A&A*, 569, A119  
 Alata, I., Jallat, A., Gavilan, L., et al. 2015, *A&A*, 584, A123  
 Bescond, A., Yon, J., Ouf, F.-X., et al. 2016, *Journal of Aerosol Science*, 101, 118  
 Blanco, A., Fonti, S., & Orofino, V. 1995, *ApJ*, 448, 339  
 Boulanger, F., Prevot, M. L., & Gry, C. 1994, *A&A*, 284, 956  
 Cardelli, J. A., Clayton, G. C., & Mathis, J. S. 1989, *ApJ*, 345, 245  
 Carpentier, Y., Féraud, G., Dartois, E., et al. 2012, *A&A*, 548, A40  
 Colangeli, L., Bussoletti, E., Pestellini, C. C., et al. 1997, *Advances in Space Research*, 20, 1617  
 Colangeli, L., Mennella, V., Blanco, A., et al. 1993, *ApJ*, 418, 435  
 Cox, P. & Leene, A. 1987, *A&A*, 174, 203  
 Dartois, E., Geballe, T. R., Pino, T., et al. 2007, *A&A*, 463, 635  
 Dartois, E., Muñoz Caro, G. M., Deboffle, D., & d'Hendecourt, L. 2004, *A&A*, 423, L33  
 Dartois, E., Muñoz Caro, G. M., Deboffle, D., Montagnac, G., & D'Hendecourt, L. 2005, *A&A*, 432, 895  
 Draine, B. T. & Lee, H. M. 1984, *ApJ*, 285, 89  
 Drilling, J. S., Hecht, J. H., Clayton, G. C., et al. 1997, *ApJ*, 476, 865  
 Duley, W. W. & Hu, A. 2012, *ApJ*, 761, 115  
 Dworschak, W. 1990, *Thin Solid Films*, 189, 257  
 Fink, J., Müller-Heinzerling, T., Pflüger, J., et al. 1984, *Phys. Rev. B*, 30, 4713  
 Fitzpatrick, E. L. & Massa, D. 1986, *ApJ*, 307, 286  
 Fitzpatrick, E. L. & Massa, D. 1988, *ApJ*, 328, 734  
 Fitzpatrick, E. L. & Massa, D. 1990, *ApJS*, 72, 163  
 Fitzpatrick, E. L. & Massa, D. 2005, *AJ*, 130, 1127  
 Fitzpatrick, E. L. & Massa, D. 2007, *ApJ*, 663, 320  
 Furton, D. G., Laiho, J. W., & Witt, A. N. 1999, *ApJ*, 526, 752  
 Gadallah, K. A. K., Mutschke, H., & Jäger, C. 2011, *A&A*, 528, A56  
 Gavilan, L., Alata, I., Le, K. C., et al. 2016, *A&A*, 586, A106  
 Giuliani, A., Jamme, F., Rouam, V., et al. 2009, *Journal of Synchrotron Radiation*, 16, 835  
 Godard, M. & Dartois, E. 2010, *A&A*, 519, A39  
 Godard, M., Féraud, G., Chabot, M., et al. 2011, *A&A*, 529, A146  
 Greenberg, J. M. & Li, A. 1999, *Advances in Space Research*, 24, 497  
 Jäger, C., Krasnokutski, S., Staicu, A., et al. 2006, *ApJS*, 166, 557  
 Jäger, C., Mutschke, H., Henning, T., & Huisken, F. 2008, *ApJ*, 689, 249  
 Jenniskens, P. & Desert, F. X. 1993, *A&A*, 275, 549  
 Joblin, C., D'Hendecourt, L., Leger, A., & Defourneau, D. 1994, *A&A*, 281, 923  
 Jones, A. P. 1990, *MNRAS*, 247, 305  
 Jones, A. P. 2012a, *A&A*, 545, C2  
 Jones, A. P. 2012b, *A&A*, 540, A1  
 Jones, A. P. 2012c, *A&A*, 542, A98  
 Jones, A. P., Fanciullo, L., Köhler, M., et al. 2013, *A&A*, 558, A62  
 Llamas Jansa, I., Jäger, C., Mutschke, H., & Henning, T. 2003, in *Astrophysics of Dust*  
 Mansurov, Z. A. 2005, *Combustion, Explosion and Shock Waves*, 41, 727  
 Markwardt, C. B. 2009, *Proc. Astronomical Data Analysis Software and Systems XVIII*, 411, 251  
 Mennella, V., Baratta, G. A., Esposito, A., Ferini, G., & Pendleton, Y. J. 2003, *ApJ*, 587, 727  
 Mennella, V., Brucato, J. R., Colangeli, L., & Palumbo, P. 2002, *ApJ*, 569, 531  
 Mennella, V., Colangeli, L., Palumbo, P., et al. 1996, *ApJ*, 464, L191  
 Peeters, E. 2014, in *IAU Symposium, Vol. 297, The Diffuse Interstellar Bands*, ed. J. Cami & N. L. J. Cox, 187–196  
 Peeters, E., Hony, S., Van Kerckhoven, C., et al. 2002, *A&A*, 390, 1089  
 Pendleton, Y. J. & Allamandola, L. J. 2002, *ApJS*, 138, 75  
 Pino, T., Carpentier, Y., Féraud, G., et al. 2015, *Highlights of Astronomy*, 16, 717  
 Pino, T., Dartois, E., Cao, A.-T., et al. 2008, *A&A*, 490, 665  
 Robertson, J. 1986, *Advances in Physics*, 35, 317  
 Robertson, J. 1991, *Journal of Non Crystalline Solids*, 137, 825  
 Robertson, J. & O'Reilly, E. P. 1987, *Phys. Rev. B*, 35, 2946  
 Rosenberg, M. J. F., Berné, O., & Boersma, C. 2014, *A&A*, 566, L4  
 Russo, C., Stanzione, F., Tregrossi, A., & Ciajolo, A. 2014, *Carbon*, 74, 127  
 Schnaiter, M., Mutschke, H., Dorschner, J., Henning, T., & Salama, F. 1998, *ApJ*, 498, 486  
 Scott, A. & Duley, W. W. 1996, *ApJ*, 472, L123  
 Sloan, G. C., Jura, M., Duley, W. W., et al. 2007, *ApJ*, 664, 1144  
 Stecher, T. P. & Donn, B. 1965, *ApJ*, 142, 1681  
 Steglich, M., Jäger, C., Rouillé, G., et al. 2010, *ApJ*, 712, L16  
 Tamor, M. A. & Wu, C. H. 1990, *Journal of Applied Physics*, 67, 1007  
 Tauc, J., Grigorovici, R., & Vancu, A. 1966, *Physica Status Solidi B-basic Solid State Physics*, 15, 627  
 Trumpler, R. J. 1930, *PASP*, 42, 267  
 Waelkens, C., Waters, L. B. F. M., van Winckel, H., & Daems, K. 1995, *Ap&SS*, 224, 357  
 Yang, X. J., Glaser, R., Li, A., & Zhong, J. X. 2013, *ApJ*, 776, 110  
 Zubko, V. G., Mennella, V., Colangeli, L., & Bussoletti, E. 1996, *MNRAS*, 282, 1321

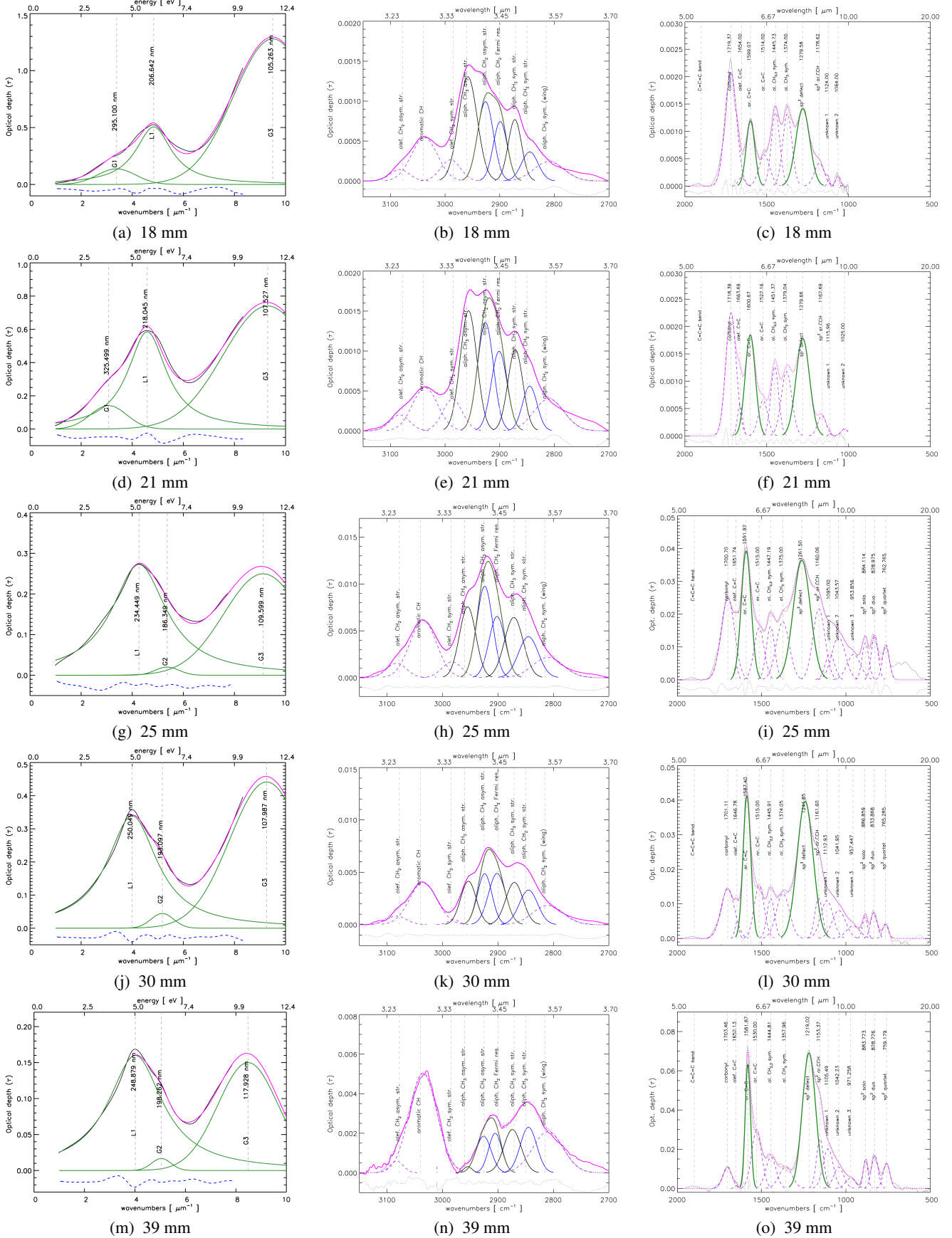
## Appendix A:

**Figure A.1.** UV-VUV and mid-infrared spectral deconvolution for soot samples prepared with a C/O = 0.82 combustion flame, retrieved at a HAB of (a) 20 mm to (g) 30 mm.

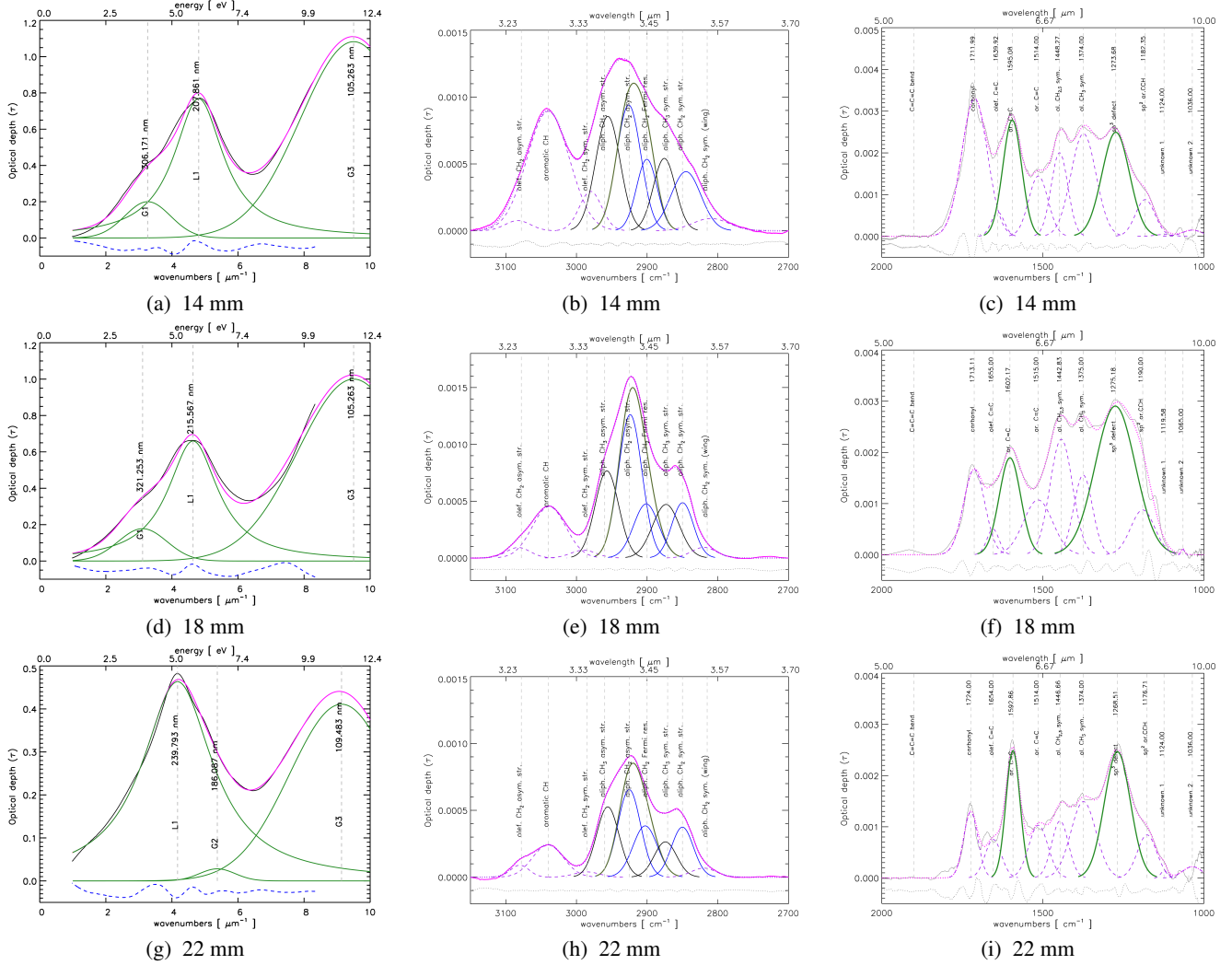




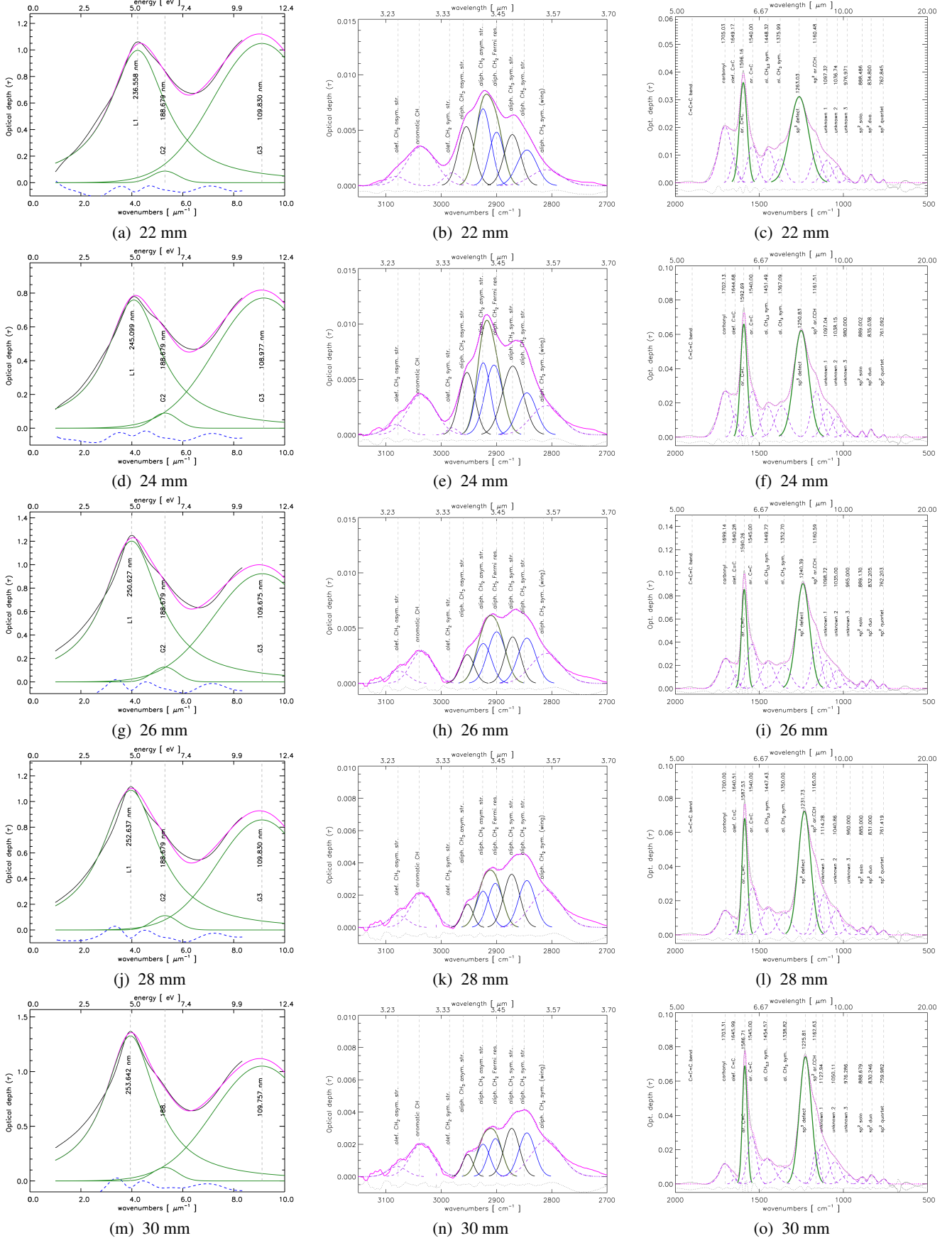
**Figure A.2.** UV-VUV and mid-infrared spectral deconvolution for soot samples prepared with a C/O = 1 combustion flame, retrieved at a HAB of (a) 18 mm to (i) 39 mm.



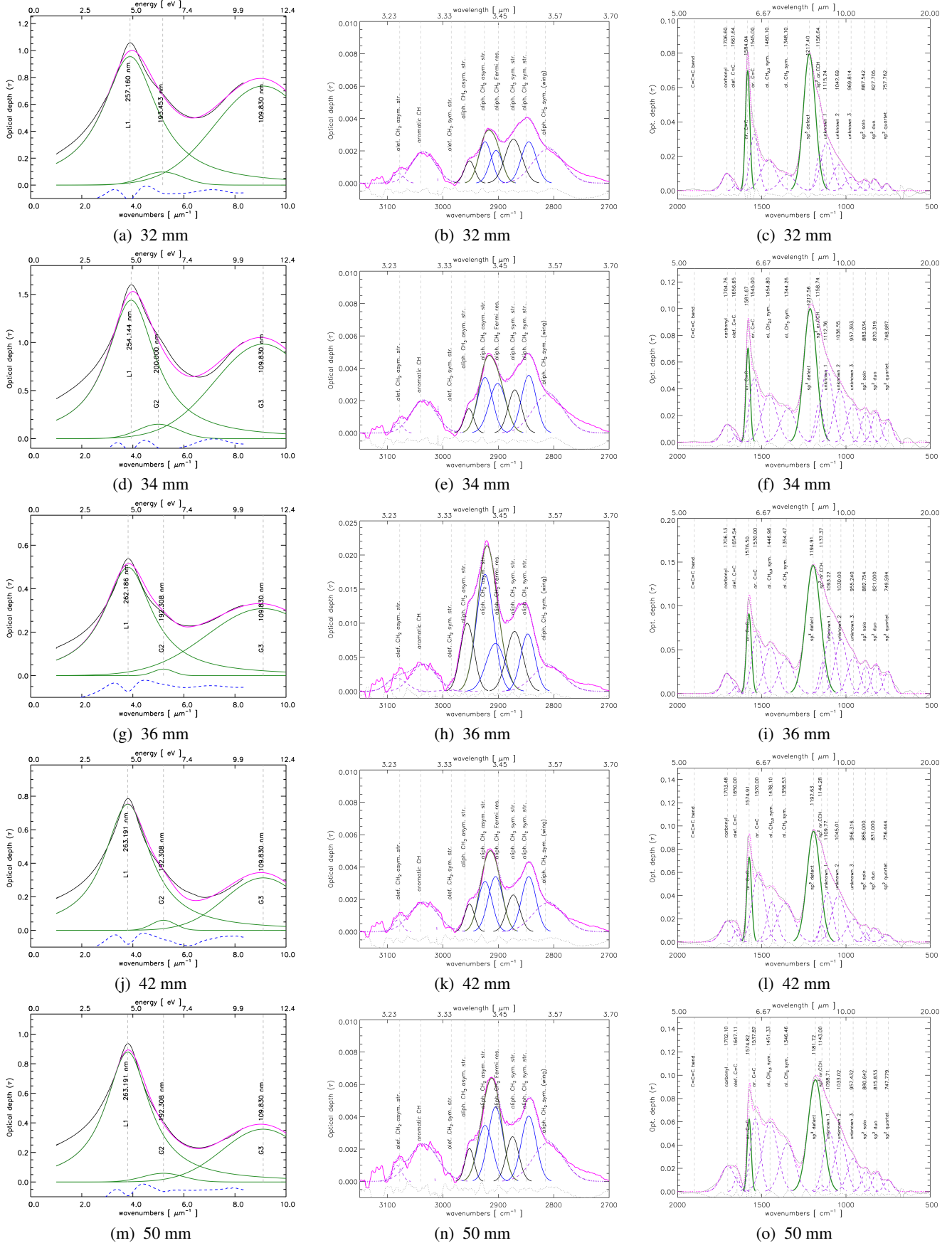
**Figure A.3.** UV-VUV and mid-infrared spectral deconvolution for soot samples prepared with a C/O = 1.05 combustion flame, retrieved at a HAB of (a) 18 mm to (e) 20 mm.



**Figure A.4.** UV-VUV and mid-infrared spectral deconvolution for soot samples prepared with a C/O = 1.05 combustion flame, retrieved at a HAB of (a) 22 mm to (j) 30 mm.

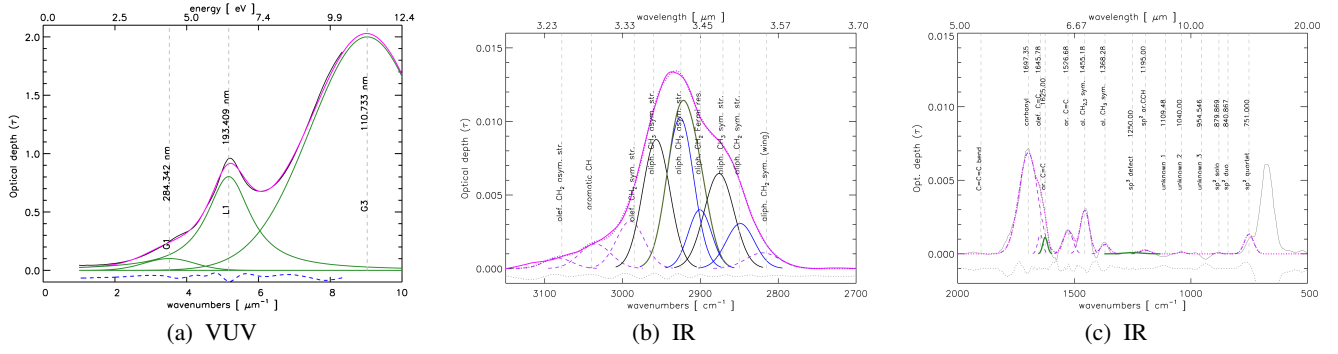


**Figure A.5.** UV-VUV and mid-infrared spectral deconvolution for soot samples prepared with a C/O = 1.05 combustion flame, retrieved at a HAB of (a) 32 mm to (j) 50 mm.





**Figure A.7.** UV-VUV and mid-infrared spectral deconvolution for an a-C:H produced with C<sub>7</sub>H<sub>8</sub>.



**Table A.1.** UV and VUV fitting parameters

flame C/O	d [ mm ]	$E_g$ [ eV ]	$\omega_c(L1)$ [ $\text{cm}^{-1}$ ]	$\omega_c(G1)$ [ $\text{cm}^{-1}$ ]	$\omega_c(G2)$ [ $\text{cm}^{-1}$ ]	$\omega_c(G3)$ [ $\text{cm}^{-1}$ ]	$\gamma(L1)$ [ $\text{cm}^{-1}$ ]	$\gamma(G1)$ [ $\text{cm}^{-1}$ ]	$\gamma(G2)$ [ $\text{cm}^{-1}$ ]	$\gamma(G3)$ [ $\text{cm}^{-1}$ ]	A(L1) [ $\text{cm}^{-1}$ ]	A(G1) [ $\text{cm}^{-1}$ ]	A(G2) [ $\text{cm}^{-1}$ ]	A(G3) [ $\text{cm}^{-1}$ ]
0.82	20	$0.82 \pm 0.20$	40123	NA	56733	91010	25118	NA	9000	43128	24725	NA	1720	50729
	21	$0.95 \pm 0.21$	39800	NA	55122	91437	21094	NA	8000	33800	2997	NA	300	7500
	22	$0.79 \pm 0.25$	40041	NA	52988	90470	22136	NA	12277	32212	6064	NA	638	8196
	30	$0.67 \pm 0.30$	39248	NA	55319	94136	21711	NA	10000	40317	14365	NA	1110	18455
1	18	$1.44 \pm 0.05$	48393	34498	NA	95960	17438	16385	NA	36810	12782	2228	NA	50100
	21	$1.11 \pm 0.08$	45862	30939	NA	97122	18124	13301	NA	47060	16240	1502	NA	39132
	25	$0.84 \pm 0.15$	42653	NA	53663	91242	25958	NA	15091	39000	11118	NA	964	10260
	30	$0.72 \pm 0.21$	39971	NA	51638	95063	24267	NA	12162	35765	12721	NA	993	17451
	39	$0.61 \pm 0.25$	40180	NA	48915	90115	26774	NA	9000	34401	6580	NA	200	8000
1.05	14	$1.46 \pm 0.02$	48509	34165	NA	91815	15879	11705	NA	38870	17806	2000	NA	35240
	18	$1.14 \pm 0.05$	46389	30894	NA	91843	18823	14482	NA	36160	19742	2187	NA	34210
	22	$0.67 \pm 0.16$	41467	NA	52544	92021	25916	NA	10000	45067	18428	NA	799	17124
1.05	22	$0.74 \pm 0.09$	42273	NA	53000	91050	26827	19165	19000	42000	NA	2999	48470	
	24	$0.65 \pm 0.16$	40800	NA	53000	91763	26000	NA	13202	19000	31000	NA	2012	37420
	26	$0.26 \pm 0.10$	39900	NA	53000	91179	26500	NA	8000	19000	50000	NA	1610	45893
	28	$0.39 \pm 0.08$	39583	NA	53000	91050	27000	NA	7254	17436	46147	NA	759	38380
	30	$0.20 \pm 0.05$	39426	NA	53000	91111	24000	NA	8000	19000	50000	NA	1544	52000
	32	$0.30 \pm 0.11$	38886	NA	51692	91050	26000	NA	10000	19000	39000	NA	1367	35000
	34	$0.01 \pm 0.01$	39348	NA	50000	91050	23000	NA	8000	19000	52000	NA	2000	45000
	36	$0.18 \pm 0.05$	38141	NA	52000	91050	23000	NA	7000	22000	18000	NA	500	51700
	42	$0.19 \pm 0.05$	37995	NA	52000	91050	22000	NA	14011	22000	26000	NA	1749	51700
	50	$0.05 \pm 0.02$	37995	NA	50000	91050	21000	NA	7999	21000	29000	NA	600	49350
1.3	25	$1.60 \pm 0.01$	48873	34283	NA	96059	16626	11415	NA	44000	18452	2000	NA	42270
	27	$1.51 \pm 0.01$	49628	33000	NA	91206	20000	9900	NA	35360	14997	1200	NA	36150
	30	$1.41 \pm 0.01$	48700	32769	NA	93890	17578	12228	NA	44000	26098	3000	NA	44990
	39	$1.00 \pm 0.03$	49305	31021	NA	96073	19126	13066	NA	49370	37108	3000	NA	69270
a-C:H	NA	$1.95 \pm 0.10$	52219	38583	NA	91175	11731	16464	NA	39323	12527	966	NA	26057

**Table A.2.** Infrared fitting parameters

flame C/O	distance [ mm ]	band positions			integrated vibrational modes							
		$\omega_c(\text{C}=\text{C})$ [ $\text{cm}^{-1}$ ]	$\omega_c\text{sp}^3$ [ $\text{cm}^{-1}$ ]	$\Delta(\text{CC} - \text{sp}^3)$ [ $\text{cm}^{-1}$ ]	$\text{CH}_{\text{arom.}}$ [ $\text{cm}^{-1}$ ]	$\text{CH}_{3,\text{aliph.}}$ [ $\text{cm}^{-1}$ ]	$\text{CH}_{2,\text{aliph.}}$ [ $\text{cm}^{-1}$ ]	$\text{CH}_{3,\text{Fermi.}}$ [ $\text{cm}^{-1}$ ]	C=O [ $\text{cm}^{-1}$ ]	C=C [ $\text{cm}^{-1}$ ]	$\text{sp}^3$ [ $\text{cm}^{-1}$ ]	$\text{sp}^2$ solo [ $\text{cm}^{-1}$ ]
0.82	20	1595	1247	348	0.05	0.10	0.10	0.10	0.63	0.41	1.97	0.40
	21	1593	1243	350	0.03	0.06	0.07	0.08	0.48	0.33	0.98	0.13
	22	1593	1242	351	0.04	0.09	0.07	0.06	0.53	0.39	1.86	0.34
	30	1590	1232	358	0.02	0.04	0.06	0.08	0.41	0.38	1.67	0.26
1	18	1599	1280	319	0.03	0.06	0.04	0.02	0.18	0.08	0.15	NA
	21	1601	1280	321	0.03	0.06	0.05	0.04	0.18	0.14	0.18	NA
	25	1592	1262	330	0.37	0.28	0.35	0.24	2.48	2.86	4.58	0.56
	30	1587	1242	346	0.25	0.15	0.16	0.19	1.44	2.33	4.70	0.23
	39	1582	1219	363	0.32	0.01	0.06	0.06	0.72	2.49	6.79	0.50
1.05	14	1595	1274	321	0.07	0.04	0.04	0.02	0.33	0.20	0.27	NA
	18	1602	1275	327	0.03	0.03	0.05	0.02	0.14	0.16	0.45	NA
	22	1593	1269	324	0.01	0.02	0.03	0.02	0.07	0.14	0.25	NA
1.05	22	1596	1262	334	0.23	0.19	0.25	0.16	2.03	2.02	4.27	0.09
	24	1592	1251	341	0.23	0.20	0.21	0.26	2.70	3.20	6.80	0.11
	26	1588	1240	349	0.15	0.08	0.13	0.19	2.60	3.53	8.86	0.23
	28	1587	1230	357	0.11	0.04	0.07	0.10	1.42	2.69	6.72	0.16
	30	1586	1225	360	0.11	0.03	0.06	0.08	1.03	2.47	6.55	0.17
	32	1582	1217	365	0.11	0.03	0.08	0.06	0.73	2.30	7.06	0.32
	34	1579	1213	366	0.12	0.03	0.12	0.12	1.07	2.19	9.51	1.39
	36	1579	1195	384	0.22	0.31	0.67	0.30	1.71	3.42	16.14	1.80
	42	1579	1191	389	0.12	0.04	0.10	0.11	1.72	2.58	9.08	0.42
	50	1575	1179	396	0.15	0.04	0.12	0.16	2.25	2.47	9.55	0.47
1.3	25	1590	1267	323	0.11	0.01	0.01	0.00	0.73	0.45	0.49	0.20
	27	1593	1261	332	0.22	0.03	0.07	0.05	0.64	0.40	0.50	0.19
	30	1600	1275	326	0.25	0.03	0.07	0.04	0.57	0.50	0.48	0.17
	33	1598	1273	325	0.57	0.06	0.12	0.10	0.69	0.83	0.61	0.48
	36	1601	1276	325	0.59	0.05	0.21	0.08	0.83	1.22	0.90	0.61
39	1597	1279	318	0.25	0.04	0.09	0.06	0.57	0.60	0.46	0.21	
a-C:H	NA	1625	NA	NA	0.08	0.38	0.44	0.15	0.69	0.03	NA	NA



# CURRICULUM VITAE

## PERSONAL INFORMATION

First name: Thi Kim Cuong

Last name: LE

Nationality: Vietnamese

Date and place of birth: February 12<sup>th</sup>, 1986, Binh Dinh, Vietnam

Family situation: married and one daughter (three year old)

## WORK ADDRESS

Institute of Molecular Science at Orsay (ISMO)

University of Paris-Sud

Building 210, rue Henri Becquerel

E-mail: [thi-kim-cuong.le@u-psud.fr](mailto:thi-kim-cuong.le@u-psud.fr), [kimcuong.physics@gmail.com](mailto:kimcuong.physics@gmail.com)

## QUALIFICATION PROFILE

- Solid experience in Raman spectroscopy of carbonaceous materials.
- Soot particles formation in combustion chamber.
- Expert in optical setup for visible Raman spectroscopy and use of commercial IR and Raman spectrometer.
- Proficient UV-VIS and VUV spectroscopy, fluorescence spectroscopy, CW and pulse laser.
- Good programming skills with Matlab. Experienced in using graphing software Origin, Excel, text editing software Microsoft Word, Power point, Latex (starting).
- Languages: Vietnamese (native), English (fluent), French (little)

## EDUCATION

- 03/2017                      Ph.D in physics. Dissertation: "Raman spectroscopy of soot produced in low pressure flames: ex situ analyses and online gas phase studies" supervised by Dr. Thomas Pino  
ISMO, University of Paris Sud
- 01/2012                      Master of Science in physics (rank 1<sup>st</sup>). Dissertation:  
"Experimental investigation of pulsed laser oscillation process by passive mode locking of a Nd:YVO<sub>4</sub> laser" by Prof. Dr. Nguyen Dai Hung

Vietnam Academy of Science and Technology

07/2008 Bachelor of Science (Physics teaching method) (rank 3<sup>rd</sup>), Qui Nhon University

### EMPLOYMENT HISTORY

10/2013 – 03/2017 PhD student at ISMO, University of Paris Saclay, France

03/2012 – 09/2013 Research assistant at the Center for Quantum Optics, Vietnam Institute of Physics, Vietnam Academy of Science and Technology.

### RESEARCH VISITS AND GRADUATE SCHOOLS

07/2015 Summer school Basic Aerosol Science in Vienna (Austria)

06/2015 Summer school SPEC-ATMOS in Frejus (France)

12/2012 International school on Optics, Spectroscopy, and Applications (Organized by Vietnam and France in Vietnam)

### PRIZES AND AWARDS

2013 Won PhD scholarship for Vietnamese teaching staff offered by the Government of Vietnam and Embassy of France

2008 Champion of Teaching Methods at Quy Nhon University.

2008 Second place in National Physics Olympic.

### PUBLICATIONS

- 1. Differential backscatter Raman cross section of several carbonaceous materials**  
K.C. Le, Christophe Lefumeux and Thomas Pino  
In preparation
- 2. On the polarization dependence of Raman scattering spectra of soot nanoparticles in the gas phase**  
Thi Kim Cuong Le, Benoit Héraud, Christophe Lefumeux and Thomas Pino  
Proceeding of the 9<sup>th</sup> International Conference on Optics and Photonics, Ninh Binh, Vietnam (2017), 88, ISBN: 978-604-913-578-1 (2017)
- 3. Polyaromatic disordered carbon grains as carriers of the UV bump: FUV to mid-infrared spectroscopy of laboratory analogs**

- L. Gavilan, K.C. Le, T. Pino, I. Alata, A. Giuliani and E. Dartois  
Astronomy & Astrophysics, (2017), accepted.
4. **VUV spectroscopy of carbon dust analogs: contribution to interstellar extinction**  
L. Gavilan, I. Alata, K.C. Le, T. Pino, A. Giuliani, E. Dartois  
Astronomy & Astrophysics, 586, A106 (2016)
  5. **Structure and high photocatalytic activity of (N, Ta)-doped TiO<sub>2</sub> nanoparticles**  
N. T. H. Le, T. D. Thanh, V.-T. Pham, T. L. Phan, V. D. Lam, D. H. Manh, T. X. Anh, T. K. C. Le, N. Thammajak, L. V. Hong, S. C. Yu  
Journal of Applied Physics, 120, 142110 (2016)
  6. **Dynamics of All Solid-state Nd:YVO<sub>4</sub> picosecond laser amplifier**  
Pham Hong Minh, Nguyen Van Hao, Le Thi Kim Cuong, Pham Huy Thong  
Proc. Of the 2<sup>nd</sup> Na. Conf. on Physics, Vietnam, 105-1100 (2011).

### CONFERENCE PRESENTATIONS

1. Talk: “Detection of the Raman spectra of soot in the gas phase”, GDR Suie conference, October 10-14, 2016, Orléans, France.
2. Talk: “Raman back-scattering cross section for various carbonaceous particles”, Black Bloom workshop, September 20-22, 2016, Marseille, France.
3. Talk: “Raman wavelength detection and ranging of black carbon and soot in the gas phase”, PhD day at Institut des Science Moléculaires d’Orsay (ISMO), April 14, 2015, Orsay, France.
4. Talk: “Raman detection and ranging of black carbon and soot in the gas phase”, Scientific day of EDOM, February 18, 2015, Orsay, France.

### REFERENCES

Dr. Thomas Pino  
CNRS research Director  
Institut des Sciences Moléculaires d’Orsay (ISMO)  
Building 210, Office 11  
Paris-Sud university  
91 405 Orsay, France  
Tel: [+33 \(0\)1 69 15 73 19](tel:+330169157319)  
E-mail: [thomas.pino@u-psud.fr](mailto:thomas.pino@u-psud.fr)

Dr. Pascale Desgroux  
CNRS research Director  
Laboratoire de Physicochimie des Processus de Combustion et de l’Atmosphère (PC2A)  
Building C11  
Lille 1 university  
59 655 Villeneuve d’Ascq Cedex, France

Tel : [+33 \(0\)3 20 43 49 30](tel:+33(0)320434930)

E-mail: [pascale.desgroux@univ-lille1.fr](mailto:pascale.desgroux@univ-lille1.fr)

**Titre :** Spectroscopie Raman de carbone-suies produites dans une flamme basse pression : analyses ex situ et directement en ligne dans la phase aérosol

**Mots clés :** carbone-suies, spectroscopie Raman, phase gazeuse, flamme basse pression

**Résumé :** Chaque année, une quantité de  $10^7$  tonnes de suie est produite à l'échelle mondiale. Le carbone-suie dans l'atmosphère a des effets graves sur le changement climatique et la santé humaine. Les impacts dépendent de nombreux facteurs comme les composés organiques adsorbés, le vieillissement et les processus de mélange. Par conséquent, afin de réduire la quantité de suie émise, outre l'examen des facteurs mentionnés, les études de la cinétique de formation, de la structure et des propriétés optiques des suies sont également essentielles. Il existe plusieurs méthodes optiques dans les études sur la suie. La spectroscopie Raman occupe un rôle particulier puisqu'elle est un outil puissant pour l'étude structurale des matériaux carbonés grâce à sa sensibilité aux structures à l'échelle moléculaire. Dans ce travail, des sections Raman différentielles de suies et quelques autres particules carbonées ont été mesurées pour progresser vers la spectroscopie Raman quantitative de ces

particules. Les suies produites par des flammes d'éthylène pré-mélangées à basse pression ont été étudiées par mesure Raman ex-situ sur des films déposés et des mesures Raman in-situ (en ligne) dans la phase gazeuse. La combinaison de la spectroscopie Raman de suies échantillonnées sur substrat avec les spectroscopies infrarouge et optique et la microscopie électronique en transmission a permis de progresser sur l'interprétation des spectres Raman de suie. Les mesures en phase gazeuse, obtenues pour la première fois, fournissent de nouvelles informations sur la naissance des suies et leurs structures dans les flammes à basse pression avec, par exemple, la détection d'une grande quantité d'atomes de carbones hybridés sp lors de la formation et de la croissance des premières suies. Ces études ouvrent la voie à la détection et à l'analyse des suies directement en phase gazeuse et à leur détection quantitative dans l'atmosphère au travers de leurs spectres Raman.

**Title:** Raman spectroscopy of soot produced in low pressure flames: ex situ analyses and online gas phase studies

**Keywords:** Soot, black carbon, Raman spectroscopy, gas phase, low pressure flame

**Abstract:** Every year, an amount of  $10^7$  tons of soot is produced on the world scale. Soot, as part of atmospheric black carbon, has serious impacts on climate change and human health. The impacts depend on many factors including adsorbed compounds, aging and mixing processes. Therefore in order to reduce the soot amount, besides considering these mentioned factors, the study of formation kinetics, structure and optical properties is also essential. There are several methods applied in soot investigations. Raman spectroscopy plays a particular role as it is a powerful tool for structural investigation of the carbon-based materials because it is sensitive to molecular structures. In this work, differential Raman cross sections of soot and some other carbonaceous particles were measured to

progress toward quantitative Raman spectroscopy. Soot particles produced by premixed ethylene flames at a low pressure were investigated by ex-situ Raman measurement on deposited films and in-situ (online) Raman measurement in the gas phase. Combination of the Raman spectroscopy of soot sampled on substrates with infrared and optical spectroscopy and transmission electron microscopy allowed progressing on the interpretation of soot Raman spectra. The online gas phase measurements provided a novel view on soot birth and structures in low pressure flames with, for instance, the detection of a large amount of sp hybridized carbon atoms during nascent soot growth. These studies pave the way to soot detection and analysis directly and quantitatively in the atmosphere.

